Dottorato di Ricerca in Ingegneria Civile e Architettura
Graduate School in Civil Engineering and Architecture

DICAr - Dipartimento di Ingegneria Civile e Architettura
Facoltà di Ingegneria, Università di Pavia
Department of Civil Engineering and Architecture
Faculty of Engineering, University of Pavia

XXX Cycle (XVI new series)

Eulerian–Lagrangian modelling of large floating debris transport during floods

Ph.D. Thesis

Elisabetta Persi

Advisors

Prof. Stefano Sibilla

Prof. Gabriella Petaccia

Ph.D. coordinator:

Prof. Ferdinando Auricchio

March 2018

Acknowledgments

First of all, I would like to thank my advisors, Prof. Stefano Sibilla and Prof. Gabriella Petaccia, who inspired this research, supported me and helped in every aspect of the thesis. Their availability and competences were of great advice for advancing in the research.

Thanks to Prof. Pilar Brufau and Prof. Pierfranco Costabile, who reviewed the Ph.D. thesis, providing insightful comments and observations.

My sincere thanks go to Prof. Pilar García-Navarro and Prof. Pilar Brufau, from the Fluid Dynamics Laboratory (LIFTEC) of the University of Zaragoza. They gave me the opportunity to work with their team, accessing to the laboratory and research facilities. Their personal commentaries and suggestions left an outstanding trace on the research. Thanks to Prof. José Ignacio García Palacín for his fundamental help in the realization of the experimental campaign and to the entire group of Fluid Dynamics of the University of Zaragoza for welcoming me and being of support during the time spent there.

Special thanks go to Dr. Andrea Fenocchi, who gave me countless great advices, shared his profuse knowledge and explained the most unknown aspects of the academic world. Personal conversations with Prof. Paolo Ghilardi and Prof. Sauro Manenti provided significant opportunities for reflection.

I would like to thank Prof. Francesco Comiti, Dr. Ana Lucía Vela and Prof. Andrea Andreoli, who shared their knowledges on wood transport in the Rienz river and their abilities in field surveys.

I am grateful to Dr. Virginia Ruiz-Villanueva for her precious advices and for data sharing, and to all the other researchers that I have met for their enthusiasm and commitment.

Thanks to Pierangelo Bergamaschi for his priceless help in the design of the hydrodynamic balance, and to Dr. Gianluca Alaimo and Dr. Stefania Marconi from Proto-lab, the additive manufacturing laboratory of the University of Pavia directed by Prof. Ferdinando Auricchio, for the realization of the 3D-printed parts.

Thanks to Maria Giovanna Balzi, Stella Cogliandro, Riccardo Castagnola and Ilaria Livraghi who contributed with their efforts to the Ph.D. research.

Thanks my entire family, who supported me and tolerated my work commitments for these long, endless three years, and to my friends, involved in conversations about floating debris by train, by phone and even at the pub, nevertheless offering aid in dark Ph.D. times.

Special thanks go to Simone for sharing good and bad times, keeping on encouraging me, no matter what. Thanks!

Table of contents

Abstract

The work presented contributes to the development of an appropriate numerical model that incorporates the motion of floating rigid bodies in the estimation of flood risk. It considers the two-dimensional transport of floating objects, predicting their trajectories, orientation and the interaction with other bodies or with inline structures.

Since the main focus is on large bodies, each object is treated as a single entity, which is reflected in the Lagrangian approach of the Discrete Element Method, one-way coupled with the Eulerian solution of the Shallow Water Equations. The forces exerted by the flow control the translation and the rotation of the bodies.

The development of the model requires to simplify the shape of the floating bodies, in order to focus on the equations and exclude complicated fluid-solid interactions. The proposed formulation focuses both on perfectly symmetric elements, spheres, and on cylinders, which are axial-symmetric and for which orientation matters. The equations of transport, i.e. of translation and rotation, take into account such variability with an appropriate computation of the forces.

The translation equations are derived by the Maxey–Riley equation, which was originally developed for small spheres in creeping flows and can be extended to large bodies and higher Reynolds numbers by taking into account the flow velocity distribution along the body length. The extension to cylinders is obtained by including the variability of the drag and side coefficients with the body orientation.

To simulate body rotation, two formulations are presented, in order to evaluate which solution has the best performances in modelling the behaviour of floating bodies. As regards spheres, the main effect of rotation is in the variation of the trajectory. For cylinders, computing rotation is extremely important to predict the body orientation before the interaction with fixed inline structures: bodies aligned with the flow have lower possibility to trigger the formation of an obstruction. This results to be the most critical aspect of the simulation, due to the high sensitivity of rotation to local turbulence, domain characteristics and features of the numerical scheme.

To assess the validity of the mathematical formulation and help in the choice of the parameters, experimental campaigns were also carried out. Firstly, the measure of the hydrodynamic coefficients of semi-submerged cylinders was performed, to obtain a law for the variation of the coefficients with orientation. The measurements were performed with a hydrodynamic balance, built and installed in a prismatic flume at the Department of Civil Engineering and Architecture of the University of Pavia. The results helped in increasing the reliability of the hydrodynamic forces estimation.

A second group of experiments was carried out at the laboratory of the Department of Science and Technology of Materials and Fluids of the University of Zaragoza, where rigid body transport was replicated in a channel with side obstacles of different shape and number, to provide useful information for the calibration of the proposed model.

The model calibration took advantage also of a real-scale experiment realized in a reach of the Rienz river by researchers of the University of Bolzano, who traced the movement of real logs during high flow events. The application of the model to this real-life fluvial case helped in adapting the formulation to a real-scale domain. The presence of distributed inline obstacles is taken into account, and wood deposition and remobilization are modelled, too.

The thesis in organized in 6 chapters. Chapter 1 describes the characteristics of floating transport, the state of the art of its modelling and introduces the methodology selected to solve the problem. The description of the mathematical model for entrainment, rigid body transport and collisions is presented in Chapter 2. The numerical implementation is reported in Chapter 3: details are provided about the final formulations tested, the coupling with the hydraulic model and the strategies to implement the various steps of the DEM. In Chapter 4 the details regarding the hydrodynamic coefficients of cylinders are summarized. The characteristics and the results of the experimental campaigns to measure the drag and the side coefficient for semi-submerged bodies with variable orientation are illustrated. Chapter 5 reports the calibration of the model on literature data and on the results of the experimental campaign performed at the University of Zaragoza. Finally, in Chapter 6, the model is applied to the real-scale case of the Rienz river.

Chapter 1
Problem description and methods

1.1. Abstract

The Chapter outlines the reasons for including the transport of floating rigid bodies in hydraulic risk assessment. To clarify the origin of the problem, the main processes involved in material entrainment are explained, with a specific focus on woody debris. Also the critical issues and the conditions that trigger obstruction formation are summarized.

The state of the art on rigid body transport is then outlined, highlighting the strengths of the existing approaches and their inspiring aspects. Several steps need to be taken into account: the incipient motion, the model of transport itself and the dynamics of the interaction among water and solids. An overview on the hydrodynamic coefficient for spheres and cylinders and on the modelling of the interactions among bodies is also presented. Finally, the line of investigation chosen for this thesis is provided.

1.2. Rigid body transport during floods

Flood risk assessment is usually carried out using 1D or 2D models which can estimate flooded areas accounting for the influence of existing man-made structures. To estimate the risk, two groups of information are generally considered: hydraulic and topographical data. However, during a flood, large amounts of materials can be transported by the flow, with different conditions according to their physical characteristics. Gravel and

heavy sands move in the deepest part, while floating objects remain near the water surface. Their presence may be unnoticed while the flood is passing, especially for bed transport, but they are well visible in post event surveys. Both tend to create large deposits once the flood has passed and their effect during the event may be even devastating.

The consequences of heavy solids transport, such as debris flow and bed erosion especially around bridge piers, are largely documented and studied. Their impact on hydraulic risk and on human safety is well known and in areas prone to this phenomena, monitoring is provided (e.g. Hürlimann et al. 2003; Comiti et al. 2014) and security measures are introduced, like check dams or metal nets (Remaître et al. 2008; Badoux et al. 2009; Takahashi 2014).

The presence of floating material is, on the contrary, normally disregarded, although it has been proved that it may significantly intensify the drawback of the flood. Vegetable materials, plastic objects and even cars or containers, which are initially located in the floodplains and may be entrained during the event, can flow on the water surface, moving downstream and reaching urban areas. In presence of bridges or culverts, they may block openings and increase the backwater effect, already triggered by the presence of piers or of channel narrowing. Generally, the problem of floating transport is solved with practical measures (Uchiogi et al. 1996; Kasai et al. 1996; Bezzola et al. 2004; Bradley et al. 2005) although, in the recent years, some attempts of physically-based design of safety structures have been proposed (Denk and Rimböck 2008; Comiti et al. 2012; Schmocker and Weitbrecht 2013).

Most of the scientific literature deals with floating body transport as a complementary aspect of river dynamics (Picco et al. 2017), focusing on wooden materials. Many researchers are interested in the morphological impact of the motion and deposition of dead wood on the river bed, studying their relation with bars and scour formation (e.g. Abbe and Montgomery 1996; Bocchiola 2011; Gurnell 2012, Ravazzolo et al. 2015). The analysis of the causes of incipient motion is a matter of research

(Braudrick and Grant 2000; Merten et al. 2010), as well as the study, with laboratory experiments, of the transport-deposition dynamics and of jam formation (Braudrick and Grant 2001; Bocchiola et al. 2005; Bocchiola et al. 2008; Bertoldi et al. 2014; Crosato et al. 2013; Welber et al. 2013). Wood motion during floods is also monitored (e.g. Ravazzolo et al. 2014), considering only its effect on river bed forms or on the aquatic ecosystem, while no attention is paid to the connection with flood risk.

A hydraulic safety-oriented approach can be found when dealing with wood transport in mountain areas. Lange and Bezzola (2006), Comiti et al. (2008) and Ruiz-Villanueva et al. (2014a) present different situations in which post-event surveys highlighted the effect of wood transport in increasing the hazardousness of the flood, also due to the presence of urban structures. To estimate the wood volume which can reach the river in a certain basin, several researchers are focusing on wood budgeting, exploiting ground imagery and other remote sensing techniques to quantify the fluxes of transported material (MacVicar and Piégay 2012; Schenk et al. 2014; Benacchio et al. 2017). This datum is, however, very variable and may be not sufficient. Extreme or unexpected events may strongly alter the usual behaviour of a basin, as observed, for example, in recent events in Italy, like in Ligury (November 2011 and October 2014, Silvestro et al. 2016a and Silvestro et al. 2016b), and in the Apennines in the Provinces of Parma and Piacenza in 2014 and 2015 (rivers Parma and Baganza near Parma, rivers Trebbia and Nure near Piacenza, Corsini et al. 2017). During these events, heavy rains triggered several landslides in rural areas and directed water, terrain and woods from the higher order basins to the main river, and then to urban areas. The transport of large amounts of floating materials from upper forested areas caused bridge clogging, calling the attention to the effects of the presence of wood during floods even in areas where wood transport had never been considered as an actual risk.

To overcome the limits highlighted by the sole consideration of the wood budgeting along a stream, the probability for wooden material to reach a

stream, or to be reached by the flow and entrained, has to be determined. Particular attention has then to be paid to the main mechanisms of wood entrainment, namely landslide and debris flow in upper basins, and bank erosion in the lower reaches (Steeb et al. 2017) as well as to the capability of tree roots to resist erosion (Holloway et al. 2017).

The origin of the wood entrained in a river can influence the feature of the transported material. Dead wood deposited from previous events and lying on the river bed is generally smooth, without branches or leaves, with small roots, weak and easy to break. Wood from landslides in burnt areas shows similar characteristics (Tinker and Knight 2000), while wood from the floodplains (Picco et al. 2016) is generally smaller, like branches, with fine attached materials, and quite resistant. Landslides, debris flow or bank erosion in forested areas entrain longer elements, as well as entire trees, strongly branched and resistant to collisions. This latter form of entrainment is considered the most dangerous for flood risk (Comiti et al. 2016).

The characteristics of the transported wood affect its behaviour in presence of obstacles. Existing classifications identify Large Wood (LW), i.e. longer than 1 m and with a diameter larger than 0.10 m (Keller and Swanson 1979; Andrus et al. 1989), and strongly branched wood as the elements more prone to clogging. The obstruction formation is the key issue for the evaluation of hydraulic risk. The understanding of its dynamic is not complete, due to the complexity of the interaction between water, floating solids, sediment and rigid structures. For this reason, clogging has been examined with a systematic observation of real events (Diehl 1997) as well as with laboratory experiments to evaluate the entrapment probability (Schmocker and Hager 2011). The effects of pier shape and of other parameters, such as wood density, log length, log type and stiffness (e.g. De Cicco et al. 2015, Hartlieb 2012) has also been investigated, to provide an evaluation of the backwater effect.

When considering the interaction of floating debris with the flow, most of the literature focuses on wooden materials, but trunks and logs are not the

only objects which may be entrained during a flood. Allen et al. (2014) studied the mobilization of small plastic object in urban environment, which can contribute to the occlusion of culverts or water drains, thus reducing the drainage capability of the sewing systems.

Even more dangerous are cars and motorbikes, as well as boats and containers (Rodríguez et al. 2006; Pritchard 2013) which can be entrained and transported by the flow in urban areas, hitting people or blocking bridge spans. Calculating the extension of the flood in a street network allows to take into account the effect of water depth and flow velocity and to verify the hazardousness for vehicles and pedestrians (Russo et al. 2013; Velasco et al. 2015; Martínez-Gomariz et al. 2016). Analysis of the entrainment of cars are carried out both numerically (Teo et al. 2013; Arrighi et al. 2015) and experimentally (Xia et al. 2011, Teo et al. 2012), although the transport of large number of cars and the clogging associated with their involvement is not yet a part of the standard procedure for flood risk assessment in urban areas.

This overview highlights how dealing with floating debris includes multidisciplinary aspects, from estimating slope stability, to botanic knowledge to evaluate wood resistance to erosion, awareness of critical sections for urban rivers and the knowledge of the most frequently flooded areas, in order to avoid the presence of elements which may be entrained by the flood. The sum of all this information is just the starting point. To make them useful for safety purposes, it is essential to introduce floating rigid body transport in hydraulic risk assessment.

1.3. Strategies to model log transport

Some attempts of modelling rigid body transport can be found in the literature, with different approaches and various extent. Early studies focus on the motion of bodies lying on the river bed, which is important both for entrainment and for re-mobilization of temporarily deposited objects.

Then, the motion on the water surface is analysed, too, with main reference to woody materials.

Wood entrainment is the first step that needs to be verified when considering the motion of floating rigid bodies. Its modelling has been theorized firstly by Braudrick and Grant (2000), accounting for the motion of cylinders and cylinders with roots. Their model, although simply based on a force balance and calibrated with laboratory flume experiments, is still the main reference used by researchers in this field. Further investigation, involving experimental and analytical studies, have confirmed that the cylinder position is essential for the initiation of motion. Logs parallel and perpendicular to the flow move differently and at different times, the latter being the first to start rolling away. A second fundamental parameter is the bed roughness, which influences the cylinder behaviour. The highest difference in log entrainment can be found between coarse, and almost immobile, materials and mobile fine material. In the second case, local scouring strongly modifies the flow distribution around the cylinder, requiring an accurate analysis of the parameters for the application of the classic entrainment model (e.g. Bocchiola et al. 2006; Crosato et al. 2013).

Dealing with floating rigid bodies, the focus moves to transport modelling. In general, a distinction is made among transport regimes, which can be uncongested, semi-congested and congested. The difference lays basically in the input rate of wood in a stream, and was verified by laboratory experiments (Braudrick et al. 1997). It has been demonstrated that these regimes involve an increasing interaction among floating elements, with the congested and semi-congested transport being more prone to jam (and obstruction) formation (Bocchiola et al. 2008; Welber et al. 2013). The amount of interactions affects also the strategy to model floating body motion, since if uncongested transport is considered, debris have a minor effect on the flow. Furthermore, the distinction can be useful to create different scenarios for hydraulic risk assessment (e.g. Ruiz-Villanueva et al. 2013).

The motion of floating bodies on the water surface can be considered as the interaction of a continuous phase (water) and a discontinuous one (debris). How to tackle the presence of discrete elements in a flow is still an open issue.

One possible approach, is to move an amount of debris entrained in the flood, trying to predict its final position following the main velocity direction along the entire river basin (Mazzorana et al. 2011). In this case, the 2D displacement of a volume of wood, computed by considering the wood budgeting, is performed. However, the physical response of the single floating objects on the water is disregarded, and only the final outcomes are considered.

A different perspective is the application of the Smoothed Particles Hydrodynamics (SPH) technique. This method provides a Lagrangian description of the motion of the water–considered as a group of particles– and of the rigid bodies–which are single large particles or rigid shells. It allows the coupling of the two phases, one- or two-way coupling, computing their reciprocal influence with high precision. 2D and 3D applications that couples the Shallow Water Equations with the motion of rigid bodies can be found in the literature (Solenthaler et al. 2011; Bilotta et al. 2014; Prakash et al. 2014; Amicarelli et al. 2015). The method is generally applied for 3D simulation, and is particularly valid for rapid events, as dam breaks, tsunamis and levee breaches (Teng et al. 2017).

Another possibility is the use of hybrid 2D methods, characterized by the coupling of two different techniques for the solution of the two phases. These methods estimate the flow velocity and calculate the motion of the rigid body with an Eulerian-Lagrangian approach. As regards the hydraulic modelling, different techniques can be applied, such as the solution of the full Navier-Stokes equations with the Volume of Fluid method (e.g. Fekken 1975), or, more frequently, the numerical solution of the Shallow Water Equations with a finite volume code. In this second case, either a kinematic or a dynamic model can be applied to compute the motion of the discontinuous phase.

Dynamic models require the computation of the hydrodynamic forces exerted by the flow on the rigid body, so that the body acceleration can be calculated. The critical aspect of this technique is the evaluation of the correct forces acting on the body and their computation, which can be integrated on the body length or approximated. Other relevant issues are (i) the method selected to take into account floating body interactions and (ii) the coupling degree, i.e. the feedback from the discrete element model to the hydraulic model. In the literature, few examples can be found (Alonso 2004; Stockstill et al. 2009) but no shared opinion exist on the most appropriate dynamic description.

Recently, Ruiz-Villanueva et al. (2014b) proposed an alternative hybrid approach, developing a kinematic model for transport, rotation and collisions of wooden cylinders, fully coupled with the Eulerian hydraulic 2D software IBER. Their contribution addresses the problem of the presence of wood during floods in an accurate manner and the kinematic approach is quite easy to implement. However, the strong simplification implied by assigning the flow velocity to the logs may reduce the accuracy in the prediction of their motion.

The degree of coupling of the two models, i.e. the one selected to represent floating body motion and the other to simulate water dynamics, is an important aspect for this kind of simulations. When an obstruction occurs, the presence of wood limits the section available to the flow, causing the increase of the water level upstream of the structure. This backwater effect should be modelled in order to realistically reproduce the consequences of clogging and the change of the flooded areas. In this case, which can be included in the above-mentioned congested or semi-congested regimes, a two-way coupling of the models is required, as done by Ruiz-Villanueva et al. (2014b). On the other hand, if the focus is on the physics of transport of singular or few elements, their effect on water flow is negligible and a one-way coupling can be sufficient to account for the action of water on the rigid bodies (uncongested regime of transport).

1.4. The dynamics of floating rigid bodies

Dynamic models for the motion of rigid bodies allow one to describe with more accuracy the physics of transport. For their proper application, it is however essential to determine which forces have to be taken into account. The approaches to deal with wood transport described up to now did not always include the same forces nor investigated in detail the contribution of each component. Furthermore, these forces were often computed as if totally submerged bodies were considered, while floating debris are in general semi-submerged objects moving on the water surface, depending on their density.

It is thus interesting to leave, for the moment, models dealing strictly with wood transport, widening the field of investigation to the general dynamic description of the motion of rigid bodies in a flow.

The Basset-Boussinesq-Oseen (BBO) equation (e.g. Corrsin and Lumley 1956) gives a general physical interpretation of the unsteady force on spherical particles settling in a fluid at rest. It was extended to the case of non-uniform flows by Maxey and Riley (1983). The so-called Maxey–Riley equation is valid for rigid small spheres in non-uniform creeping flows (i.e. with a particle Reynolds number $Re_p \ll 1$). The total force acting on the rigid body is the sum of different components. The equation considers the following contributions to the total force acting on a particle:

- the viscous Stokes drag force, which is the component of the hydrodynamic force in the direction of the relative velocity;
- the added mass force, that is the force related to the additional inertia of the fluid surrounding the particle;
- the pressure gradient force;
- the buoyancy force, since the equation describes the settling of a body in a fluid;

- the Basset history term, which arises because of the delayed development of the boundary layer due to the viscous-unsteady effects, and is the only non-linear term of the equation.

External forces may also be included in order to model, for example, particle interaction. The validity in case of non-uniform flows is provided by the computation of the Lagrangian derivative for the flow acceleration.

The reasons for including each term depend on the physics of the problem considered, and will be thus analysed in detail with reference to the transport of floating bodies in Chapter 2.

Several authors employed this equation to solve problems related to the motion of small particles at low Reynolds numbers (Magnaudet and Eames 2000; Tagawa et al. 2013). Recently, the equation was extended to higher Reynolds number flows and to the case of non-spherical particles (Yin et al. 2003; Mandø and Rosendahl 2010). These extension is obtained by implementing a general expression for the hydrodynamic force, abandoning the Stokes flow limitation and including the effects of variability with the Reynolds number and with the body shape in the choice of the proper coefficients.

When dealing with spheres, an update of the Maxey–Riley equation is provided by the inclusion of the lift force, which is a component of the hydrodynamic force perpendicular to the relative velocity. This force, analytically studied by Saffman (1965), arises because of the different pressure distribution around a spherical body in a uniform shear flow, and is often referred to as the *shear-induced lift force* (Auton et al.1988). It contributes to deviate the body trajectory and depends on the flow vorticity.

In addition to the shear-induced lift, if a sphere is forced to spin in a uniform flow, the Magnus effect arises and increases the lift force on the particle, by augmenting the lift coefficient. The two effects are expected to be superimposable, at least for small Reynolds number (Magnaudet and Eames 2000). The combination of these two phenomena was studied experimentally (e.g. Bagchi and Balachandar 2002; Truscott and Techet

2009) showing that the distinction of the corresponding coefficients is not easily identifiable. Basically, the effect of both terms is the deviation of the sphere trajectory. For this reason, a unified lift coefficient is provided, as a function of the body rotation rate. In order to compute the proper coefficient and thus to adequately model the shear-induced lift force and the Magnus effect, the body rotation has to be computed, too.

The body shape affects strongly rotation: for symmetrical bodies it only influences the lift coefficient, while for elongated bodies it alters the entire hydrodynamic force. For this reason, a joint computation of planar and angular displacement needs to be provided.

The torque on spheres is computed by applying the conservation of linear and angular momentum (Bagchi and Balachandar 2002). For non-spherical bodies, the pressure distribution on the body surface varies with orientation. It is thus necessary to take into account the displacement of the centre of pressure–i.e. where the hydrodynamic force is applied–with respect to the body centre of gravity (Mandø and Rosendahl 2010). The torque on the elongated body is computed as the sum of three components: offset torque, resistance torque and cross terms, which are originated by the different moment of inertia with the different orientations and are meaningful for 3D modelling.

The torque due to the offset depends strongly on the computation of the location of the pressure centre, which can be estimated in different ways but generally is located at a maximum distance of one quarter of the length from the mass centre (Marchildon et al. 1964; Rosendahl 2000; Yin et al. 2003).

The torque due to resistance represents the viscous effects for rotation and tends to diminish the rotation of the body. Its expression has been derived for spherical particles and then extended to ellipsoids and elongated particles under Stokes condition (Jeffery 1992; Cox 1970; Cox 1971). For higher Reynolds number, the integral on the body length of the appropriate drag force expression is required.

1.5. Hydrodynamic and added mass coefficients

Overall, the computation of translation and rotation of spherical or cylindrical bodies depends on the correct evaluation of the forces, and in particular of the added mass and the hydrodynamic coefficients.

The added mass coefficient, which represents the additional water volume accelerated when the body is accelerating with respect to the flow (made non dimensional with the water volume displaced by the body), varies mainly with the body shape and orientation. For spheres, which are perfectly symmetric, the choice of the correct coefficient is generally simple. The added mass coefficient is constant, equal to $\frac{1}{2}$ for submerged bodies (Batchelor 1967), corresponding to an increase of half volume to the body original one.

The drag and lift coefficients depend on several parameters, such as the particle Reynolds number, the body roughness, shape and orientation, when applicable. The drag coefficient is widely studied in the literature. Empirical curves, or equations, exist, taking into account the variation with the particle Reynolds number ($Re_p = \frac{\boldsymbol{V}D}{\nu}$, where $\boldsymbol{V}$ is the velocity, D is the particle diameter and ν the kinematic viscosity of the fluid) and the surface roughness (see for example Hoerner 1985 or Chow 1979).

The estimation of the lift coefficient is more complicated. It can be set equal to zero for the case of a sphere simply translating in a uniform flow and has different values if a shear is present, or if the sphere itself is rotating. This two contribution corresponds to the formerly mentioned shear-induced lift and Magnus-induced lift.

These effects are often evaluated separately The shear-induced lift is derived by analytical and experimental studies of a sphere in a shear flow (Auton 1987; Van Nierop et al. 2007). Experiments on spinning spheres in wind tunnel or in water basins lead to the evaluation of the Magnus-induced lift coefficient, generally parametrized on the body rotation rate, on surface roughness or on the ratio of the maximum peripheral speed on

the speed of the sphere's centre (Watts and Ferrer 1986; Bluemink et al. 2009). The correlation with the Reynolds number appears weaker than for the drag coefficient.

Generic values are also available, including the shear and the Magnus effects. Such values are obtained both theoretically (e.g. Saffman 1965; Rubinow and Keller 1961; Auton 1988) and experimentally (e.g. Barkla and Auchterlonie 1971; Tsuji et al. 1985; Sridhar and Katz 1994, Truscott and Techet 2009). The results are expressions of the variation of the side coefficient as a function of the ratio between the maximum peripheral speed ($\boldsymbol{\omega} r$, i.e. the product of the angular velocity $\boldsymbol{\omega}$ and of the body radius r) on the relative velocity at the body centre of mass.

The interaction between cylinders and fluids has been widely investigated in the past with reference to a number of diverse engineering applications (Zdravkovich 1997), from cylindrical bridge piers (e.g. Ahmed and Rajaratnam 1998; Melville 1975) to cables (Newman and Karniadakis 1997; Zhao et al. 2009) or elongated particles in industrial flows (Yin et al. 2003; Geng et al. 2007). In this dissertation, the focus is on finite cylinders which can freely move on the water surface, examining the variation of the hydrodynamic coefficients of small wooden rods, whose shape and characteristics are similar to the large woody elements modelled for hydraulic risk assessment.

The added mass coefficient is generally considered equal to 1 for submerged cylinders aligned with the flow (Dean and Dalrymple 1991). The effect of the variable orientation is taken into account for elliptical bodies, but only parallel and perpendicular configurations are considered (e.g. Brennen 1982). No detailed analysis are available for cylinders, and in particular for floating ones.

Drag and side coefficients are commonly expressed in relation to the particle Reynolds number (e.g. Chhabra et al. 1999), but several other parameters should be taken into account, as the body features, slenderness, roughness and Mach number, when applicable (Hoerner 1985). Some re-

searchers studied the drag of trunks, but focused on vertical cylinders to resemble the effects of bridge piers or of emerging vegetation (e.g. Troesch and Kim 1991; Sarpkaya 1986; Nepf 1999).

The study of the hydrodynamic coefficients of horizontal cylinders is performed with laboratory (Gippel 1996) or field experiments on real-size logs (Chaplin and Subbiah 1998; Hygelund and Manga 2003) for fully submerged elements. The variation with orientation, body submergence and blockage ratio is taken into consideration.

A benchmark for the estimation of the hydrodynamic coefficients for yawed cylinders is the work of Hoang et al. (2015). The measure of the lift and side coefficients, in addition to drag, for an infinite yawed cylinder in a wind tunnel is provided for the first time. Although the experimental configuration differs from the application to floating bodies transport (finite cylinders floating on the water surface) this result is the only available in the literature with a detailed description of the orientation effects on the hydrodynamic coefficient, becoming the most significant reference for the dissertation.

1.6. Rigid body collision

Floating bodies that are free to move on the water surface may encounter other objects, both moving or not, and be involved in a collision. It is thus necessary to model such condition, in order to calculate the post-collisional velocity of the body (or bodies) and the eventual deviation of their trajectory.

Some models to deal with collisions of transported logs are available in the literature. In some cases the estimation of the maximum impact force of logs on existing structures is computed (Haehnel and Daly 2004). This may be useful in case of endangered inline structures. Standard collisions among logs are computed with different strategies according to the method selected for the modelling of the discontinuous phase. If the dynamic

approach is chosen, it is possible to add an external force to the equation of translation (Stockstill et al. 2009). For kinematic models a simplified strategy is required. The post-collisional velocity may be computed, for example, considering the elastic kinematic response of two punctual bodies (Ruiz-Villanueva et al. 2014b).

Widening the view to problems not only related to floating body transport, other approaches are presented. Brach (1989) proposes a parametrical computation of collision response based on the friction and on the restitution coefficient, joined to the analysis of the loss of energy during collision. Another method, proposed by Baber (2006), is based on the constraining of bodies and on the computation of the action of forces among each element.

Hecker (1997) developed a simplified method to compute collision response by applying the Newton's restitution principle. In this case, the only parameter that needs to be calibrated is the restitution coefficient.

1.7. Outlines of the Ph.D. research

Rigid bodies transport is modelled with various approaches, mainly due to the different aims of the researchers. From this diversity, it is possible to derive the lines of investigation which are aligned with the aim of the dissertation.

First of all, the incipient motion is modelled with the classic method, based on the force balance. The effects of the different orientation of the cylinders and of the local 3D conditions, in the case of mobile bed, are implemented in the choice of the apparent drag coefficient. The same model is used to simulate the arrest of the bodies, which occurs when the dynamic friction with the bed exceeds the forces acting on the body.

Continuum and discrete phases are modelled with a hybrid method, where the Eulerian description of water flow is coupled with a Lagrangian approach to model the motion of rigid bodies, considered as single entities.

The choice of a 2D model is consistent with the requirement of the addressed physical problem. In fact, the main focus of this dissertation is on the transport of bodies floating on the water surface (considered as a 2D surface) and not on the detailed description of body entrainment, bridge clogging or similar locally 3D flow situations. Therefore, the effect of the vertical distribution of velocity can be neglected.

The Shallow Water Equations (SWE) written in conservative form (Cunge et al. 1980) are solved with ORSA2D, a code developed at the University of Pavia (Petaccia et al. 2010, Petaccia et al. 2016). ORSA2D is based on a first order upwind numerical solver with finite volume discretization.

High precision is required in order to predict the realistic movement of single bodies and assess their behaviour in presence of instream obstacles. This excludes the possibility to use a strictly kinematic model or a general description of the motion of volume of woody debris, because they are less accurate in the reproduction of the physics of transport. A dynamic approach based on the forces exerted by the flow on each single object results more appropriate, and the one-way coupling with a 2D hydraulic model is sufficient for this first step of the research, dealing mainly with uncongested transport, not investigating in detail the effect of clogging. The accurate description of the dynamics of floating objects, wooden spheres and cylinders, is provided by implementing a Discrete Element Method (DEM) based on the solution of Newton's equation of motion.

The transport model is based on the Maxey-Riley equation, which is extended to the description of the two dimensional motion of spheres and cylinders floating on the water surface. A unified formulation is provided, where the difference among body shapes is included in the force computation and in the estimation of the drag and side coefficients.

The rotation formulation suggested in literature is extended to the case of floating objects, by simply including the correct forces in the torque computation. To take into account the velocity gradient along the body main

dimension, an alternative formulation is introduced, which is compared with the literature one.

For spheres, the values of the drag and side coefficients are taken from literature. As regards the added mass coefficient, it is considered as constant in a first approximation both for spheres and cylinders, but is adapted to the case of semi-submerged bodies, as shown in Chapter 5. The drag and side coefficients for cylinders are measured experimentally, in order to include the effect of rotation and flotation.

The resulting model, named ORSA2D_WT, includes collisions between bodies and between bodies and side walls, by implementing the method proposed by Hecker (1997). To extend his formulation to the case of floating bodies, a calibration of the restitution coefficient is provided. In case of elastic collisions, this coefficient is equal to 1. However, due to the presence of the fluid phase around the discrete elements, the collision is expected to be far from elastic. For this reason, the value has been adjusted on the basis of experimental observations.

Chapter 2
Mathematical model

2.1. Abstract

In this Chapter the mathematical outlines of ORSA2D_WT are presented. The focus is, firstly, on the formulation of incipient motion, which rules the mobility and the arrest of the floating objects. Then, a detailed description of the terms of the equation of motion is provided, in order to present their applicability to the physical problem addressed by the dissertation. The transport equation is modified with respect to the models found in literature: not all the described forces are included, and the side force, formerly defined lift force, is introduced for both spherical and cylindrical bodies. Its different meaning for the two body shapes is explained.

Two approaches are suggested for the rotation model. The first one is similar to the literature method, despite some variations in the resistance torque. The second equation of rotation is developed as a parallel formulation to translation. It requires the computation of the angular momentum and introduces an additional resistance torque term similar to an added inertia term. Both these strategies are valid for spheres and cylinders, with the proper expressions of forces and coefficients.

In the final section, the model of collisions is presented. The proposed method is derived from the literature and is based on collision kinetics. The effects on the rigid body trajectories depends on the restitution coefficient, which needs to be calibrated for floating rigid bodies.

2.2. Entrainment and arrest

The entrainment of rigid bodies depends on their density, dimensions and orientation in the case of not axisymmetric objects (e.g. Bocchiola et al. 2006). It can occur in three main ways: flotation, rolling and sliding. The first happens when the buoyancy force on the body exceeds its weight force, while the other two occur when the body is not yet floating. In particular, an elongated body starts to roll when it is perpendicular to the flow, while sliding occurs if rotation is not allowed, for example when a cylinder is aligned with the flow. For spheres, only floating and rolling can take place.

When the water level is sufficient for buoyancy, wooden rigid bodies start floating. A detailed analysis of such phenomena is out of the scope of this work, and can be found in the literature (e.g. Braudrick and Grand 2001). Here, only the main results with reference to floating bodies are included, in order to verify the flotation condition. This is accomplished by implementing the model proposed by Braudrick and Grant (2000), which requires the computation of a floating parameter on the basis of a force balance.

First of all, the net weight $\boldsymbol{W}$ of the body is computed:

$$\boldsymbol{W} = m_b \boldsymbol{g} - Vol_{sub} \rho_f \boldsymbol{g} \tag{2.1}$$

where m_b is the mass of the body, $\boldsymbol{g}$ stands for the gravitational acceleration, Vol_{sub} is the submerged volume, calculated taking into account the submerged part of each body and ρ_f is the density of the fluid. The first term on the right-hand side is the real weight of the body and the second term is the buoyancy force.

To compute the net weight, the body is supposed to be on the bottom of the channel: if the water level is higher than the body's height, the entire volume is submerged, while if the body's height is higher than the water level, only the actually submerged part has to be taken into account (Fig.

2.1). If the net weight has a negative value, the body floats, and the equations of transport can be applied.

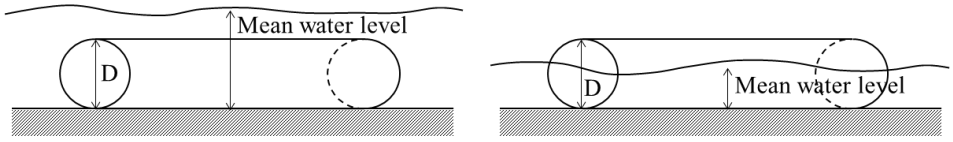

Figure 2.1 Scheme of the computation of the submerged volume for a cylinder. a) The mean water depth is higher than the body height and buoyancy is computed on the entire volume; b) the mean water depth is lower than the body height, and only the submerged volume is considered.

If the net weight is positive, the force balance is computed in order to take into account the motion due to rolling or sliding. In these cases, even if the bodies do not properly flow, their motion is computed to avoid the underestimation of the initiation of motion.

The force balance requires the computation of the effect of gravity (F_{grav}) on a sloping bottom, the static friction (F_{frict}) between the bottom and the body and the drag force (F_{drag}) on the body:

$$\boldsymbol{F}_{grav} = \boldsymbol{W} \sin(\alpha) \tag{2.2}$$

$$\boldsymbol{F}_{frict} = \mu_{fr} W \cos(\alpha) \frac{\boldsymbol{V}}{|\boldsymbol{V}|} \tag{2.3}$$

$$\boldsymbol{F}_{drag} = \frac{1}{2} C_{D\ app} \rho_f A' \boldsymbol{V} |\boldsymbol{V}| \tag{2.4}$$

where, in addition to known symbols, α is the horizontal angle of the channel bottom, μ_{fr} is the coefficient of friction between the bottom and the body, $C_{D\ app}$ is the apparent drag coefficient, which is specific for the incipient motion computation, A' the area on which the force acts and V the relative velocity. The area A' is different according to the body shape and to the water level, as detailed in Chapter 3.

In the original model by Braudrick and Grant (2000), the orientation of the cylinder, which affects the entrainment of the body, is included in the

computation of the drag area A'. In our approach, on the contrary, the orientation is incorporated in the drag coefficient computation, as detailed in Chapter 5.

Selecting the drag coefficient for the computation of incipient motion of a cylinder is not trivial. This value depends on the Reynolds number, the Froude number, the body slenderness and roughness. Moreover, due to the simplification of the model of Braudrick and Grant (2000), it has to include all the other 3D phenomena which arise in real conditions, such as the local scouring in mobile bed, acceleration and variation of the water level upstream and downstream the body (Crosato et al. 2014). Although no shared results can be found in the literature, an appropriate value seems to have been found by Bocchiola et al. (2006) who averaged a series of experiments on sand and gravel bed, with wooden cylinders parallel and perpendicular to the flow. The difference among these configurations shows that the mobilization is easier if cylinders are perpendicular to the flow, because they are able to roll on the channel bottom. These results are useful to include the variation of the apparent drag coefficient with log orientation, as it will be shown in detail in the following chapters.

Spheres are introduced in the thesis mainly to assess on a simpler shape the hypothesis of the formulations extended on elongated bodies. Their entrainment does not have a practical interest (spherical floating debris are rarely found during real events) and less accuracy can be used in the choice of the apparent drag coefficient, which is simply computed as the standard drag (see Chapter 5 for details).

The friction coefficient contributes to define the mobility of the rigid body and depends mainly on the roughness of both the bottom and the body surface. Since the interest is on wooden elements, the incipient motion is computed with friction coefficients depending on the bottom material and varies for artificial and real channels, as shown in Tab. 2.1.

Bed material	μ_{fr}
Wood	0.47[a]
Wet metal	0.20[b]
Gravel	0.64[a]
Sand	0.47[c]

Table 2.1 Coefficient of friction for incipient motion, between wooden elements and different bed material. References: [a] Crosato et al. 2014; [b] Murase 1984 ; [c] Ishikawa 1989.

Once that the forces included in the model are computed adopting the appropriate drag and friction coefficients, the floating parameter can be calculated as the ratio between the forces in favour to (gravity and drag) and those opposed to the motion (friction):

$$\frac{\boldsymbol{F}_{grav} + \boldsymbol{F}_{drag}}{\boldsymbol{F}_{frict}} \tag{2.5}$$

If the ratio is higher than 1, the body floats, otherwise, the equations of motion are not computed.

The same model is applied to verify also the arrest of the rigid bodies, and for this reason the incipient motion condition is verified at each time step. If the net weight becomes positive, the force balance is computed again to check if the flow may still move the object. In this case, however, the body is moving on the bottom of the channel, so the friction among the surfaces becomes dynamic and the friction coefficient have to be consequently reduced (Rabinowicz 1951). The values implemented in ORSA2D_WT are reported in Tab. 2.2.

Bed material	μ_{fr}
Wood	0.30[a]
Wet metal	0.15[b]
Gravel	0.48[c]
Sand	0.35[c]

Table 2.2 Coefficient of kinematic friction, between wooden elements and different bed material. References: [a] value approximated from Blau 2001; [b] Murase 1984 ; [c] value obtained by reducing the static coefficient of 25%, as suggested by Murase 1984.

2.3. Mathematical model for translation

The forces included in the model of the motion of a rigid body may be different and depend on the characteristics of the body and of the flow. In general, the so-called Maxey–Riley equation, valid for rigid small spheres in non-uniform creeping flows (particle Reynolds number $Re_p \ll 1$), presents the following terms:

$$\boldsymbol{F}_{body} = \boldsymbol{F}_{Stokes\ drag} + \boldsymbol{F}_{added\ mass} + \boldsymbol{F}_{pressure\ gradient} + \boldsymbol{F}_{Basset\ history} + \boldsymbol{F}_{buoyancy} \tag{2.6}$$

Other external forces may be taken into accounted, if needed. Not all the components are included in the existing models of rigid body transport, so the reasons for considering or not these terms are here discussed.

The *drag force* is the component of the hydrodynamic force (i.e. the force due to the fluid stress distribution on the body surface) in the direction of the relative velocity. In Eq. 2.7 only the viscous Stokes drag is considered, since the original form of the equation was derived for the motion of a small sphere in creeping flow conditions, with low Reynolds numbers. Under such hypothesis, the drag force of a sphere is:

$$\boldsymbol{F}_{Stokes\ drag} = 6\pi\mu r\boldsymbol{V} \tag{2.7}$$

where μ is the fluid dynamic viscosity, r the sphere radius and $\boldsymbol{V}$ is the relative velocity of the flow with respect to the body.

The extension of the drag force to higher Reynolds numbers is obtained by considering the standard definition of the hydrodynamic drag force:

$$\boldsymbol{F}_{drag} = \frac{1}{2} C_D \rho_f A \boldsymbol{V}|\boldsymbol{V}| \tag{2.8}$$

where, in addition to known symbols, C_D is the drag coefficient and A is the area on which the force acts. To derive the value of the drag coefficient for a sphere in Stokes conditions, Eq. 2.7 and Eq. 2.8 are compared,

obtaining a value equal to $C_D = \frac{24}{Re_p}$, by considering the standard expression of the particle Reynolds number $\left(Re_p = \frac{VD}{\nu}\right)$.

In general, the drag coefficient varies with the Reynolds number and with other parameters, such as the body shape and orientation. The values implemented in the model are specified in Chapter 4.

The *added mass force* is connected to the inviscid effects of the relative acceleration of the flow with respect to the body, which involves the motion of a layer of fluid surrounding the rigid body. In addition, the force exerted on a volume of fluid equal to the body volume in the undisturbed flow has to be considered (Batchelor 1967) and corresponds to the *pressure gradient force*. Originally, these forces were evaluated for uniform unsteady flow but to make their expressions valid in case of non-uniform flow the following formulations are proposed (e.g. Maxey and Riley 1983, Auton et al. 1988) :

$$\boldsymbol{F}_{added\ mass} = \frac{1}{2} C_{AM} m_f \left(\frac{D\boldsymbol{V}_f}{Dt} - \frac{d\boldsymbol{V}_b}{dt}\right) \tag{2.9}$$

$$\boldsymbol{F}_{pressure\ gradient} = m_f \left(\frac{D\boldsymbol{V}_f}{Dt}\right) \tag{2.10}$$

where C_{AM} is the added mass coefficient, m_f is the mass of fluid corresponding to the body volume, $\boldsymbol{V}_b$ is the velocity vector of the body, $\boldsymbol{V}_f$ is the velocity vector of the undisturbed flow at the body centre and $\frac{D\boldsymbol{V}_f}{Dt} = \frac{\partial \boldsymbol{V}_f}{\partial t} + (\boldsymbol{V}_f \cdot \boldsymbol{\nabla})\boldsymbol{V}_f$ is the material derivative of the flow velocity, which allows one to take into account both the temporal and the spatial acceleration and corresponds to the Lagrangian derivative following the fluid mass.

The *Basset history force*, like the added mass force, arises from the discrepancy of the velocities between the body and the fluid. But while the added mass is linked to the inviscid effects, the history term is due to the

viscous-unsteady effects that delay the development of the boundary layer. The term has an integral formulation, which reads:

$$\boldsymbol{F}_{Basset\ history} = 6r^2\rho_f\sqrt{\pi\nu}\int_0^t \frac{1}{\sqrt{t-\tau}}\frac{d}{d\tau}\Big(\boldsymbol{V}_f(\tau) - \boldsymbol{V}_b(\tau)\Big)\,d\tau \quad (2.11)$$

where r is the body radius and ν is the kinematic viscosity of the fluid. The integral needs to be evaluated over the complete history of the body motion, and is non-linear when the velocity field is space-dependant. In order to avoid the complexity and the memory and time consumption connected to the term, it is often neglected in modelling the motion of rigid bodies. However, due to its importance for transport in turbulent flows or in the case of bed-load transport (e.g. Niño and García 1998; Mordant and Pinton 2000) some strategies are suggested for its inclusion in the computation, based on Laplace transformation or approximation of the term (Michaelides et al. 1992; Dorgan and Loth 2007; Bombardelli et al. 2008; van Hinsberg et al. 2010).

In the presented formulation, however, the Basset term is neglected to reduce the costly procedures and not to overload the computation in case of multiple logs transport.

The *buoyancy effect* is included in the Maxey–Riley equation since it was developed with reference to the settling of a body in a fluid. Its expression is:

$$\boldsymbol{F}_{buoyancy} = Vol\big(\rho_f - \rho_b\big)\boldsymbol{g} \quad (2.12)$$

where *Vol* is the body volume, ρ_f and ρ_b are the fluid and the body density, respectively and $\boldsymbol{g}$ is the gravitational acceleration.

The presence of buoyancy depends on the reference system and on the characteristics of the body motion. The term is not included in the model of the transport of rigid body during floods because it is directed perpendicularly to the plane of motion. However, for calibration purposes and in

order to reproduce literature experiments, the term can be easily implemented in the formulation.

Auton et al. (1988) include in Eq. 2.6 the *shear-induced lift force*, which arises because of the different pressures around a spherical body in a uniform shear flow. This force, analytically studied by Saffman (1965), is perpendicular to the relative velocity and alters the body trajectory.

$$\boldsymbol{F}_{lift} = \rho_f C_L Vol(\boldsymbol{V}_f - \boldsymbol{V_b}) \times \boldsymbol{\omega} \tag{2.13}$$

where C_L is the lift coefficient and $\boldsymbol{\omega}$ is the vorticity upstream of the sphere, which means that the flow vorticity, and not the sphere angular velocity, is considered to compute the lift force.

2.3.1. Extension to floating rigid bodies

In the dissertation, the two-dimensional motion of a rigid body in a fluid is modelled by computing the acceleration of the body centre of mass due to the drag force (extended to high Reynolds numbers), the added mass force and the pressure gradient force.

In addition, the component of the hydrodynamic force perpendicular to the drag, namely the side force, is included for both body shapes. For spheres, it accounts for the effect of the shear-induced and the Magnus-induced lift, while for cylinders it reproduces the effect of the deviation of the flow in case of yawed objects. In fact, if a cylinder is not aligned nor perpendicular to the flow, it deviates the streamlines in a non-symmetrical pattern, which alters the pressure distribution and generates a side component of the hydrodynamic force (e.g. Mandø and Rosendahl 2010). Fig. 2.2 qualitatively illustrates how the components of the hydrodynamic force change according to the orientation of the cylinder.

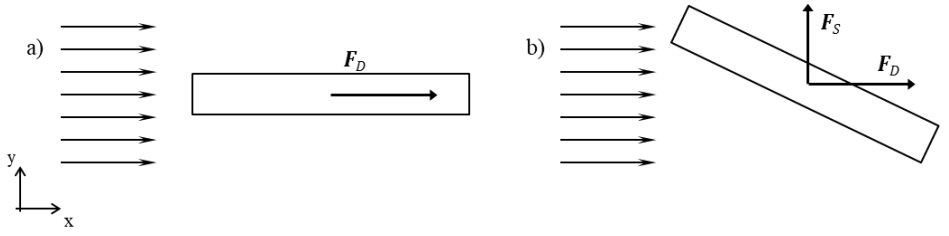

Figure 2.2 Components of the hydrodynamic force on a cylinder; a) when the cylinder is parallel to the relative velocity, the hydrodynamic force is aligned, too, and drag is the only relevant component; b) when the cylinder is yawed, a component of the hydrodynamic force perpendicular to the relative velocity and opposite to flow deviation (i.e. the side force) appears.

The side force can be expressed as in Eq. 2.8 for the drag force, with an appropriate side coefficient C_S which varies according to the body shape and orientation.

Eq. 2.14 sums up all the force components included in the ORSA2D_WT model.

$$\boldsymbol{F}_{body} = \boldsymbol{F}_{drag} + \boldsymbol{F}_{side} + \boldsymbol{F}_{added\ mass} + \boldsymbol{F}_{pressure\ gradient} \tag{2.14}$$

By making explicit the forces in Eq. 2.14, the translation equation implemented in the DEM model of ORSA2D_WT results:

$$\begin{aligned}\left(m_b + \frac{1}{2}C_{AM}m_f\right)\frac{d\boldsymbol{V}_b}{dt} &= \frac{1}{2}\rho_f C_D A\left(\boldsymbol{V}_f - \boldsymbol{V}_b\right)\left|\boldsymbol{V}_f - \boldsymbol{V}_b\right| \\ &+ \frac{1}{2}\rho_f C_s A\left[\left(\boldsymbol{V}_f - \boldsymbol{V}_b\right)\left|\boldsymbol{V}_f - \boldsymbol{V}_b\right|\right] \times \boldsymbol{i}_z \\ &+ \rho_f\left(1 + \frac{1}{2}C_{AM}\right)Vol\frac{D\boldsymbol{V}_f}{Dt}\end{aligned} \tag{2.15}$$

where $\boldsymbol{i}_z$ is the unit vector normal to the 2D flow plane.

2.4. Mathematical model for rotation

Modelling rotation has a different importance depending on the body shape. The main effect of rotation on spheres is the deviation of the their trajectory. Orientation is usually not considered, because it is not supposed to alter the interaction between the body and the flow thanks to the perfect symmetry of the sphere. Since the sphere angular velocity is one of the main parameter to compute the side coefficient (which corresponds to the joint shear-induced and Magnus-induces lift coefficient), it has to be calculated. In the present work, the rotation of the sphere is computed with the same formulation as for cylinders, with the proper coefficients and moment of inertia. In this way, the angular velocity is calculated to perform a more accurate computation of the side force and, consequently, of the body trajectory.

Orientation plays a crucial role for cylinder motion, because the hydrodynamic force acting on the body itself depends strongly on it. For this reason, it is extremely important to compute also the rotation of the body, together with its displacement.

The model of rotation here adopted refers to the proposal of Mandø and Rosendahl (2010) and is based on the computation of torques:

$$\boldsymbol{T}_{body} = \boldsymbol{T}_{resistance} + \boldsymbol{T}_{offset} + \boldsymbol{T}_{cross} \tag{2.16}$$

The *resistance torque* is computed by integrating the drag force on the body main dimension. Mandø and Rosendahl (2010) suggested a formulation, derived with a drag coefficient from White (1991), which is valid for a cylinder in a cross-flow rotating around its minor axis:

$$|\boldsymbol{T}_R| = \rho d\left(\omega_f - \omega_b\right)^2 L^4 \left\{ \frac{1}{64} + \left[3.36 \left(\frac{\rho d \left|\omega_f - \omega_b\right| L}{\mu} \right)^{2/3} \right]^{-1} \right\} \tag{2.17}$$

The *offset torque* is originated by the application of the hydrodynamic force in the centre of pressure, which is not coincident with the centre of gravity of the body when the body and the flow are not aligned (Fig. 2.3).

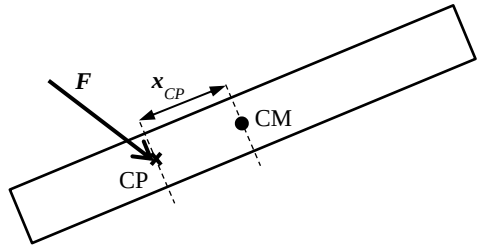

Figure 2.3 The hydrodynamic forces (***F***) are applied in the centre of pressure (CP), at a distance x_{CP} from the centre of mass (CM).

Then, the offset torque is computed by summing the forces ***F*** acting on the cylinder, since they are all applied in the centre of pressure:

$$\boldsymbol{T}_{offset} = \boldsymbol{x}_{CP} \times \left(\sum \boldsymbol{F} \right) \tag{2.18}$$

where $\boldsymbol{x}_{CP}$ is the distance of the centre of pressure from the centre of gravity. To compute such distance, the expression suggested by Yin et al. (2003) has been selected.

The *cross terms* proposed in Eq. 2.16 are evaluated on the basis of the cross momentum of inertia and angular velocities. For example, if one considers the rotation of the cylinder around the *z* axis, Eq. 2.16 becomes:

$$I_z \frac{d\omega_z}{dt} = T_{resistance\ z} + T_{offset\ z} + \omega_x \omega_y (I_x - I_y) \tag{2.19}$$

where I_x, I_y, I_z are the momenta of inertia of the body with respect to each local axis. In our formulation, only the rotation around the *z* axis is considered and cross angular velocities are considered equal to zero, so this term can be neglected.

This formulation accounts for the different pressure distribution around the body, which reflects in the application of the hydrodynamic force in the centre of pressure instead of in the centre of mass. Moreover, it has been studied for the settling of elongated bodies in calm water. On the contrary, the main interest of this thesis is the case of spheres and cylinders floating on the water surface, rotating on an horizontal plane, not subject to gravity and involved in a non-uniform flow.

Due to the dissimilar condition of derivation with respect to the real case situation, the literature formulation does not suit exactly to the case of interest and has been slightly modified. In a first attempt, a different formulation of the resistance torque, already described, is suggested. A second approach is then proposed, which totally modifies the terms provided by the literature, considering torques due to the angular momentum and to an added inertia term.

2.4.1. Offset and resistance torques

As said in the previous paragraph, Eq. 2.16 is implemented disregarding the cross term because only the motion on the plane *(x,y)* is modelled, so that the cross angular velocities are zero. Only the toque due to offset and the torque due to resistance are then considered. The equation of rotation becomes:

$$I\frac{d\boldsymbol{\omega}_b}{dt} = \boldsymbol{x}_{CP} \times \left(\boldsymbol{F}_{drag} + \boldsymbol{F}_{side} + \boldsymbol{F}_{added\ mass} + \boldsymbol{F}_{pressure\ gradient}\right) + \boldsymbol{T}_{res} \tag{2.20}$$

where I is the momentum of inertia, equal to $\frac{1}{12}m_b\left(\frac{3}{4}D^2 + L^2\right)$ for a cylinder and $\frac{2}{5}m_bR^2$ for a sphere; $\boldsymbol{\omega}_b$ is the angular velocity of the body and $\boldsymbol{x}_{CP}$ is the relative distance vector between the centre of pressure and the centre of mass, computed as suggested by Yin et al. (2003): $\boldsymbol{x}_{CP} = 0.25L(\cos(\alpha_{REL}))^3$, where α_{REL} is the angle between the cylinder and the relative velocity.

The added mass in Eq. 2.20 corresponds to the complete term, which includes the relative acceleration:

$$\boldsymbol{F}_{added\ mass} = \frac{1}{2}\rho_f C_{AM} Vol\left(\frac{D\boldsymbol{V}_f}{Dt} - \frac{d\boldsymbol{V}_b}{dt}\right) \tag{2.21}$$

The torque due to resistance is modified with respect to Eq. 2.18. That formulation is valid for a specific value of the drag coefficient which depends on the Reynolds number and in the subcritical regime. Mandø and Rosendahl (2010) merge the drag force expression with the angular relative velocity, just providing an example of how the resistance should be modelled.

To keep the formulation simple and linear, the presented model provides, as a first attempt, a resistance torque computed with the angular relative velocity but with a different coefficient, which needs to be calibrated. Eqs. 2.22 and 2.23 compare the Mandø and Rosendahl (2010) and the modified formulations, expressed in an integral form:

$$\boldsymbol{T}_{res} = 2\int_0^{L/2} \frac{1}{2}\rho_f C_D A\left(\boldsymbol{\omega}_f - \boldsymbol{\omega}_b\right)^2 l^2 dl \tag{2.22}$$

$$\boldsymbol{T}_{res} = 2\int_0^{L/2} \frac{1}{2}\rho_f C_{res} Vol\left(\boldsymbol{\omega}_f - \boldsymbol{\omega}_b\right)^2 l dl \tag{2.23}$$

The two formulations are similar, although Eq. 2.23 considers a resistance term independent from the drag force. A resistance coefficient C_{res}, which is not necessarily equal to the drag coefficient, controls the torque magnitude, which is proportional to the differences among angular velocities. Carrying out the integral in Eq. 2.23, the resistance torque results:

$$\boldsymbol{T}_{res} = \frac{1}{8}\rho_f C_{res} Vol\left(\boldsymbol{\omega}_f - \boldsymbol{\omega}_b\right)^2 L^2 \tag{2.24}$$

Eventually, the complete form of the formulation adapted from Mandø and Rosendahl (2010) reads:

$$\begin{aligned} I\frac{d\boldsymbol{\omega}_b}{dt} = \Big[& -b_{CPy}\Big(\frac{1}{2}\rho_f C_D A\left(u_f - u_b\right)\left|\boldsymbol{V}_f - \boldsymbol{V}_b\right| \\ & + \frac{1}{2}\rho_f C_S A\left(v_f - v_b\right)\left|\boldsymbol{V}_f - \boldsymbol{V}_b\right| \\ & + \rho_f\left(1 + \frac{1}{2}C_{AM}\right) Vol\frac{Du_f}{Dt} - \frac{1}{2}\rho_f C_{AM} Vol\frac{du_b}{dt}\Big) \\ & + b_{CPx}\Big(\frac{1}{2}\rho_f C_D A\left(v_f - v_b\right)\left|\boldsymbol{V}_f - \boldsymbol{V}_b\right| \\ & + \frac{1}{2}\rho_f C_S A\left(u_f - u_b\right)\left|\boldsymbol{V}_f - \boldsymbol{V}_b\right| \\ & + \rho_f\left(1 + \frac{1}{2}C_{AM}\right) Vol\frac{Dv_f}{Dt} \\ & - \frac{1}{2}\rho_f C_{AM} Vol\frac{dv_b}{dt}\Big)\Big] \\ & + \frac{1}{8}\rho_f C_{res} L^2 Vol\left(\boldsymbol{\omega}_f - \boldsymbol{\omega}_b\right)\left|\boldsymbol{\omega}_f - \boldsymbol{\omega}_b\right| \end{aligned} \tag{2.25}$$

2.4.2. Angular momentum and added inertia torques

A second formulation has been tested, involving two terms: the torque due of the forces acting on the log with respect to the centre of mass, CM, defined $\boldsymbol{T}_{CM}$, and a term of resistance related to the different angular acceleration between the log and the flow, $\boldsymbol{T}_{added\ inertia}$:

$$I\frac{d\boldsymbol{\omega}_b}{dt} = \boldsymbol{T}_{CM} + \boldsymbol{T}_{added\ inertia} \tag{2.26}$$

The angular momentum is computed by taking into account the distribution of the forces (drag, side, added mass, pressure gradient) on the main body length, and refers to the centre of mass of the body, not to the centre of pressure. Note that the added mass term is computed by considering the relative angular acceleration, as in Eq. 2.21.

The variation of the forces on the body main dimension is a consequence of the velocity gradient on large bodies. To properly represent this phenomenon, which is particularly important in non-uniform flows, the forces are evaluated not only in the centre of mass but in different sections along the body (see Chapter 3). This allows the computation of the angular momentum with respect to the centre of mass.

As suggested by Mandø and Rosendahl (2010), a second term is needed, which acts as a resistance to rotation. The authors computed the term by integrating the effect of the drag force along the cylinder, as shown in Eq. 2.22. In this second formulation, the resistance term is computed as a torque due to the added moment of inertia:

$$\boldsymbol{T}_{added\ inertia} = \frac{1}{2}C_{AI}I\left(\frac{D\boldsymbol{\omega}_f}{Dt} - \frac{d\boldsymbol{\omega}_b}{dt}\right) \tag{2.27}$$

The added inertia torque depends on the relative angular acceleration, obtained by considering the angular acceleration of the flow $\boldsymbol{\omega}_f$ (with the total derivative) and the global angular acceleration of the body $\boldsymbol{\omega}_b$.

The value of the added moment of inertia coefficient C_{AI} has to be calibrated through a sensitivity analysis.

The final form of this second original formulation reads:

$$
\begin{aligned}
I\frac{d\boldsymbol{\omega}_b}{dt} = \Bigg[& -b_{CMy}\Bigg(\frac{1}{2}\rho_f C_D A\left(u_f - u_b\right)\left|\boldsymbol{V}_f - \boldsymbol{V}_b\right| \\
& + \frac{1}{2}\rho_f C_S A\left(v_f - v_b\right)\left|\boldsymbol{V}_f - \boldsymbol{V}_b\right| \\
& + \rho_f\left(1 + \frac{1}{2}C_{AM}\right)Vol\frac{Du_f}{Dt} \\
& - \frac{1}{2}\rho_f C_{AM} Vol\frac{du_b}{dt}\Bigg) \\
& + b_{CMx}\Bigg(\frac{1}{2}\rho_f C_D A\left(v_f - v_b\right)\left|\boldsymbol{V}_f - \boldsymbol{V}_b\right| \\
& + \frac{1}{2}\rho_f C_S A\left(u_f - u_b\right)\left|\boldsymbol{V}_f - \boldsymbol{V}_b\right| \\
& + \rho_f\left(1 + \frac{1}{2}C_{AM}\right)Vol\frac{Dv_f}{Dt} \\
& - \frac{1}{2}\rho_f C_{AM} Vol\frac{dv_b}{dt}\Bigg)\Bigg] + \frac{1}{2}C_{AI} I\left(\frac{D\boldsymbol{\omega}_f}{Dt} - \frac{d\boldsymbol{\omega}_b}{dt}\right)
\end{aligned}
\tag{2.28}
$$

2.5. Collision modelling

Both in natural streams or in laboratory channels, floating bodies can interact with each other as well as with the side walls or other large obstacles located along their trajectories.

The collisions considered in the present model occur on the horizontal plane, i.e. the water surface, and involve cylinders and side walls, as well as obstacles found in the channel. The collision of spheres is not modelled, since no occurrence was found in the laboratory experiments, and the transport of spherical bodies is not modelled in real events.

It is worth highlighting that collisions affect only the motion of cylinders, not their shape, nor integrity. This simplification acts in favour of hydraulic safety, since shorter logs, which may result from the breaking of longer elements, have less probability to clog openings and flow easily under bridge decks (e.g. Hartlieb 2012).

Modelling collisions requires the following steps:

- collision detection;
- body position adjustment;
- evaluation of the collision outcome.

The first two steps are performed by taking into account the reciprocal position of the bodies involved in the collision, cylinders or fixed obstacles. Since the overlap of bodies is possible, due to the finite time step used for the computation of motion, the position of the bodies needs to be corrected. The implementation of these steps is described in detail in Chapter 3.

Once that the collision is detected and the bodies are moved to avoid overlapping, the effect of the impact can be estimated. The model adopted in ORSA2D_WT implements the collision response method developed by Hecker (1997), where the impulse momentum *J* is first calculated as:

$$J = \frac{-(1+e)\boldsymbol{V}_{rel}^{i} \cdot \boldsymbol{n}}{\frac{1}{m_{b1}} + \frac{1}{m_{b2}} + \frac{(\boldsymbol{r}_1 \times \boldsymbol{n})^2}{I_1} + \frac{(\boldsymbol{r}_2 \times \boldsymbol{n})^2}{I_2}} \tag{2.29}$$

when two moving bodies are involved in the collision, or as:

$$J = \frac{-(1+e)\boldsymbol{V}_{rel}^{i} \cdot \boldsymbol{n}}{\frac{1}{m_{b1}} + \frac{(\boldsymbol{r}_1 \times \boldsymbol{n})^2}{I_1}} \tag{2.30}$$

when a cylinder impacts a rigid wall.

In Eqs. 2.29 and 2.30, *e* is the restitution coefficient (*e=1* for elastic collisions), $\boldsymbol{V}_{rel}^{i}$ is the relative velocity between the bodies, $\boldsymbol{n}$ is the unit vector normal to the hit body, with components $\boldsymbol{n}_x$ and $\boldsymbol{n}_y$, $\boldsymbol{r}_1$ and $\boldsymbol{r}_2$ are the distances between the impact point and the centre of mass of the bodies.

After the impulse momentum has been estimated, the post-collision velocities can be computed for the colliding cylinder (2.31) and for the hit cylinder (2.32):

$$u_{b1}^{f} = u_{b1} + \frac{J\boldsymbol{n}_x}{m_{b1}};\ v_{b1}^{f} = v_{b1} + \frac{J\boldsymbol{n}_y}{m_{b1}};\ \omega_{b1}^{f} = \omega_{b1} + \frac{\boldsymbol{r}_1 \times J\boldsymbol{n}_x}{I_1} \qquad (2.31)$$

$$u_{b2}^{f} = u_{b2} - \frac{J\boldsymbol{n}_x}{m_{b2}};\ v_{b2}^{f} = v_{b2} - \frac{J\boldsymbol{n}_y}{m_{b2}};\ \omega_{b2}^{f} = \omega_{b2} - \frac{\boldsymbol{r}_2 \times J\boldsymbol{n}_x}{I_2} \qquad (2.32)$$

If the collision occurs between a cylinder and a fixed obstacle, only Eq. 2.31 is applied.

To realistically model the collision among floating objects, a key aspect is the correct estimation of the restitution coefficient. As shown in Chapter 5, the value of this coefficient can be deduced from the experimental results.

Chapter 3
Numerical modelling and implementation

3.1. Abstract

A synthesis of the numerical strategies adopted for the implementation of the proposed model is here provided. The solution method for the Shallow Water Equations (SWE) is briefly reported together with the overall scheme of the code, which enumerates the implemented procedures and shows how the one–way coupling between the Eulerian and the Lagrangian methods is performed.

To take, at least approximately, into account the velocity gradients on large bodies, a subdivision scheme of the body itself in sub-segments is proposed. In this way, forces can be computed for each portion of the body, allowing one to extend the translation and rotation models, originally developed for punctual bodies, to cylinders and large spheres. To properly model the transport of floating bodies, it is important to assign the correct undisturbed flow velocity used to compute the hydrodynamic forces. A location algorithm, that allows to determine the exact cell where the points on the body lay, is therefore described followed by the procedure for the assignment of the correct flow velocity to the points. The entrainment model takes advantage of the body subdivision and localization to verify if the elements can be transported by the flow.

The Discrete Element Method (DEM) model for the transport and rotation of rigid bodies is presented in its final form. The strategies for the computation of the forces, depending on the body shape, and of the velocity gradients are also outlined. Its solution with a fourth order Runge–Kutta time-integration method is described.

Finally, the implementation of the collision model is discussed, detailing how collisions are detected and how rigid bodies are relocated in order to avoid overlapping.

3.2. Shallow Water Equations and one–way coupling

3.2.1. Numerical solution of the Shallow Water Equations

To compute the roto-translation of rigid bodies, the hydraulic variables of the flow are needed, so that the hydrodynamic forces exerted on the body can be calculated.

In the proposed model, flow velocity and water level are computed through a full two-dimensional SWE model, solved by the finite volume code ORSA2D (Petaccia et al. 2010, Petaccia et al. 2016). To reduce computational costs, some authors suggested the implementation of a diffusive approximation of the SWE (Aronica et al. 1998, Fewtrell et al. 2011, Hunter et al. 2008), which proved to be effective both in rural and urban settings. However, Costabile et al. (2016) demonstrated that the solution of the complete SWE model is more reliable when one is interested in modelling the water flow around rigid structures, as is the case of floating debris coming across an inline structure.

The code implements a Roe's Riemann solver, 1st-order accurate in time and space (Roe 1981), applying an upwind discretization to the bottom slope source term (Bermúdez et al. 1998), while the friction slope is evaluated in a semi-implicit way (Costabile at al. 2015). To avoid the presence of non-physical results due to the linearization procedure, the ver-

sion of the Harten-Hyman entropy fix is used (Toro 2009). The time step is evaluated according to the Courant-Friedrichs-Lewy (CFL) condition (Alcrudo and Garcia Navarro 1993).

ORSA2D can work on both structured and un-structured meshes, and requires appropriate initial and boundary conditions for each test case. It has been applied to the analysis of several flow cases, such as flooding due to dam-break (Petaccia et al. 2016) or circulations in shallow lakes (Fenocchi et al. 2016). Here the results of the hydraulic simulation, i.e. flow velocities and water depths, are used to compute the forces acting on a floating rigid body.

For the sake of completeness, the SWE are here reported in conservative form:

$$\frac{\partial h}{\partial t} + \frac{\partial q_x}{\partial x} + \frac{\partial q_y}{\partial y} = 0$$

$$\frac{\partial q_x}{\partial t} + \frac{\partial}{\partial x}\left(\frac{q_x^2}{2} + g\frac{h^2}{2}\right) + \frac{\partial}{\partial y}\left(\frac{q_x q_y}{h}\right) = gh\left(S_{0x} - S_{fx}\right) \qquad (3.1)$$

$$\frac{\partial q_y}{\partial t} + \frac{\partial}{\partial x}\left(\frac{q_x q_y}{h}\right) + \frac{\partial}{\partial y}\left(\frac{q_y^2}{2} + g\frac{h^2}{2}\right) = gh\left(S_{0y} - S_{fy}\right)$$

where h is the water height, q_x and q_y are the specific discharge in x and y direction, S_{0x} and S_{0y} are the component of the bottom slope, S_{fx} and S_{fy} represent the loss of energy through the boundary resistance, both appearing in the source terms. The first line refers to the mass continuity, while the other two are the momentum conservation in the two considered directions. For a complete analysis of the Eulerian solution of the SWE implemented in the code ORSA refer to Petaccia (2003).

3.2.2. SWE-DEM coupling

The Eulerian solution of the SWE is one-way coupled with the Lagrangian model of the transport of floating bodies. It means that the flow quantities computed by the SWE module are available at each time step to determine the forces acting on the floating bodies, while the reaction of the bodies on the flow is neglected.

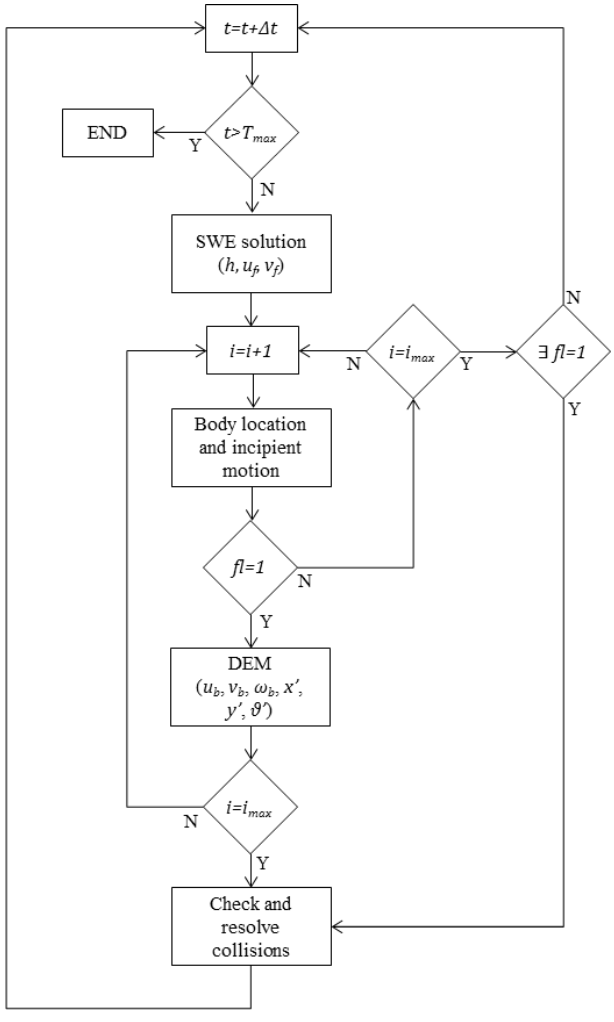

Figure 3.1 Flow chart of the SWE-DEM one-way coupling: *t* is time step, *i* is index of the rigid body considered. In brackets the quantities of interest for the flow (water height and velocities) and for the rigid bodies (linear and angular velocities, final position and orientation).

This strategy is acceptable because, in the dissertation, the motion of one, or at least few solid bodies, is considered. The simulation of obstruction formation due to large amounts of floating debris, on the contrary, would require a two-way coupling strategy of the models, to compute the back-water effect. The flowchart in Fig. 3.1 shows how the coupling is implemented in ORSA2D_WT.

Both the Eulerian and the Lagrangian models are inserted in a time loop, with a unique time step computed to satisfy the Courant-Friedrichs-Lewy condition:

$$\Delta t = \frac{CFL\ \Delta x}{a} \tag{3.2}$$

where a is the maximum velocity reached by the flow and Δx is the mesh discretization. A Courant number $CFL = 0.5$ is used everywhere.

Given the total number of the rigid bodies, i_{max}, the index i, set equal to 0 at each time step, is used as a counter. For each rigid body, the cells where the computation points are located are found with a location algorithm and the incipient motion is computed. If the flotation index fl is grater or equal to 1, the body is able to move and the Discrete Element Method is applied to calculate its motion, obtaining the final velocities, position and orientation. This procedure is repeated for each floating rigid body, then the model of collision between bodies or with the side wall is applied. After that, the time step is increased.

3.3. Body localization and entrainment

This paragraph focuses on how the discrete phase, i.e. the rigid bodies, are considered in ORSA2D_WT. First of all, the conceptual discretization of each element in sub-segments is described, followed by the procedure implemented to localize the bodies in the exact cell of the domain. Then, the procedure to assign the correct velocity to the body segments and the implementation of the entrainment model are described.

3.3.1. Subdivision procedure

ORSA2D_WT extends the equation of transport and rotation to the case of large bodies, whose main dimension is larger than the scale of variation the flow. The extension of the transport equations provided by Mandø and Rosendahl (2010) to elongate bodies is performed by computing the body rotation while the forces acting on the body are estimated from the undisturbed flow velocity at the position of the centre of mass of the considered object. However, if the flow is not uniform and the body is larger with respect to the flow variation, it is possible to find different velocities in different sections of the object. The forces computed in the body centre of mass may not be representative of the real force distribution.

For this reason, a *subdivision procedure* is here proposed, which allows to take into account the variation of velocity on the main dimension of the body, i.e. the diameter of a sphere or the length of a cylinder, as shown in Fig. 3.2.

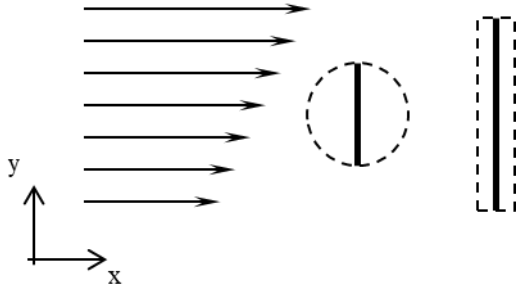

Figure 3.2 Planar view of a simple shear flow on a sphere (dashed circle) and on a cylinder (dashed rectangle). The variation of velocity on the circle's diameter and cylinder's length (solid lines) is taken into account in the present formulation.

According to this approach, the main length is divided in 4 parts (Fig. 3.3) and all the forces (drag and side forces, as well as added mass and pressure gradient) are computed by considering the flow velocity in the position of the centre of each segment (points 1 to 4 in Fig. 3.3). The areas and volumes used to calculate the forces are computed according the subdivision, too.

For the sections of a cylinder, the area and the volume are a quarter of the total frontal area (*LD*, i.e. cylinder length, *L*, times cylinder base diameter, *D*) and of the total volume, respectively. For a sphere, these values vary depending on which point is considered. The area is *0.196A* for segments 1 and 4, and is *0.304A* for segments 2 and 3, where *A* is the total circle area. The volume corresponds to the volume of a spherical cap of height $\frac{R}{2}$ for segments 1 and 4 (named Vol_1), while for segments 2 and 3 it is $\frac{Vol}{2} - Vol_1$.

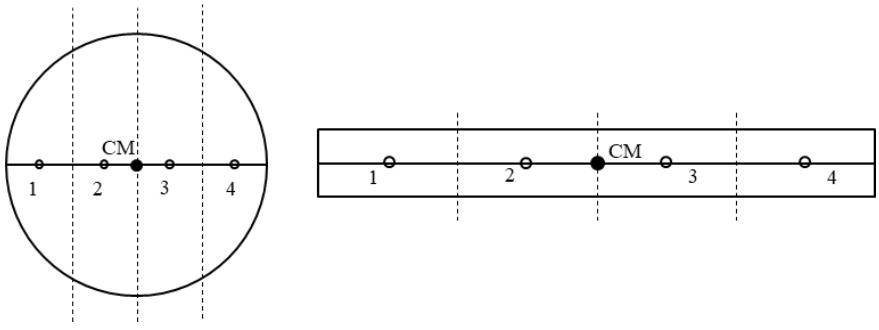

Figure 3.3 Scheme of the division of the transported body. Forces are evaluated at the centre of each segment (points 1 to 4); the corresponding volume is highlighted by dashed lines.

The added inertia of each segment (I_i) is computed by simply dividing by 4 the added inertia of the entire body (Eq. 3.3 for a sphere and Eq. 3.4 for a cylinder).

$$I_i = \frac{2}{20} m_b r^2 \tag{3.3}$$

$$I_i = \frac{1}{48} m_b \left(\frac{3}{4} D^2 + L^2\right) \tag{3.4}$$

The velocity and acceleration of the centre of mass of each segment are computed from the centre of mass velocity, by applying the kinematic relations for rigid bodies:

$$\boldsymbol{V}_{bi} = \boldsymbol{V}_b + \boldsymbol{\omega}_b \times \boldsymbol{b}_i \tag{3.5}$$

$$\frac{d\boldsymbol{V}_{bi}}{dt} = \frac{d\boldsymbol{V}_{bi}}{dt} + \frac{d\boldsymbol{\omega}_b}{dt} \times \boldsymbol{b}_i + \boldsymbol{\omega}_b \times (\boldsymbol{\omega}_b \times \boldsymbol{b}_i) \tag{3.6}$$

where $\boldsymbol{V}_{bi}$ is the velocity of the centre of each segment (point 1 to 4 in Fig. 3.3), $\boldsymbol{\omega}_b$ is the angular velocity, $\boldsymbol{b}_i$ is the distance between the body centre and the four computation points.

This proposed division allows the evaluation of the effects of the flow distribution on an elongated body. It can be considered as an approximation of the real force distribution acting on it: actually, the real hydrodynamic behaviour is non-linear and hence the effects on the isolated parts are not expected to sum up exactly.

Details about the consequent changes in transport and rotation formulation are given in the following paragraphs, together with proofs of the validity of such division.

3.3.2. Body localization and assignment of flow velocity

The initial conditions required for the simulation of the rigid body motion are the position of the centre of mass, the body dimensions, orientation, density, initial linear and angular velocity, if known. Then, the coordinates of the four centres of each body segment are calculated by simply considering their distance from the centre of mass and the main diameter orientation.

To compute the forces acting on such points, the cell in which the point is located has to be identified. Two limit cases can be considered, depending on the size of the neighbouring cells: the cell average dimension is smaller than the body main dimension (Fig. 3.4a) or, on the other hand, cells are large enough to include the body in only one element (Fig. 3.4b).

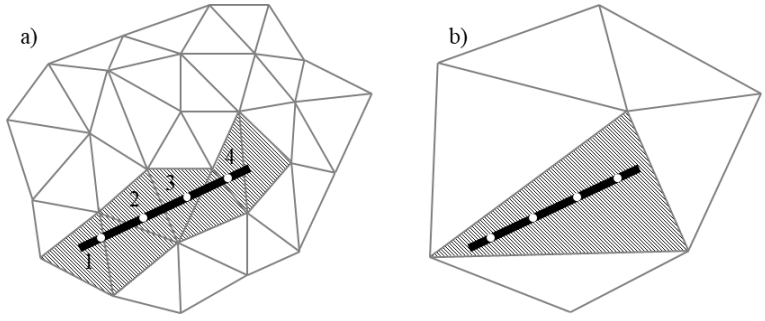

Figure 3.4 Cells and rigid body reciprocal dimension. Black solid line is the rigid body diameter or length and white points are the centre of the four segments. a) the main dimension of the rigid body is larger than the cells' average dimension; b) the main dimension of the rigid body is smaller than the cells' average dimension.

These two limit configurations involve a different number of cells, but in both cases it is essential to assign to each point the correct velocity, independently from the cells dimension.

3.3.2.1. Cell location algorithm

As a first attempt, the cell in which a point resides may be identified as the cell whose centre of mass is nearer to the point of interest . This basic strategy is appropriate in the case of a structured Cartesian mesh but may result unsuccessful if the shape of the cells is triangular or irregular. Fig. 3.5 shows an example in which the nearest cell is not the cell in which the point is located.

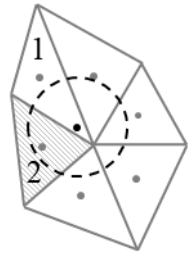

Figure 3.5 Missing point location: the black point is located in cell 1, but the nearest cell centre found (grey lines) is that of cell 2. Dashed black lines approximates the minimum distance between the point and the cells' centres.

According to the *nearest cell centre criterion*, the nearest cell is cell 2, although the point actually lays in cell 1. Such a mismatch, during the

simulation, may result in abrupt variations of the flow velocities assigned to the computational point and has an impact on the computation of the relative velocity and angle, as well as of the hydrodynamic coefficients (which depend on the relative angle).

For this reason, a new method was developed, inspired to the one proposed by Soukal et al. (2011) and easily integrated in the numerical procedure already drafted (the *nearest cell centre criterion*). The main idea behind the *hybrid walk method* by Soukal et al. (2011) is the use of the rotation matrix to align on an oriented horizontal line one vertex of the mesh, belonging to a randomly selected cell, and the point of interest. Then, it compares the transformed coordinates of the vertices of all the triangles located between the first vertex considered and the point, until it finds a vertex with the *x* coordinate (transformed) higher than the *x* coordinate of the point of interest. From this point, it identifies the exact triangle through the Remembering Stochastic Walk algorithm by Devillers et al. (2001).

The method proposed in this dissertation takes advantage of the fact that the triangle found with the *nearest cell centre criterion* is already very near to the correct one, so no much walk is required. Starting from that triangle, the idea is to check if the point is inside it or not. A side of the triangle is selected, and the coefficients for the rotation matrix are computed as in Eq. 3.7.

$$\begin{aligned} k\cos(\beta) &= x(1) - x(2) \\ k\sin(\beta) &= y(1) - y(2) \end{aligned} \tag{3.7}$$

where β is the angle between that side and an horizontal line, x and y are the coordinates of the two vertices of that side. The presence of k refers to the fact that, according to this formulation, the sine and cosine are multiplied by the side length.

Figure 3.6 shows an example of the localization of a point p in a triangular cell, reporting the rotated coordinate system (x', y'). Selecting side α

of the triangle, the y coordinate of one of the vertex of the side (alternatively 1 or 2) is transformed to y' and set as the reference horizontal axis ($y'(1)$ in Fig. 3.6). Then, the y coordinates of the point of interest p and of the vertex not already used for the rotation matrix (vertex 3, to follow the numbers of this example) are transformed, too, and their distance with respect to the new horizontal axis is computed as shown in Eqs. 3.8a and 3.8b:

$$y'_p = -x_p k \sin(\beta) + y_p k \cos(\beta); \qquad d_p = y'_p - y'(1) \tag{3.8a}$$

$$y'(3) = -x(3)k \sin(\beta) + y(3)k \cos(\beta);\ d_3 = y'(3) - y'(1) \tag{3.8b}$$

where the vertex 1 is selected as a reference for the horizontal axis.

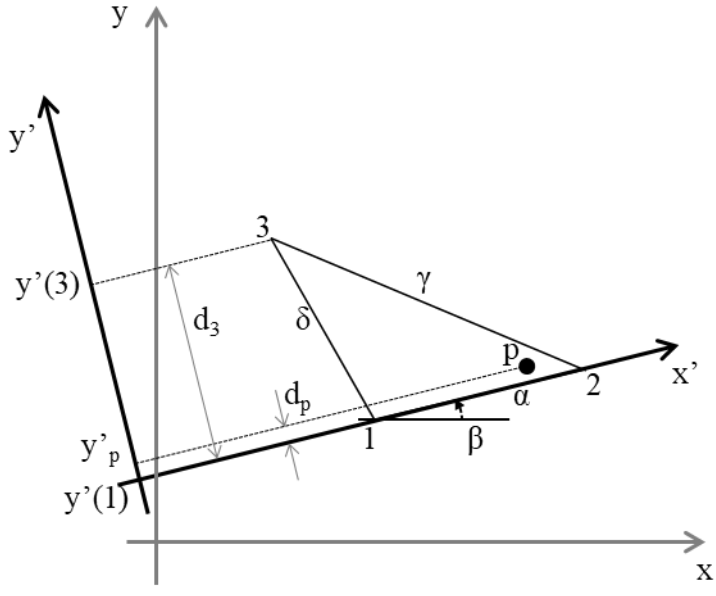

Figure 3.6 Graphical illustration of the localization procedure. p is the point of interest; α, γ and δ are the sides of the cell and 1, 2 and 3 its vertex. The new rotated reference system (x', y') is aligned with the side α of the triangle and β is the angle of rotation. The transformed coordinates are shown on the y' axis and the distances (d_3 and d_p) from the new horizontal axis are displayed.

If the product of the distances d_p and d_3 is greater or equal to zero, the point of interest is on the same side of the free vertex, so it is possible that

it is inside the considered triangle. To assess if it is true, the same procedure is repeated for each side of the triangle, computing the new rotation matrix, the new horizontal reference and the product of the distances of the point *p* and of the free vertex. If the result is greater or equal to zero for each side, it means that the point is actually located in that triangle.

On the contrary, when the product of the two distances is lower than zero, the point and the free vertex are not on the same side, so the point is certainly not in the triangle. The procedure moves to the triangle adjacent to that side and all the above mentioned steps are repeated.

This algorithm is quite simple, requires few operations for each repetition and only three recurrences if the cell found with the *nearest cell centre criterion* is already the correct one. It is applied to each of the four computational points (the four centres of the segments) when the mesh is triangular, and regardless the shape of the triangular cell, it is able to find the exact one. If the mesh is Cartesian, the first criterion is sufficient, thanks to the great regularity of the elements.

3.3.2.2. Separating the assignment of velocity from the cells size

Once that the correct cell is located, the correct flow velocity has to be assigned to the point of interest. The finite volume method for the solution of the SWE provides the results at each cell centre. In means that, in the configuration of Fig. 3.4a, the values of cells from 1 to 4 may be assigned to the four points of the rigid body, while in the configuration of Fig. 3.4b, only one value can be assigned to each of the four points, totally missing the distribution of the flow velocity on the body main dimension.

To maintain the effectiveness of the subdivision of rigid bodies in subsections, the interpolation of the velocity from the cell centres is required. Furthermore, to ensure the success of the interpolation for any location of the points, two steps are performed: firstly, the nodal values are interpolated from the values at the cell centres (Fig. 3.7a) and then the value for each point is interpolated from the nodal quantities (Fig. 3.7b). It is worth

highlighting that the interpolation procedure has to be performed for each of the centres of the body subsections.

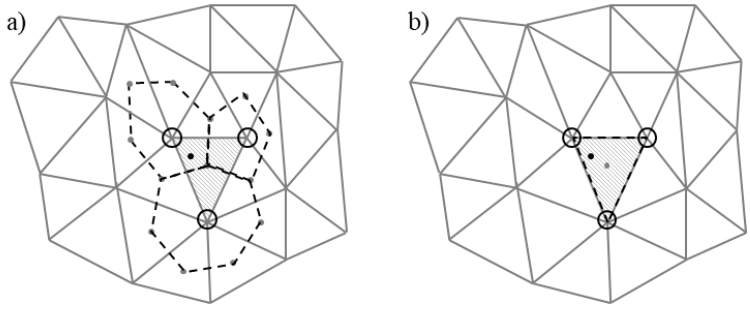

Figure 3.7 a) First step of interpolation: from cells values to vertices values; b) second step of interpolation: from vertices values to point values.

A general scheme of interpolation valid for a two-dimensional domain is:

$$U(x) = \sum_{i=1}^{n} \phi_i(x) U_i(x) \tag{3.9}$$

where $U(x)$ is the value of the scalar function (such as a component of flow velocity, or the water level) at the point of interest, $\phi_i(x)$ is the shape function for the node of interpolation i and $U_i(x)$ is the known value at node of interpolation.

To perform the interpolation from centred values to nodal values (Fig. 3.7a), the number of cells n sharing the same vertex is *a priori* unknown. The shape functions have thus to be valid for any irregular convex n-gons, satisfying the following properties, as shown by Sukumar and Tabarrei (2004):

$$0 \leq \phi_i(x) \leq 1 \tag{3.10a}$$

$$\sum_{i=1}^{n} \phi_i(x) = 1 \tag{3.10b}$$

$$\phi_i(x_j) = \delta_{ij} \tag{3.10c}$$

Eqs. 3.10a and 3.10b summarize the fact that the shape function has to be positive, it has to be a partition of unity and that the interpolated value must lay between the minimum and maximum values assumed at the nodes of interpolation. According to Eq. 3.10c, the shape function is equal to the Kronecker-delta if the point of interpolation corresponds to one of the interpolation node. It means that, if the points overlap, the exact value of the node of interpolation has to be assigned to the point of interest.

To ensure the validity of the shape function, with the above-described properties, the generalization to convex irregular *n*-gons of the Wachspress shape functions is implemented. These functions for polygonal elements are based on the ratio of polynomial functions, and their generalization is provided by Meyer et al. (2002):

$$\phi_i(x_j) = \frac{w_i(x)}{\sum_{j=1}^{n} w_j(x)} \tag{3.11a}$$

$$w_i(x) = \frac{Ar(p_i, p_{i-1}, p_{i+1})}{Ar(p_{i-1}, p_i, p)Ar(p_i, p_{i+1}, p)} = \frac{\cot(\gamma_i) + \cot(\delta_i)}{\|\boldsymbol{x} - \boldsymbol{x}_i\|^2} \tag{3.11b}$$

where $w_i(x)$ is the Wachspress weight function, here computed on the basis of the generalization which takes into account the signed areas of the triangles shown in Fig. 3.8a. The second part of Eq. 3.11b is the computation of the areas as suggested by Meyer et al. (2002), where the angles γ_i and δ_i are show in Fig. 3.8b, $\boldsymbol{x}$ is the coordinate vector of the point of interest and $\boldsymbol{x}_i$ is the coordinate vector of the considered node of interpolation. The method can be implemented, as demonstrated by Sukumar and Tabarrei (2004), combining dot and cross products of the coordinates of the vertices of the triangles for the computation of the cotangents:

$$\cot(\gamma_i) = \frac{(\boldsymbol{x}_p - \boldsymbol{x}_{p_i}) \cdot (\boldsymbol{x}_{p_{i-1}} - \boldsymbol{x}_{p_i})}{|(\boldsymbol{x}_p - \boldsymbol{x}_{p_i}) \times (\boldsymbol{x}_{p_{i-1}} - \boldsymbol{x}_{p_i})|} \tag{3.12a}$$

$$\cot(\delta_i) = \frac{\left(\boldsymbol{x}_{p_{i+1}} - \boldsymbol{x}_{p_i}\right) \cdot \left(\boldsymbol{x}_p - \boldsymbol{x}_{p_i}\right)}{\left|\left(\boldsymbol{x}_{p_{i+1}} - \boldsymbol{x}_{p_i}\right) \times \left(\boldsymbol{x}_p - \boldsymbol{x}_{p_i}\right)\right|} \tag{3.12b}$$

Refer to Fig. 3.8b for the order of the points involved in the cotangents computation.

The weight function is computed for the centre of each cell that has a vertex p (e.g. 7 cells in the case shown in Fig. 3.8a), then the corresponding shape function is computed with Eq. 3.11a and the value for the vertex p is calculated by applying Eq. 3.9. The procedure is repeated for each vertex of the selected cell, so that the flow velocity (as well as other quantities of interest) at each node is obtained.

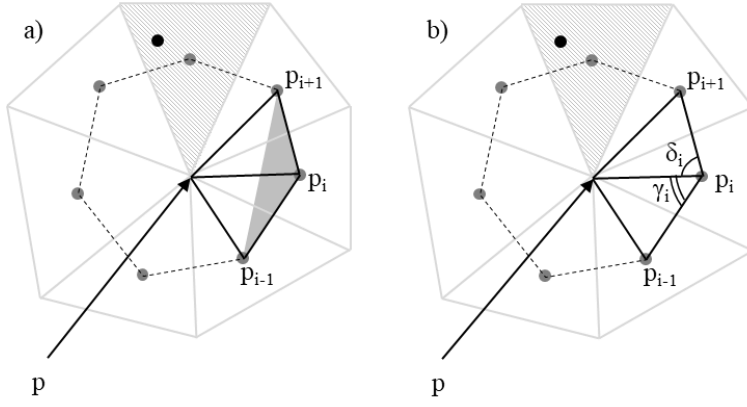

Figure 3.8 Adapted from Sukumar and Tabarrei (2004) a) Areas involved for the computation of the weight function for the point p_i; solid grey triangle is the numerator area of Eq. 3.11b while empty black lined triangles are the denominator areas of Eq. 311b; b) angles for the computation of the weight function for the point p_i according to the second part of Eq. 3.11b.

The velocities at the mesh nodes, interpolated from central values as shown, are then used to estimate the flow velocity for each body subsegment (Fig. 3.7b). In the case of a triangular mesh, the linear interpolation on the triangle is implemented. The shape function is computed as follows:

$$N(i) = a_i x_i + b_i y_i + c_i \tag{3.13}$$

Where the weights a_i, b_i and c_i are computed as shown in the equations:

$$a_i = \frac{y_{i+1} - y_{i-1}}{2Ar} \tag{3.14a}$$

$$b_i = \frac{x_{i-1} - x_{i+1}}{2Ar} \tag{3.14b}$$

$$c_i = \frac{(x_{i+1}y_{i-1} - x_{i-1}y_{i+1})}{2Ar} \tag{3.14c}$$

$$\begin{aligned} 2Ar = {} & (x_i y_{i+1} + x_{i+1}y_{i-1} + x_{i-1}y_i) \\ & - (y_i x_{i+1} + y_{i+1}x_{i-1} + y_{i-1}x_i) \end{aligned} \tag{3.15}$$

The shape function is computed for each node, and then the value of velocity, or of water height, for the point of interest is computed with Eq. 3.9.

This two-steps interpolation allows to maintain a detailed description of the velocity distribution on the body. However, several recurrences are needed, first of all to obtain the values of the flow variables at the vertices of each cell of interest –in which the computation points are located– and then to interpolate from the vertices values to the computation points values. For this reason, the interpolation is performed only for the cells in which the computational points are located.

3.3.3. Implementing the entrainment model

Once that the bodies are located on the mesh and the flow velocity distribution is known, the entrainment is computed by following the model proposed by Braudrick and Grant (2000). The computation of the quantities and parameters implemented is here detailed taking into account the extension to the case of large bodies.

The body net weight is firstly computed. If the body is totally submerged, the total volume is computed, while in case of partial submergence the submerged volume V_{sub} needs to be calculated. For a sphere, the partially submerged volume corresponds to the volume of a spherical cap with a

height equal to the water level (averaged on the water levels on the four sub-segments). For a cylinder the volume is $Vol_{sub} = A_{sub}L$, and the submerged area, A_{sub}, is computed as:

$$A_{sub} = \frac{D^2}{8}\left(2arccos\left(1-2\frac{h}{D}\right) - sen\left(2arccos\left(1-2\frac{h}{D}\right)\right)\right) \tag{3.16}$$

Note that in Eq. 3.16 h is the average water level, i.e. the mean value on the four body sub-segments (Fig. 3.9).

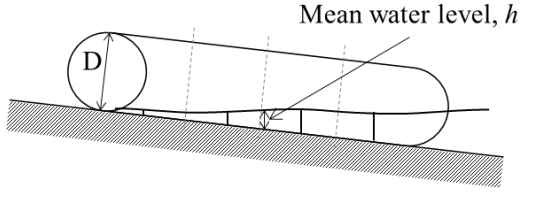

Figure 3.9 Cylinder on an inclined bed. The water level used to compute the submerged area is the average value of the water level observed on each sub-segment.

If the body net weight is positive, it cannot float and the force balance is computed, accounting for the body submersion. Forces are calculated for each sub-section, and then are summed to provide a global estimation of entrainment. The effect of gravity, the friction and the drag force on each element becomes:

$$\boldsymbol{F}_{grav\,i} = \boldsymbol{W}_i \sin(\alpha) \tag{3.17}$$

$$\boldsymbol{F}_{frict\,i} = \mu_{fr} W_i \cos(\alpha) \frac{\boldsymbol{V}_{fi} - \boldsymbol{V}_{bi}}{\left|\boldsymbol{V}_{fi} - \boldsymbol{V}_{bi}\right|} \tag{3.18}$$

$$\boldsymbol{F}_{drag\,i} = \frac{1}{2} C_{D\ app\ i} \rho_f A'_i \left(\boldsymbol{V}_{fi} - \boldsymbol{V}_{bi}\right)\left|\boldsymbol{V}_{fi} - \boldsymbol{V}_{bi}\right| \tag{3.19}$$

The symbols in the equation are those already seen in Chapter 2, while the subscript *i* refer to the single body sub-segment. The relative velocity is make explicit and includes the undisturbed flow velocity, $\boldsymbol{V}_{fi}$, estimated at the four computational points and the segments velocity, $\boldsymbol{V}_{bi}$, computed as in Eq. 3.5.

The area of application of the drag force A'_i is obtained by dividing by 4 the total area. This area depends on the body and on the relation between the water level and the body diameter, as shown in Tab. 3.1.

	$h \geq D$	$h < D$
Cylinder	$A' = LD$	$A' = Lh$
Sphere	$A' = \pi r^2$	Eq. 3.16

Table 3.1 Drag force area for the incipient motion, depending on submergence and on the body shape.

As regards the apparent drag coefficient, its estimation requires different accuracy depending on the body shape. Modelling incipient motion is significant for real applications, and spherical objects are not easily found during a flood. For this reason, the apparent drag coefficient for a sphere is set equal to the drag coefficient implemented in the DEM, specified in the following paragraphs.

The incipient motion of cylinders requires an accurate evaluation of the *apparent drag* coefficient. From the experiments of Bocchiola et al. (2006) an average value equal to *1.41* is obtained. But if the results are grouped according to cylinder orientation, two values can be obtained: *1.24* is the apparent drag for cylinders perpendicular to the flow, while *1.59* is the average value for cylinders parallel to the flow. To take into account the orientation of the cylinders, the apparent drag is interpolated among these values. The curve implemented for the interpolation is presented in Chapter 4.

3.4. Discrete Element Modelling (DEM)

In this paragraph the Lagrangian model for the transport of floating objects is resumed. The equations of ORSA2D_WT for translation and rotation are extended to large bodies thanks to the *subdivision procedure* described in Paragraph 3.3.1. The coefficients implemented for spheres and cylinders are presented, in order to clarify how the formulation adapts to the different body shapes, and the technique for the computation of gradient for a triangular mesh is illustrated. The numerical method implemented for the solution of the DEM is finally described.

3.4.1. Model equations

The equations of the forces have to be adjusted to take into account the subdivision of the rigid body in sub-segments. The modified expressions of the forces present the area and the volume of the single sub-segments, as well as a relative velocity estimated at each computational point. The translation equation then reads:

$$\begin{aligned}\left(m_b + \frac{1}{2}C_A m_f\right)\frac{d\boldsymbol{V}_b}{dt} &= \frac{1}{2}\rho_f \sum_{i=1}^{4} C_{Di}A_i\left(\boldsymbol{V}_{fi} - \boldsymbol{V}_{bi}\right)\left|\boldsymbol{V}_{fi} - \boldsymbol{V}_{bi}\right| \\ &+ \frac{1}{2}\rho_f \sum_{i=1}^{4} C_{Si}A_i\left[\left(\boldsymbol{V}_{fi} - \boldsymbol{V}_{bi}\right)\left|\boldsymbol{V}_{fi} - \boldsymbol{V}_{bi}\right|\right] \times \boldsymbol{i}_z \\ &+ \rho_f\left(1 + \frac{1}{2}C_{AM}\right)\sum_{i=1}^{4} Vol_i \frac{D\boldsymbol{V}_{fi}}{Dt}\end{aligned} \tag{3.20}$$

Comparing Eq. 3.20 with Eq. 2.15, the evaluation of the forces performed in each segment is resumed in the summations of the drag, side, pressure gradient and added mass contribution on the four sections of the body. The values of the drag, side and added mass coefficients, as well as the segment area and volume, depend on the body shape.

The rotation formulation has to be modified, too, to take into account the computation of forces on the body sections.

3.4.1.1. Offset and resistance torques

When considering the forces exerted on the body segments, since the relative velocities are different, the forces orientation varies, too. The centre of pressure is computed according to such orientation, so its position has to be computed for each subsection. Figure 3.10a shows how forces may vary their orientation while in Fig. 3.10b the qualitative position of the pressure centre varies accordingly. When the forces are nearly perpendicular to the body, the position of the pressure centre is nearer to the body mass centre, otherwise it moves towards $\pm 0.25L$, according to the equation proposed by Yin et al. (2003), where α_{RELi} is the angle between the cylinder and the local relative velocity:

$$\boldsymbol{x}_{CP} = 0.25L(\cos(\alpha_{RELi}))^3 \tag{3.21}$$

The term is modified to account for the velocity distribution on large bodies by introducing the distances b_{CPxi} and b_{CPyi} among the mass centre and the different pressure centres. The forces on each segment are multiplied by this distance and sum over the number of segments (first right term in square brackets in Eq. 3.22).

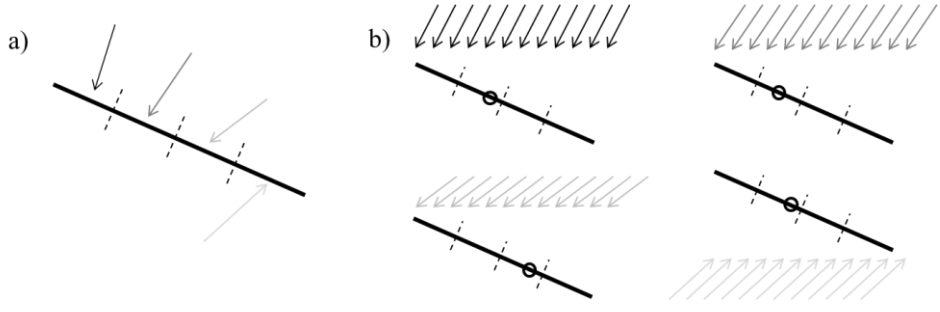

Figure 3.10 a) Qualitative force distribution on the body main length; b) Variation of the position of the centre of pressure according to the force orientation.

As regards the resistance torque, the term has to be evaluated for each body section. In particular, the flow angular velocity is estimated for each

subsection (from the mesh values), while the body angular velocity is kept constant, in agreement with the rigidity of the body.

The final form of the first formulation tested for rotation reads:

$$
\begin{aligned}
I\frac{d\boldsymbol{\omega}_b}{dt} = \Bigg[\sum_{i=1}^{4} -b_{CPyi}\Big(&\frac{1}{2}\rho_f C_{Di}A_i(u_{fi}-u_{bi})\left|\boldsymbol{V}_{fi}-\boldsymbol{V}_{bi}\right| \\
&+\frac{1}{2}\rho_f C_{Si}A_i(v_{fi}-v_{bi})\left|\boldsymbol{V}_{fi}-\boldsymbol{V}_{bi}\right| \\
&+\rho_f\left(1+\frac{1}{2}C_A\right)Vol_i\frac{Du_{fi}}{Dt}-\frac{1}{2}\rho_f C_A Vol_i\frac{du_{bi}}{dt}\Big) \\
&+\sum_{i=1}^{4} b_{CPx}\Big(\frac{1}{2}C_{Di}A_i(v_{fi}-v_{bi})\left|\boldsymbol{V}_{fi}-\boldsymbol{V}_{bi}\right|\rho_f \\
&+\frac{1}{2}\rho_f(u_{fi}-u_{bi})\left|\boldsymbol{V}_{fi}-\boldsymbol{V}_{bi}\right| \\
&+\rho_f\left(1+\frac{1}{2}C_A\right)Vol_i\frac{Dv_{fi}}{Dt}-\frac{1}{2}\rho_f C_A Vol_i\frac{dv_{ib}}{dt}\Big)\Bigg] \\
&+\frac{1}{8}\rho_f C_{res}L^2\sum_{i=1}^{4} Vol_i\left[\left(\boldsymbol{\omega}_{fi}-\boldsymbol{\omega}_b\right)\left|\boldsymbol{\omega}_{fi}-\boldsymbol{\omega}_b\right|\right]
\end{aligned}
\tag{3.22}
$$

3.4.1.2. Angular momentum and added inertia torques

The computation of the forces distribution allows one to evaluate the angular equilibrium with respect to the mass centre. The forces are applied at the centre of each segment, and the torque is computed by multiplying the force summation by the distance between the entire rigid body mass centre and the local one (b_{xi} and b_{yi}, first right term in square brackets in Eq. 3.23).

The torque due to the added inertia is evaluated by taking into account local flow vorticity and the body angular acceleration, which is grouped on the left term in Eq. 3.23.

$$
\begin{aligned}
I\left(1+\frac{1}{2}C_{AI}\right)\frac{d\boldsymbol{\omega}_b}{dt} &= \left[-\sum_{i=1}^{4} b_{yi}\left(\frac{1}{2}\rho_f C_{Di}A_i(u_{fi}-u_{bi})\left|\boldsymbol{V}_{fi}-\boldsymbol{V}_{bi}\right|\right.\right. \\
&+\frac{1}{2}\rho_f C_{Si}A_i(v_{fi}-v_{bi})\left|\boldsymbol{V}_{fi}-\boldsymbol{V}_{bi}\right| \\
&+\rho_f\left(1+\frac{1}{2}C_A\right)Vol_i\frac{Du_{fi}}{Dt}-\frac{1}{2}\rho_f C_A Vol_i\frac{du_{bi}}{dt}\Big) \\
&+\sum_{i=1}^{4} b_{xi}\left(\frac{1}{2}\rho_f C_{Di}A_i(v_{fi}-v_{bi})\left|\boldsymbol{V}_{fi}-\boldsymbol{V}_{bi}\right|\right. \\
&+\frac{1}{2}\rho_f C_{Si}A_i(u_{fi}-u_{bi})\left|\boldsymbol{V}_{fi}-\boldsymbol{V}_{bi}\right| \\
&+\left.\left.\rho_f\left(1+\frac{1}{2}C_A\right)Vol_i\frac{Dv_{fi}}{Dt}-\frac{1}{2}\rho_f C_A Vol_i\frac{dv_{ib}}{dt}\Big)\right)\right] \\
&+\frac{1}{2}C_{AI}\sum_{i=1}^{4}\left(I_i\frac{D\boldsymbol{\omega}_{fi}}{Dt}\right)
\end{aligned}
\tag{3.23}
$$

To sum up, the adaptation of the translation and rotation equations is performed by evaluating the forces at the centre of mass of the single body segments and superimposing their effect under the rigidity constraint. The variation of the area, of the volume and of the moment of inertia derived by the body subdivision were presented in Paragraph 3.3.1.

It is not trivial to demonstrate the validity of such an approach, since the single body entities (i.e. body segments) do not behave exactly as the entire sample. For example, focusing on cylinders, the two segments nearest to the mass centre do not present free ends, so their hydrodynamic behaviour is not the same of a single large body. However, the subdivision allows a detailed description of the flow on the body, which is fundamental to account for the different conditions that it may encounter in a real stream.

The application of the method in Chapter 5 will show the acceptability of this hypothesis of superimposition of effects.

3.4.2. Implemented coefficients

Equations 3.20, 3.22 and 3.23 can be applied both to spherical and cylindrical bodies. The variation of the drag, side, apparent drag and added mass coefficients according to the body shape is here reported.

The values of the resistance coefficient C_{res} and of the added inertia coefficient C_{AI} are not reported in this paragraph, since they need to be calibrated with laboratory experiments.

3.4.2.1. Values for cylinders

For a cylinder, the drag and side coefficients depend on the body orientation. Since in literature no complete data are available for the case of partially submerged cylinders, an experimental campaign was performed to obtain these values, as described in Chapter 4. The coefficients are computed for each sub-segment, based on the local orientation of the relative velocity.

The apparent drag for a cylinder, which is used to compute and verify the body entrainment, is different from the classical drag, since it has to account for other local phenomena typical of a body lying on the river bed. Its variability with the body orientation can be derived from the studies realized by Bocchiola et al. (2011). However, the researchers only provided values for a cylinder parallel (1.59) and perpendicular to the flow (1.24), while intermediate values are not available. In this dissertation, the variation of the apparent drag is supposed similar to the variation with orientation of the classical drag coefficient. The resulting equation is also shown in Chapter 4.

The added mass coefficient is assumed constant, since no data exist on its variation for semi-submerged cylindrical bodies. Literature values refer to totally submerged bodies and need to be adapted to the case of floating objects. For submerged cylinders, the literature value is 1 (Dean and Dalrymple 1991). Note that in the expression of the added mass force proposed in Eq. 3.20, the added mass coefficient should be equal to 2, since

the force is halved with respect to the standard equation. Overall, the value of the added mass coefficient for a cylinder means that the added mass corresponds to a mass of fluid of the same volume as the sample.

To represent the additional mass, one can consider that the transported cylinder has a volume equal to the double of its original volume. In Fig. 3.11a, the solid line represent the solid volume, while the dashed line represent the augmented volume, which accounts for the body inertia. Since the submerged part of the real cylinder can be computed by multiplying the volume by the density ratio, the submerged volume of the doubled cylinder can be consequently estimated (Fig 3.11b).

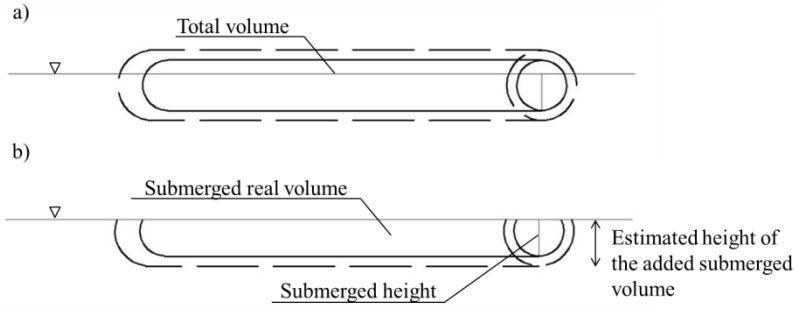

Figure 3.11 Diagram for the estimation of the added mass coefficient. a) Volume of the cylinder (solid line) and added volume (dashed lines); b) Volumes are adjusted for sinking and the submerged height for the added volume can be estimated.

The added mass coefficient for a semi-submerged cylinder is then computed by dividing the submerged added mass volume (dashed line in Fig. 3.11b) by the body volume (solid line in Fig. 3.11a). The value obtained refers to a wooden cylinder with density equal to 774 kg/m^3:

$$C_{AM} = \frac{submerged\ added\ mass\ volume}{cylinder's\ volume} = 1.41 \qquad (3.24)$$

3.4.2.2. Values for spheres

For a sphere, the drag coefficient depends on the Reynolds number and is computed according to the values found in the literature (e.g. Chow 1979, Fig. 3.12).

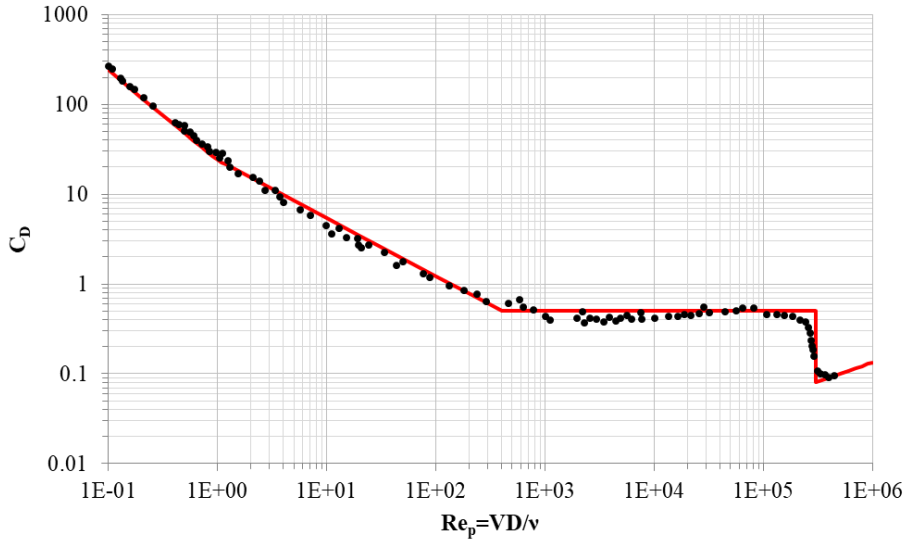

Figure 3.12 Drag coefficient for a sphere (Chow 1979) as a function of the particle Reynolds number Re_p. The red line shows the values implemented in ORSA2D_WT.

In the model, the value is computed by implementing four equations, valid for different Re_p ranges, as shown in Tab. 3.2:

Re_p	C_D
$Re_p \leq 1$	$24/Re_p$
$1 < Re_p \leq 400$	$24/(Re_p^{0.646})$
$400 < Re_p \leq 3.0E5$	0.5
$3.0E5 < Re_p \leq 2E6$	$0.000366 Re_p^{0.4275}$

Table 3.2 Drag coefficient for a sphere, as a function of the Reynolds number.

The side coefficient implemented in the formulation resumes the effect of the share-induced and of the Magnus-induced lift, on a 2D plane. It is

made of two parts: a numerical value, which is generally found in literature for specific values of Reynolds number and body angular velocity (e.g. Truscott and Techet 2009), and the sign which allows to take into account the combined effects of flow vorticity and body angular velocity:

$$C_S = C_{S\,literature} sgn\left(\left(\boldsymbol{V}_{fi} - \boldsymbol{V}_{bi}\right) \times \left(\boldsymbol{\omega}_{fi} - \boldsymbol{\omega}_b\right)\right) \tag{3.25}$$

The subscript *i* refers to the four body segments.

The apparent drag coefficient is not significant for spherical objects, at least for the applications provided in this dissertation. For this reason it is set equal to the standard drag coefficient (Eq. 3.25).

The added mass coefficient is assumed equal to 1 in the proposed formulation for totally submerged spheres, so that the added volume is equal to half of the sphere volume. Since it is half of the added mass coefficient for a cylinder, the value for semi-submerged spheres is obtained by halving the added mass computed with Eq. 3.24, and results equal to 0.7.

3.4.3. Side force computation

The side force is one of the key term for the simulation of spheres and cylinder transport. In both cases it accounts for the displacement of the body in the direction perpendicular to the relative velocity.

Regarding spheres, its versus and direction are given from combining the side force expression with the coefficient in Eq. 3.25, while for cylinders, the sign of the side force is computed by taking into consideration the angle between the relative velocity of each sub-segment and the cylinder orientation. Note that if the relative velocity and the cylinder are aligned or perpendicular, the side force is zero, to respect the theoretical origin of the side force, which arises only if there is a non-symmetrical deviation of the flow around the body.

3.4.4. Gradient computation

The material derivative of the flow velocity requires the computation of partial derivatives in *x* and *y*, for both the component of the linear and angular velocities:

$$\frac{Du_f}{Dt} = \frac{\partial u_f}{\partial f} + u_f \frac{\partial u_f}{\partial x} + v_f \frac{\partial u_f}{\partial y} \tag{3.26}$$

$$\frac{Dv_f}{Dt} = \frac{\partial v_f}{\partial f} + u_f \frac{\partial v_f}{\partial x} + v_f \frac{\partial v_f}{\partial y} \tag{3.27}$$

$$\frac{D\omega_f}{Dt} = \frac{\partial \omega_f}{\partial f} + u_f \frac{\partial \omega_f}{\partial x} + v_f \frac{\partial \omega_f}{\partial y} \tag{3.28}$$

For a quadrilateral mesh, such derivatives are easily computed by applying the numerical stencil for derivatives to the cells surrounding the cell in which the point of interest is located.

For a triangular mesh, a different strategy is required due to the irregularities of the cell coordinates. The trapezoidal interpolation suggested by Hirsh (2007) is then implemented:

$$\frac{\partial X}{\partial x} = \frac{1}{2Ar} \sum_{i=1}^{n} X_i (y_{i+1} - y_{i-1}) \tag{3.29}$$

$$\frac{\partial X}{\partial y} = \frac{1}{2Ar} \sum_{i=1}^{n} X_i (x_{i+1} - x_{i-1}) \tag{3.30}$$

$$Ar = \frac{1}{2} \sum_{i=1}^{n} x_i (y_{i+1} - y_{i-1}) \tag{3.31}$$

where n is the number of nodes of the cell of interest, X is the variable whose derivative is being computed (u_f, v_f or ω_f), x and y are the nodal coordinates and Ar is the cell area.

The computation of gradients takes advantage of the interpolation from cell central values to nodal values (Eqs. 3.9 and 3.11) and is performed only for those cells in which the computational points are found.

3.4.5. Runge-Kutta method

The DEM is solved by implementing an explicit 4th order Runge-Kutta method. Positions and orientations (x, y and ϑ) and linear and angular velocities (u, v and ω) are computed according to the following equation:

$$X_{n+1} = X_n + \frac{h}{6}(\Delta_{1X} + 2\Delta_{2X} + 2\Delta_{3X} + \Delta_{4X}) \tag{3.32}$$

where X_{n+1} is one of the variables that have to be estimated, X_n is its value at the current time n, h is the time step and Δ_{kX} are the incremental weights for the computation of the weighted average.

The weights are computed with the following sets of equations, where Eqs. 3.33 are applied to position and orientation, while Eqs.3.34 are applied to velocities:

$$\Delta_{1x} = F(\dot{x}) \quad ; \quad \Delta_{2x} = F\left(\dot{x} + \frac{h}{2}\Delta_{1\dot{x}}\right); \quad \Delta_{3x} = F\left(\dot{x} + \frac{h}{2}\Delta_{2\dot{x}}\right); \quad \Delta_{4x} = F(\dot{x} + h\Delta_{3\dot{x}}) \tag{3.33}$$

$$\Delta_{1\dot{x}} = F(x, y, \vartheta, u, v, \omega, t)$$

$$\Delta_{2\dot{x}} = F\left(X + \frac{h}{2}\Delta_{1X}, t\right) \; with \; X = x, y, \vartheta, u, v, \omega$$

$$\Delta_{3\dot{x}} = F\left(X + \frac{h}{2}\Delta_{2X}, t\right) \tag{3.34}$$

$$\Delta_{4\dot{x}} = F(X + h\Delta_{3X}, t)$$

In Eq. 3.33 the term $F(\,)$ refers to the kinematic relations that allow one to compute linear and angular displacement from velocities for each time step. In Eq. 3.34 t is the instant considered for the computation, which is

kept constant within the same instant of the time loop, and *F( )* represents the right side of Eq. 3.20 for linear velocities and 3.22 or 3.23 for angular velocity computation.

In practice, within the main time loop, the four weights have to be computed, by considering the position, orientation and velocities adjourned with the weight of each inner step. Finally Eq. 3.32 is applied to compute the new velocities of the centre of mass and the final position and orientation.

3.5. Implementing the model of collision

The collisions between rigid bodies and between bodies and side walls are modelled in order to account for possible interactions both in channel experiments and in real world situations. In particular, cylindrical bodies are considered, since no collision among spheres were observed, nor similar bodies are used for real scale experiments. Furthermore, only dual collisions are modelled, which means that multiple collisions are possible but are treated in sequence, as two-by-two collisions.

The mathematical model adopted has been described in Chapter 2 and does not require particular measures for its implementation. On the contrary, more accuracy has to be provided for the collision detection and the correction of the overlaps among bodies.

Once that these procedures are performed and the final configuration of collision is obtained, the post-collisional linear and angular velocities are computed according to Eqs. 2.31 and 2.32. The new positions, velocities and acceleration become the initial condition for the following time step.

To check whether a collision takes place or not, the model considers at any time step all those pairs of cylinders whose centres of mass are located at a distance smaller than half of the sum of the two body lengths (Fig. 3.13a). Then, a collision (Fig 3.13b) is detected as shown in paragraph 3.5.1. The same procedure is repeated between cylinders and walls, where

any mesh boundary, or boundary of an in-stream obstacle, is assumed to be a wall.

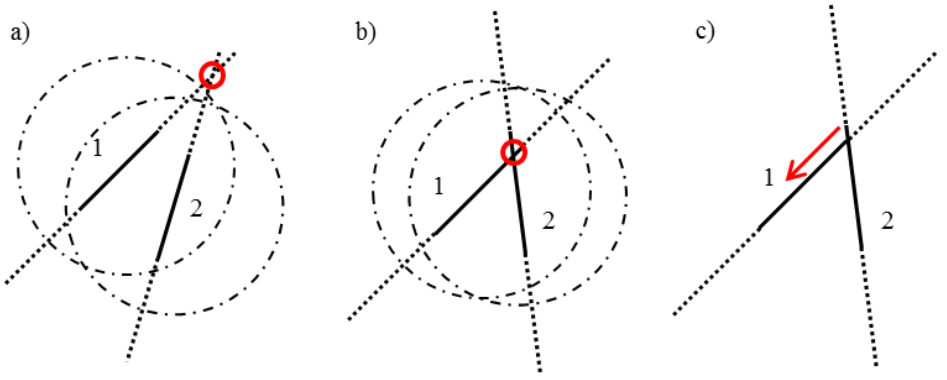

Figure 3.13 Interaction between two logs; black thick line is the log axes, dotted lines are the axes extensions, dot-line circumferences highlight the influence area of each body, which radius is half of the sum of the cylinders' length ; a) intersection without collision; b) collision with overlap; c) repositioning of the colliding log.

Since the interaction requires a certain overlap between the two elements, owing to the finiteness of the computational time step, before computing the post-collisional values the position of the involved bodies is adjusted by moving the *colliding cylinder*. When a collision with boundaries occurs, only the cylinder position can be adjusted; when two floating objects are involved, the *colliding cylinder* is considered to be the one whose centre of mass is farther from the collision point, and is thus shifted (Fig. 3.13c, after adjustment).

3.5.1. Collision detection

The detection of a collision is based on the possibility of intersection between the considered bodies, and has been treated in different ways for cylinder-cylinder and cylinder-wall interactions. In the first case, 2D rigid bodies are considered, while in the latter, the walls are 1D objects, represented by their major axis.

3.5.1.1. Cylinder-cylinder collision detection

A collision between two floating bodies, represented as rectangles with sides *L* and *d*, is detected by verifying if any edge of one of the rectangles lies inside the area of the other.

First of all, the coordinates of the edges of one of the rectangles (e.g. rectangle A in Fig. 3.14) are calculated, and then the lines parallel and perpendicular to the axis of the other rectangle (B in Fig. 3.14), crossing each edge of body A, have to be computed. The comparison of the *y*-intercepts of these lines allows to identify any interaction: a collision occurs if the *y*-intercepts of the lines from at least one edge of rectangle A are included in the intervals (black thick lines in the figure) drawn by the *y*-intercepts of the sides of rectangle B. In the figure, only the lines across one edge are represented, for graphical clarity, but the procedure is performed for each edge of both rectangles.

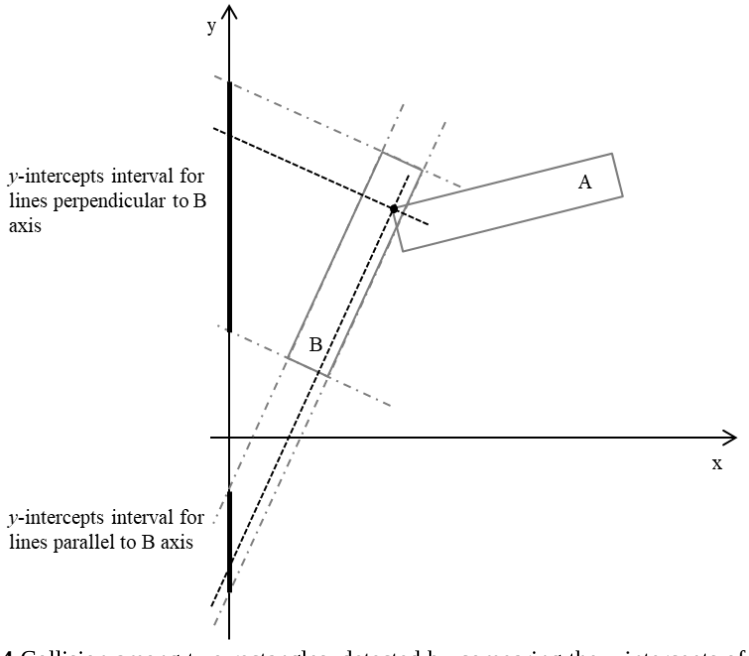

Figure 3.14 Collision among two rectangles, detected by comparing the *y*-intercepts of the extensions of the sides of rectangle B and the two lines, parallel to the sides, passing across one edge of rectangle A. Black thick lines show the interval in which the edges' lines have to be simultaneously contained.

3.5.1.2. Cylinder-wall collision detection

The collision between cylinders and walls is computed if side walls (as for laboratory channels) or solid still objects are present in the domain. Such objects are part of the mesh, but are characterized by an abrupt increment of height, such as bridge piers or in stream obstacles, which obstruct both the water and the sediment flow. For computational purposes, the floating rigid bodies are represented again as rectangles, while the walls are represented by lines, with a centre, a length and an orientation, as well as a height, which corresponds to the maximum level reached by the solid still object.

In general, a collision among lines and rectangles is computed only if the two bodies are close enough to satisfy the condition of proximity and if the cylinder vertical position, equal to the average water level in that point, is lower than the obstacle top level. In this case, a collision can be detected, otherwise, the solid body can flow above the obstacle, which is submerged and becomes an active part of the mesh.

If a collision is possible, the reference coordinate system *(x,y)* is rotated counter-clockwise and vertically aligned to the line axis (rotated reference *(x',y')* in Fig. 3.15a). The coordinates of the rectangle centre and edges are rotated, too. A collision occurs if the distance among the rectangle centre (CM) and one of the vertex, in the rotated reference, is higher than the distance between the centre CM and the line, and if the vertex is included between the line ends. The first condition is verified by considering the rotated *x'* coordinated of the points, and the latter by considering the rotated *y'* coordinate of the edges and of the line ends.

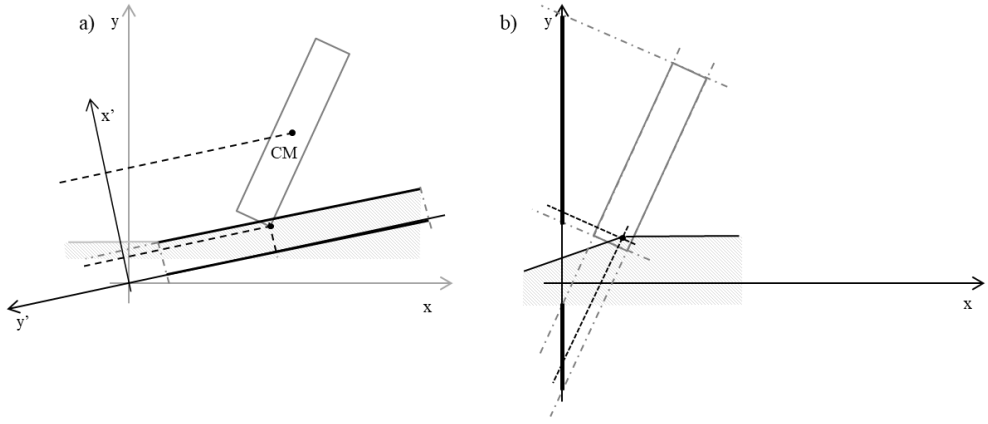

Figure 3.15 Collision with a side wall: a) in the rotated coordinate system *(x',y')* distances in *x'* and *y'*-intercepts are compared to check if collision occurs; b) if the side wall presents a corner, it is verified if it is inside the rectangle by comparing y-intercepts parallel and perpendicular to the major axis.

A special case is that of the collision with corners, which may be present if the obstacle changes its orientation or shape, as shown in Fig. 3.15b. In this case, a collision occurs if the corner is inside the rectangle, and the procedure of *y*-intercepts comparison, already described for cylinder-cylinder collision, is performed, as if the corner was the edge of a second rectangle.

3.5.2. Body repositioning

At each time step, the cylinders change their positioning and, due to the finite displacement in the finite time interval, it is possible that overlaps occur. Luckily enough, the time step is generally small, so a small super-imposition is expected, which is however sufficient to detect collisions. Then, the appropriate configuration, which does not include overlapping, has to be restored.

For the case of collision among two rigid bodies, the first step is to decide which body has to be moved. In the proposed model, the body farther with respect to the point of intersection (the edge of the rectangle that lies inside the other object) is the one that will be re-positioned. Then, the co-ordinates of the centre of mass of the selected cylinder are modified, to

obtain a configuration in which no overlaps exist and the contact point among the cylinders is the previously mentioned edge. The procedure implemented requires the rotation of the coordinate system in order to align the y'-axis to the axis of the still rectangle (counter-clockwise). Then, the coordinates of the centre of both rectangles, and the selected edge are transformed, the body is repositioned and the back-transformation is performed. This procedure is valid for any orientation of the cylinders.

If the collision is with a side wall, only the colliding cylinder has to be moved. Also in this case, the reference frame is rotated and the coordinates of the centre of mass of the rectangle are adjusted to reach a final configuration in which the only contact point between the two bodies is the edge of the rectangle (in the case of Fig. 3.15a) or the side wall corner (for the case shown in Fig, 3.15b).

Chapter 4
Hydrodynamic coefficients of floating bodies

4.1. Abstract

The hydrodynamic coefficients play a fundamental role for the correct estimation of the forces exerted by the flow. Drag and side coefficients vary with body shape and, for non-symmetrical objects, with their orientation. In addition, since the model is applied to the case of floating objects, the coefficients have to be evaluated for this specific condition, rarely taken into account in literature.

The present study on hydrodynamic coefficients wants to fill this gap, thus measuring the drag and side coefficients for semi-submerged cylinders and providing data that can be included in the 2D numerical simulation of log transport.

This Chapter reports the description of the laboratory activities performed during the Ph.D. research to measure the drag and side coefficients for a semi-submerged cylinder with variable orientation. Forces were measured using a hydrodynamic balance specifically designed for the tests, and its calibration is described. The details about the experimental campaign are provided, too, together with the analysis of the results and the comparison with literature data. The final curves implemented in the code are illustrated.

4.2. Experimental set-up

Typically, the measure of the hydrodynamic coefficients (drag, lift or side) is realized in a wind tunnel (e.g. Hoang et al. 2015). To reproduce the configuration of wooden logs floating on the water surface, it is necessary to perform such measurements in an open channel, as done by Gippel (1996) and Hygelund and Manga (2003). To realize such measures a specific hydrodynamic balance was built and the tests were planned to vary the submergence of the body and its orientation.

4.2.1. Channel and flow characterization

The experimental campaign was realised in a laboratory flume at the Hydraulics division of the Department of Civil Engineering and Architecture (DICAr) at the University of Pavia. The flume (Fig. 4.1) is 9.40 m long and 0.48 m large, with a horizontal metallic bottom and Plexiglas sides of 0.80 m height. The inlet discharge is measured through a triangular weir at the inlet section, just downstream a loading basin. The water level on the weir is measured by a piezometer, that allow to avoid the oscillation of the water surface near the weir, gaining a higher accuracy in water level measurement (about 0.001 m). The maximum discharge provided by the lab hydraulic system is 0.033 m^3s^{-1}, and the weir equation, obtained by adapting the Thomson equation to discharge values measured experimentally and varying the weir angle, is:

$$Q = \frac{8}{15} 0.6\, tg(18°) \sqrt{19.62} h^{5/2} \tag{4.1}$$

where h (m) is the measured water level at the piezometer.

To dissipate the flow energy, some devices are positioned downstream of the weir (see Fig. 4.1): in A, metal nets are placed to break the flow, and then in B concrete blocks contribute to the energy dissipation. Then, the flow is straightened through two walls of bricks, and a floating backwater device (C) dissipates the remaining surface waves.

The water level and the velocity in the channel are controlled through a vertical sluice gate in the final section. A piezometer is located in the measuring section, and provides the undisturbed water level (when the balance is not installed).

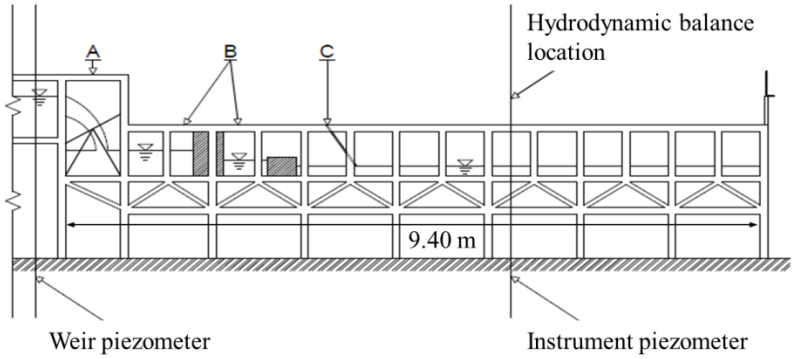

Figure 4.1 The laboratory flume: letters A, B and C show the energy dissipating devices. The location of the hydrodynamic balance and of the piezometers is shown.

The analysis of the channel rating curve provides the possible functioning points (Fig. 4.2). By varying the discharge and the sluice gate opening, the water level is measured and the corresponding velocity is computed.

4.2.2. The hydrodynamic balance

The hydrodynamic balance measures the two horizontal components of the force on a cylindrical sample: the drag force, parallel to the relative velocity, and the side force, perpendicular to the relative velocity on the horizontal plain. The measure of the lift force was not performed, since the 2D numerical modelling of log transport aims at reproducing only the planar motion of the cylinder.

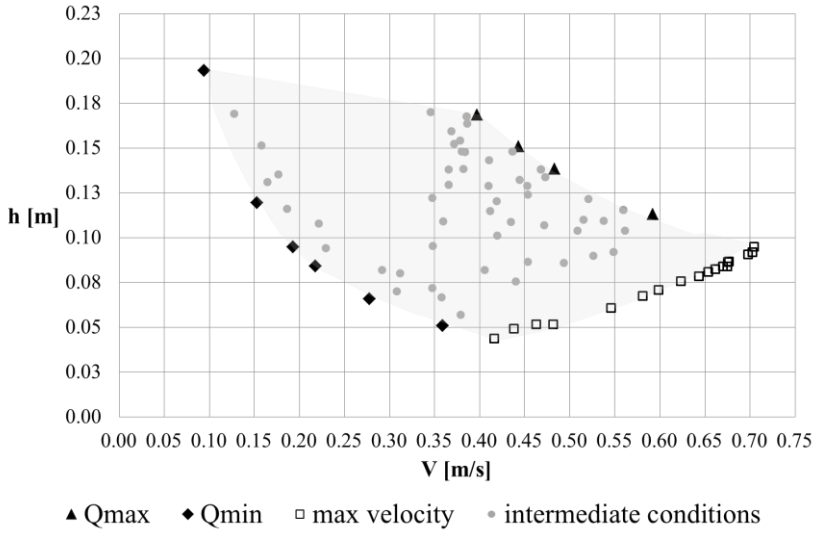

Figure 4.2 Characterization of the channel: water level and flow velocity are related for variable discharge and sluice gate openings. The maximum velocity for each discharge and the functioning points for the discharge maximum and minimum value are highlighted.

In Fig. 4.3a a picture of the instrument is shown. The balance is fixed to the channel with an horizontal aluminium bar. Two aluminium vertical columns allow its vertical displacement. At the bottom of the two column, an horizontal plate is placed, which is the base on which the load cells are leaning. The balance functioning is based on leverages: inside the aluminium plate, a spherical joint acts as the fulcrum of the lever; under the fulcrum, a vertical bar allows one to place the sample in the water. The upper part of the bar is made of steel (ø 0.010 m, 0.10 m length from the fulcrum) and is connected to an aluminium bar (ø 0.006 m, 0.19 m length from the steel bar to the sample centreline) with a threaded end, to which the sample is screwed.

The length and the diameter of the two bars were chosen to avoid excessive flexion of the instrument under the effect of the maximum hydrodynamic force. The final part is thinner in order to minimize the disturbance of the flow when the cylinder is totally submerged.

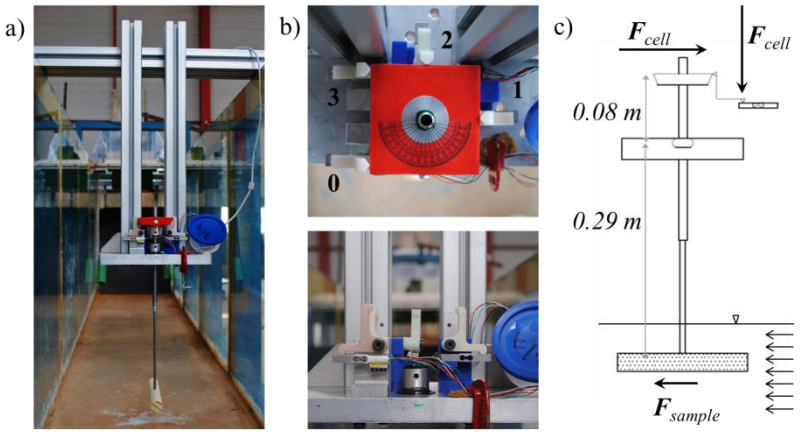

Figure 4.3 The hydrodynamic balance : a) the balance installed in the channel; b) detail of the configuration of the load cells and of the presser with cells that measure the drag (2) and the side (0, 1, 3) force; c) scheme of the leverage functioning.

Max weight capacity	780 g
Max overload	936 g
Creep	1.6 g/h
Zero balance	11.7 g
Max repeatability error	±390 mg
Non-linearity & Hysteresis	390 mg
Temperature effect	39 mg/°C

Table 4.1 Resume of load cell specifications, from Phidgets Inc.

Above the spherical joint, a 3D printed presser (in red in Fig. 4.3b) is fixed on the steel bar with the upper side at a distance of 0.08 m and transmits the force exerted on the cylinder to the load cells. The presser acts on four 3D printed "L-shaped" indifferent levers (in white in Fig. 4.3b), which turn the horizontal force into a vertical one, since the cells are sensitive only to vertical loads. Four shear load cells (Phidgets, Micro Load Cell (0-780g)) are positioned to measure the drag (cell 2 in Fig. 4.3b) and the side force (cells 0, 1, 3 in Fig. 4.3b). The load cells are firmly screwed to four independent bases, the blue ones being 3D printed, and are placed horizontally in order to be solicited by the L-shaped leverages with a vertical force. In Fig. 4.3c a scheme of the leverage functioning is

provided. All the 3D printed components were realized by Proto-Lab, the laboratory for additive manufacturing at DICAr.

The load cells characteristic are reported in Tab. 4.1.

4.2.3. Configuration of the experiments

The hydrodynamic coefficients are measured for a wooden cylinder 0.15 m long and with a diameter of 0.024 m. The cylinder is initially aligned with the channel axis but its orientation can be changed.

A fundamental parameter in the realization of hydrodynamic measurements is the blockage ratio. It is computed as the ratio between the maximum transverse area of the sample and the effective area of the flow, which is the water level times the channel width. West and Apelt (1981), who studied the effect of blockage variation, showed that, for a cylinder in flow at a Reynolds number 10^4-10^5, when the blockage ratio is smaller than 6% the measures are not influenced by the presence of walls and channel bottom. Although drawn when analysing cylinders immersed in an air flow, these conclusions can be assumed to be valid also in the present configuration, dealing with submerged and semi-submerged bodies.

The maximum frontal area of the cylinder is its longitudinal section, when the cylinder is perpendicular to the flow, and is computed as the product of its length and diameter (LD). The width of the channel is fixed while the water height can vary by changing both the discharge and the opening of the sluice gate, as shown by the tests on discharge and water level measurements, in Fig. 4.2.

For a known water level, the wet area is known, too, so the blockage ratio can be computed. The results in Tab. 4.2 show that the minimum level to avoid undesired effects of the boundary on the pressure distribution is around 0.13 m.

h [m]	Blockage [%]
0.044	17
0.113	6.6
0.12	6.3
0.139	5.4
0.193	3.9

Table 4.2 Blockage ratio for the minimum and maximum water level obtained during channel characterization. Intermediate values show the blockage variation around the minimum acceptable value according to West and Apelt (1981).

Before beginning the experimental campaign, the maximum expected force acting on the cell was estimated, in order to verify if it was within the load cell range (7.65 N). By considering the maximum velocity obtained in the channel with the highest discharge and the corresponding water level (see Fig. 4.2), the theoretical force acting on the cylinder is computed with Eq. 4.2. Then, the force acting on the body is transformed in the force acting on the cell by applying the leverage relation (Eq. 4.3).

$$\boldsymbol{F}_{sample} = \frac{1}{2} C_D \rho_f A \boldsymbol{V} |\boldsymbol{V}| \tag{4.2}$$

$$\boldsymbol{F}_{cell} = \boldsymbol{F}_{sample} \frac{0.29}{0.08} \tag{4.3}$$

Since this procedure was performed before the realization of the tests, the drag coefficient was assumed from the literature to be equal to 1.2 (Gippel 1996). The area included in Eq. 4.2 is the longitudinal section of the cylinder and the velocity is the undisturbed velocity of the flow upstream the sample. In Eq. 4.3 the force on the sample is multiplied by the leverage arms ratio: 0.29 m is the distance from the fulcrum to the sample and 0.08 m is the distance from the fulcrum to the tip of the L-shaped leverage (Fig. 4.1c). For the maximum velocity obtained in the channel, the forces on the sample and on the cell are reported in Tab. 4.3, showing that the expected value of the force acting on the load cell is acceptable.

$\boldsymbol{Q}$ [m^3s^{-1}]	h [m]	$\boldsymbol{V}$ [$m\ s^{-1}$]	$\boldsymbol{F}_{sample}$ [N]	$\boldsymbol{F}_{cell}$ [N]
0.033	0.095	0.705	1.26	4.57

Table 4.3 Forces computation for the maximum discharge and maximum velocity.

4.3. Experimental campaign

The measure of the hydrodynamic coefficient is performed under static conditions, imposing a constant discharge and varying the sample orientation and submergence. The hydrodynamic balance can then be statically calibrated, maintaining its alignment and changing the direction of force application in order to stress each load cell.

Once that the calibration curves are obtained, the relation among the cells response (in mV/V) and the force (or mass) applied to the sample is known. Then the measurement can be performed: the force exerted by the flow on the sample is recorded and from this value the hydrodynamic coefficients are estimated.

4.3.1. Hydrodynamic balance calibration

The static calibration is performed by applying a known weight (from 5 g to 200 g) to one end of the sample (Fig.4.4a). Due to the positioning of the cells (Fig. 4.4a), the drag force cell 2 and the side force cell 1 are independent, while side load cells 0 and 3 are stressed simultaneously.

Data are acquired through the bridge interface PhidgetBridge 4-Input, a high-resolution analog-to-digital converter which allows the connection of the four loads cells at one time.

A Matlab script, with the specific library for Phidgets products, is used for data acquisition, selecting the duration of each test (30 s) and the Data Rate, or acquisition time of the single measure (8 ms). The average measure and the standard deviation are computed for each weight, so that the relation among the applied weights and the cell response is obtained.

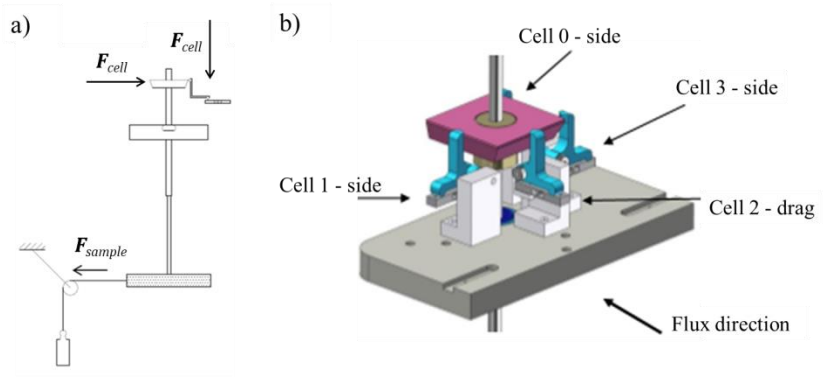

Figure 4.4 a) Scheme of the force application for calibration; b) detail of the balance, with pressor (magenta) and load cells position.

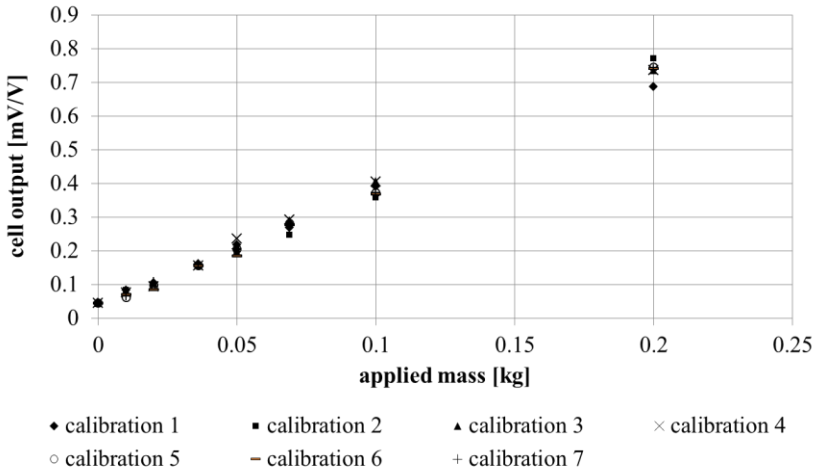

Figure 4.5 Calibration curves for cell 1.

The calibration procedure is performed 5-7 times for each cell, in order to verify the repeatability of the measurements. Then, the curve with the higher determination coefficient is selected, as shown in Tab. 4.4. In Fig. 4.5 the different measures for the calibration of cell 1 are reported.

Cell	Equation	R^2
0	$y = 3.859x - 0.006$	0.999
1	$y = 3.482x - 0.036$	0.999
2	$y = 3.221x - 0.053$	0.999
3	$y = 3.431x - 0.027$	0.999

Table 4.4 Equation of calibration for each cell. *y* states for the cell response [mV/V] and *x* for the applied mass [kg].

4.3.2. Measurement error estimation

To estimate the error of the measure of the hydrodynamic coefficients, the error in force estimation and in velocity computation are considered. The error in velocity can be derived by the error in measuring the water level both on the weir and in the channel. In fact, if one considers the flow velocity as the ratio among the discharge (Eq. 4.1) and the wet area (A_w=Wh), the expression of the hydrodynamic coefficient becomes:

$$C = \frac{F}{\frac{1}{2}\rho_f A \frac{K^2}{W^2} h^3} \tag{4.4}$$

where, beyond the known symbols, C and F are the generic hydrodynamic coefficient and force, respectively, K groups all the constants in equation 4.1 and W is the channel width.

The relative error in the estimation of the drag or side coefficient is computed according to Eq. 4.5.

$$\frac{\partial C}{C} = \sqrt{\left(\left(\frac{F}{C}\frac{\partial C}{\partial F}\frac{\delta F}{F}\right)^2 + \left(\frac{h}{C}\frac{\partial C}{\partial h}\frac{\delta h}{h}\right)^2\right)} \tag{4.5}$$

The partial derivatives are calculated from Eq. 4.4, while the relative uncertainties need to be estimated. As regards the force, the relative uncertainty $\delta F/F$ is derived by considering the maximum drag force measured by the instrument during the experimentation (0.34 N, corresponding to 0.035 kg) and dividing the standard deviation obtained in the calibration

by such force. In detail, the standard deviation obtained during calibration by applying a mass of 0.036 kg is 0.0028 kg, so the relative uncertainty is 0.078. As for the water level, the relative uncertainty is computed by dividing the absolute measurement error, 0.001 m, by the water level set for the experiments, 0.15m, resulting in 0.007.

By combining the error relative of each quantity (force and water level), the relative error in the estimation of the drag coefficient is about 8.1%.

As regards the side coefficient, the maximum force observed during the experimentation is 0.20 N, corresponding to nearly 0.020 kg. The standard deviation obtained in the calibration for such mass is 0.0023 kg, and the corresponding relative uncertainty is 0.115. The relative error in the estimation of the side coefficient, obtained by applying Eq. 4.4, becomes 11.7%.

4.3.3. Drag and side force measurements

Drag and side forces are measured on the cylindrical sample (0.15 m long, with diameter 0.024 m) under stationary conditions, as reported in Tab. 4.5. The discharge is slightly smaller than the maximum discharge released by the system, to guarantee stable conditions for the duration of the experiments. The water level is imposed by regulating the sluice gate and allows one to test the effect of different submergences by maintaining the sample away from the channel bottom.

The particle Reynolds number shows that tests are performed in subcritical condition. From the Strouhal number, the shedding frequency of 3.33 Hz is estimated, which corresponds to a vortex period of 0.30 s.

Four configurations are tested: three for a submerged cylinder, with different submergence values $h_s = h - h_{top}$ (Fig. 4.6a-c: 0.05 m, 0.015 m and 0 m, with the upper part of the cylinder, h_{top}, placed at the undisturbed water level) and one for a semi-submerged cylinder, with the axis placed at the undisturbed water level (negative submergence, Fig. 4.6d).

Discharge	Q [m^3 s^{-1}]	0.029
Water level[1]	h [m]	0.15
Water velocity[1]	V [m s^{-1}]	0.40
Blockage ratio	B [%]	4.95
Froude number	Fr [-]	0.33
Particle Reynolds number	Re_p [-]	1E+04
Strouhal number	St [-]	0.20

Table 4.5 Experimental campaign conditions. [1]undisturbed flow conditions.

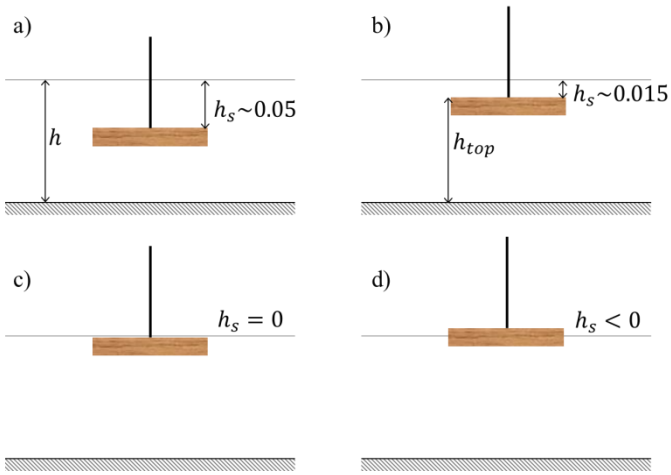

Figure 4.6 Sketch of the configurations tested. The light grey line represents the undisturbed water level while the cylinder position is varied according to the configurations tested: a) maximum submergence; b) intermediate submergence; c) zero submergence; d) negative submergence.

For each configuration, the cylinder orientation varies from 0° (cylinder parallel to the flow) to 90° (cylinder perpendicular to the flow), with a pace of 10°. Each test has a duration of 30 s, ten times higher than the shedding period, and a data rate of 0.008 s. During one measure, 3750 data are recorded. The average and the standard deviation are computed to give the drag and side force values for each orientation. Then, the test is replicated to check the repeatability, varying the direction of rotation of the cylinder (from 0° to 90° and vice versa) to avoid bias due to load-unload processes. An example of the output of one measure is reported in Fig. 4.7, where the single data and the average value are shown.

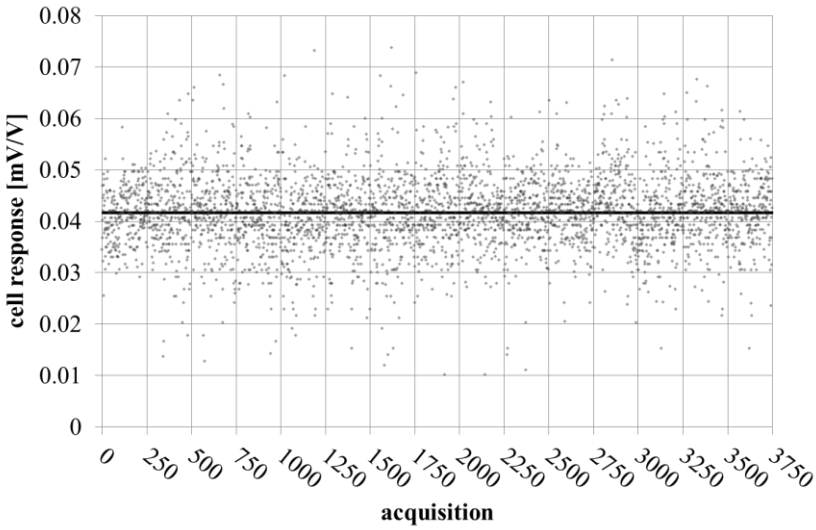

Figure 4.7 Typical outcome of one measurement. The response in mV/V of cell 2 is reported, with the single values (light grey spots) and the average value (black line), for cylinder orientation equal to 50°.

Once that the average response is computed, the force on the cylinder can be estimated. As regards the drag force, it is sufficient to transform the cell response in the corresponding mass by reversing the calibration equation of cell 2 (Tab. 4.4) and then computing the drag force taking into account gravitational acceleration.

To obtain the side force, the responses of cells 1 and 3 have to be combined. If the sample is rotated, it tends to laterally displace the presser and to make it rotate, too. By orienting the sample in a counter-clockwise direction, cells 1 and 3 are stressed as shown in Fig. 4.8. The side force for the two cells is then obtained by transforming the cells' responses in the applied mass, reversing the equations in Tab. 4.4, and multiplying by the gravitational acceleration. Then, the total side force is the difference between the side force on cell 1 and the side force on cell 3.

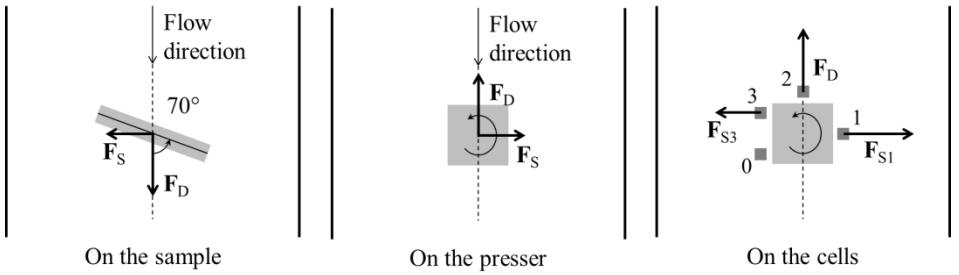

Figure 4.8 Free body diagram on the sample, on the presser and on the cells. The direction of forces varies because of the leverage system. The rotation induced by the sample orientation stresses cell 3 producing a response that needs to be accounted for to correctly estimate the side force.

Finally, the drag and side coefficient for each orientation are obtained with the following equations:

$$C_D = \frac{F_D}{\frac{1}{2}\rho_f A V^2} \tag{4.6}$$

$$C_S = \frac{F_{S1} - F_{S3}}{\frac{1}{2}\rho_f A V^2} \tag{4.7}$$

where A is the crossflow area (LD) and V is the module of the undisturbed flow velocity, which corresponds to the relative velocity since the body is motionless.

It is worth highlighting that for submerged cases (a and b in Fig. 4.6) the bar which holds the sample is submerged, too. The force acting on the submerged part is evaluated with appropriate measurements (without the sample) and is then subtracted to the drag force measured by cell 2. For configuration (a) the force on the submerged part of the bar is 0.024 N while for configuration (b) it is 0.008 N.

4.4. Analysis of the results

For each configuration and orientation, the measure has been repeated 5 times. The results, in term of drag and side coefficient, are reported, to-

gether with average values and root mean square. Then, the differences among configurations and with respect to the literature results are reported.

4.4.1. Configuration (a) – maximum submergence

The upper part of the cylinder is placed at about 0.05 m from the undisturbed water level, so that the body is totally submerged. This configuration has been tested in order to verify the accuracy of the results for submerged cylinder through the comparison with the values available in the literature. In Fig. 4.9 some pictures of the experiments are shown.

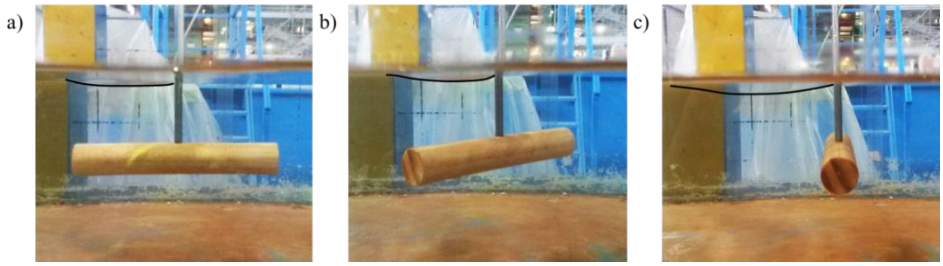

Figure 4.9 Photographs of configuration (a). a) Cylinder parallel to the flow; b) cylinder oblique to the flow; c) cylinder perpendicular to the flow. Black thick line follows the wave lower profile. Water flows from the right.

The flow does not appear strongly influenced by the presence of the sample, except for a small surface wave downstream of the bar. This wave (black line in Fig. 4.9) shows little variation among the three orientation: it is shorter for the aligned and oblique cylinder, becoming more evident for the crossflow configuration showing the higher disturbance in the latter configuration. This reflects in the values of the drag and side coefficients (Fig. 4.10): the drag coefficient grows from the aligned to crossflow configuration, when it reaches a maximum value of 1.12 (average on the five measurements). The side coefficient is nearly zero when the cylinder is aligned or perpendicular to the flow and the deviation of the streamlines is symmetrical. It reaches a maximum of 0.56 (average on the five measurements) when the orientation is 45°, and has a nearly symmetric distribution around this orientation.

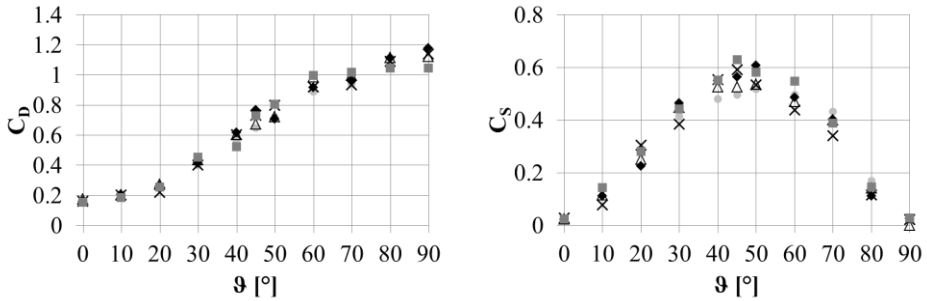

Figure 4.10 Drag and side coefficient diagrams for totally submerged cylinder. Different symbols correspond to different tests.

The average values and the standard deviations are reported in Tab. 4.6. The maximum deviation is observed for the maximum values of the drag and side coefficient, respectively at 90° and 45°, and tends to diminish for smaller values.

Angle [°]	Mean C_D	Mean C_S
0	0.163 ±0.008	0.025 ±0.002
10	0.199 ±0.008	0.112 ±0.027
20	0.253 ±0.023	0.265 ±0.035
30	0.422 ±0.023	0.431 ±0.031
40	0.581 ±0.039	0.532 ±0.031
45	0.710 ±0.048	**0.561 ±0.052**
50	0.751 ±0.047	0.556 ±0.038
60	0.941 ±0.048	0.487 ±0.040
70	0.971 ±0.037	0.393 ±0.033
80	1.096 ±0.030	0.137 ±0.024
90	**1.122 ±0.055**	0.019 ±0.013

Table 4.6 Mean values and standard deviation of the drag and side coefficients for totally submerged cylinder, with maximum submergence and variable orientation.

4.4.2. Configuration (b) – intermediate submergence

To assess how the cylinder behaves for different submergences, an intermediate configuration is tested, with the upper part of the sample 0.015 m below the undisturbed water level. In Fig. 4.11 two pictures of an experiment with such configuration are shown. As for the previous case, a sur-

face wave is the only clue of the interaction among the sample and the flow. But for this intermediate configuration, the wave is upstream of the bar, and is originated by the abrupt deviation of the flow against the cylinder circular base. A stronger interaction with the free surface is evident, if compared with the previous configuration.

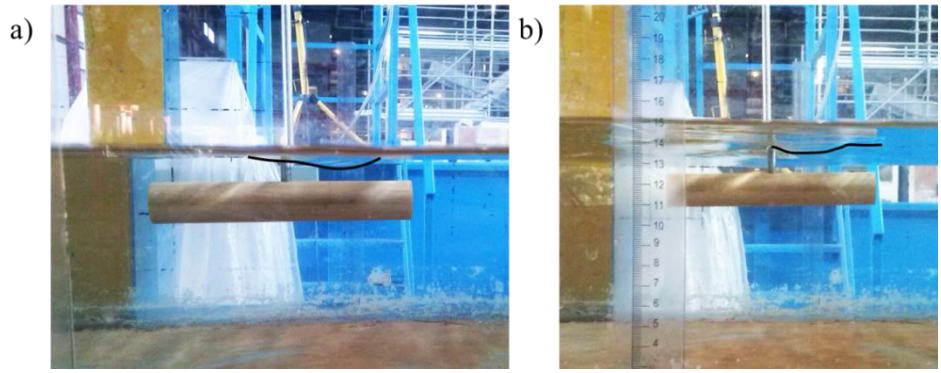

Figure 4.11 Photographs of configuration (b). The cylinder is aligned to the flow, the picture are taken orthogonally (a) and upward (b) to highlight the shape of the surface wave. Black thick line follows the wave lower profile. Water flow from the right.

The drag and side coefficients are shown in Fig. 4.12, while the average values and standard deviations are reported in Tab 4.7.

The maximum drag coefficient is obtained for an orientation of 80°, and is 1.31, while the maximum side coefficient is 0.64 from 40° to 50° (average on 4 repetition). In this case, the highest values are obtained for angles slightly different from the expected ones, 80° instead of 90° for the drag, 40° to 50° instead of a single peak at 45° for the side. However, the overall trends are in agreement with the values obtained for configuration (a).

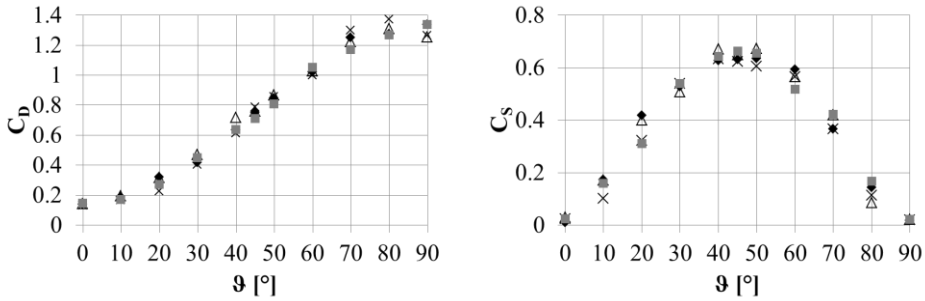

Figure 4.12 Drag and side coefficient diagrams for totally submerged cylinder with intermediate submergence. Different symbols correspond to different tests.

Angle [°]	Mean C_D	Mean C_S
0	0.141 ±0.006	0.022 ±0.009
10	0.181 ±0.014	0.152 ±0.034
20	0.286 ±0.044	0.363 ±0.054
30	0.436 ±0.030	0.529 ±0.015
40	0.651 ±0.046	**0.644 ±0.019**
45	0.753 ±0.031	0.642 ±0.018
50	0.846 ±0.026	0.642 ±0.028
60	1.026 ±0.023	0.561 ±0.031
70	1.236 ±0.054	0.394 ±0.031
80	**1.307 ±0.048**	0.128 ±0.033
90	1.299 ±0.045	0.020 ±0.002

Table 4.7 Mean values and standard deviation of the drag and side coefficients for totally submerged cylinder, with intermediate submergence and variable orientation.

4.4.3. Configuration (c) – zero submergence

To test the effect of the interaction with the water surface, the upper profile of the cylinder is set as coincident with the undisturbed water level. Interactions are shown in Fig. 4.13, where the variation with orientation appears evident. For a cylinder aligned to the flow (Fig. 4.13a-b), the abrupt deviation of the streamlines against the cylinder base causes the elevation of the water level at the cylinder upstream end and a lowering of the water level just downstream. This wave is more evident than in the previously examined configurations. Increasing the angle between the

flow and the cylinder, until the latter reaches a crossflow position (Fig. 4.13c-d), the interaction with the free surface increases, and the upstream wave becomes larger and longer. The wave surmounts the cylinder, and turbulence is observed below the free-surface, downstream of the sample.

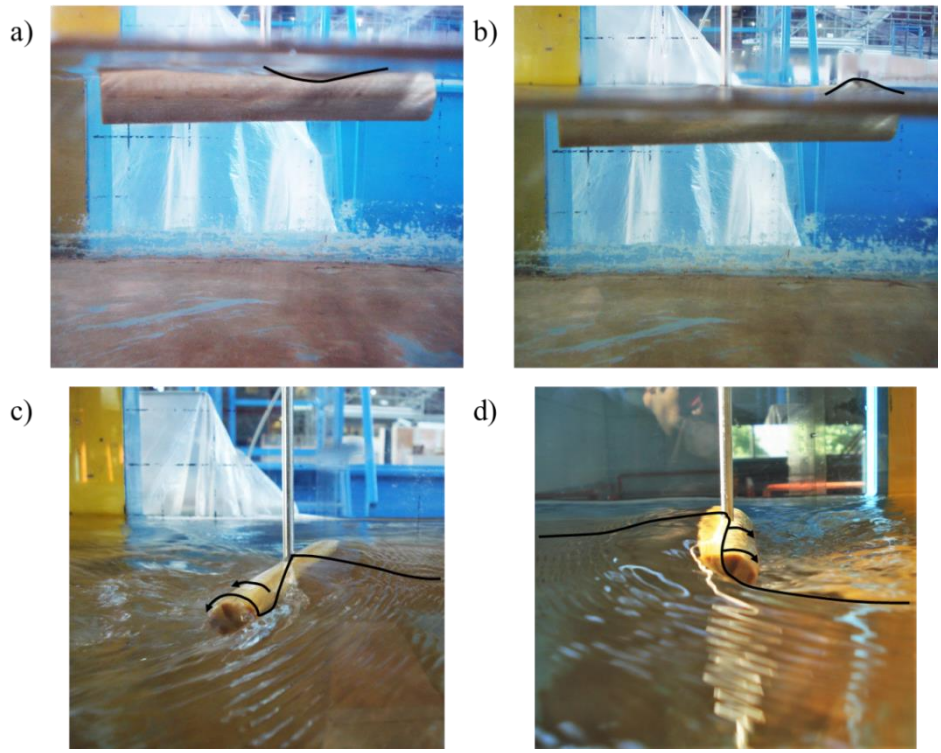

Figure 4.13 Photographs of configuration (c). a) Cylinder is aligned to the flow, picture upward; b) Cylinder aligned and picture at the free surface level; c) 80° orientation; d) 90° orientation. Black thick line follows the wave lower profile, while black arrows show the wave surmounting the sample. Water flow from the right in pictures a, b, c; from left in d.

The drag and side coefficient are shown in Fig. 4.14, while the average values and standard deviation are reported in Tab 4.8.

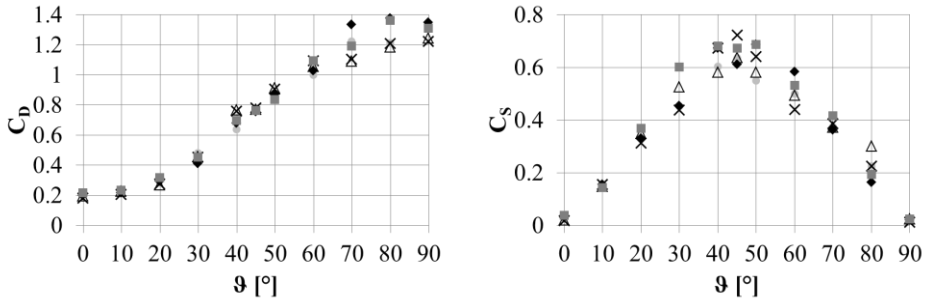

Figure 4.14 Drag and side coefficient diagrams for a cylinder with zero submergence. Different symbols correspond to different tests.

The maximum drag coefficient is obtained for an orientation of 90°, and is 1.28, while the maximum side coefficient is 0.66 at 45° (average on 5 repetition). The trends are as expected but large standard deviation are observed for the drag coefficient at 70°-80°.

Angle [°]	Mean C_D	Mean C_S
0	0.198 ±0.015	0.026 ±0.009
10	0.220 ±0.013	0.150 ±0.005
20	0.288 ±0.021	0.340 ±0.024
30	0.451 ±0.025	0.494 ±0.069
40	0.708 ±0.054	0.643 ±0.047
45	0.770 ±0.011	**0.656 ±0.044**
50	0.876 ±0.033	0.629 ±0.062
60	1.055 ±0.041	0.510 ±0.053
70	1.190 ±0.099	0.382 ±0.021
80	1.269 ±0.093	0.221 ±0.051
90	**1.281 ±0.058**	0.020 ±0.005

Table 4.8 Mean values and standard deviation of the drag and side coefficients for totally submerged cylinder, with intermediate submergence and variable orientation.

4.4.4. Configuration (d) – semi-submerged cylinder

Finally, the drag and side coefficients for a semi-submerged cylinder are estimated. The axis of the sample is placed at a distance from the bottom equal to the undisturbed water level. The interaction with the water surface is different from the configurations previously examined (Fig. 4.15).

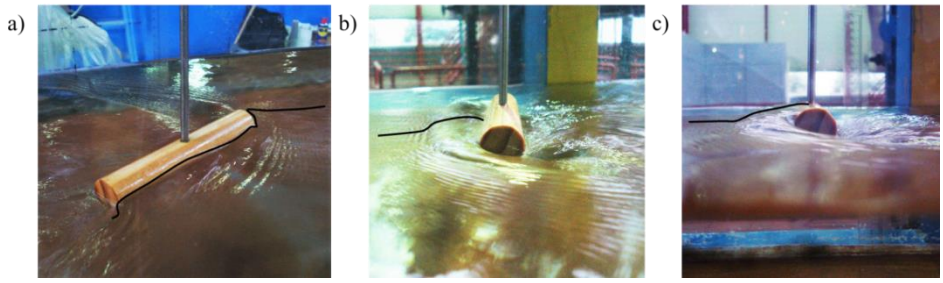

Figure 4.15 Photographs of configuration (d). a) 30° orientation; b) Cylinder aligned and picture at the free surface level; c) 80° orientation; d) 90° orientation. Black thick line follows the wave profile. Water flow from the right in pictures a, from left in b and c.

The water surface is affected by the presence of the sample: for each orientation, surface waves and abrupt changes in water level are observed near the body. Since the cylinder is only partially submerged, the upper part is never surmounted by the flow. This affects the measured forces and, consequently, the drag and side coefficients (Fig. 4.16), since the flow acts on a smaller part of the sample. The maximum values obtained are lower than in the other configurations: 0.64 for the drag coefficient at 80° and 0.32 for the side coefficient at 50°. The orientation at which the peak is measured are slightly different from the expected values, but the trend is well replicated for both coefficients. In Tab. 4.9 the average values on 5 measurements and the standard deviation are reported.

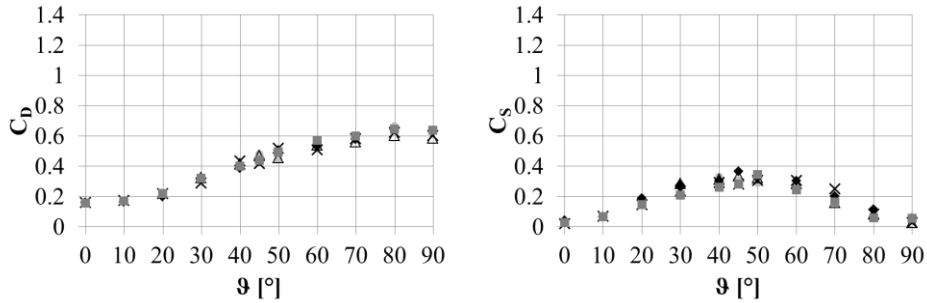

Figure 4.16 Drag and side coefficient diagrams for a cylinder with zero submergence. Different symbols correspond to different tests.

Angle [°]	Mean C_D	Mean C_S
0	0.162 ±0.003	0.030 ±0.008
10	0.170 ±0.005	0.069 ±0.002
20	0.216 ±0.011	0.167 ±0.025
30	0.312 ±0.014	0.258 ±0.032
40	0.411 ±0.018	0.301 ±0.025
45	0.449 ±0.026	0.314 ±0.036
50	0.485 ±0.032	**0.317 ±0.021**
60	0.535 ±0.024	0.280 ±0.028
70	0.580 ±0.014	0.191 ±0.037
80	**0.636 ±0.024**	0.080 ±0.021
90	0.621 ±0.026	0.042 ±0.013

Table 4.9 Mean values and standard deviation of the drag and side coefficients for totally submerged cylinder, with intermediate submergence and variable orientation.

4.5. Discussion and validation

4.5.1. Effect of submergence and orientation

To analyse the effect of submergence on the drag and side coefficients, the polynomial interpolations for each configurations are compared in Figs. 4.17 and 4.18.

To interpolate the experiments, polynomial curves of third order for the drag and of fourth order for the side force are considered, obtaining a determination coefficient among 0.95 and 0.99.

Concerning the drag, the reduction of submergence leads to an overall increase of the coefficient, especially for larger orientation angles with respect to the experiments with maximum submergence (a). The average values for configurations (b) and (c) are nearly overlying, although the experiments with submergence equal to 0 (c) present slightly higher values at the smallest orientation angles. The interaction with the water surface certainly affects the drag force, which becomes higher because of the

increasing disturbance of the free surface, as highlighted by the presence of higher waves upstream of the sample.

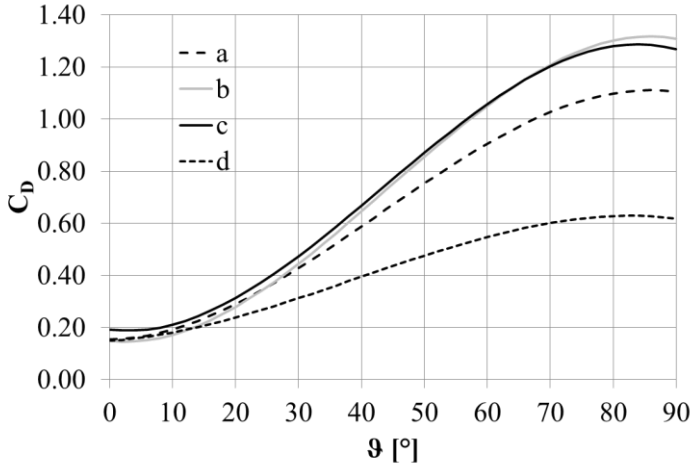

Figure 4.17 Comparison of the drag coefficient for configurations a, b, c and d.

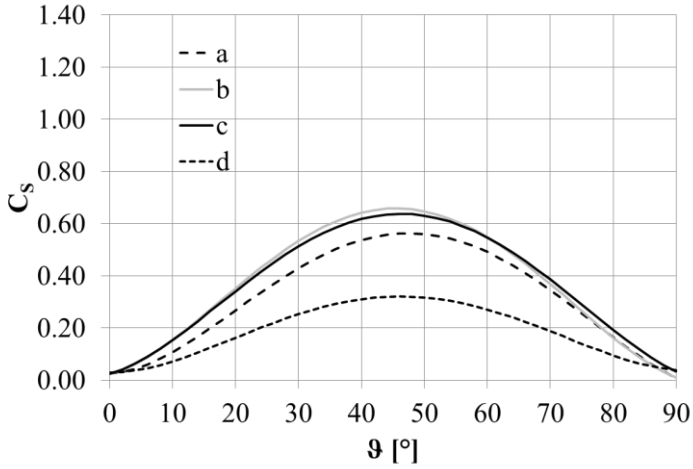

Figure 4.18 Comparison of the side coefficient for configurations a, b, c and d.

If the body is only partially submerged (d), the force exerted on the sample diminishes significantly. This is mainly due to the fact that the portion of body on which the flow acts is reduced due to the partial submersion. It should be noticed that the reference area for the computation of the force coefficients is kept constant and equal to *LD*, independently from the

body sinking. Despite that, the reduction of the coefficient is not proportional to the area reduction: for instance, as shown in Fig. 4.17, the semi-submerged drag is not equal to half of the totally submerged drag (a). Tab. 4.10 reports the ratio of the semi-submerged and totally submerged drag, showing a gradual separation among the values. For the smaller orientation, semi-submderged values are similar to submerged ones, while the difference increases for increasing angles.

Angle [°]	$\frac{C_D(d)}{C_D(a)}$
0	97%
10	94%
20	82%
30	73%
40	67%
45	65%
50	63%
60	60%
70	59%
80	57%
90	56%

Table 4.10 Ratio between the semi-submerged (d) and the totally submerged (a) drag coefficient with variable orientation.

As a general conclusion, the drag coefficient is higher when the sample is near to the crossflow configuration (90°) and becomes smaller while the orientation is reduced, reaching as expected a minimum when the cylinder is aligned to the flow (0°). The reduced difference highlighted for configurations (a), (b) and (d) for lower angles (below 15°) is uncertain. For such orientations, the force measured by the balance is very small, due to the reduction of the area available to the flow (which tends to the cylinder base area), and it is possible that the balance inner friction swallows the variation of force due to submergence. On the contrary, when the disturbance of the free surface is evident, as in configuration (c), a difference can be noticed even at small angles.

Figure 4.18 shows the variation of the side coefficient with submergence and orientation. As for the drag coefficient, the interaction with the free surface tends to increase the side force ((b) and (c)) with respect to a deeply submerged body (a), while if the body is partially submerged the force is reduced. The percentage of the side coefficient measured in the semi-submerged case with respect to the totally submerged case is shown in Tab. 4.11. The semi-submerged side coefficient varies among the 50% and 70% of the one in configuration (a), and therefore it is not proportional to the area reduction (which is halved).

The maximum side coefficient is obtained around 45°, when the asymmetry of the fluid stream is maximum, independently from the tested configuration. For lower or higher angles, the coefficient smoothly diminishes, maintaining an acceptable symmetry, until it becomes nearly zero at 0° and 90° when the flow distribution around the cylinder is symmetrical. The residual values observed are probably due to the accidental movement or vibration of the sample.

Angle [°]	$\frac{C_S(d)}{C_S(a)}$
10	67%
20	61%
30	59%
40	58%
45	57%
50	56%
60	55%
70	54%
80	58%

Table 4.11 Ratio between the semi-submerged (d) and the totally submerged (a) side coefficient with variable orientation.

4.5.2. Comparison with literature results

Only two references are available to compare the measures of the drag and side coefficient of a yawed cylinder. Gippel et al. (1996) measured the drag coefficient as a function of cylinder slenderness and orientation in an open channel, while Hoang et al. (2015) measured the drag, lift and side coefficients of a bar in a wind tunnel, varying its yaw and incidence.

Figures 4.19 and 4.20 compare the results obtained for submerged and semi-submerged cylinder with those from the literature.

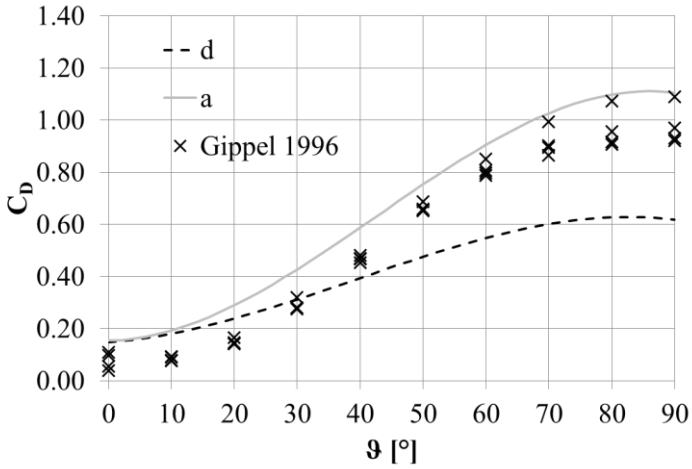

Figure 4.19 Comparison of the drag coefficient for configurations a and d and literature values.

Concerning submerged cylinders, the measured C_D values agree substantially with those found by Gippel et al. (1996). It should be highlighted that Gippel results were originally obtained with reference to the log projected area: here they have been multiplied by the sine of the yaw angle to have the same reference area used for the present measurements (*LD*).

The remaining differences between the outcomes are probably due to the dissimilar configurations adopted in the experiments. Literature measurements were realized on PVC cylinders with a slenderness (*L/D*) ranging from 6 to 21 and at Froude numbers ranging from 0.35 to 0.63, while the wooden cylinder in the present experiments had a slenderness of 6,

and the tests were realized at Froude number 0.33. The smoothness of the cylinder and the different flow characteristics may therefore justify some of the differences in the results.

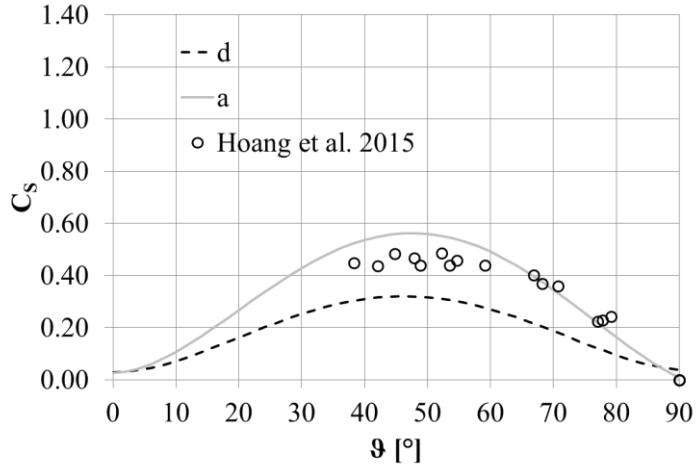

Figure 4.20 Comparison of the side coefficient for configurations a and d and literature values.

The comparison with the C_S values measured by Hoang et al. (2015) is instead reported only as a qualitative reference, since their measure, variable with cylinder orientation, are the only available in the literature. It must be noticed that these results were measured in a wind tunnel, at higher Reynolds numbers (up to $9\ 10^4$), with the cylindrical model at non-zero yaw and incidence, leaning on both the side wall and the bottom of the wind tunnel, thus avoiding any tip effect. To obtain a meaningful comparison, the C_S values were evaluated in a rotated frame of reference in which the model presents zero incidence to the upstream flow, through a suitable composition of the side-force and lift values measured by Hoang et al. (2015). The correct trend and order of magnitude of the side coefficient with the yaw angle appears to be obtained also in our experiments, even if the difference in the maximum measured value is relevant (around 15%). This probably owes to the mentioned differences in the two experimental set-ups, in particular to the tip effect which alters the flow and pressure distribution around the cylinder.

Although no data are available in literature for a floating cylinder, the reliability of the values obtained can be inferred by the reliability of the measured coefficients for a submerged cylinder.

4.6. Implemented values of drag and side coefficient for floating cylinder

To simulate rigid body transport, with particular reference to the case of floating cylinders, the values obtained from the experiments on semi-submerged cylinders were implemented. The semi-submerged drag is interpolated with a logistic-like curve, which reproduces the S-shape of the diagram and keeps the maximum and minimum values at 90° and 0° respectively. The curve, with a determination coefficient of 0.983, is shown over the data in Fig. 4.21, and it is given in Eq. 4.8.

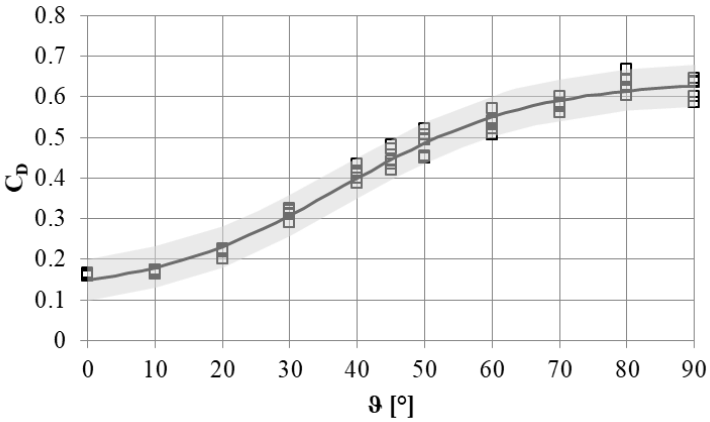

Figure 4.21 Interpolation of the drag coefficient for a semi-submerged body with a logistic-like curve.

$$C_D(\vartheta) = \frac{0.5243}{\left(1 + e^{(-0.07097(\vartheta - 37.5))}\right)} + 0.1143 \tag{4.8}$$

The expression, which is valid for angles from 0° to 90°, is centred on 37.5°, and not on 45° as it may be expected. For larger angles, it is adequately implemented accounting for angle variation above 90°. In Fig.

4.22 the diagram extended up to 360° is shown for the sake of completeness.

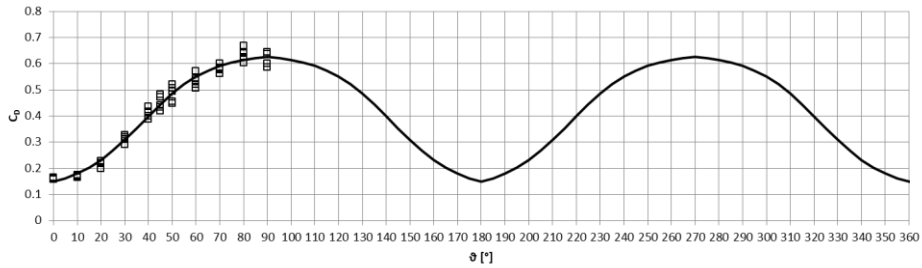

Figure 4.22 Implemented drag coefficient for semi-submerged cylinder, for relative angle from 0° to 360°. Empty squares are the experimental data presented in Chapter 4.

The side coefficient is interpolated with a beta-like curve, as shown in Fig. 4.23 over the experimental data. The determination coefficient is 0.955 and the expression is reported in Eq. 4.9.

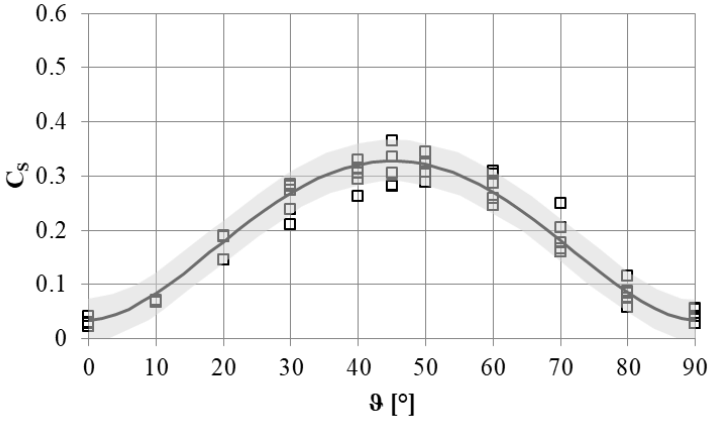

Figure 4.23 Interpolation of the side coefficient for a semi-submerged body with a beta-like curve.

$$C_S(\vartheta) = 1.591 * 10^{-7}(\vartheta^{1.9})(90 - \vartheta)^{1.819} + 0.0335 \tag{4.9}$$

In ORSA2D_WT, the equation is extended to values higher than 90° (Fig. 4.24). Furthermore, to keep the formulation congruent with the physics, when the cylinder is parallel or perpendicular to the flow, the side force is set exactly equal to zero even if the measured side coefficient is not.

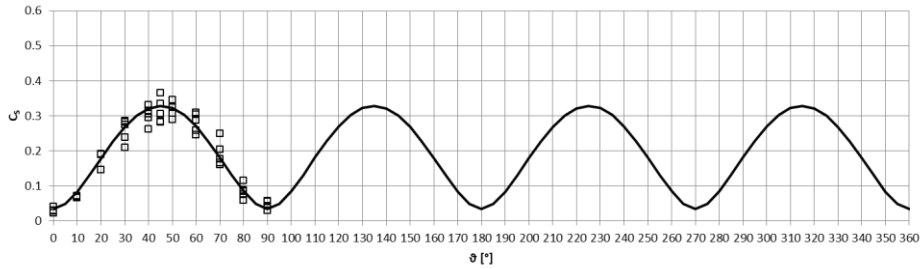

Figure 4.24 Implemented side coefficient for semi-submerged cylinder, for relative angle from 0° to 360°. Empty squares are the experimental data presented in Chapter 4.

The coloured areas shown in Figs. 4.21 and 4.23 are obtained by applying the relative error estimated for the maximum measured value for the drag and side coefficients (see paragraph 4.3.2). The error sums up both the instrument accuracy and the errors in the estimation of the flow velocity, and is compliant with the observed repeatability of the experiments.

4.6.1. Apparent drag coefficient

An additional remark about the apparent drag coefficient should be made. This coefficient is different from the standard drag, but literature experiments have demonstrated that it varies with the body orientation (Bocchiola et al. 2011). The value of the apparent drag coefficient has not been measured in the present experimental campaign but, taking advantage of literature data, its variation with the body orientation can be modelled.

A logistic-like equation, similar to that obtained for floating cylinders drag coefficient (Eq. 4.8) is adopted. The expression is adapted from Eq. 4.8 by varying the coefficient, in order to obtain a variation between the minimum and maximum values derived by Bocchiola et al. (2011) (Fig. 4.25):

$$C_{D\ apparent}(\vartheta) = \frac{0.35}{(1 + e^{(-0.095(\vartheta - 37.5))})} + 1.24 \qquad (4.10)$$

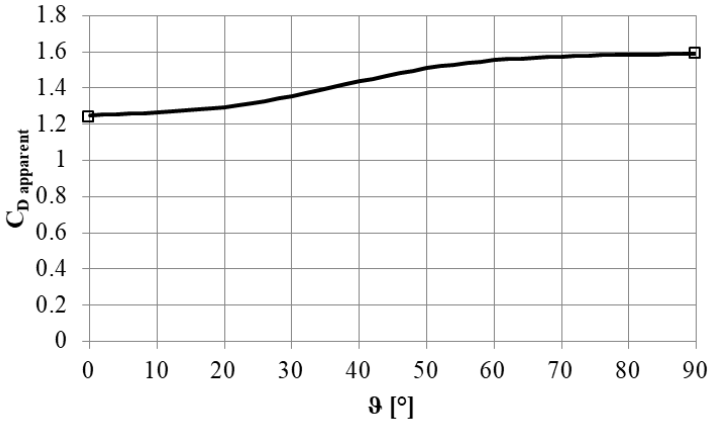

Figure 4.25 Implemented apparent drag coefficient for cylinders, for relative angle from 0° to 90°. Empty squares are the experimental data obtained by analysing the experiments by Bocchiola et al. 2011.

As for the drag and side coefficients, the expression is extended also above 90°. The variation of the entrainment with orientation is modelled with increasing accuracy. The validity of this approximation will be examined for the case of wood transport modelling in the real-scale experiment. However, the exact curve should be obtained with specific experiments, accounting for the orientation of a cylinder on a mobile bed.

Chapter 5
Model calibration

5.1. Abstract

In this Chapter, the model proposed for simulating the transport of floating spheres or cylinders is calibrated. First of all, literature experiments are considered as a reference, to test the proposed formulation on the translation and rotation of a sphere and on the translation of a floating cylinder.

No accurate data can be found in literature about the rotation of elongated bodies. For this reason, an experimental campaign was carried out in collaboration with the Fluid Dynamics group of the University of Zaragoza. Tests were performed to provide reliable observations of the rotation and translation of cylinders and spheres transported in a flow. The data collected during this campaign on the displacement and rotation of floating bodies in different transport conditions are used to calibrate the rotation model, and to choose the best formulation among the two proposed.

A sensitivity analysis on the model parameters is also performed, in order to evaluate those which have the major influence on the simulation results. The effect of the body subdivision in sub-segments for force computation is also analysed, as well as the effect of different methods to represent inline obstacles.

Experiments involving the simultaneous motion of several cylinders were also realized, in order to check the simulation of multiple logs transport and to calibrate the restitution coefficient for collision modelling.

5.2. Calibration against literature results

Taking advantage of the analytical solutions and of experiments available in literature, a preliminary calibration of the model ORSA2D_WT is performed. The aim of this calibration is to assess the translation formulation against simple experiments on spheres, verifying the correct implementation of the terms. As concerns floating cylinders, the experiments performed by Ruiz-Villanueva et al. (2014b) are the only existing benchmark for the analysis of translation. However, these experiments do not provide detailed information about body rotation.

5.2.1. A sphere in a uniform stationary flow

The first test simulated considers a simple configuration in which the only forces are the drag and the body inertia. In fact, the sphere is not rotating, so no Magnus effect arises, and the flow is uniform. The absence of shear and of flow acceleration allows one to completely disregard the side force, the flow inertia and the pressure gradient force. Furthermore, the sphere is considered as fully submerged in the flow and rotation is not computed.

A sphere initially at rest (d = 0.03 m, ρ_p = 720 kg m^{-3}, initial velocity $\boldsymbol{V}_b$ = 0 m s^{-1}) is ideally placed in a uniform, stationary flow with streamwise velocity V_{fx} = 0.5 m s^{-1} (Fig. 5.1a). According to the analytical solution of the translation equation, the streamwise component of the sphere velocity is:

$$\boldsymbol{V}_b = \boldsymbol{V}_f \left(1 - \frac{1}{\boldsymbol{V}_f \dfrac{\frac{1}{2}\rho C_D A}{\left(m_b + \frac{1}{2} m_f C_A\right)} (t - t_0) + 1} \right) \tag{5.1}$$

where, besides known symbols, t is time and t_0 is the initial time. The drag coefficient varies with the Reynolds number, as in Chow (1979).

The problem is simulated in a domain with dimensions 0.60 m x 6.00 m, with a triangular unstructured mesh of about 74000 cells (see Fig. 5.1a for the initial configuration and the flow direction). Fig. 5.1b compares the analytical solution of Eq. 5.1 with the streamwise velocity (V_{bx}) computed by ORSA2D_WT. The sphere starts to accelerate, and its velocity tends to the flow velocity (horizontal line in the figure). The results of the simulation totally overlap the analytical solution.

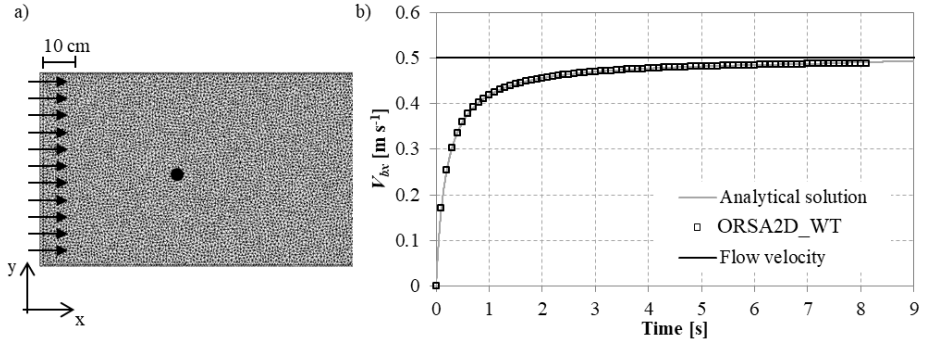

Figure 5.1 a) Detail of the mesh, with the sphere and the flow direction; b) comparison of the analytical and the computed sphere velocity, with the flow velocity in black.

5.2.2. Spherical projectile

The effect of gravity can be included in the model, as verified by reproducing a numerical example by Chow (1979) regarding the motion of a spherical projectile in air. The projectile has a diameter D equal to 0.05 m and density equal to 8000 kg m^{-3}. Its initial velocity has component 43.3

m s^{-1} and 25.0 m s^{-1}, in *x* and *y* direction respectively. It is thrown in still air (air density 1.23 kg m^{-3}).

In this case, the motion involves gravitational acceleration and buoyancy, while the side force and the body rotation are not computed, as done by the reference author. The drag coefficient depends on the particle Reynolds number, as in Chow (1979) and the added mass coefficient has the standard value for submerged spheres. Since the projectile moves in still air, the fluid velocity is not calculated and the domain discretization has no influence on the computation. A mesh of 200x50 m, with regular triangular elements with dimension around 10 m, is considered.

Fig. 5.2 shows the trajectory of the body (a), its horizontal (b) and vertical (c) velocity, comparing the results from Chow (1979) with those obtained with ORSA2D_WT. The results of the proposed model basically overlay the results of the numerical example. This was expected, since the same parameters are implemented, but it is a good demonstration of the fact that the subdivision procedure of the body does not introduce mistakes in the simulation.

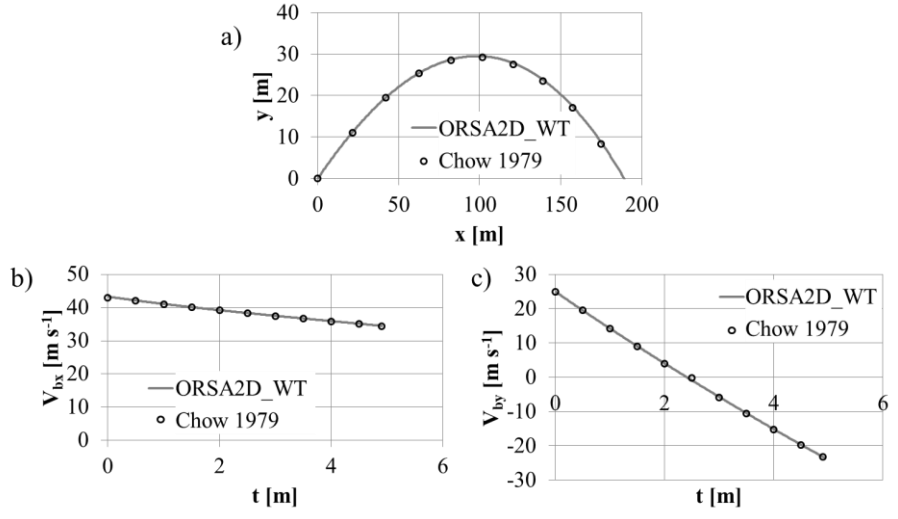

Figure 5.2 Trajectory (a), horizontal velocity (b) and vertical velocity (c) of the spherical projectile.

5.2.3. Water entry of a spinning sphere

To assess the effect of the side force, the trajectory of a sphere moving in a column of still water is computed. One of the experiments by Truscott and Techet (2009) is simulated. A spinning billiard ball (D = 0.0572 m, ρ = 1740 kg m^{-3}) is thrown in a column of still water, with known vertical and angular velocity (V_{by} = -5.47 m s^{-1} and $\boldsymbol{\omega}$ = -266.78 rad s^{-1}, with an initial spin parameter $S_0 = \frac{\boldsymbol{\omega} r}{\boldsymbol{V}} = 1.4$). The sphere enters the water and follows a curve trajectory, due to the Magnus effect, which is reproduced in the simulation by the side force. The computational domain is a square of 0.60 x 0.60 m, with a triangular unstructured mesh (about 7400 cells).

Since, owing to the test geometry, the ball experiences both gravity and buoyancy, these external forces were also included in the computation, as well as drag, side and body inertia. The resulting equation reads:

$$\begin{aligned}\left(m_b + \frac{1}{2} C_A m_f\right) \frac{d\boldsymbol{V}_b}{dt} &= \sum_{i=1}^{4} \frac{1}{2} \rho C_D A_i \left(\boldsymbol{V}_{fi} - \boldsymbol{V}_{bi}\right) \left|\boldsymbol{V}_{fi} - \boldsymbol{V}_{bi}\right| \\ &+ \sum_{i=1}^{4} \frac{1}{2} \rho C_S A_i \left|\boldsymbol{V}_{fi} - \boldsymbol{V}_{bi}\right| \left(\boldsymbol{V}_{fi} - \boldsymbol{V}_{bi}\right) \times \boldsymbol{i_z} \\ &+ m_f \left(1 + \frac{1}{2} C_A\right) \frac{D\boldsymbol{V}_f}{Dt} + (m_f - m_b)\boldsymbol{g}\end{aligned} \tag{5.2}$$

where $\boldsymbol{g}$ is the gravitational acceleration. The drag and side coefficients obtained by Truscott and Techet have been implemented in the formulation to reproduce the test.

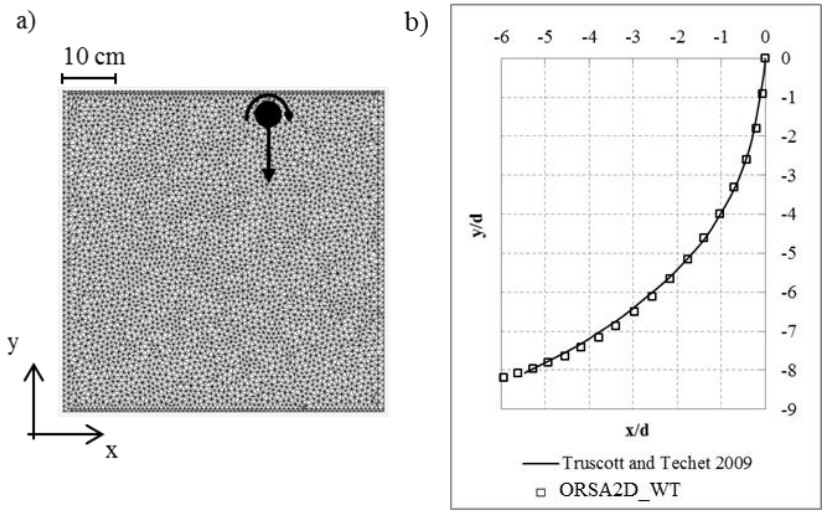

Figure 5.3 a) Detail of the mesh, with the sphere, linear and angular velocity; b) comparison of the trajectory measured by Truscott and Techet, and computed with ORSA2D_WT. The coordinates are divided by the sphere's diameter.

Figure 5.3 shows the computational domain and the initial position of the sphere (a), and compares Truscott and Techet's trajectory with the outcome of ORSA2D_WT simulation (b). The implemented formulation of rotation accounts for the added inertia and torque computed with reference to the centre of mass. The good agreement between the experimental and numerical results is a proof of the accuracy of the adopted translation equation.

5.2.4. Motion of a floating wooden cylinder

To assess the formulation for the transport of floating rigid bodies, one of the experiments described in Ruiz-Villanueva et al. (2014b) is reproduced. The simulated experiment is realized in a horizontal flume, 7 m long with six side obstacles (rectangular prisms, with a base of 0.13 m x 0.18 m) and a final weir of 0.058 m height. A constant discharge of 0.018 m^3 s^{-1} provides a steady and non-uniform flow. Water velocity (V_{fx}) is measured at the centreline and at both sides of the channel (Ruiz-

Villanueva 2012) and the trajectory of a wooden cylinder (ρ = 720 kg m^3, L = 0.20 m, D = 0.018 m) is recorded.

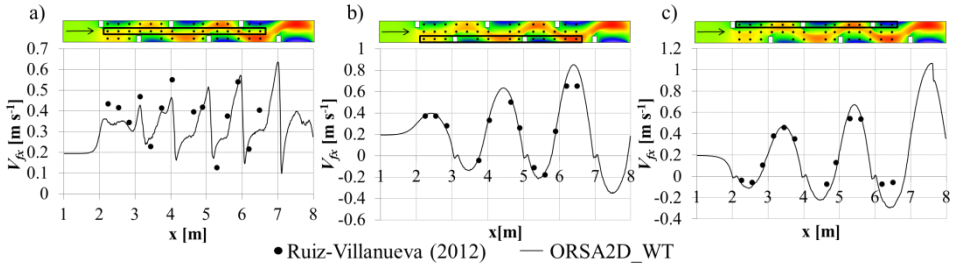

Figure 5.4 Comparison between the streamwise component of the flow velocity measured by Ruiz-Villanueva (2012) and simulated with ORSA2D at a) centreline, b) right side and c) left side; contour maps on the top show the streamwise velocity field and the points were values are recorded.

The water flow in the channel is simulated with ORSA2D, with an unstructured triangular grid (about 83000 cells) and a Manning coefficient equal to 0.01 s m$^{-1/3}$. Figure 5.4 shows the comparison between the streamwise component of the velocity measured by Ruiz-Villanueva (2012) and the values computed by ORSA2D. On the right and left sides (Figs. 8b and 8c), ORSA2D is able to reproduce quite well the evolution of velocities, with a correlation coefficient of 0.986 and 0.985 respectively. In the mid-channel (Fig. 8a), maximum and minimum peaks are modelled, even if a lower precision is found, with the correlation coefficient reducing to 0.829 (which is similar to the correlation found by Ruiz-Villanueva (2012), R^2 = 0.84).

The motion of the cylinder is computed with the proposed formulation for transport and rotation. For the drag and side coefficients, the logistic-like and the beta-like curves described in section 4.6 are respectively implemented, and the added mass value for a semi-submerged cylinder is considered.

Figure 5.5 shows that the trajectory measured by Ruiz-Villanueva et al. (2014b) is well replicated using the proposed formulation until around the third obstacle. Then, the simulated log hits the right wall and the two trajectories separate slightly, to become more similar again in the final part.

On overall, the correlation coefficients between computed and measured log positions are 0.999 in *x* and 0.773 in *y*. The simulation is performed with the formulation of rotation that takes into account the torque and added inertia terms. However, since no exact information about log orientation is available, the results in term of rotation are not verified.

Figure 5.5 Comparison of the data measured by Ruiz-Villanueva and the trajectory simulated with ORSA2D_WT.

5.3. Description of the experimental campaign

For elongated bodies, and for spherical bodies rotating in a flow, it is essential to model both translation and rotation since the two phenomena are strictly connected. To fill the gap in the calibration, specific experiments with spheres and cylinders floating on the water surface are performed. The goal is to obtain information about the linear and angular displacement of these bodies in different flow conditions. The proposed formulation is later tested on such experiments.

5.3.1. Experimental set-up

The experimental campaign was performed at the Department of Science and Technology of Materials and Fluids of the University of Zaragoza, in a prismatic channel 6 m long. For the measurements, only the first part, 3.25 m long, with horizontal bottom, is employed. Then the water flows in a second part, which is hydraulically disconnected from the upper channel, and is recirculated.

Tests were first performed without obstacles, to assess the behaviour of the cylindrical samples in uniform steady flow, and then with one side

rectangular obstacle, with two side rectangular obstacles and with one side smooth obstacle, as shown in Fig. 5.6.

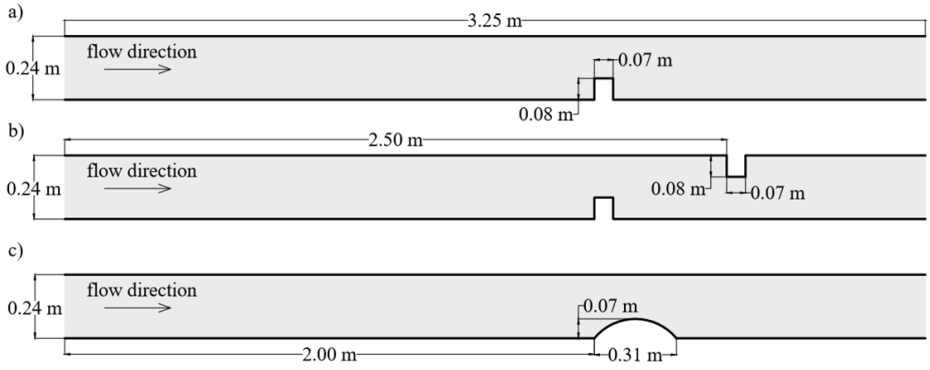

Figure 5.6 Sketch of the channel, with obstacles. a) One side rectangular obstacle; b) two side rectangular obstacles; c) one side smooth obstacle

The bottom, 0.24 m wide, and the walls of the channel, 0.16 m high, are made of transparent poly methyl methacrylate (PMMA). The obstacles are made of plastic and present a smooth surface comparable to that of the acrylic. The single rectangle and the curve are placed at 2.00 m from the inlet section, on the right-hand side of the channel. For the configuration with two rectangular obstacles, the first one is placed on the right-hand side at 2.00 and the second is placed on the left-hand side, at 2.50 m from the inlet.

The pumping system provides a constant discharge, by feeding a loading basin which releases water in the channel. Discharge is measured by an electromagnetic flow meter (COPA-XE DE43F by ABB, which has an accuracy of 0.5% of the maximum rate, 60 m^3 h^{-1}). For each of the four tested configuration (one without obstacles, and three with different side obstacles) the discharge is set at 15.3 m^3 h^{-1} and the tests are performed in steady conditions.

The employed samples are wooden cylinders obtained from pinewood bars, a wooden sphere and a plastic sphere filled with a solution of water and alcohol, in order to make it sink by a half, being similar to light wood. In 10 cylindrical samples, a weight imbalance between the cylinder

extremities was simulated by inserting a spike in one end. This resembles the presence of a heavier portion, as with a root wad, although maintaining the regular shape of the body. The wooden samples are made smooth and waterproof with a varnish.

To avoid the influence of the inlet flow, which may be not exactly symmetric due to the presence of the outlet pipe in the basin, the samples are released about 1.25 m downstream of the inlet section. Spheres are released manually, while a specific device was built for cylinders (designed and realized at the University of Zaragoza, Fig. 5.7).

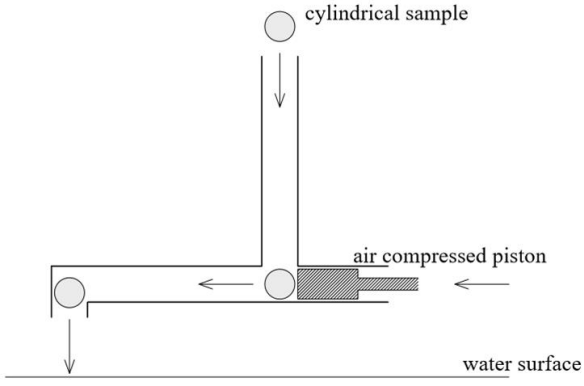

Figure 5.7 Section of the device for cylindrical objects release. The insertion of the cylinder, its motion, as well as the motion of the piston, are shown. The cylinder is released just 0.02 m above the water surface.

One cylinder is inserted in a vertical box, and then is slowly pushed forward in an horizontal box thanks to an air compressed piston, until it reaches an opening and falls on the water surface. The device is placed at about 0.02 m above the water surface. In this way, cylinders enter in the stream with a small drop and in an un-controlled manner, not influenced by the operator manual dexterity. However, the device does not allow to replicate the exact initial condition for each test, since the push of the piston and the water entering do not occur exactly in the same conditions.

The samples characteristics are shown in Tab. 5.1.

Sample type	N°	D [m]	L [m]	Vol [m^3]	m_b [kg]	ρ_b [kg m^{-3}]
Wooden sphere	1	0.042	-	3.88E-05	0.0269	694
Plastic sphere	1	0.039	-	3.29E-05	0.0163	494
Cylinder	8	0.073	0.01	5.73E-06	0.0045	774
Cylinder with spike	10	0.073	0.01	5.73E-06	0.0046	802

Table 5.1 Samples dimensions, mass and density.

Values in Tab. 5.1 are averaged on the sample set for cylinders with and without the spike. The density of the cylinders with spike accounts for the increase due to the presence of metal.

Tests were realized by releasing in sequence the two spheres or the cylinders, in order to avoid any interference. In this way, the focus is on the description of the motion of the singular element, and allows the evaluation of the effect of the sole flow on the body.

Few tests were realized involving all the cylindrical samples, with and without spike, in order to obtain some collisions between the samples and provide information for the calibration of the collision model.

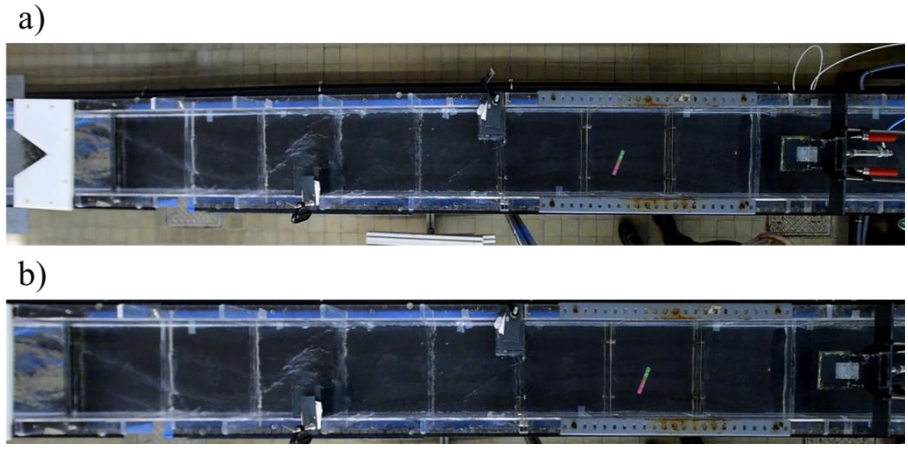

Figure 5.8 Top view of the channel during an experiment with two side obstacles. a) Original snap from the video; b) orthorectified frame. Flow from right to left.

The experiments were recorded from top view, hanging a Nikon camera (Nikon D810, with a Nikon 24-70mm f/2.8G lens, set at a focal distance of 24mm) which provides videos with a resolution of 30 fps. In Fig. 5.8a a snap from a video is shown. Due to the distortion introduced by the lens, the orthorectification of the images is performed (Fig. 5.8b).

5.3.2. Hydraulic measurements

Measures of water level and water velocity are performed for the three configurations with obstacles, as a comparison with the simulated values.

The water levels are measured near the channel sidewalls and are resumed in Tab. 5.2 for the different channel configurations.

	1 rectangular obstacle		**2 rectangular obstacles**		**1 smooth obstacle**	
x [m]	***h* [m]**		***h* [m]**		***h* [m]**	
	Right	**Left**	**Right**	**Left**	**Right**	**Left**
0.00	0.067	0.067	0.072	0.072	0.062	0.062
0.25	0.067	0.067	0.072	0.072	0.062	0.062
0.50	0.067	0.067	0.071	0.072	0.061	0.062
0.75	0.067	0.067	0.071	0.072	0.060	0.061
1.00	0.065	0.066	0.070	0.072	0.060	0.060
1.25	0.064	0.064	0.070	0.070	0.059	0.058
1.50	0.064	0.064	0.070	0.070	0.059	0.057
1.75	0.064	0.063	0.069	0.069	0.059	0.057
2.00	0.066*	0.059	0.073*	0.064	0.060*	0.056
2.25	0.030	0.026	0.055	0.058	*	0.038
2.50	0.032	0.016	0.057	0.065*	0.035	0.019
2.75			0.029	0.025	0.027	
3.00			0.017	0.030		

Table 5.2 Water level measured near the right and left side of the channel, for the three configurations with side obstacles. The star means that the water level was measured on the obstacle or, for the smooth obstacle, no measurement is available.

On overall, the configuration with two obstacles presents the higher water level, due to the higher contraction of the channel section.

Water velocity was measured, too. In a first step, a digital flowmeter (MiniAri20, with the probe Mini 95.0004 by PCE Instruments) was employed. The streamwise component (u) and the transverse component (v) are measured in two points, one nearer to the surface, the other nearer to the bottom, and then the average value is considered. For the smooth obstacle configurations, measures are replicated with an Acoustic Doppler Velocimeter (MicroADV 16MHz, by Sontek), in order to provide an accurate description of the velocity near the obstacle. Due to the dimension of the ADV probe, only one measure is recorded for each point. The points of measure are shown in Fig. 5.9 for the flow meter and in Fig. 5.10 for the MicroADV.

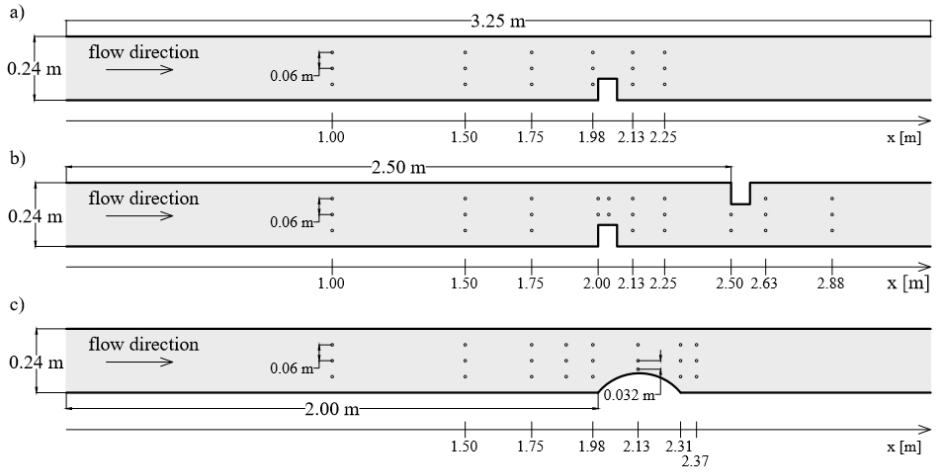

Figure 5.9 Planar view of the channels with the point of measure of flow velocity (digital flow meter measurements).

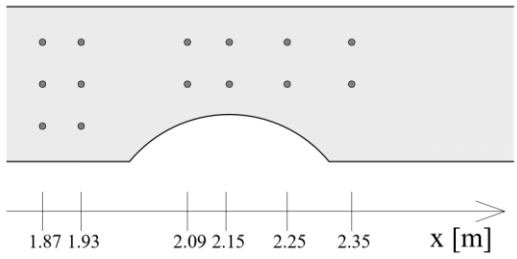

Figure 5.10 Detail of the planar view of the channel with smooth obstacles. Circles show the points where velocity was measured with the ADV.

In each configuration, the velocity is smaller near the inlet section (around 0.30 m s^{-1}) and increases downstream (around 0.80-0.90 m s^{-1}). Both *x* and *y* components are measured, with the latter becoming more significant in presence of abrupt obstacles. Detailed values are presented together with simulated results, for comparison.

5.3.3. Analysis of the results

A brief analysis of the outcome of the experiments is provided, in order to highlight the behaviour of the floating bodies depending on their shape and on the channel configurations.

5.3.3.1. Motion of a sphere

Focusing on the configuration with the smooth side obstacle, which provides a gradual deviation of the flow, the outcome of 9 replications of the same experiment, with wooden sphere, is shown in Fig. 5.11.

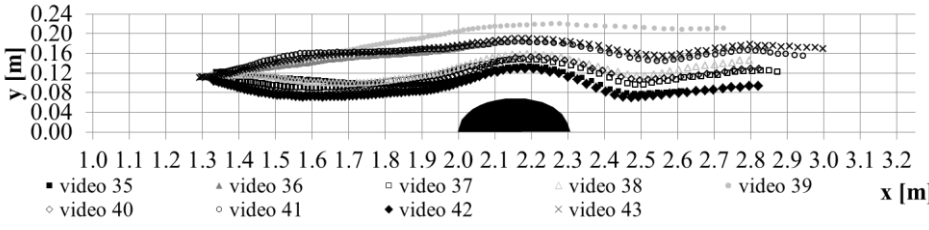

Figure 5.11 Trajectories of a wooden sphere in the channel with a smooth side obstacle. The diagram corresponds to the planar view of the channel, with the right side corresponding to the x-axis.

Three main trends are shown: a lower trajectory, nearer the x-axis, which presents a curved trace, then an intermediate trajectory around 0.16 m and, for one experiment, a trajectory very near to the left side of the channel, above 0.20 m. The latter presents a straighter trend, probably due to the effect of the near boundary. Despite the scarce number of experiments here analysed, it appears that the bodies tend to spread and to occupy the central part of the channel, despite being released in the same location.

The analysis of the videos shows also that the releasing method (which is manual for spheres) affects strongly the behaviour of the bodies and their motion. For this reason, the initial condition are extracted from the videos few centimetres downstream of the actual releasing point, which is 1.25 m in x and 0.12 m in y.

In all cases, the planar rotation of the sphere was not significant.

5.3.3.2. Motion of a cylinder

The trajectories of a series of experiments for each configuration are presented in Figs. 5.12 to 5.15, for the channel without obstacles, with one rectangular obstacle, with two rectangular obstacles and with one smooth obstacle respectively. In the figures, the centre of mass of each cylinder is tranced. Note that the tests are named after the name of the sample (eight cylinders, from T0 to T7) followed by the analysed video.

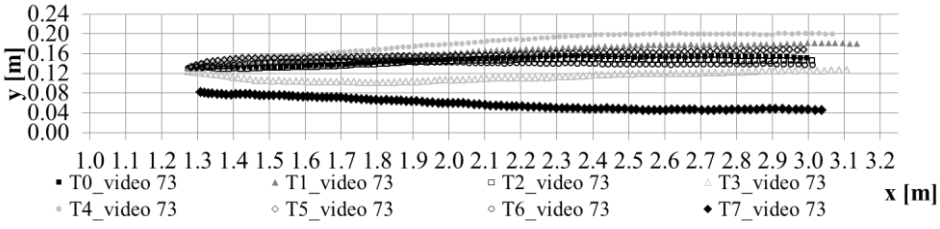

Figure 5.12 Trajectories of wooden cylinders in the channel without side obstacles. The diagram corresponds to the planar view of the channel, with the right side corresponding to the x-axis.

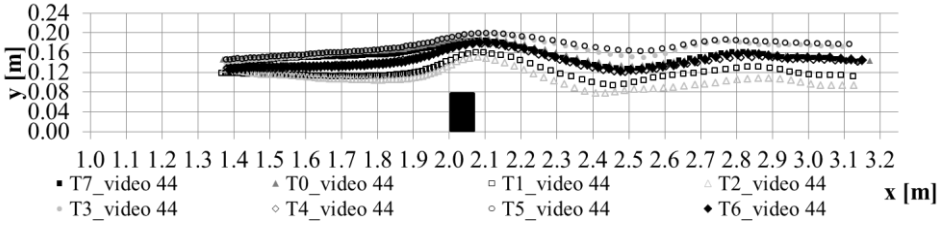

Figure 5.13 Trajectories of wooden cylinders in the channel with one rectangular obstacle. The diagram corresponds to the planar view of the channel, with the right side corresponding to the x-axis.

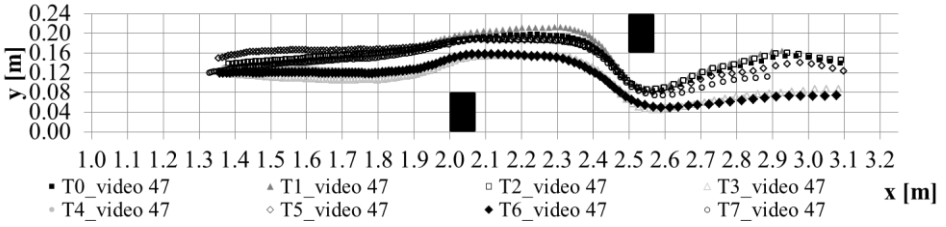

Figure 5.14 Trajectories of wooden cylinders in the channel with two rectangular obstacles. The diagram corresponds to the planar view of the channel, with the right side corresponding to the x-axis.

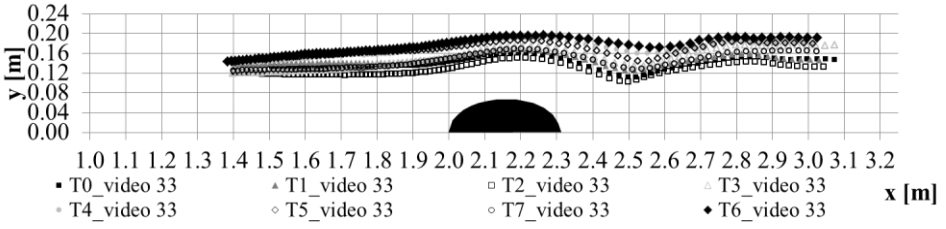

Figure 5.15 Trajectories of wooden cylinders in the channel with one smooth obstacle. The diagram corresponds to the planar view of the channel, with the right side corresponding to the x-axis.

The cylinders move downstream from the release point and their trajectories tend to spread over a large part of the section. In particular, the larger spread is observed for the channel with one rectangular obstacle, where the recorded positions of the cylinders at the outlet are approximately distributed along half of the section. A smaller dispersion is found for the configurations with no obstacles and with one smooth obstacle (the possible trajectories spread over 1/3 of the section, neglecting T6 in Fig. 17). A peculiar trend is observed in Fig. 5.13, for the channel with two rectangular obstacles, in which two main trajectories appear, one reaching a maximum *y* position around 0.16 m and the other that reaches 0.20 m. On

overall, the cylinder trajectories tend to the left side of the channel, even in absence of obstacles.

The rotation observed in the experiments, for the different channel configurations, is reported in Figs. 5.16 to 5.19. Cylinders are released nearly perpendicular to the flow (angle near 180° in the diagrams). Angles of 90° and 270° denote the alignment between the cylinder and the channel axis.

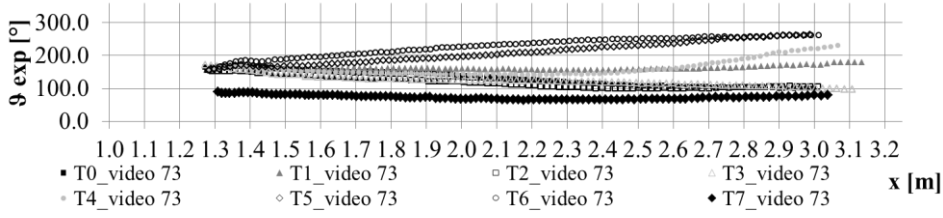

Figure 5.16 Experimental angle evolution of wooden cylinders in a channel without side obstacles. The diagram shows the variation of the angle in relation with the *x* position of the body.

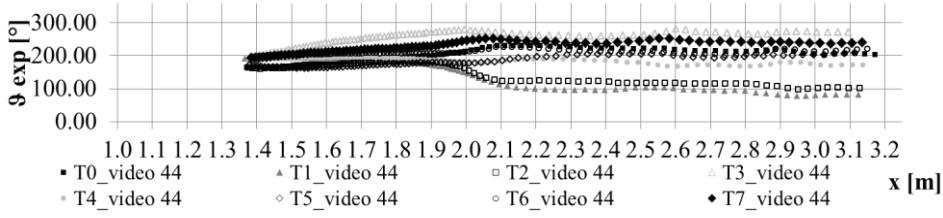

Figure 5.17 Experimental angle evolution of wooden cylinders in a channel with one rectangular obstacle. The diagram shows the variation of the angle in relation with the *x* position of the body.

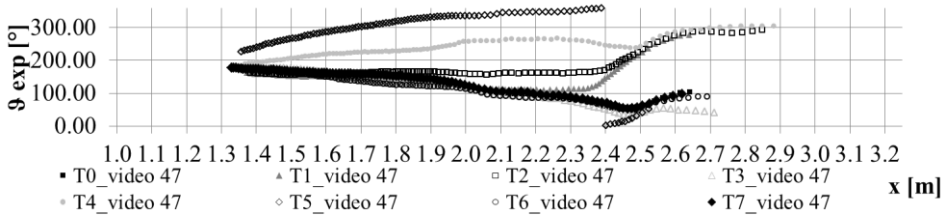

Figure 5.18 Experimental angle evolution of wooden cylinders in a channel with two rectangular obstacles. The diagram shows the variation of the angle in relation with the *x* position of the body.

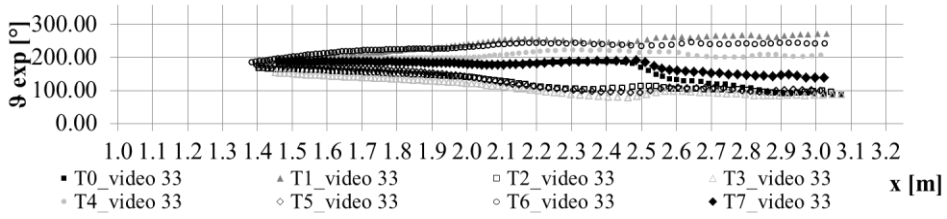

Figure 5.19 Experimental angle evolution of wooden cylinders in a channel with one smooth obstacle. The diagram shows the variation of the angle in relation with the *x* position of the body.

The orientation of the cylinder is strongly affected by the channel configuration. If no obstacles are present in the channel, cylinders tend to rotate with a nearly constant angular velocity, which is reduced in the final part of the channel. In all the experiments (except for the case T7_video 47 in Fig. 5.21, which had a problem in the release) cylinders are introduced with an angle between 150° and 180° and end with a wider range of angles, from 80° to 270°. No sharp variations nor particular tendencies in rotation are observed.

When one rectangular obstacle is placed in the channel (Fig. 5.17), the evolution of the cylinder rotation depends on its orientation just upstream of it. When the approaching angle is higher than 170°, it tends to increase (i.e. the cylinder tends to flip on its axis and to align its aft end with the flow), while if it is smaller, it decreases (i.e. the cylinder simply tends to align in the flow direction). The final angles are between 180° and 270° in the first case and 90°-100° in the second.

When considering two rectangular obstacles, the strongest variation is observed near the second obstacle (placed at 2.50 m from the inlet). In the first part (up to 1.95 m from the inlet), the orientation varies smoothly, possibly because the initial conditions have a greater influence than the flow. Then, when the cylinders encounter the first obstacle, most of the samples tend to an alignment with the flow, which is maintained also when flowing near the second obstacle. Those which maintain their transverse orientation at the first obstacle, tend instead to flip and reverse theta orientation. The final angles are markedly grouped around 50°-100° and 280°-300°, but are not correlated to the initial angle.

Figure 5.19 shows the results for the configuration with a smooth obstacle. Also in this case, in the first part of the channel the orientation varies according to the initial condition, until the obstacle starts to influence it (between 2.00 m and 2.40 m). In the final part, the presence of a surface wave downstream of the curves boundary contributes to increase the orientation variation, with final angles ranging from 80° to 270°.

On overall, the rotation of cylindrical floating bodies appears strongly variable. It is somehow connected to the flow field, although the large ranges observed for the final orientations highlight a certain randomness in determining this datum. The origins of such unpredictability are probably related to the turbulence and to the local variation of the water surface, like small surface waves. However, the experiments are simulated in order to verify if the proposed model is able to reproduce the overall behaviour, being aware that a deterministic approach is only partially reliable, due to the high number of uncertainties highlighted.

5.4. Numerical simulation of laboratory experiments

5.4.1. Hydraulic simulations

The simulation of the flow in the various configurations with obstacles and the comparison with the measured water level and velocity are presented. The aim of this step is to verify that the simulated quantities relative to the flow corresponds to the measured ones, assessing that the geometry, the discharge and the channel roughness are correctly reproduced.

The hydraulic simulations, with an unstructured triangular mesh of about 8500 elements, are performed with a constant discharge of 4.25 l s^{-1} and critical flow as downstream boundary condition. The resistance to the flow is modelled by the Manning coefficient, which is set equal to 0.01 s $m^{-1/3}$.

Measured and simulated water levels are compared in Fig. 5.20, 5.21 and 5.22 for the right and left side of the channel. The comparison of velocity is shown in Fig. 5.23 for the configuration with one side obstacle, while the results for the other configurations are resumed in Appendix A.

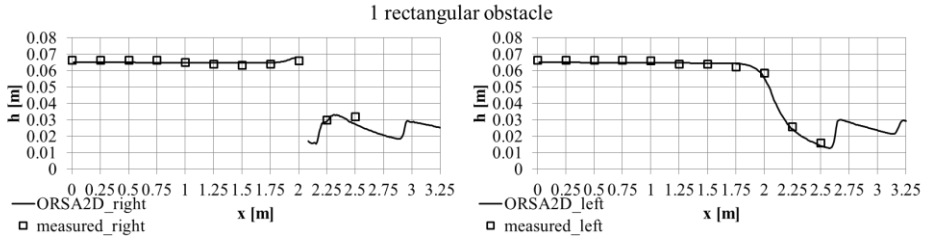

Figure 5.20 Simulated and measured water level for the configuration with one rectangular side obstacle. The obstacle is on the right side, at x = 2.00 m.

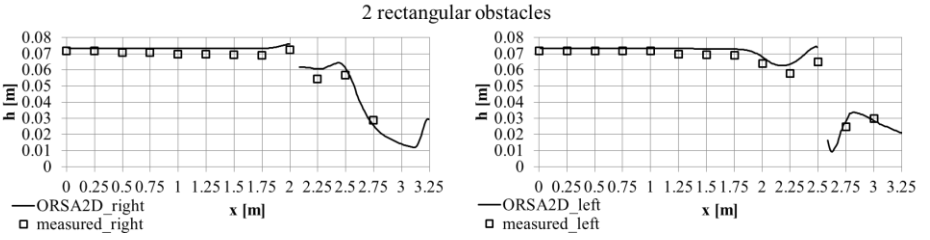

Figure 5.21 Simulated and measured water level for the configuration with two rectangular side obstacles. The first obstacle is on the right side, at x = 2.00 m; the second obstacle is on the left side, at x = 2.50 m.

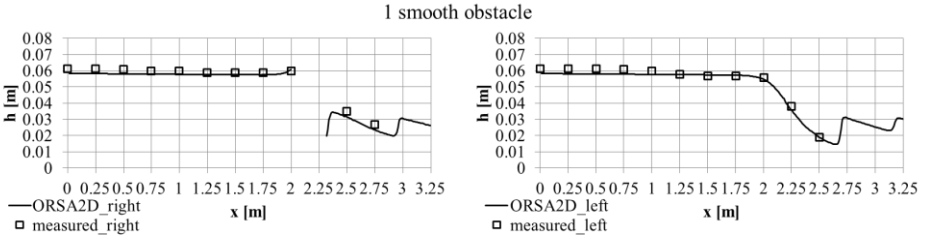

Figure 5.22 Simulated and measured water level for the configuration with one curve side obstacles. The obstacle is on the right side, at x = 2.00 m.

Measured and simulated water levels are well comparable. For all the configurations and for both sides, the determination coefficient is greater than 0.99. The largest differences are observed for the configuration with two obstacles, in which the water height is slightly overestimated. At x = 2.25 m the maximum difference observed among measured and simulated

water height is 0.006 m for both sides, corresponding to an error of 8% over the maximum measured level. The maximum error is 6% for the configuration with one side obstacle (right wall, x = 2.50 m), and reduces to 4% for the configuration with one smooth obstacle (right wall x = 2.50 m, left wall x = 0.50 m).

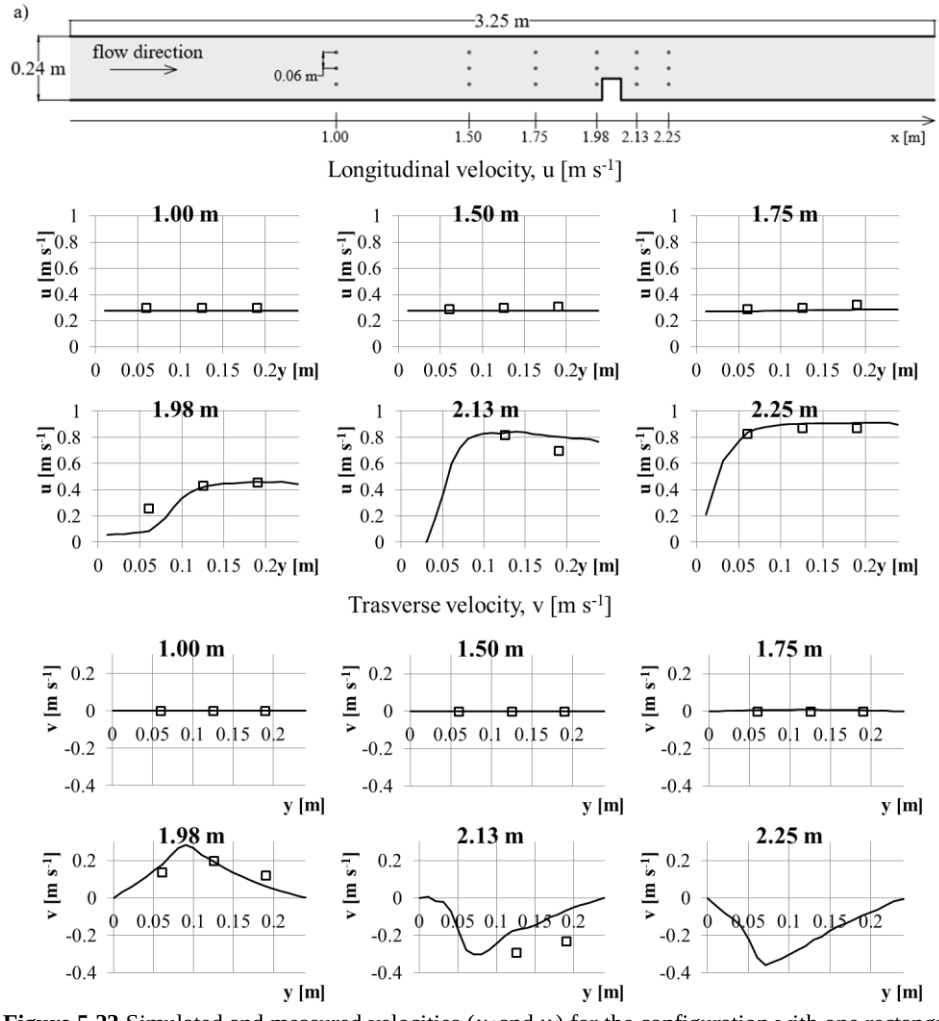

Figure 5.23 Simulated and measured velocities (u_f and v_f) for the configuration with one rectangular obstacles. The distance from the inlet section is indicated above each diagram.

Regarding velocity, in the first part of the channel the transversal component is zero and the streamwise component is nearly constant in the entire

section, as shown by measured and simulated values. Then, both the components increase, and vary across the section. In general, the simulation of the longitudinal velocity component is more accurate than that of the transversal one, especially in the last sections. Note that for the section at 2.25 m from the inlet it was impossible to measure the transversal velocity, due to the reduction of the water level, which became comparable to the transversal dimension of the digital flowmeter. In Fig. 5.23 only the simulated profile is shown for that section.

The accuracy of the hydraulic simulation is slightly different depending on the channel configuration, as shown by comparing the determination coefficients obtained for the velocities at the channel axis and at the sides (Tab 5.3 for the streamwise velocity component, u_f, and Tab. 5.4 for the transversal one, v_f). The determination coefficients are obtained by comparing the simulated and measured values in the points shown in Fig. 5.9. The right section is placed at y = 0.06 m, the axis is at y = 0.12 m and the left section is at y = 0.24 m.

	Right side	**Channel axis**	**Left side**
1 rectangular obstacle	0.972	**1.000**	0.992
2 rectangular obstacles	0.739	**0.939**	0.666
1 smooth obstacle	0.994	**0.998**	0.995

Table 5.3 Comparison of the determination coefficients for the streamwise component of velocity, u_f, for the three configurations.

	Right side	**Channel axis**	**Left side**
1 rectangular obstacle	**0.999**	0.980	0.980
2 rectangular obstacles	**0.875***	0.846	0.172
1 smooth obstacle	0.963	**0.976**	0.928

Table 5.4 Comparison of the determination coefficients for the transversal component of velocity, v_f, for the three configurations. *correlation performed on only 6 values over 10, since in the other points the measure was not possible.

The configurations with one rectangular obstacle and with one smooth obstacle present the best correlation among measured and simulated data.

For the case of two side obstacles, the correlation is reduced for the channel axis and is even worst for the side sections. It is possible that this configuration introduces some three dimensional effects which are not well reproduced by the 2D model. Refer to Appendix A for a graphical comparison of the data.

To sum up, the hydraulic simulation shows that the flow is in general well reproduced for the configurations with one side obstacle (both rectangular or smooth). The configuration with two side obstacle presents, on the contrary, some inaccuracies, both in level and in velocity, which have to be taken into account when coupling the solution with the floating bodies model.

5.4.2. First formulation for rotation

The experiments with two side rectangular obstacles are simulated with the first proposed model for rotation, i.e. the one which adapts the rotation formulation by Mandø and Rosendahl (2010).

The offset torque is computed with a position of the pressure centre that varies for each sub-segment. The resistance term is computed, as a first attempt, with a coefficient C_{res} set equal to the added mass coefficient for a semi-submerged cylinder, 1.41.

Since for the channel configuration with two rectangular side obstacles the orientation evolution appears more influenced by the flow conditions – and less affected by randomness – , this case is selected for the comparison of the two proposed formulations. Linear and angular displacements computed with the first formulation are compared with experimental results in Fig. 5.24 to 5.26.

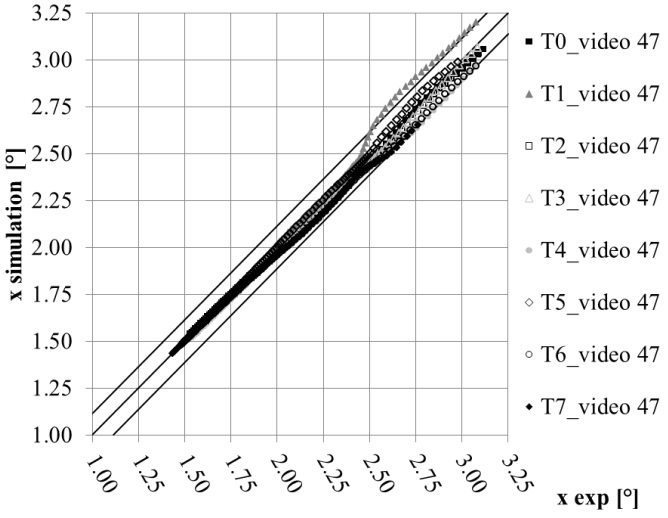

Figure 5.24 Comparison of the experimental and simulated displacement in *x* direction. The confidence interval is limited by the outer solid lines.

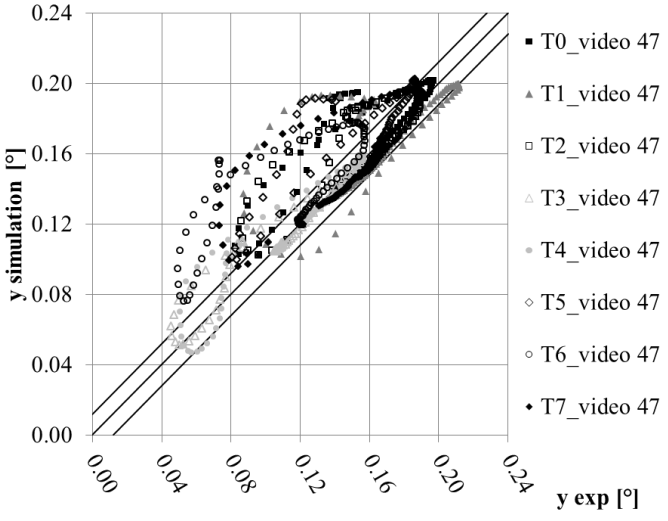

Figure 5.25 Comparison of the experimental and simulated displacement in *y* direction. The confidence interval is limited by the outer solid lines.

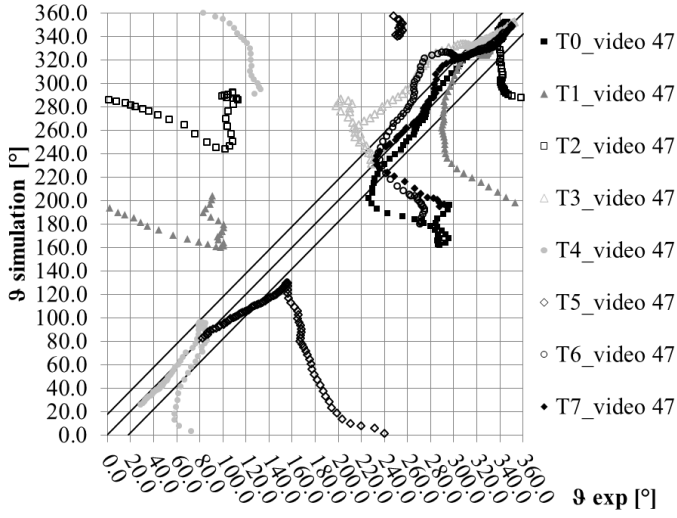

Figure 5.26 Comparison of the experimental and simulated angular displacement. The confidence interval is limited by the outer solid lines.

A confidence interval is outlined for each displacement, set as ±5% of the possible range of variation, which is 2.25 m in *x*, 0.24 m in *y* and 360° for ϑ. The figures show that the best correspondence among experimental and simulated displacement is obtained in *x*, i.e. in the direction of the channel axis. The lateral displacement appears to be less accurately represented, with simulated *y* positions being higher, i.e. nearer to the channel side opposite to the upstream obstacle, than the experimental one. As regards rotation, even if initially the simulated angles are close to the experimental results, when the cylinder reaches the obstacles the disagreement from the expected outcome is complete.

5.4.3. Second formulation for rotation

The second proposed formulation accounts for the torque of the forces distributed on the body (around the body mass centre) and introduces an added inertia term, which plays the role of a resistance term. The adopted value for the added inertia coefficient (C_{AI} = 1.4) is set equal to the added mass inertia and to the resistance coefficient of the first formulation.

The outcome of the simulation of the same experiments shown in the previous paragraph, but modelled with the second formulation, is compared with experimental results in Fig. 5.27 to 5.29.

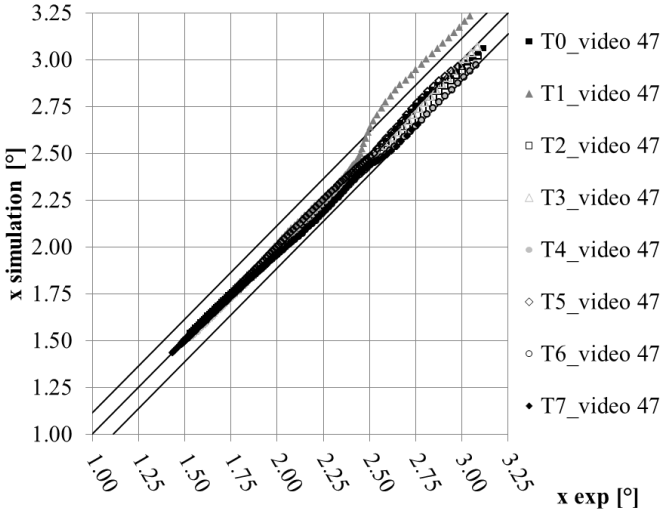

Figure 5.27 Comparison of the experimental and simulated displacement in *x* direction. The confidence interval is limited by the outer solid lines.

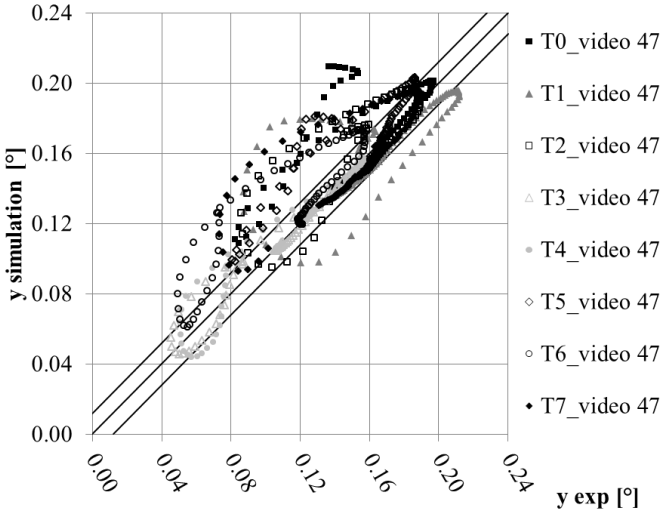

Figure 5.28 Comparison of the experimental and simulated displacement in *y* direction. The confidence interval is limited by the outer solid lines.

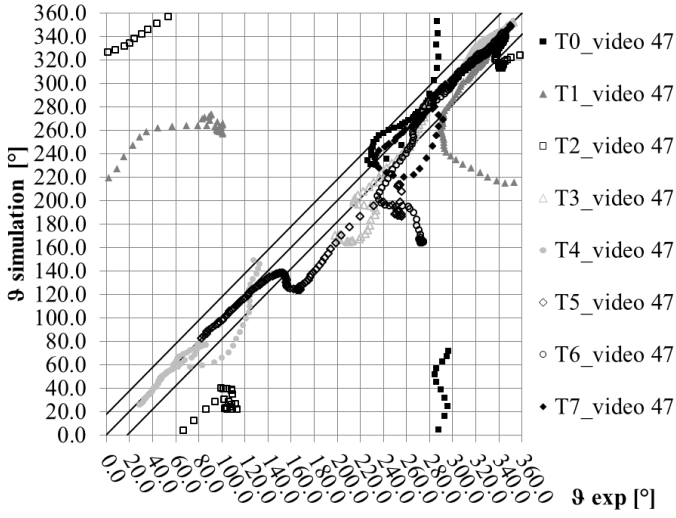

Figure 5.29 Comparison of the experimental and simulated angular displacement. The confidence interval is limited by the outer solid lines.

Also in this case the confidence interval is outlined for each displacement, and has the same amplitude as in the previous paragraph. The *x* displacement is very similar to Fig. 5.29, although experiment T1 presents a slightly worst outcome above 2.40 m; *y* displacement is still overestimated, but less than with the previous formulation. The larger difference between the two formulations is observed with orientation: here the ϑ values appear more aligned with experiments, although several deviations are still appreciable.

5.4.4. Choice of the final formulation

Both formulations show a satisfactory modelling of the *x* displacement, while the accuracy of *y* and angular displacement reproduction is lower. Although a visual comparison of the results presented in Figs. 5.27–5.29 shows a definitely better performance of the second formulation on angular displacements, the number percentage of data included in the confidence interval are compared in Tab. 5.5 to provide a quantitative evaluation for the selection of the best formulation.

Formulation	x	y	ϑ
Offset & resistance	**93%**	**71%**	58%
Torque & added inertia	92%	70%	**70%**

Table 5.5 Comparison of the percentage of data in the confidence interval for the two proposed formulations.

The first formulation, with the offset torque and the resistance term, is slightly more accurate in modelling the linear displacement, while the second one clearly presents better results with regards to orientation, despite a slightly lower accuracy in *x* and *y* displacements.

This result is unexpected, since the translation is computed with the same equations in both cases, and a more accurate prediction of the body orientation should lead to the reduction of the errors in the linear displacement, too. This may happen because, in the translation equation, the added mass coefficient is set as a constant, while it should vary with the body orientation as the drag and side coefficients. The variation of such coefficient with the angle is suggested by the experiences of naval engineering (e.g. Salvesen et al. 1970) but is disregarded in this case due to the lack of data with reference to semi-submerged cylinders.

To confirm the choice of the second formulation, computed angular velocities are also compared with the values estimated from the experiments: these last are computed as the difference among two angular values (in two successive frames) divided by the time interval.

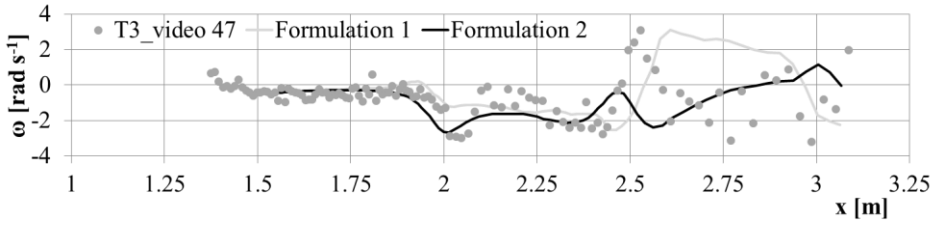

Figure 5.30 Comparison of the experimental and simulated angular velocity, for both formulations. Grey linen for formulation 1 and black line for formulation 2.

In Fig. 5.30 the angular velocity of experiment T3 is compared with the values computed by the configuration. It is possible to observe a decrease in the measured angular velocity around 2.00 m and a sharp increase around 2.50m, corresponding respectively to the passage of the sample near the first and the second obstacle. The formulation with offset and resistance misses the first variation and delays the second, resulting in a worst modelling of rotation, while the formulation with torque and added inertia is able to reproduce such behaviour, despite underestimates the increase in angular velocity at 2.50 m. The angular velocity trends for the other experiments are shown in Appendix B.

Due to the best accuracy provided, the second formulation is selected for the model here proposed, and its performances are evaluated on a larger set of experiments, after a sensitivity analysis on the parameters to calibrate the entire model.

5.5. Analysis of the sensitivity to model parameters and initial conditions

The effects of the variation of the added mass and added inertia coefficients are verified through a sensitivity analysis. Furthermore, the sensitivity of the formulation to the initial conditions, such as the body position and orientation, as well as to the method to represent the instream obstacles, is investigated.

5.5.1. Effect of the added mass coefficient

As previously said, the added mass coefficient is set constant due to the lack of data for the specific conditions of a semi-submerged cylinder. The value assigned, equal to 1.41, is derived with reference to a floating cylinder in cross flow configuration, while no values are provided for a body oblique or aligned with the flow.

Different values of the added mass coefficient are tested, in order to verify its effect on the trajectory and on the cylinder orientation. The drag and side coefficients are computed with the logistic-like and beta-like curves, respectively, and the added inertia coefficient is set equal to 1.4.

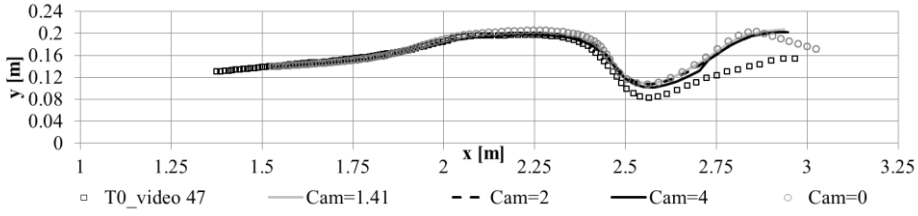

Figure 5.31 Comparison of the simulated trajectories with different values of the added mass coefficient for experiment T0. Empty squares are the experimental data, light grey line for 1,41, dashed line for 2, solid line for 4 and empty circles for 0.

The trajectory (Fig. 5.31) does not appear to be strongly affected by the variation of the added mass coefficient. The largest difference for non-zero values is observed with $C_{AM} = 4.0$, especially in correspondence of the second obstacle ($x = 2.50\ m$). If the added mass is not included ($C_{AM} = 0.0$), a slight variation in the final part of the trajectory can be observed.

A strongest influence is instead detected when examining the orientation, as shown in Fig. 5.37. Results with $C_{AM}=1.41$ and $C_{AM}=2.0$ are nearly overlying, except for the final part of the trajectory, while the other two values provide a worse correspondence with experimental data, resulting into smaller occurrences within the confidence interval.

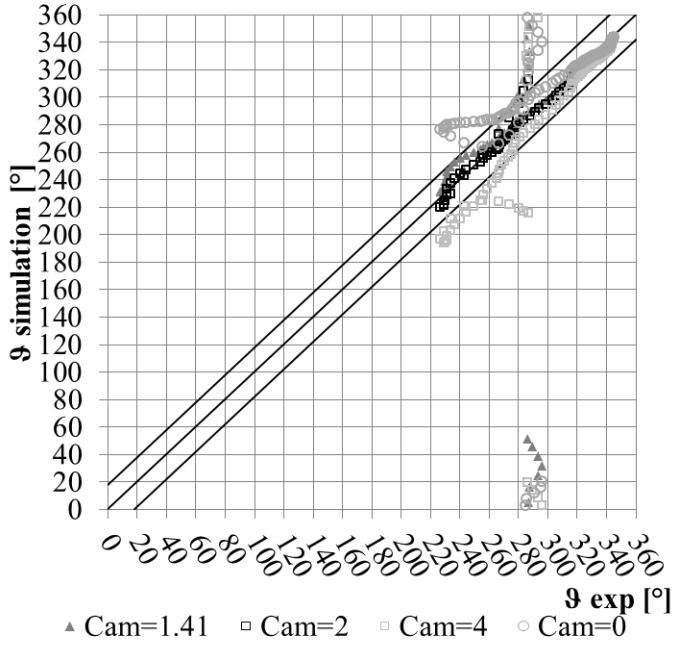

Figure 5.32 Comparison of the simulated angles with different values of the added mass coefficient versus experimental data, for experiment T0. The confidence interval (±20%) is shown.

In Tab. 5.6 the overall determination coefficient obtained for the configuration with two side obstacles are shown (average on 8 experiments).

C_{AM}	x	y	ϑ
0.0	91%	67%	69%
1.41	**92%**	**70%**	**70%**
2.0	92%	70%	67%
4.0	94%	72%	63%

Table 5.6 Comparison of the percentage of data in the confidence interval for different values of the added mass coefficient. In bold the results with the added mass coefficient assumed for a floating cylinder.

The trajectories computed with the added mass coefficient of a submerged cylinder ($C_{AM} = 2.0$) present the same accuracy as those computed with $C_{AM} = 1.41$ in x and y. while the orientation appear to be reproduced slightly worse on average. Increasing the added mass coefficients further leads to an unexpected result: the simulation of the trajectories is improved,

while the accuracy on the orientation strongly decreases. Such a behaviour can be related to a possible unbalance among the translational and rotational inertia, and can be further investigated considering the effect of the added inertia coefficient.

The worst results are obtained for $C_{AM}=0.0$, which confirms the need to include the added mass in the model.

5.5.2. Effect of the added inertia coefficient

The value of the added inertia coefficient was initially set equal to the added mass coefficient, basically to provide a benchmark result for the comparison among the two formulations for rotation. This value, however, can be calibrated in order to improve the accuracy of the simulation. The effects of the variation of the added inertia coefficient are shown in Fig. 5.33 and 5.34 for experiment T0 with two side obstacles. The drag and side coefficients are again computed with the logistic-like and beta-like curves, respectively, and the added mass coefficient is set equal to 1.41.

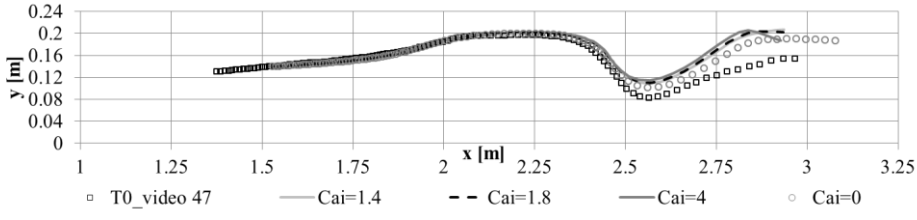

Figure 5.33 Comparison of the simulated trajectories with different values of the added mass coefficient for experiment T0. Dark points are the experimental data. Empty squares are the experimental data, light grey line for 1.4, dashed line for 1.8, solid line for 4 and empty circles for 0.

The variation of the added inertia coefficient does not affect considerably the cylinder trajectory (Fig. 5.33). For $C_{AI} = 0.0$ a trajectory nearer to the experimental data is obtained, at least for the considered experiment.

As regards rotation (Fig. 5.39), the effect of the variation of the added inertia coefficient is noticeable, especially for $C_{AI} = 0.0$, which once

again gives the best result for the considered experiment, and for $C_{AI} = 4.0$ which, on the contrary, show the worst performance.

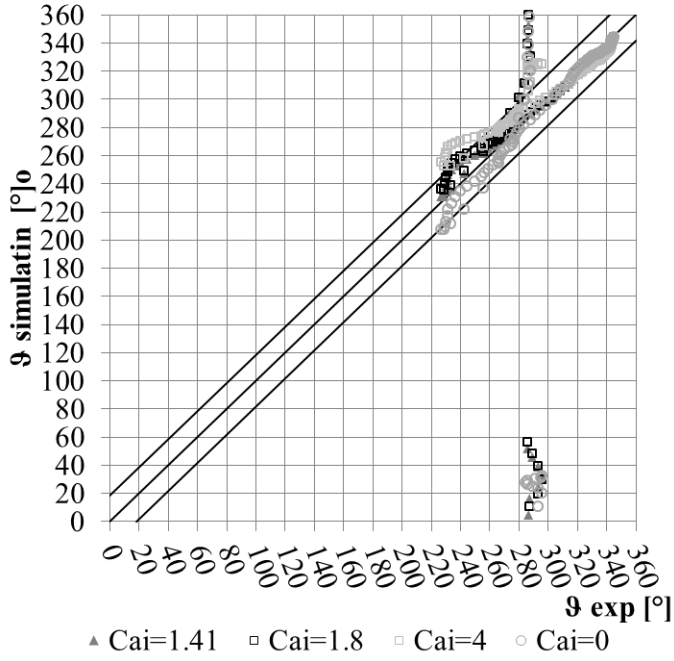

Figure 5.34 Comparison of the simulated angles with different values of the added inertia coefficient versus experimental data, for experiment T0. The confidence interval (±20%) is shown.

However, for a complete evaluation of the effect of the added inertia coefficient, 8 tests performed with the two side obstacles configuration are considered. In Tab. 5.7 the percentages of data included in the confidence interval for the 8 cylinders are resumed.

C_{AI}	x	y	ϑ
0.0	92%	70%	65%
1.4	**92%**	**70%**	**70%**
1.8	92%	70%	77%
4.0	92%	69%	79%

Table 5.7 Comparison of the percentage of data in the confidence interval for different values of the added inertia coefficient. In bold, the value originally implemented.

As expected, the variation of the added inertia coefficient does not influence much the computation of cylinders trajectories. On the contrary, the effect on rotation are clear and well visible. It appears that the higher the value of the added inertia, the higher the accuracy of computed orientation. For the maximum value tested, $C_{AI} = 4.0$, almost 80% of the data lay inside the confidence interval, although a slight reduction in the accuracy in *y* direction is observed.

Since the added inertia formulation showed good performances also with the added mass coefficient set as $C_{AM} = 4.0$, the experiments for the configuration with two side obstacles were repeated also by setting both the added mass and the added inertia coefficient equal to 4. Although this value has no real physical meaning for the added mass, whose correct value should be 1.41, the effect of this choice is nevertheless evaluated due to the good performances highlighted separately in the sensitivity analysis for each coefficient. The results for the 8 tests realized are shown in Figs. 5.35 to 5.37.

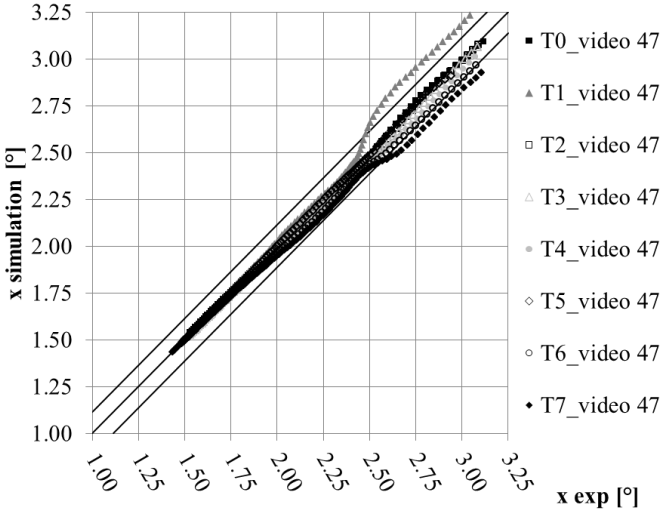

Figure 5.35 Comparison of the experimental and simulated displacement in *x* direction. Simulations are realised with $C_{AM}=4.0$ and $C_{AI}=4.0$. The confidence interval is limited by the outer solid lines.

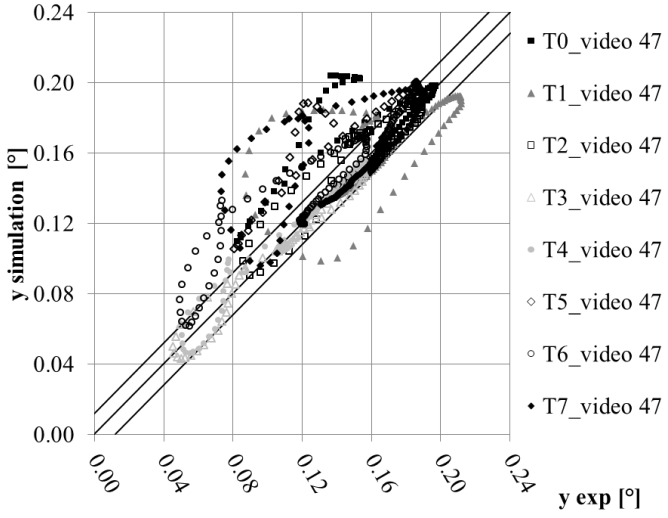

Figure 5.36 Comparison of the experimental and simulated displacement in *y* direction. Simulations are realised with $c_{AM}=4.0$ and $c_{AI}=4.0$. The confidence interval is limited by the outer solid lines.

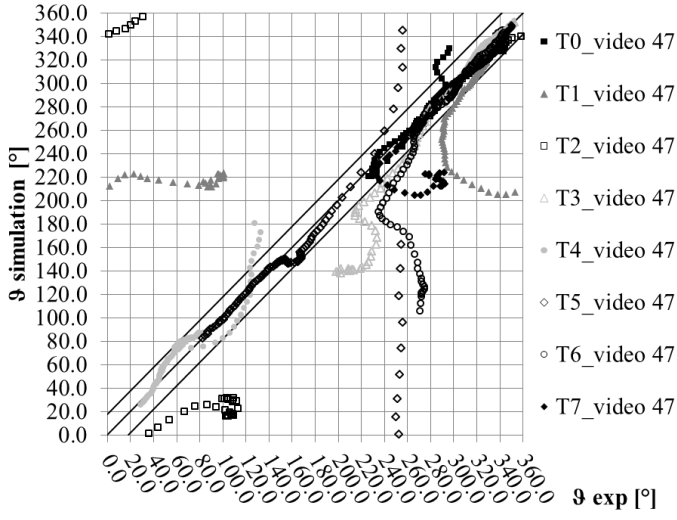

Figure 5.37 Comparison of the experimental and simulated angular displacement. Simulations are realised with $c_{AM}=4.0$ and $c_{AI}=4.0$. The confidence interval is limited by the outer solid lines.

A slightly higher number of occurrences in the confidence intervals is found for the three variables (93% for *x*, 70% for *y* and 75% for *ϑ*) if compared with the results obtained with standard values (see Tab. 5.5 for a comparison). However, comparing these three figures with Figs. 5.27 to

5.29, obtained with the standard values (C_{AM}=1.41 and C_{AI}=1.4), the data result more confused. In particular, data out of the confidence interval present a stronger variation in Figs. 5.35 and 5.36, for *x* and *y* displacements.

It is worth highlighting that, in general, the occurrences out of the confidence range refer to angles and positions in the final reach of the channel, where the flow velocity is higher and, in general, model results are less adherent to experimental data.

The fact that high values of added mass and added inertia coefficients provide an exacerbation of the differences between the well-reproduced data (in the upstream part of the channel) and the wrong-reproduced ones (in the downstream part of the channel) can be considered a sign of the limits of the formulation itself. It is possible, for instance, that assuming constant values for the added mass and added inertia coefficients, instead of considering their dependence on Reynolds number and body orientation, contributes to increase the model inaccuracies. However, this issue has not been further investigated up to now.

Because of the irregular behaviour presented, the added mass and added inertia coefficient are not set equal to the maximum tested value, even if it provides slightly better results for rotation.

The added inertia coefficient is then set equal to 1.8, since in Tab. 5.7 this value provides significantly better results for rotation than 1.4 (77% of data in the confidence interval against 70%), while the added mass coefficient remains 1.41. In Figs. 5.38 to 5.40 the outcomes of the simulations with these values are presented, showing that they actually ensure an improvement in rotation (with respect to Fig. 5.29) and do not introduce excessive variation in linear displacement (in comparison with Figs. 5.35 to 5.37).

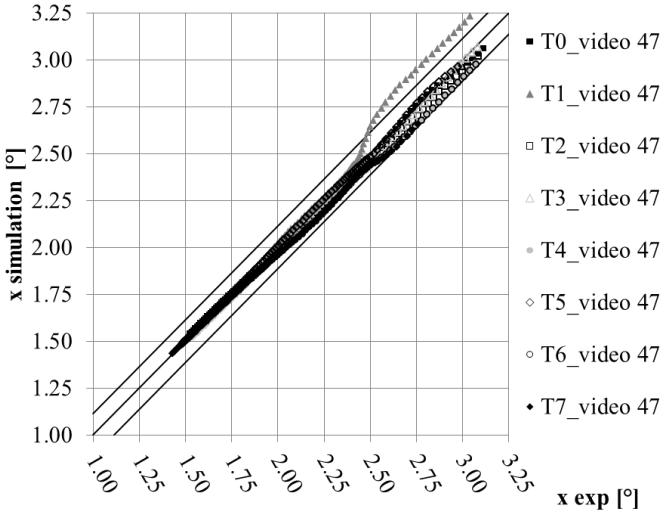

Figure 5.38 Comparison of the experimental and simulated displacement in *x* direction. Simulations are realised with C_{AM}=1.41 and C_{AI}=1.8. The confidence interval is limited by the outer solid lines.

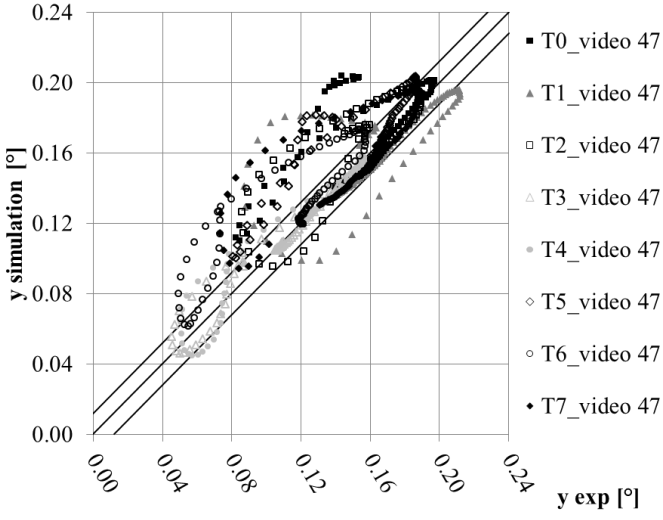

Figure 5.39 Comparison of the experimental and simulated displacement in *y* direction. Simulations are realised with C_{AM}=1.41 and C_{AI}=1.8. The confidence interval is limited by the outer solid lines.

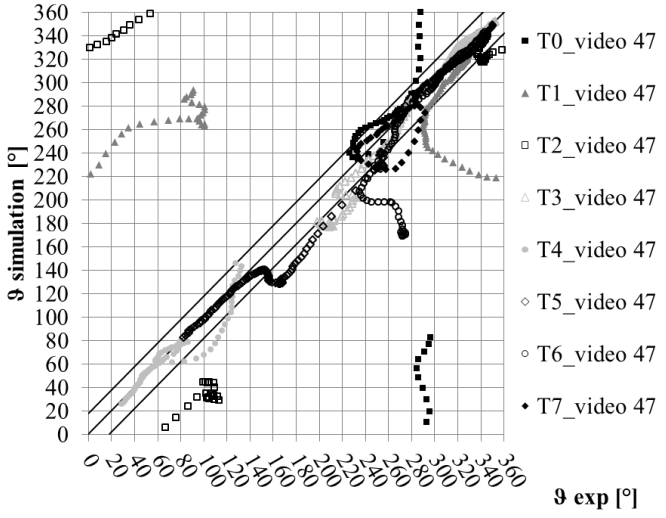

Figure 5.40 Comparison of the experimental and simulated angular displacement. Simulations are realised with C_{AM}=1.41 and C_{AI}=1.8. The confidence interval is limited by the outer solid lines.

5.5.3. Effect of the initial conditions

The simulation of log trajectories is influenced by the initial conditions, i.e. location, orientation, linear and angular velocity. For the choice of the formulation and for the sensitivity analysis, these values are obtained by extracting information from the orthorectified videos: for cylinders, the position of the ends is traced, and then the position of the centre of mass and the orientation are computed. By dividing the linear and angular displacement by the time step, the corresponding linear and angular velocities are computed, too.

Random errors may indeed be introduced during the extraction of data, which is done both visually or automatically by the software (TRACKER, a free tool developed to extract physical information from videos, Brown and Christian 2011) depending on the video quality. Usually, the image quality is higher near the release point, and decreases when the body reaches the final part of the channel, due to increasing velocity and the side view of the camera. The orthorectification process corrects some mistakes, but some inaccuracies may be introduced even during this pro-

cess, due to the difficulties in determining the exact water level (which is deduced by locating the water surface profile along the channel walls) and to the variability of the water level itself along the channel axis.

A maximum error of 0.005 m in the log positioning has been estimated, especially for the transversal positioning. Higher errors may happen in angular displacement and velocity, due to some uncertainties in maintaining the correct alignment of the two ends and to video resolution.

In order to analyse if the spread in the experimental data can be due to a strong dependency of log trajectories and orientation on the initial conditions, a sensitivity analysis of the numerical results on these conditions is performed.

To analyse how initial conditions affect the simulation, the following ranges are tested:

- position, transversal displacement: $\Delta y = \pm 0.005$ m;
- streamwise component of velocity: $\Delta u = \pm 0.05$ m s^{-1};
- transversal component of velocity: $\Delta v = \pm 0.003$ m s^{-1};
- angular velocity: $\Delta \omega = \pm 0.1$ rad s^{-1};
- initial angle: $\Delta \theta = \pm 3°$.

Figs. 5.41 to 5.45 show the effect of the variation of the initial conditions on the trajectory and orientation of the cylinder.

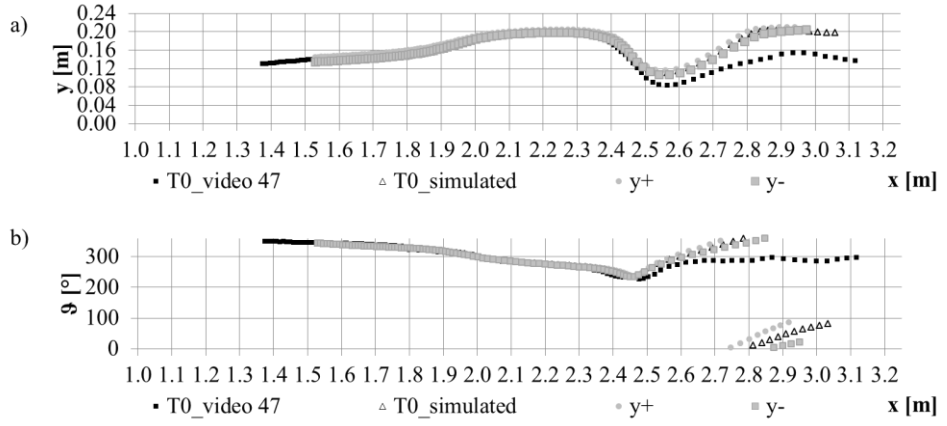

Figure 5.41 Comparison of the experimental and simulated trajectory (a) and angle (b) as a function of the *x* displacement. Empty triangles show standard simulation outcome, solid grey triangle and square show the results obtained by varying the transversal position, *y*.

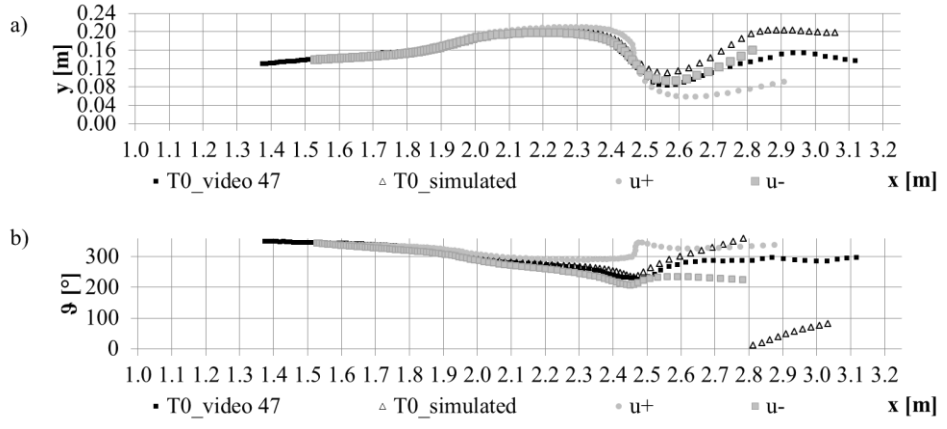

Figure 5.42 Comparison of the experimental and simulated trajectory (a) and angle (b) as a function of the *x* displacement. Empty triangles show standard simulation outcome, solid grey triangle and square show the results obtained by varying the streamwise component of velocity, *u*.

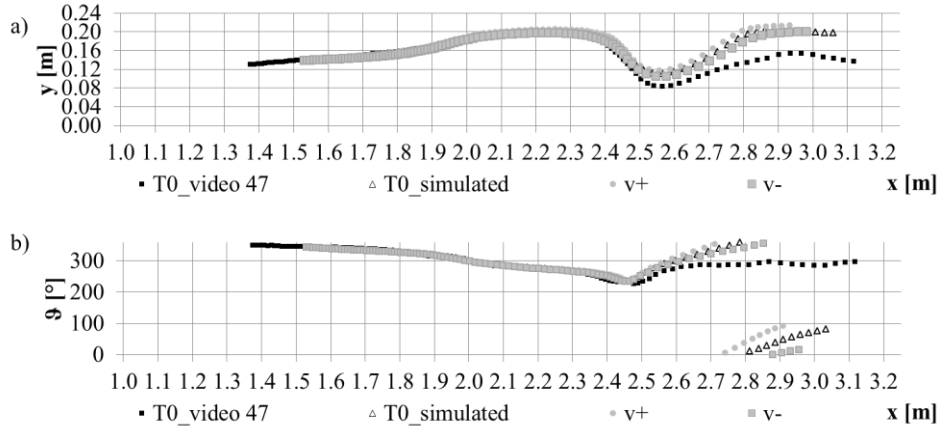

Figure 5.43 Comparison of the experimental and simulated trajectory (a) and angle (b) as a function of the *x* displacement. Empty triangles show standard simulation outcome, solid grey triangle and square show the results obtained by varying the transversal component of velocity, *v*.

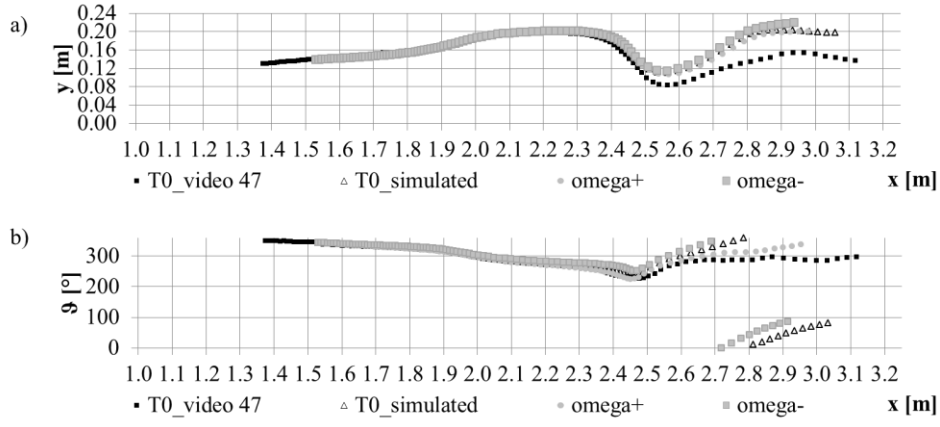

Figure 5.44 Comparison of the experimental and simulated trajectory (a) and angle (b) as a function of the *x* displacement. Empty triangles show standard simulation outcome, solid grey triangle and square show the results obtained by varying the angular velocity of the body, ω_b.

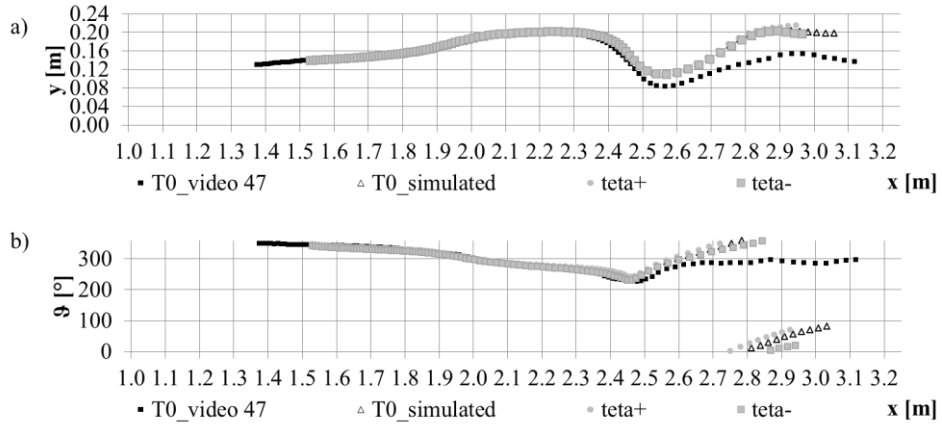

Figure 5.45 Comparison of the experimental and simulated trajectory (a) and angle (b) as a function of the *x* displacement. Empty triangles show standard simulation outcome, solid grey triangle and square show the results obtained by varying the initial orientation, ϑ.

The results show that the body motion and rotation are sensitive to small variations of the initial streamwise velocity component and angular velocity. In particular, when the streamwise velocity is increased, a collision with the second obstacle occurs. As regards orientation (Fig. 5.42b) the effect of collision is also well visible. Moreover, in general the simulated trajectories appear to be less sensitive to initial conditions, while predicted rotation angles exhibit a wider spreading downstream of the second obstacle.

To conclude, even if the uncertainties of the initial condition do certainly influence the outcome of the simulations, their effect is not so evident. Apart from the case of streamwise velocity, the main characteristics of the trajectory and of the angular displacement are maintained, reducing the differences in the final reach of the channel.

5.5.4. Effect of body subdivision

The proposed model divides the cylinder in 4 sub-sections, computing the forces as if each section were independent and considering as force centres each local centre of mass, which are located in ±0.125L and ±0.375L from the global centre of mass of the cylinder.

To assess if the subdivision leads to any mistake in predicting the log motion, two more approaches are tested: in one case, the forces are computed in 4 points, which are two to two equal, positioned at a distance ±0.25L from the body centre of mass. In this way, the cylinder is divided in 2 parts, while 4 forces are computed, which differ only by geometrical conditions. The second approach keeps the division of the cylinder in 2 parts, and computes the forces in 2 points, located at ±0.25L from the body centre of mass. This test allows one to verify if any distortion is introduced by the subdivision. In fact, in these two cases, the computed forces should be equal, since the flow velocities and the body velocities are the same. The only difference is the area, or volume, on which the force acts, which should sum up exactly.

The results obtained by varying the procedure of cylinder subdivision are compared, for one test with two side obstacles, in Fig. 5.46. In the figure, the outcome of the standard adopted procedure (named as T0_simulated, with the cylinder divided in 4 parts and the forces computed in 4 different points) is reported, too.

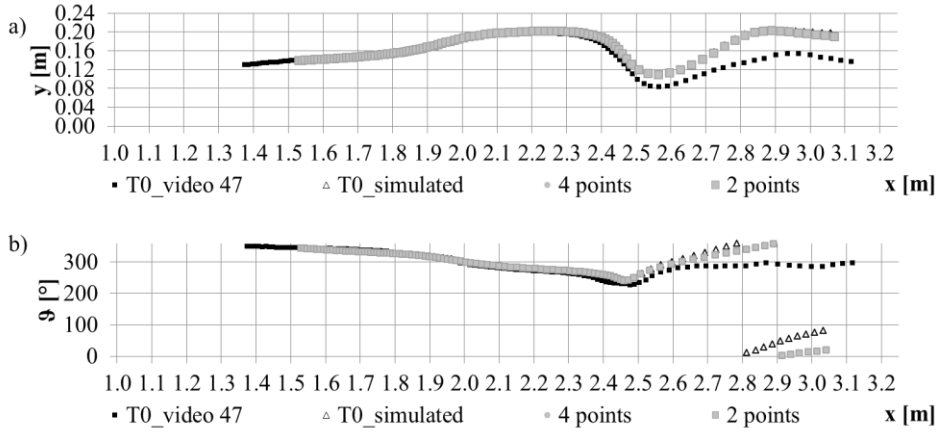

Figure 5.46 Comparison of the experimental and simulated trajectory (a) and angle as a function of the *x* displacement (b). Empty triangles show standard simulation outcome, solid grey triangles show the results for 4 points positioned at *±0.25L* and solid grey squares show the results obtained with 2 points positioned at *±0.25L*.

The results show that the trajectory and the angle computed with 2 or 4 points at ±0.25L overlap perfectly. This confirms that the number of

points for which forces are computed do not introduces mistakes, and validate the adopted procedure.

When comparing the results obtained with the subdivision in 2 parts and in 4 parts, some differences are observed. The orientation computed for the two-parts subdivision differs slightly from the original simulation, especially in the final part, presenting a smoother variation at least in the considered case. This is probably due to the smaller velocity gradient on the body, since a shorter part is considered (the two points are nearer to the body mass centre). On the contrary, the trajectory appears to overlap for both the subdivision procedures.

This test shows that the subdivision procedure does not introduce distortions in the computation of the forces acting on the body, and that the number of points considered does not affect evidently the outcome of the simulations.

5.5.5. Effect of obstacles representation

The effect of the mesh on the flow computation, and thus on the rigid body motion, is analysed by comparing results obtained with the same geometry but with different ways to schematize the side obstacles. As an example, for the case of two side obstacles, Fig. 5.47 show the alternative approach tested. In Fig. 5.47a the obstacles are excluded from the mesh, which means that the flow (and the cylinders) encounter a solid wall and are deviated.

In the second case (5.47b) the obstacles are included in the mesh, and their effect is modelled by varying the Manning coefficient locally (the cells inside the obstacles are represented with a different colour with respect to the channel bottom). The value of the Manning coefficient is set equal to 10 s $m^{-1/3}$ to provide a good reproduction of the velocity measured in the channel.

A third option is to represent obstacles as if the domain was 3D, by increasing the cells vertical height (Fig. 5.47c). In this way, nearly vertical cells surround the obstacle area, and the flow is computed only if the water level surmounts the obstacle cells.

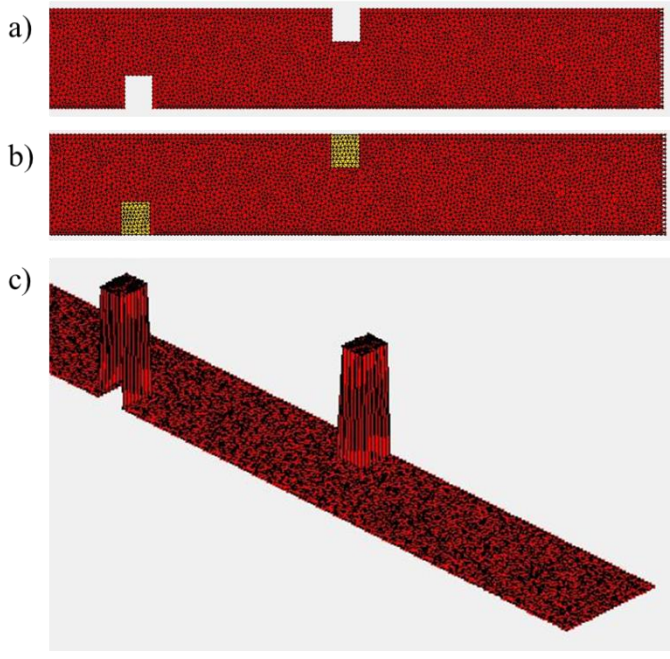

Figure 5.47 Detail of the mesh for the case of two side obstacles. a) The obstacles are excluded from the mesh; b) obstacles are included and are modelled with a high Manning coefficient; c) the obstacles have higher elevation than the channel bottom.

The flow velocity obtained with the 3 configurations is compared with the velocity measured during the experiments. This comparison helps in detecting the effect of the different representation of side obstacles.

The sections where flow velocity is measured are shown in Fig. 5.48 (same points as in Fig. 5.19b).

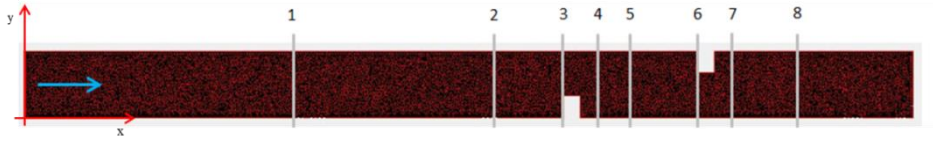

Figure 5.48 Planar view of the channel, with flow direction (blue arrow) and the section where velocity is measured.

In Fig. 5.49 the plots of the streamwise component of velocity are displayed, while in Fig. 5.50 the results for transversal velocity are shown.

The results for the streamwise velocity are very similar for the three different methods, with some differences for the method based on an increased value of the Manning coefficient (B) in sections 1 and 2, where velocity is slightly higher, and in sections 7 and 8, where the velocity is slightly lower.

The biggest differences in the simulated velocities appear in sections 3, 4 and 7 (near the right bank, y = 0.0 m), but a good agreement is generally observed, also in the reproduction of the negative velocity values in the section just downstream of the side obstacles, where recirculation occurs.

As for the transversal component of velocity, in some sections they simulated values are markedly different from the measured ones. In sections 3 and 4 much lower values are computed; in section 5, where the computed velocity is negative, the measured one is positive while in section 8 the computed values are higher. Furthermore, the method b shows lower values in the two final sections than the methods based on boundary conditions (a) or on mesh elevation (c).

Obstacle representation method	Right side	Channel axis	Left side
a	0.753	0.941	0.648
b	**0.767**	**0.952**	**0.941**
c	0.755	0.941	0.700

Table 5.8 Comparison of the determination coefficients for the streamwise component of velocity, u_f, for the three methods. The bold character indicates the best values.

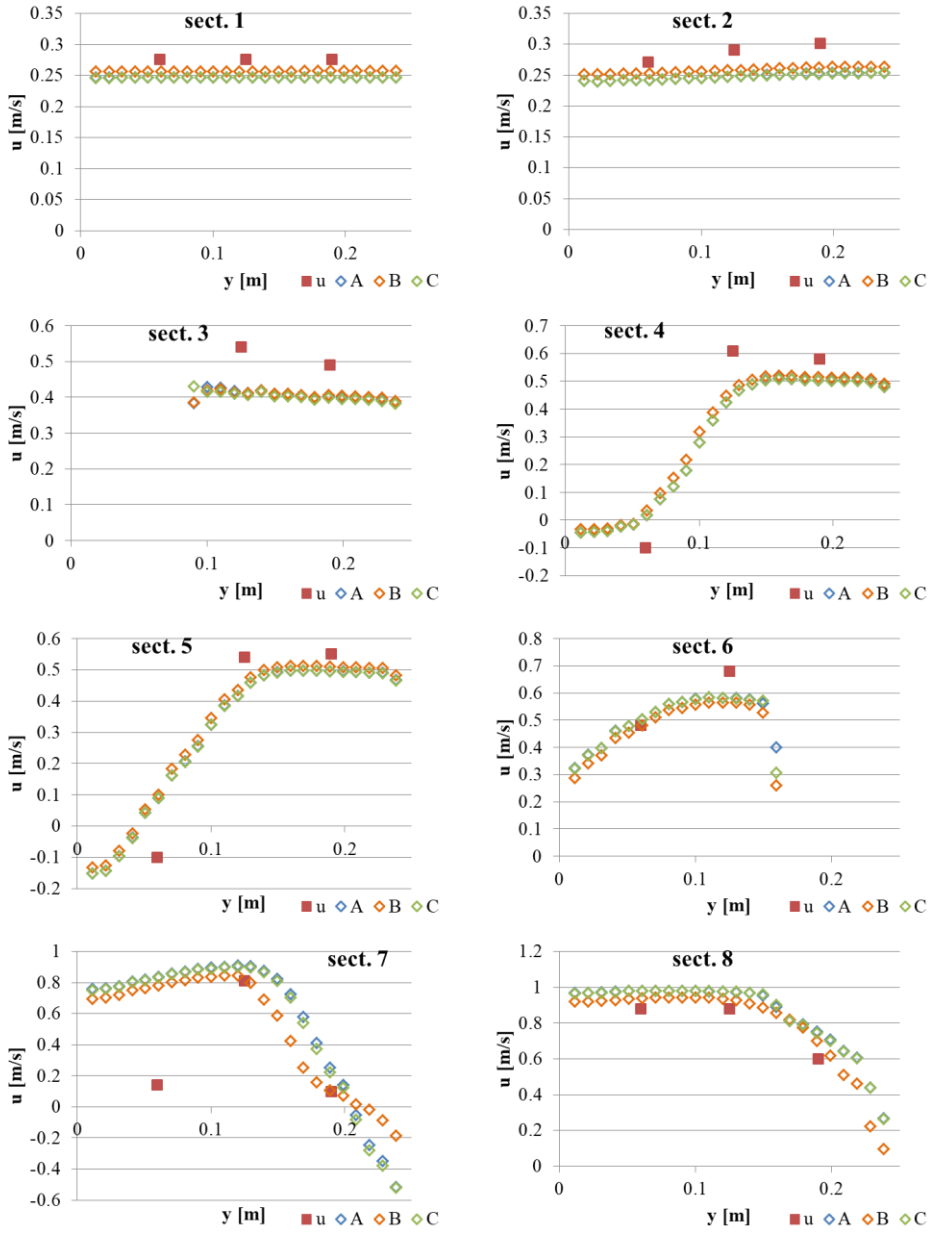

Figure 5.49 Comparison of the streamwise component of velocity for each section. Red squares (*u)* refer to measured values while diamonds refer to the different way to represent obstacles: A: no mesh; B: high Manning coefficient; C: higher elevation.

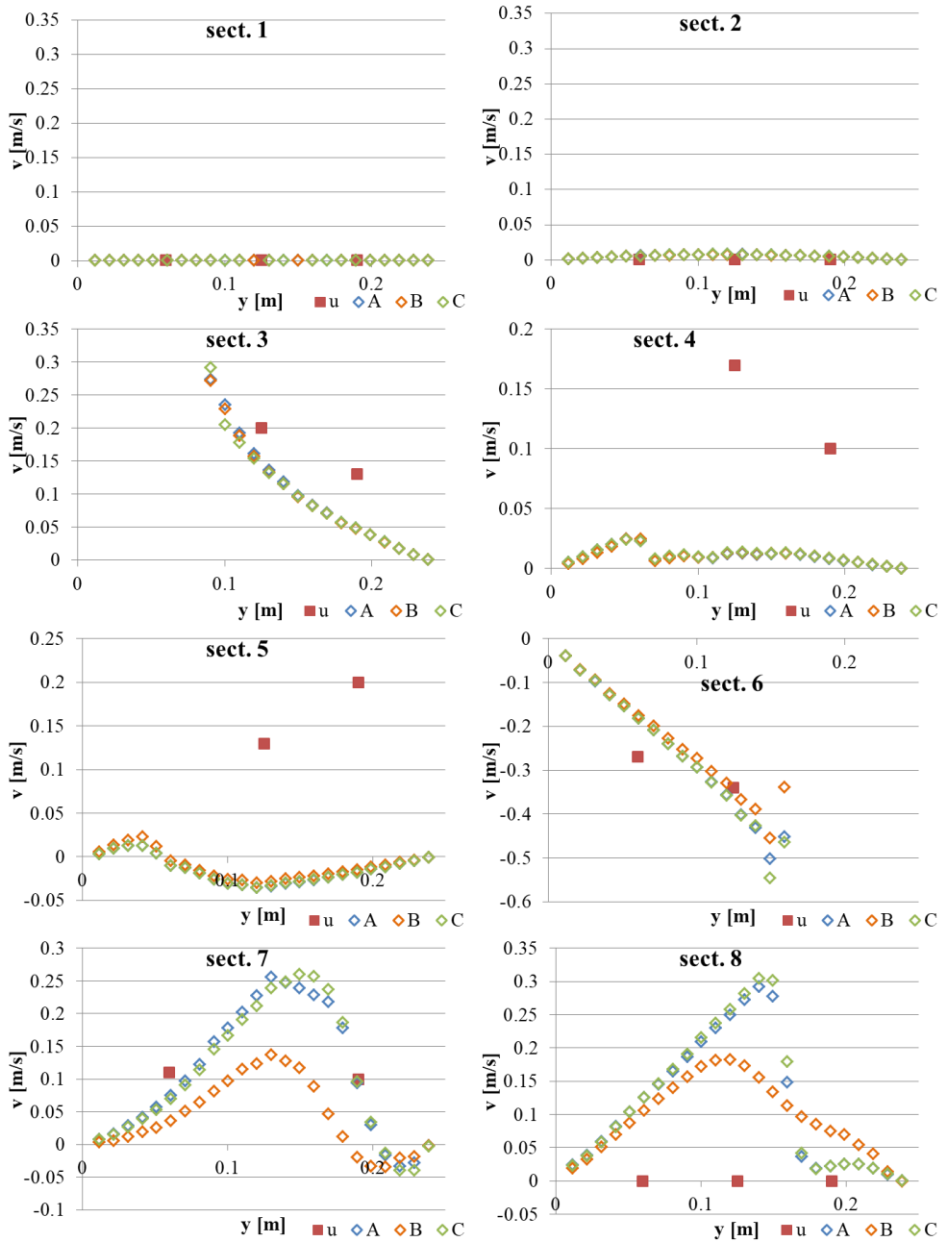

Figure 5.50 Comparison of the transversal component of velocity for each section. Red squares (*u)* refer to measured values while diamonds refer to the different way to represent obstacles: A: no mesh; B: high Manning coefficient; C: higher elevation.

Obstacle representation method	Right side	Channel axis	Left side
a	0.882	0.919	0.105
b	0.859	0.920	-0.312
c	**0.886**	**0.922**	**0.190**

Table 5.9 Comparison of the determination coefficients for the transversal component of velocity, v_f, for the three methods. The bold character indicates the best values.

The determination coefficient, computed for the longitudinal sections set in y = 0.06 m, y = 0.12 m and y = 0.24 m are shown for the three methods in Tables 5.8 and 5.9, for the longitudinal and transversal velocity, respectively.

This comparison shows that method b provides the best correlation with measured longitudinal velocities, while for the transverse one the best correlation is obtained with method c. On overall, all the methods present worst results for the transversal velocity, especially in sections 3, 4, 5 and 8. The lower value of the correlation coefficient in the left section for method b can be traced back to the results shown in sections 7 and 8, where the velocity distribution differs strongly from that obtained with methods a and c.

By representing the velocity field, it is possible to locate and analyse more precisely the differences yielded by the different obstacle representations. In Fig. 5.51 the velocity vectors for each method are shown.

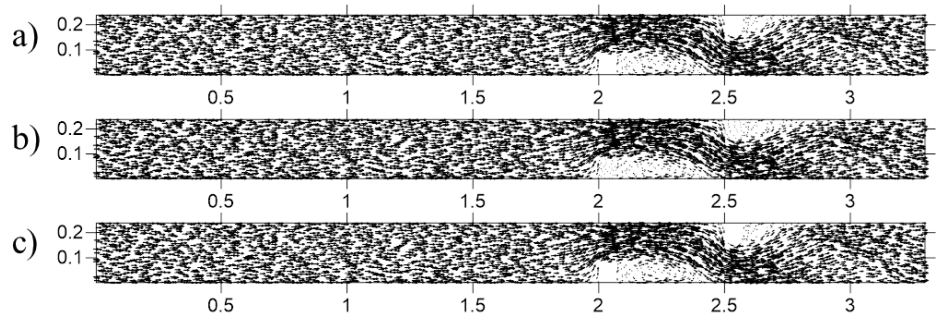

Figure 5.51 Velocity vectors for the three different methods to represent the side obstacles.

Note that the Manning coefficient for the obstacles in configuration b has been selected to reproduce qualitatively the recirculation area downstream of the obstacles. The three vector maps appear to be similar, albeit some differences occur near the obstacles and in the length of the recirculation areas. Fig. 5.52 and 5.53 show the contour maps with the streamwise and transversal components, which are shown separately to highlight the characteristics of each method.

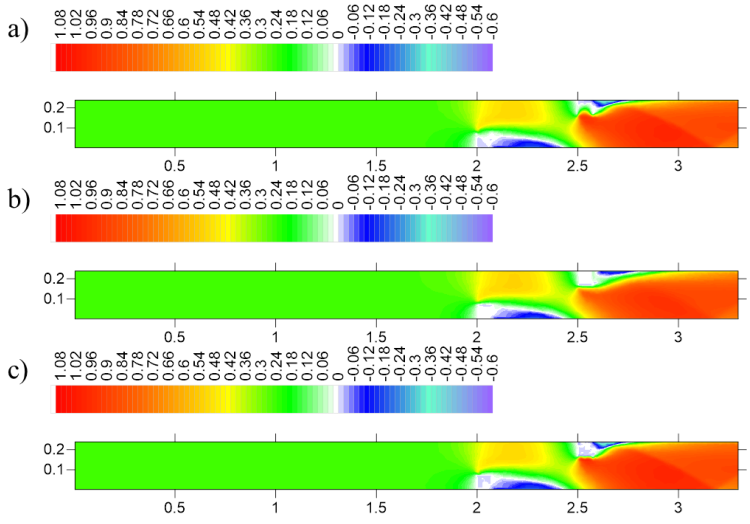

Figure 5.52 Streamwise component of velocity, u [m s^{-1}], for the three different representation methods of the side obstacles.

As regards the streamwise component of velocity, methods a and c yield more similar results, while some differences appear for method b, which presents a smoother transition of velocity in the area between the two obstacles and in the final part, with a larger recirculation tail downstream of the second obstacle.

Also for the transversal component, the first and third yield more similar values, reaching higher velocities than those obtained with method b. As for the streamwise component, the latter shows a smoother transition than the other two.

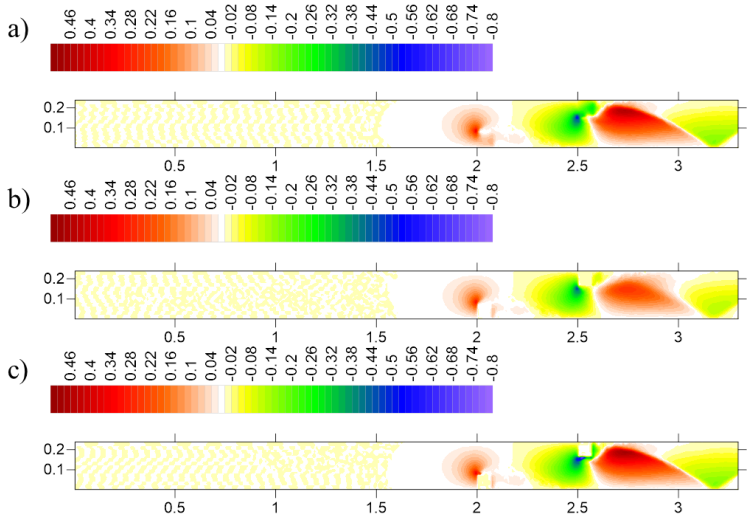

Figure 5.53 Transversal component of velocity, v [m s^{-1}], for the three different representation methods of the side obstacles.

To verify to which extent the effects of the different representations of the obstacles reverberate on the body transport, the experiment T0 is simulated with all three methods. The results are shown in Fig. 5.54, where a visual comparison of the log displacement is also presented. The black lines represent the cylinder axis in the experiment, while the blue lines are the axis of the simulated cylinders.

The small differences highlighted in the flow simulation determine differences in the trajectory and orientation of the transported body , mostly in the downstream reach of the channel. Once again, representing the obstacles with a higher elevation or with wall boundaries (methods c and c) yield very similar results, showing a collision around x = 2.70 m which did not occur in the experiment. The method b based on a higher Manning coefficient provides more accurate results, since no collision occurs, and the alignment of the experimental and simulated cylinder is maintained even in the final part.

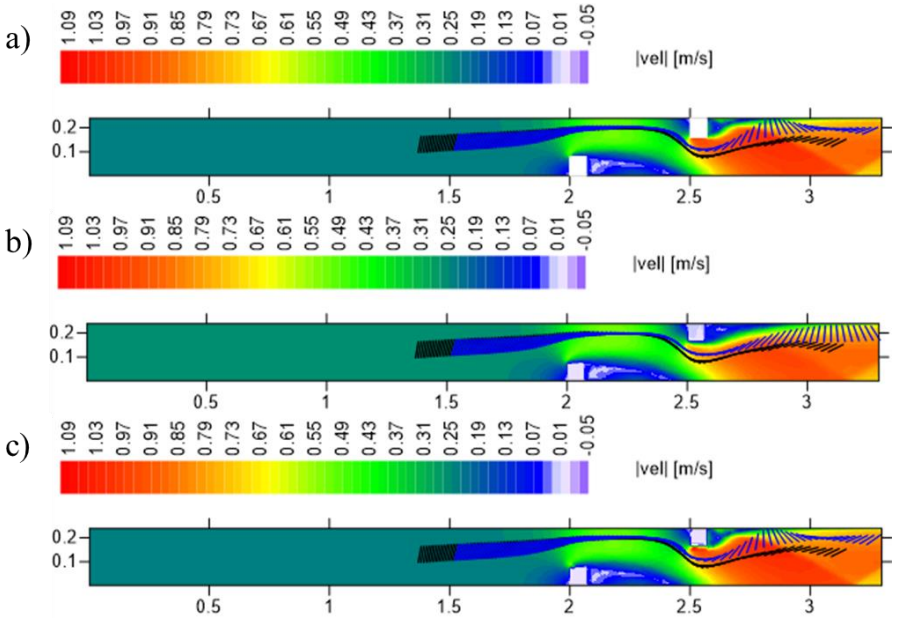

Figure 5.54 Motion of cylinder during experiment T0, with two side obstacles represented as boundary walls (a), with higher Manning coefficient (b) and with higher elevation (c). Black lines represent the experimental cylinder location, black lines show the simulated trajectory.

The determination coefficients for the considered experiment are shown in Tab. 5.10. The technique that provides the best results, at least for the considered experiment, is the representation of the obstacles as cells with higher resistance to the flow.

Obstacles representation	***x***	***y***	***ϑ***
a	100%	67%	79%
b	**100%**	**69%**	**87%**
c	100%	66%	77%

Table 5.10 Comparison of the percentage of data in the confidence interval for different way to represent obstacles in the domain.

However, the difference in the percentages is small, and should be verified over the entire set of experiments, or at least with one configuration. Furthermore, the roughness of the obstacle in the test simulation has been calibrated in order to adjust the velocity simulated by method b to the measured values. This procedure is totally dependent on the availability

of information about measured flow velocity, a condition which is not always easily satisfied, especially in field applications.

5.6. Simulating semi-congested transport

Few tests were realized by releasing all the cylindrical samples prepared for the experimental campaign, thus mixing standard cylinders and cylinders with a heavier ends due to presence of a spike (on overall, 18 cylinders). The experiments were performed with two side obstacles in the channel.

The releasing of a large number of bodies on the water surface is problematic: it is not possible to release each single element because they would flow rapidly away, not interacting with each other. Furthermore, any attempts to place the samples upstream a vertical barrier highlighted the tendency of the bodies to sink, creating a 3D distribution on the barrier and passing under its lower side. The cylinders were then placed in a metallic net which was slowly sunk in the flow, maintaining all the bodies parallel to the water surface, and then removed in order to obtain a planar release of all the bodies. Clearly, this process interferes with the flow, and for this reason the initial condition for the simulation were set at the instant when the cylinders were located approximately 0.50 m downstream of the releasing point.

Performing these experiments was fundamental in order to obtain at least one collision between cylinders, to give an indication for the calibration of the restitution coefficient. Furthermore, data to realize the simulation of the interaction of large number of logs were collected.

5.6.1. Restitution coefficient calibration

The implemented collision model needs the calibration of the restitution coefficient, for the specific conditions considered in the simulation, i.e.

the collision of bodies floating on the water surface and surrounded by water.

The calibration is performed by considering one experiment with three cylinders and two sequential collision, which involve only two logs at a time. The first collision occurs at around 0.3 s from the initial time, and the second around 1.39 s. Figure 5.55 and 5.56 show the cylinder configuration before, during and after the collision.

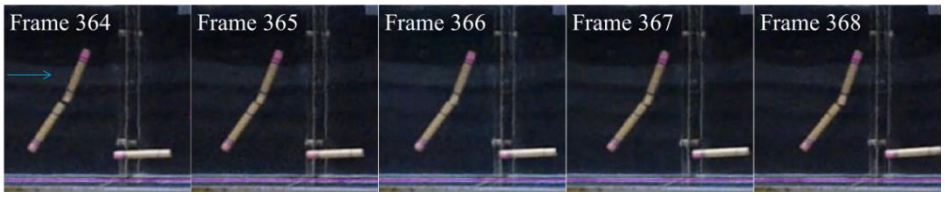

Figure 5.55 Frame sequence with the first collision, which occurs in frame 366, when the distance among the ends of the cylinders is smaller. The blue arrow shows the flow direction.

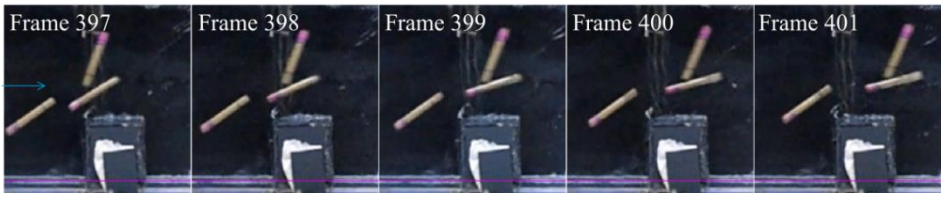

Figure 5.56 Frame sequence with the second collision, which occurs in frame 399. The blue arrow shows the flow direction.

Figure 5.57 shows the results obtained with values ranging from $e = 1$, corresponding to an elastic collision, to $e = 0.1$, compared with the experimental results.

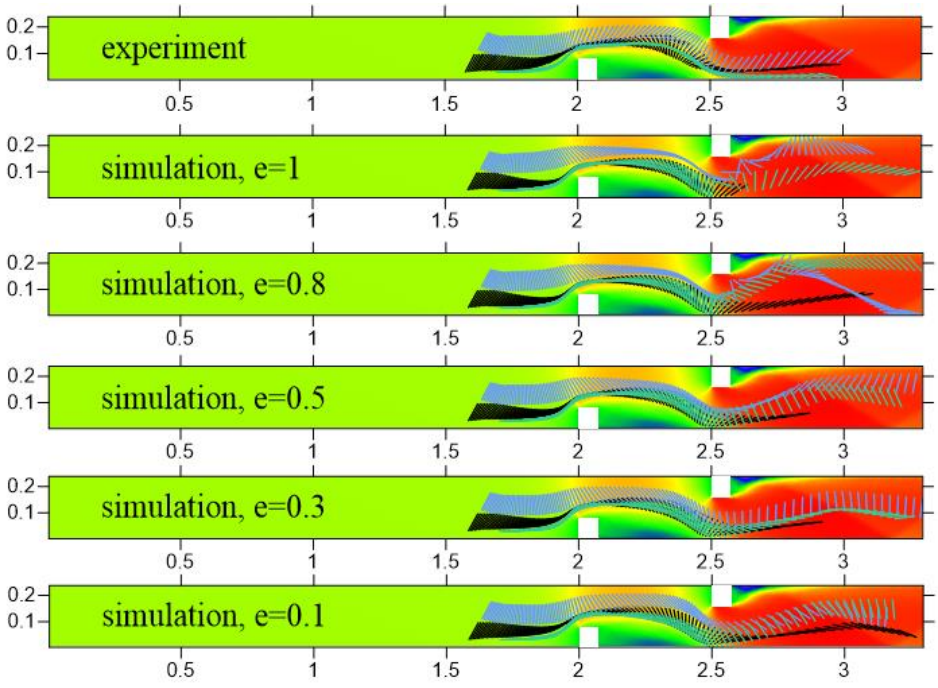

Figure 5.57 Planar view of the channel with the trajectories of colliding logs: experimental data and outcome of simulation with different values of the restitution coefficient, *e*.

Results obtained with elastic coefficient totally diverge from the expected outcome. The two colliding logs (black and light blue lines) separates too quickly, and the trajectories and orientation are totally modified.

By reducing the coefficient, the separation of the two cylinders involved in the first collision is reduced, too. The best approximation is obtained for *e=0.1*, so for an almost inelastic collision. As expected, the effect of the water surrounding the bodies influences the impact outcome, strongly damping collisions and reducing the variation of the bodies final velocities.

In the simulation with *e=0.1*, the two collisions occur around 0.3 s and 1.42 s, almost simultaneously to the real event collisions. However, the simulated trajectories and orientation with *e=0.1*, do not overlap exactly with the experimental data. In particular, the orientation of two cylinders (represented in Fig. 5.57 by the green and the blue lines) are incorrect, as

well as the final part of the trajectories. The detailed analysis of the correlation among the experimental and simulated trajectories are shown in Figs. 5.58 to 5.60.

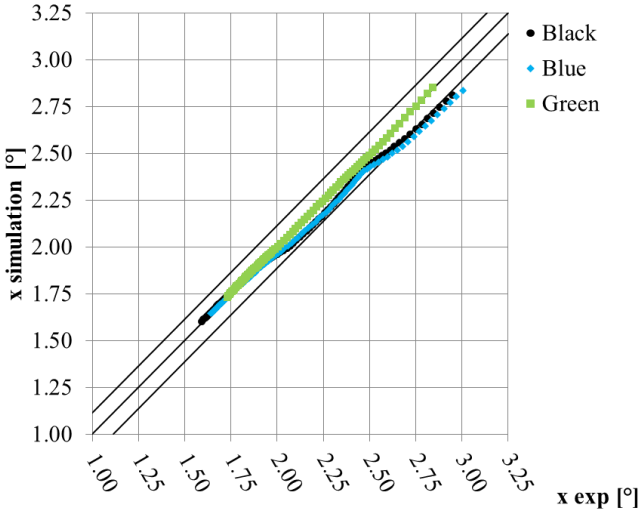

Figure 5.58 Correlation among experimental and simulated *x* coordinates for the three cylinders. The colours and the legend names refer to the colour-code in Fig. 5.57.

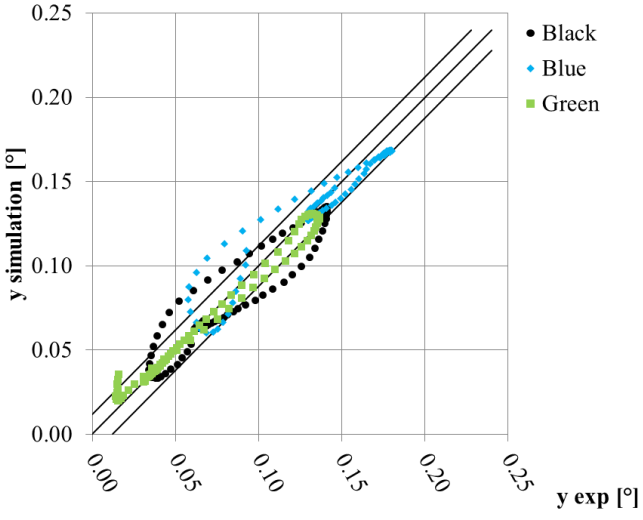

Figure 5.59 Correlation among experimental and simulated *y* coordinates for the three cylinders. The colours and the legend names refer to the colour-code in Fig. 5.57.

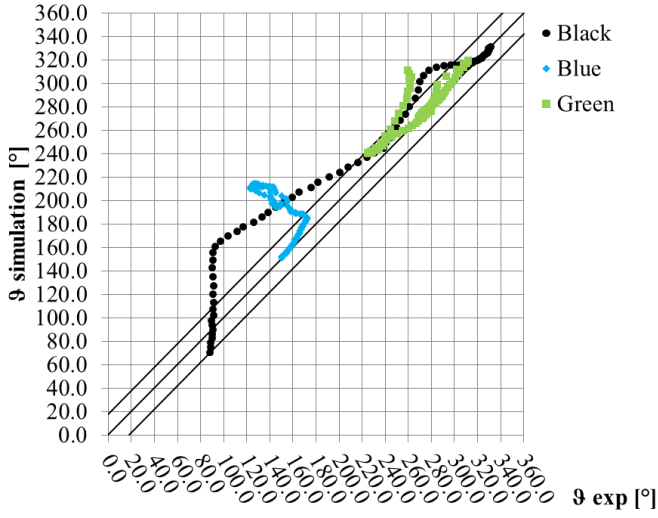

Figure 5.60 Correlation among experimental and simulated orientation for the three cylinders. The colours and the legend name refer to the colour-code in Fig. 5.57.

The percentage of occurrences inside the confidence interval for the linear displacement are in line with what observed for the experiments with single elements (92% in x and 82% in y), while lower accuracy is observed for the orientation. Only 63% of occurrences lies inside the confidence range, while for single element transport this value was slightly higher (above 70%, see Tab. 5.7).

The differences between the simulated and the observed trajectories may occur for two reasons, one connected to the presence of multiple logs, and the other to the collision model. Even if few cylinders are considered, they affect the local flow velocity distribution and, since the bodies are near, they are subject to the modified flow field. This alterations are not included in the one-way coupled simulation, which considers the undisturbed flow velocity to compute forces even when cylinders are near each other.

On the other end, the collision model here implemented neglects the friction among bodies and it was not developed by taking into account the

presence of fluid around the body. It is possible that these limitations introduce some inaccuracies in reproducing the body motion.

5.6.2. Qualitative results for semi-congested transport

Due to the uncertainties in realizing experiments with many logs and in modelling their motion, as highlighted in the previous paragraph, the simulation of semi-congested transport has only a qualitative meaning. It is nevertheless performed since it may help in identifying how to improve the simulation, and to check how the model behaves in presence of more than one sample.

One video with 18 cylinders and two rectangular side obstacles in then modelled. The initial location of the samples is shown in Fig. 5.61.

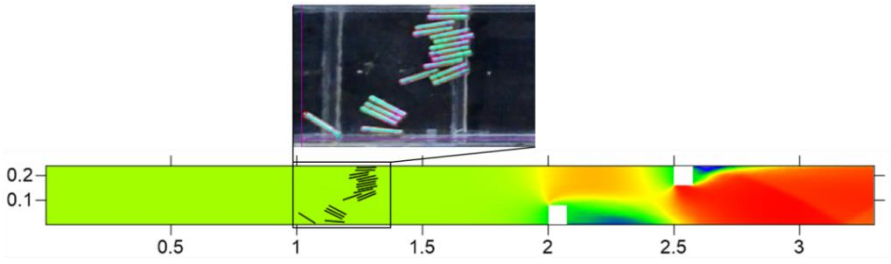

Figure 5.61 Initial position and orientation of the 18 cylinders. The values in the simulation are compared with a detail from the video.

The outcome of the simulation, which is performed with the same discharge and parameters used for the experiments with one single cylinder, is compared with the images extracted from the video. Results are compared with a time step of 1 s, which allows to evaluate the overall trend of the trajectories and orientation.

The images show that the simulation does not exactly reproduce the trajectories and orientation of each cylinder. In particular, the interaction among some cylinders (e.g. Fig. 5.62, highlighted in red) provokes a variation in their positioning even at earlier times.

However, differences are not attributable only to some inaccuracies in the simulation. For example, the cylinder highlighted in Fig. 5.63 has a peculiar behaviour, which cannot be reproduced in the simulation. In fact, it starts floating near the wall, and when encounters an irregularity on the wall (due to the junction of the Plexiglass modules), it stops, starts rotating and moves toward the mid-channel. This is the blue cylinder which was involved in the collision described in the previous paragraph.

Since the domain in the simulation does not present any wall discontinuities, the log keeps on floating and its trajectory is totally modified, as well as that of the other cylinders: the collision previously examined cannot occur and other cylinders, which in the simulation have no contact with this element, may be affected by its presence.

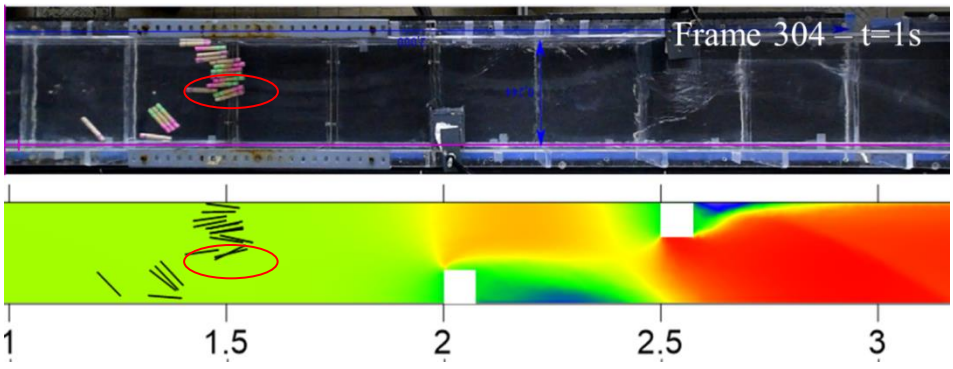

Figure 5.62 Experimental and simulated distribution of the cylinders after 1s from the initial time. Flow from the right.

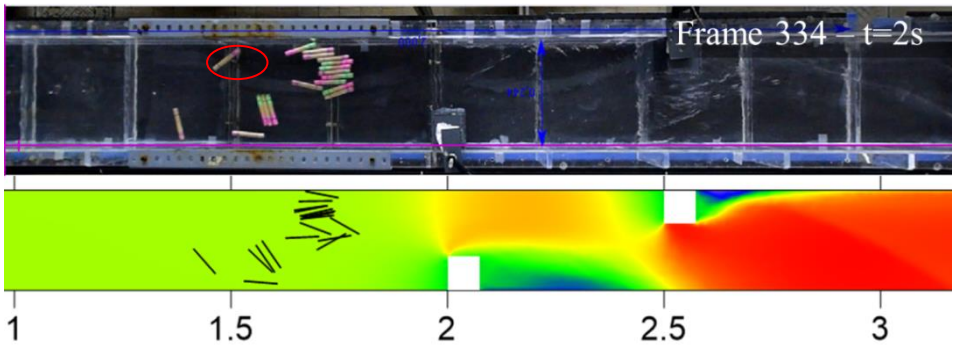

Figure 5.63 Experimental and simulated distribution of the cylinders after 2s from the initial time. Flow from the right.

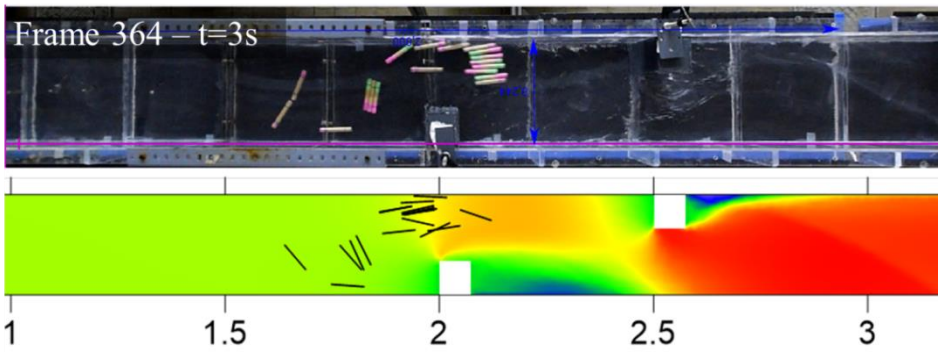

Figure 5.64 Experimental and simulated distribution of the cylinders after 3s from the initial time. Flow from the right.

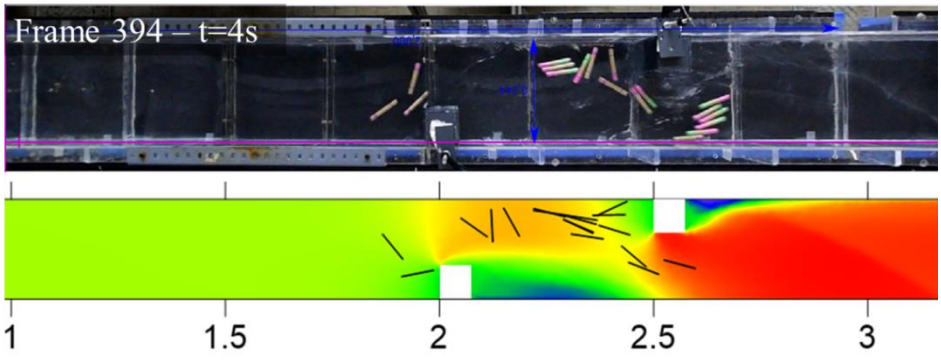

Figure 5.65 Experimental and simulated distribution of the cylinders after 4s from the initial time. Flow from the right.

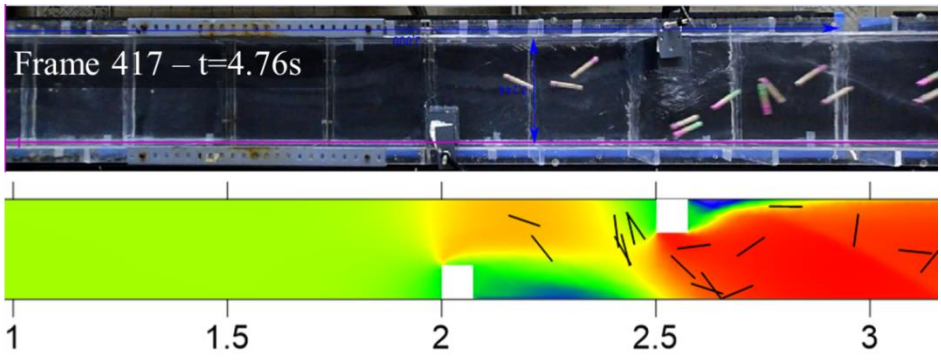

Figure 5.66 Experimental and simulated distribution of the cylinders after 4.76s from the initial time. Flow from the right.

The interactions among very near cylinders is not completely satisfactory. In the experiment, they tend to remain near each other and groups of two or more logs are observed until t=4s (Fig. 5.65). On the contrary, in the

simulation they divide more rapidly, probably due to an overestimation of the consequences of collisions and/or to the hypothesis of negligible frictional effects during the collision. Small groups are observed at t=3s, Fig. 5.64, but then each element tends to flow separately.

On overall, the transport of the entire group of cylinders is replicated with a certain accuracy. A positive aspect is that, at different times, the cylinders in the simulation occupy similar areas of the channel as those occupied by real logs. This is an important aspect, because the tendency of the floating elements to diffuse on the water surface may change the interaction with inline structures. Large groups of elements close to one another are easily involved in jam formation, due to the higher number of interactions, while isolated bodies can flow away more easily. Being able to reproduce their diffusive behaviour is a step towards the inclusion of the floating cylinder effect in the hydraulic risk assessment.

Chapter 6
Model application to the Rienz river

6.1. Abstract

As previously described, the calibration of the model and its first application were performed on laboratory experiments, to verify if the formulation is able to simulate floating bodies transport under controlled conditions. To assess the model reliability also in real condition, its application to a real-scale case is carried out.

Taking advantage of an experimental campaign realized by researchers of the University of Bolzano, the model is applied to reproduce the logs transport in a reach of the Rienz river. The displacement of cylindrical logs during a high flow event was monitored. It is therefore computed and the results are compared with the data surveyed during the experimental campaign.

It is found that particular attention needs to be paid to the interaction with large boulders located in the riverbed, in order to assess if they are able to stop the displacement of cylinders also in the numerical modelling, as it happens in real conditions.

6.2. Experiment on wood transport along the Rienz river

The Rienz river is located in Trentino Alto Adige, in the province of Bolzano, and is a tributary of the Adige river. The possibility of wood transport in its basin is well known since the XIX century and defence structures have been built just upstream of the city of Brunico (Comiti 2012, Fig. 6.1) to stop the logs before they can reach the urban area. The area has also been involved in the study of integrated management of sediment and large wood within the European project SedAlp, which aimed at developing strategies to reduce the sediment-related risks in the alpine area.

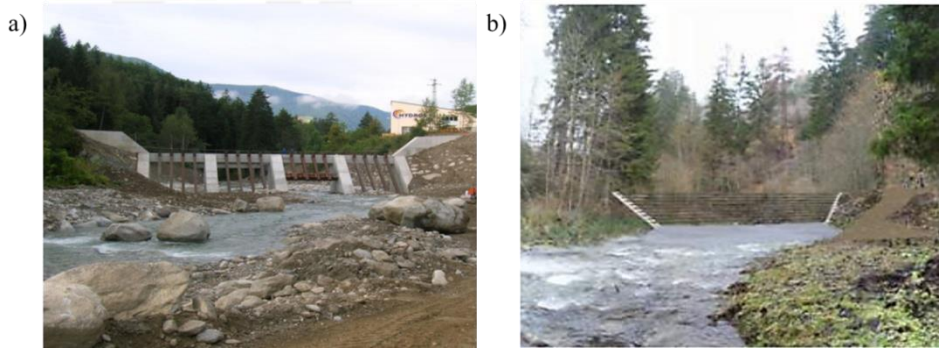

Figure 6.1 Retention structures installed in the Rienz river, upstream Brunico. a) Check dam; b) rope net. Pictures from Lenzi et al. 2013.

Within this river basin, several studies on wood transport were carried out by researchers of the University of Bolzano, who performed a field experiment to monitor the motion of wooden elements (Lucía et al. 2015). By placing over 100 logs in, or nearby, the stream, they periodically monitored the displacement of wooden samples in the period from June 2012 to November 2014, in order evaluate their motion. Since the water levels were regularly measured in the section upstream of the area interested by the experiments, a relation between water levels and log motion could be inferred.

The area chosen for the experiment is located between the village of Valdaora di Sotto and Brunico. However, to simulate log transport with ORSA2D_WT, only the initial part of the study area is considered. In Fig. 6.2, S1 is the section where hydraulic measurements are performed and S2 is the final section considered in the numerical model.

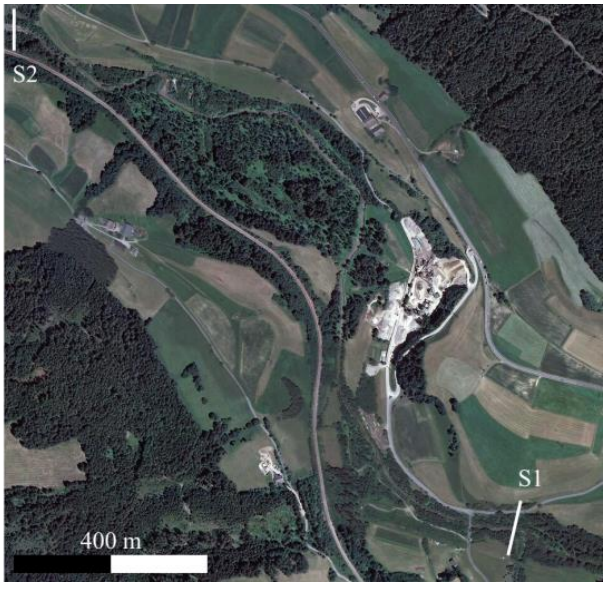

Figure 6.2 Detail of the reach of the Rienz river interested by the experiments on log transport and considered for the numerical model. S1 is the section where the pressure transducer is located, S2 is the final section of the reach.

6.2.1. Topographic data

For the numerical modelling of wood transport in the Rienz river, the study area is reduced to that shown in Fig. 6.2. This area was selected because it is quite regular, presenting an average slope of 0.9% and a width that varies from 7.00 m to 12.00 m.

The DTM of the entire study area, with a resolution of 2.50 m, was provided by the Province of Bolzano. To improve the data resolution in the channel and measure the exact bottom elevation (the DTM refers only to the water level elevation since it cannot detect the bed surface across the water) specific field surveys were performed. In the first one, carried out

by researches of the University of Bolzano, 9 sections were measured in the area of interest (Fig. 6.3), in addition to the section where the pressure transducer is located. Each section is representative of a corresponding sub-reach, based on the channel characteristics, such as width, bottom regularity and material dimensions.

At a later time, in April 2015, a detailed survey was performed by the Author together with A. Lucía and A. Andreoli of the University of Bolzano, to get accurate information about the channel bottom elevation and the distribution of boulders and steps along the stream. During the field survey a total length of about 800 m was mapped using total station (TS) and GPS. The TS survey covered the central part of the reach, which is more regular and thus suitable to the first application of the model on a real scale, and where major wood transport was observed.

The GPS survey was carried out to accurately describe the sections where boundary conditions are assigned in the numerical model and to obtain TS bases (covering up to 1km of the reach length).

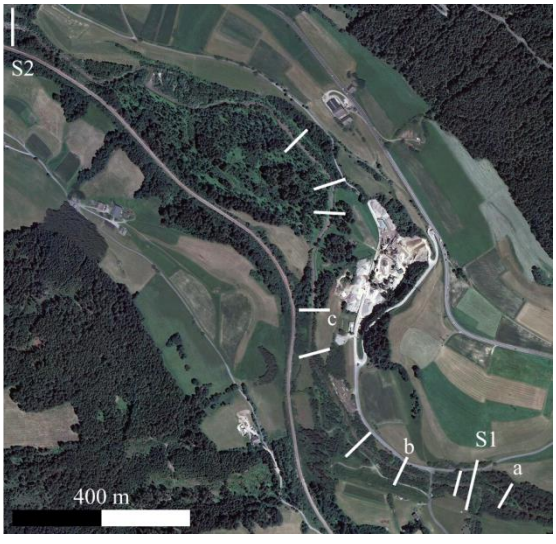

Figure 6.3 Detail of the reach of the Rienz river were wood transport is modelled. S1 is the section where the pressure transducer is located, S2 is the final section of the reach. The other white lines show the sections measured by Comiti and Lucía. Sections a, b and c refer to the placement of wooden cylinders.

Particular attention was paid to measure those elements which are relevant to wood deposition, like boulders, bars and ripples. For each boulder, 4 to 6 points were surveyed to provide information about their location, height and dimension, while bars and ripples were located by surveying their outer limits and some mid points (Fig. 6.4). The DTM was then integrated with the additional points and elevations, resulting in a detailed point cloud which was used to define the topographical domain for the model application.

Information about channel roughness was also provided for each surveyed section by researchers of the University of Bolzano, who followed the method by Thorne and Zevenbergen (1985). It was found that the value of d_{84} (i.e. the grain dimension equal or higher than the size of the 84% of the bed material) ranges between 360 mm and 680 mm, allowing one to identify areas with uniform roughness, as it will be shown in the paragraph about the numerical computation.

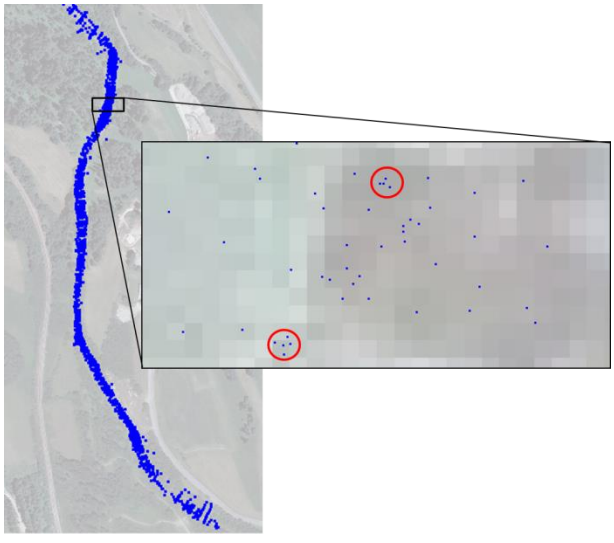

Figure 6.4 TS and GPS surveyed point. The detail shows the points recorded for two boulders: the inner point is the boulder top, while the others show its perimeter.

6.2.2. Hydraulic data

The surface of the Rienz basin is about 640 km^2, evaluated at the section upstream Brunico. However, the discharge in the river is strongly dependant on the release from the dams of the hydroelectric plants which are located on the Rienz river – the Monguelfo dam, about 4 km upstream of section S1– and on the three tributaries which flow into the Rienz river between the dam and the upstream section S1 (Bruns, Furcia and Anterselva streams).

A pressure transducer was placed in section S1, to measure the water level for a period of over 2 years (June 2012-November 2014, Fig. 6.5). Unfortunately, there is a gap in level measurements for a period of 6 months, from November 2012 to April 2013, because of a problem with instrumentation. For some events, the discharge was also measured (Tab. 6.1).

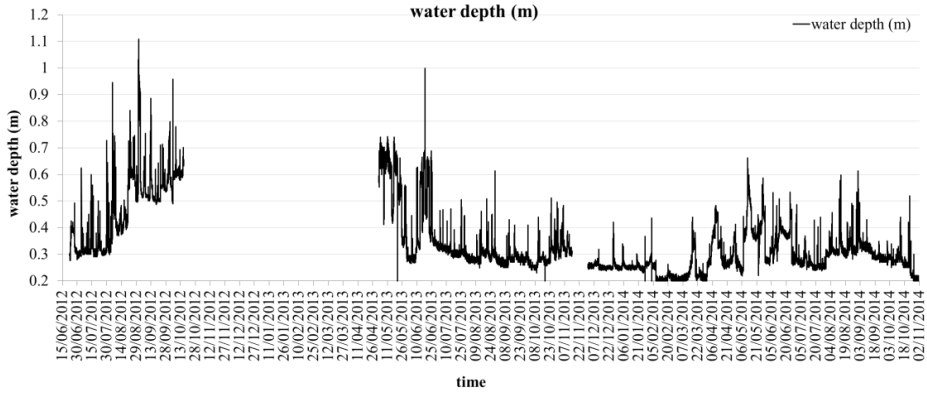

Figure 6.5 Water level measured at section S1. Missing data between November 2012 and April 2013 is due to a problem with the instrument.

Periodical measurement of the water level in the other sections of interest was also performed, in order to monitor the variation of the water height during the experimental period.

Date	h [m]	Q [$m^3 s^{-1}$]
22/07/2013	0.298	3.15
22/07/2013	0.302	3.33
22/07/2013	0.307	3.27
21/04/2014	0.256	2.98
21/08/2014	0.320	3.31
24/09/2014	0.248	2.63

Table 6.1 Measured discharge and levels measured (A. Lucía)

6.2.3. Data on wood transport

Data on wood transport were obtained by the experiment performed by the researchers of the University of Bolzano. The most relevant aspects for the simulation are here resumed.

In the area of interest, 41 logs were placed in different parts of the reach. In particular, 13 logs were located in the sub-reach of section *a*, 13 in the sub-reach of section *b* and 15 in the sub-reach of section *c* (see Fig. 6.3 for the location of the sections). Conifer and broad leaves trunks were cut to be cylindrical and without branches. Their length varies among 2.00 m and 10.50 m, the diameter is in the range 0.20 m–0.55 m. They were placed in the channel, or just outside it, parallel, perpendicular or with random orientation with reference to the local flow direction.

Their displacement was monitored by periodic field survey, during which all the useful information about logs motion were collected: the final position and orientation (parallel, perpendicular or oblique to the section), their inclusion in jams, the presence of anchor points and the overall distance travelled since the previous survey.

6.3. Numerical modelling of wood transport

The availability of topographic, hydraulic and wood displacement data allows one to apply the model to the simulation of wood transport events detected during the experimental campaign. From the data provided by

the A. Lucía, it can be seen that the major wood transport event in the considered area occurred between the surveys performed on June, 26th 2012 and July, 5th 2012. This time interval was therefore chosen to simulated the displacement of the logs along the reach of the Rienz river.

6.3.1. Domain discretization

The topographic information are provided as a point cloud which joints the DTM by the Province of Bolzano and the specific survey performed to get the detailed description of the bottom elevation.

Since the field observation showed that the presence of obstacles in the stream, such as large boulders, plays a fundamental role in stopping the logs displacement, a special accuracy was paid in representing these elements.

The domain is thus discretized with triangular cells with different average dimensions: in the outer parts of the domain, where the elevation is much higher than the riverbed, they have a dimension of 5.00 m; an intermediate area with cells of about 3.50 m side is then connected to the stream, where the discretization is kept around 2.50 m. In this part, the cell average side is equal to the DTM pace, while the elevation is adjusted taking into account the values measured with TS and GPS. To introduce boulders, a local refinement is performed around the point which represents the boulder top, with cell average sizes of about 1.20-1.50 m. Then, one point is lifted in order to represent the correct height of the stone, which is thus represented as a pyramidal solid with three or more faces depending on its dimensions. An example of how boulders are modelled in the mesh is shown in Fig. 6.6.

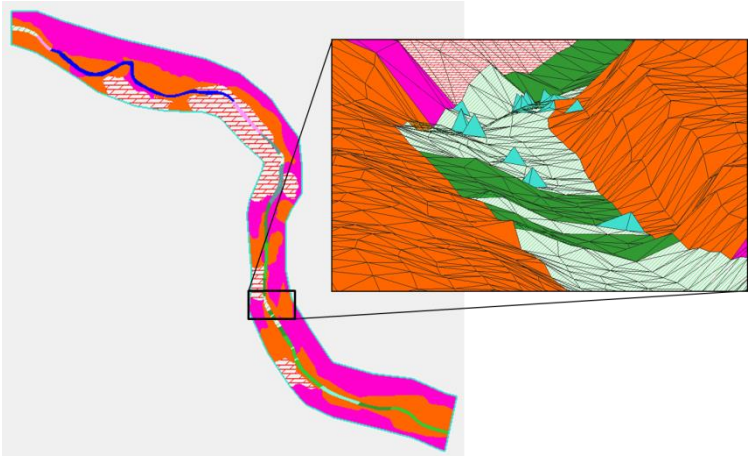

Figure 6.6 Planar view of the entire discretized domain and perspective view of a reach with boulders, which are represented by light blue pyramids. Other colours represent the variable roughness of the domain.

The different colours shown in Fig. 6.6 refer to the roughness assigned to the domain. Roughness is represented by the Manning coefficient, whose estimate is based on the material of the considered area. For the riverbed, the coefficient is selected following the procedure proposed by Cowan (1956) and, in detail, implementing the suggested base value, which varies between 0.03 and 0.07 s $m^{-1/3}$ for coarse cobbles and boulders according to the local grain size (the estimated value of d_{50} is always greater than 210 mm). The maximum value is assigned to the areas with boulders and to the cells representing each boulder, while a value of 0.045 s $m^{-1/3}$ is assigned to those reaches with a smaller grain size. For flood plains and outer forested areas, the values are selected according to Chow (1959): 0.04 s $m^{-1/3}$ for meadows and cultivated areas near the river, 0.07 s $m^{-1/3}$ for sparse forests and 0.08 s $m^{-1/3}$ for denser forested areas.

The areas are identified from the geo-referenced aerial view of the domain, and the result of the roughness assignment is shown in Fig. 6.6.

6.3.2. Hydraulic simulation

The hydraulic simulation during the period of interest is preliminarily performed in order to obtain the flow field which induces the wood transport.

The level variation, measured at the gauged section in the period June, 26th and July, 5th 2012 are presented shown in Fig. 6.7.

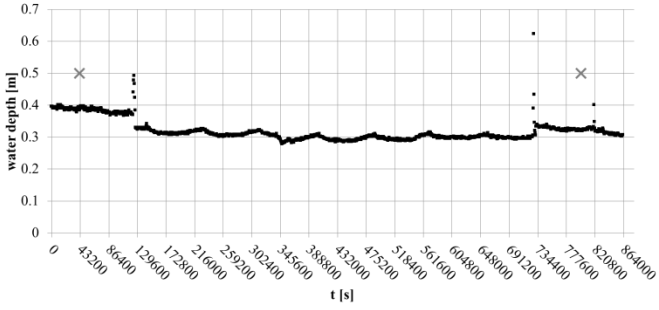

Figure 6.7 Water depth history in section S1 in the selected period. Initial time is set coincident with the 26/06/2012 00:00. The crosses show the days when the surveys were performed, on the 26th of June and on the 5th of July.

The level measured by the pressure transducer shows two peaks between the two field surveys (shown by a cross in the figure), which lasted a few hours each and occurred both in the morning (June, 27th at 10:30 and July, 4th at 10:40). No heavy rains were observed in the considered period on this part of the Rienz basin, nor on the tributaries, as shown, for example, by the daily rain data in Tab. 6.2 for the meteorological station of Rio Anterselva di Mezzo.

Date	Rain [mm]
26/06/2012	2.2
27/06/2012	0.0
08/06/2012	0.0
29/06/2012	1.5
30/06/2012	0.0
01/07/2012	0.0
02/07/2012	0.0
03/07/2012	0.8
04/07/2012	0.2
05/07/2012	0.6

Table 6.2 Rain data, provided by the Province of Bolzano.

The lack of rain and the short duration and regularity in time of the two peaks can be related to their artificial nature, since they were probably

caused by the periodical discharge of water from the outlet of Monguelfo dam for maintenance operations.

To compute the discharge in the channel, the rating curve for the Rienz river has to be estimated. Some data for the rating curve were provided by the A. Lucía, who measured the water discharge and the corresponding water levels for the dates, as shown in Tab. 6.1. However, since the data provided are very similar among each other (water level varied between 0.248 m and 0.320 m) and smaller than the maximum water level measured on July, 4th 2012, two additional events were considered, not related to their observations.

Heavy rain was observed on November, 5th and November 11th, 2012. For these dates, the researchers from Bolzano provided measures of the water level, obtained during the field surveys and not with the pressure transducer, since in that period it was not installed. An estimate of the discharge during these two events was obtained by summing the discharge of the Anterselva river and the environmental flows for the Rienz river and for the Bruns and Furcia streams. Data about the Anterselva river, which is the major tributary of the Rienz river in the reach of interest and the less regulated one, were provided by the Province of Bolzano. The environmental flows for the Rienz river and for the other tributaries were instead supplied by the hydro-power plants manager, EDISON S.r.l.

The resulting rating curve, obtained through a logarithmic interpolation among the available water levels and discharge values is:

$$Q = 4.24 \ln(h) + 8.47 \tag{6.1}$$

and is plot in Fig. 6.8, together with the maximum discharge calculated for the two maximum water levels observed in the period of interest for the simulation: 0.50 m on June, 27th and 0.62 m on July, 4th, which correspond to a maximum discharge of 5.53 m^3s^{-1} and of 6.44 m^3s^{-1}.

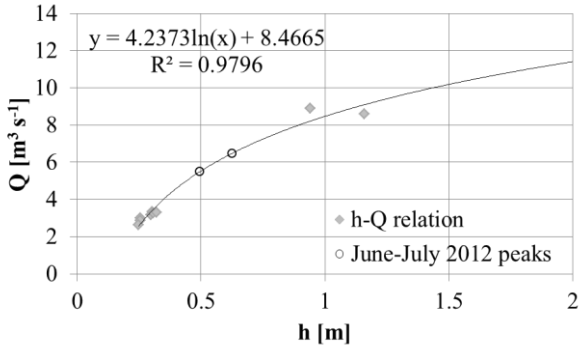

Figure 6.8 Rating curve for the Rienz river, in the area of interest. Solid diamonds show the relation among the measured water levels and the measured, or estimated, discharges; empty circles refer to the maximum discharge computed with the interpolated rating curve for the events considered in the numerical simulation.

Log transport is here studied with reference to the simulation of both the peaks observed in the period of interest. The hydrograph for the initial section of the domain (Fig. 6.9) is obtained by computing the discharge for each water level, measured by the pressure transducer, with the rating curve of Fig. 6.8. Intermediate values are obtained by linear interpolation. The simulation starts with a stationary condition, obtained with the constant discharge of 4.00 $m^3 s^{-1}$, in order to model the stationary water level observed before the peak. To avoid an excessive duration of the test, and since the logs should not be transported under steady conditions among the peaks, the two peaks are considered in sequence and the overall duration is 4.50h (16200s).

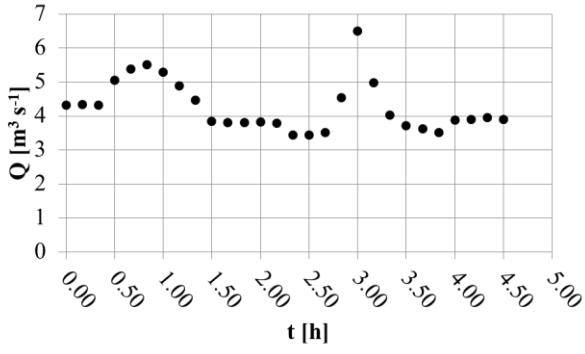

Figure 6.9 Hydrograph for the event of the selected period. The second peak, occurring on July, 4th, is translated in time (anticipated) in order to be consecutive to the first one.

Unfortunately, for the considered event the water level in each river section is not available, since the field survey and the measure of the water elevation were not performed on those days. To verify if the hydraulic simulation is correct and if the domain and the roughness values are in agreement with the real situation, the stationary level obtained with the constant discharge is compared with the water level measured during the field survey of July, 5th. In Fig. 6.10 the water level measured along the river axis is compared with the measures for each cross section. In Fig. 6.11, the comparison between the water elevation is shown.

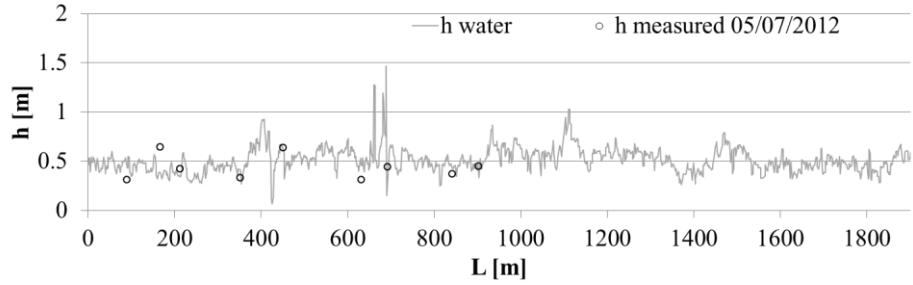

Figure 6.10 Comparison of simulated (grey line) and measured (empty circles) water levels.

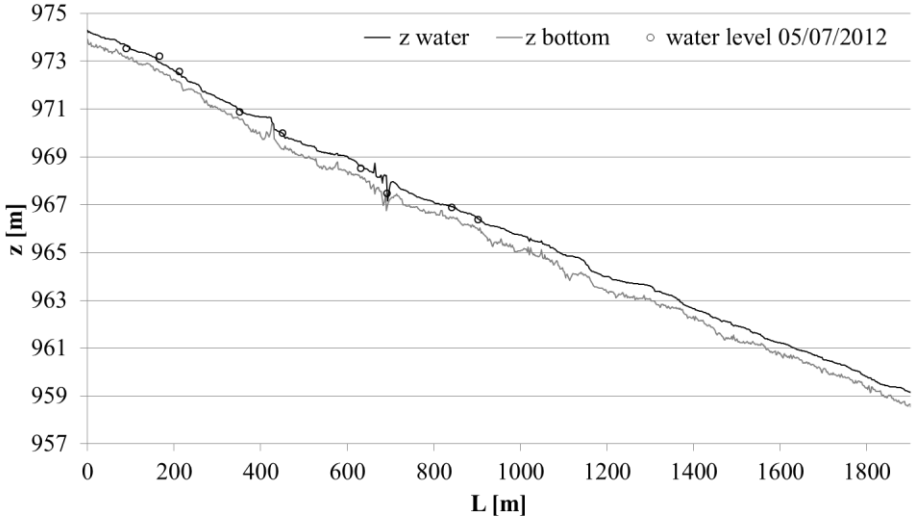

Figure 6.11 Comparison of simulated (black line) and measured (empty circles) water levels. The lower grey line is the channel bottom elevation.

The stationary discharge implemented is equal to 4.00 $m^3 s^{-1}$. The maximum difference observed in the water level is around 0.28 m, in the seventh measurement section indicated in Figs. 6.10 and 6.11, where a large variation of the water level occurs. In the other sections, the average difference is around 0.12 m.

The comparison among measured and simulated data has mainly a qualitative value, since some differences in the section location and geometry may influence the outcome of the simulation. However, overall, the simulated water levels are in good agreement with the surveyed ones.

6.3.3. Modelling wood transport

The survey that precedes the considered event is that of the 26th of July, when 35 logs were found along the reach of interest of the Rienz river. The logs are found in three main areas, as shown in Fig. 6.12. The log orientation in the simulation was assigned according to the information obtained from the survey; furthermore, for oblique logs, a random orientation was given following the pictures taken in the survey, since no details were provided about the real angle. Note that, as for channel experiments, the orientation refers to the general reference system, with 0° corresponding to the alignment of the log with the vertical axis shown in Fig. 6.12.

The characteristics of the logs (length, diameter, initial angle) as well as the location of their midpoint and their density are summarized in Appendix C.

Since wood density was not measured, its value has to be assigned based on theoretical hypothesis. Recent researches have shown that the density of instream wood is higher than the standard literature values (Ruiz-Villanueva et al. 2016). Acceptable values are set to 700 kg m^{-3} for conifers and 800 kg m^{-3} for broadleaves, the latter being heavier than the first one. This datum, however, should be accurately determined on the basis of the wood moisture, since wet elements present even higher densities

(e.g. Cadol and Wohl 2010; Merten et al. 2013). Since no detailed data are available, the possibility of inaccuracies due to a mistake in wood density have to be taken into account.

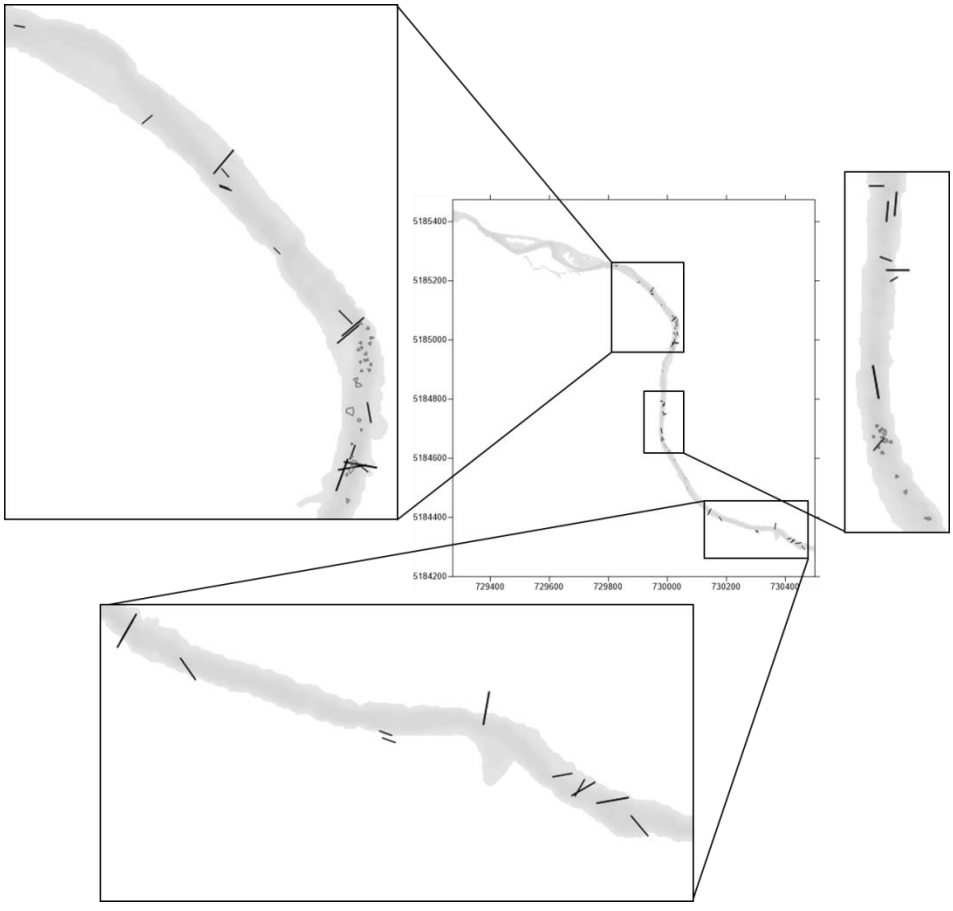

Figure 6.12 Initial location of the logs (black lines), derived from the data collected by the field survey on the 26/06/2012. The light grey area is the wetted area at the beginning of the simulation, dark grey spots mark the boulder positions, as they are represented in the mesh.

The logs are ideally positioned on the channel bottom: their elevation is computed as the sum of the elevation of the cell where the body centre is located and half of the diameter. Then, since the simulation starts from stationary conditions, i.e. with a non-zero water elevation, buoyancy is computed and, if the logs float, the position of their centre is set equal to the water level.

Thanks to the field survey realized on July, 5th 2012, it is possible to evaluate the displacement of the cylinders. In Tab. C.2, in Appendix C, the coordinates, displacement and the final orientation are reported.

Except for two elements (r1-01 and r4-06 I Appendix C), all the logs move. 9 logs move for a distance smaller than their length, while 2 of them (in italic in Tab C.2) go beyond the final section of the considered reach (section S2 in Fig. 6.3) and other 2 could not be found anymore. On average, the displacement is about 250 m, and the maximum distance travelled is 1426 m. Regarding the cylinder orientation, the exact angle was not surveyed. Only the indication of whether the log was parallel, perpendicular or oblique with respect to the channel was made available.

As a first attempt, the transport of logs is modelled with stationary conditions, in order to verify if the cylinders move. In fact, the anchoring of logs to small boulders (smaller than those implemented in the domain) or to irregularities and trees on the river banks, is not modelled, as well as their vertical displacement from the channel bottom (logs may be lifted from the bottom as shown in Fig. 6.13). These factors may anticipate the entrainment of the rigid bodies and lead to an overestimation of their final displacement. It is worth highlighting that the field surveys were realized either before or after the peaks, and at those times logs were not moving. It should be thus expected that, away from the peaks, no displacement is observed.

This preliminary test is performed with a discharge of 4.00 $m^3 s^{-1}$, and has a duration of 1000s of simulated time. The coefficients used in the simulation are equal to those implemented for the calibration of the model in the laboratory channel tests, except for the bed friction coefficient of the gravel bed, which is set to $\mu_{fr} = 0.64$ or $\mu_{fr} = 0.48$ for the static and the dynamic cases, respectively.

Figure 6.13 Photograph of one log laying above the river bottom. Photo courtesy Ana Lucía Vela.

The log positions at 1000s is shown in Fig. 6.14. By comparing this position with the initial ones (Fig. 6.11), some differences can be observed. Logs result more disperse in the river reach than they were in the first survey, meaning that the transport has occurred. The maximum registered displacement is about 360 m. The measured and simulated displacements are in Fig. 6.15.

The image shows that the model predicts logs movement even with the stationary discharge. Furthermore, the displacement of some of them is larger than that measured in the field survey.

These results suggest that ORSA2D_WT strongly anticipates the entrainment of the logs with respect to the real situation. Such a mismatch can be attributed to several concurring model assumptions: (i) the model computes the anchoring of cylinders only if they are stuck against inline obstacles; (ii) it does not account for local conditions which depend on the section profile; (iii) the 2D model does not consider the log vertical position, which may also affect their entrainment; (iv) the friction coefficient and the log density may differ from the values implemented in the simulation, due to the fact that the logs are wet and possibly heavier.

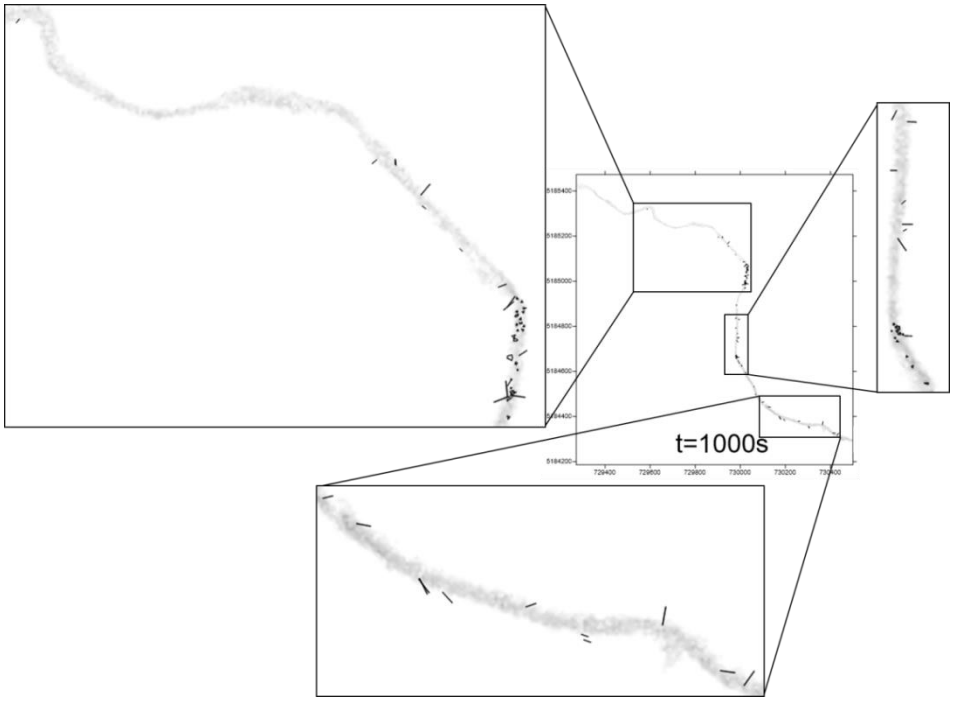

Figure 6.14 Position of the cylinders at the end of the simulation with stationary flow (t = 1000s).

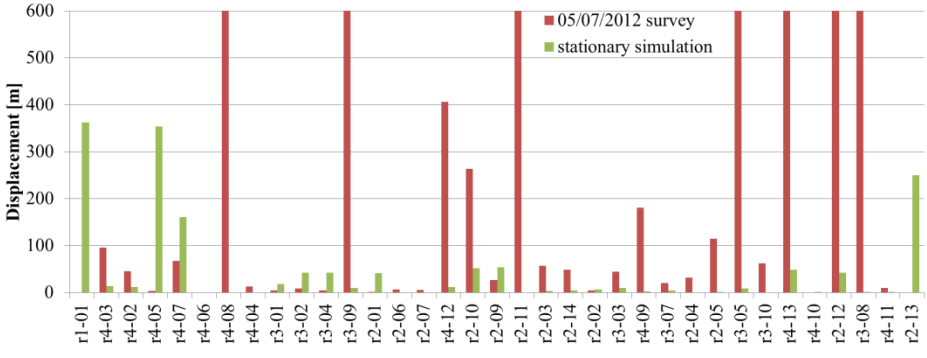

Figure 6.15 Comparison of the displacement between the field survey and the stationary simulation. The vertical axis is limited at 600 m for visualization purposes.

To avoid problems connected with the anticipation of the entrainment, the simulation of the two peaks is performed starting from t = 0.33h, i.e. when the discharge begin to increase (refer to the hydrograph in Fig. 6.9). All the other parameters are left unchanged with respect to the stationary simulation. In particular, the bed friction coefficient and the wood density are not modified, despite the doubt on the accuracy of their values, because there are no references for their variation. The simulation is performed until the tail of the second peak reaches the final section of the domain (about t = 4.00h), while the final part of the hydrograph is not simulated to avoid possible the overestimation of the transport of logs in stationary conditions.

In Fig. 6.16 the displacement of the logs after the first peak (at t = 1.72h), just before the second peak (t = 2.56h) and at the final time (set as 4.00h) are again compared with the measured displacement, which is computed as the difference among initial (26th June) and final (5th July) GPS positions. Note that logs r4-10 and r2-13 were not found in post-event survey, so only their simulated displacement is presented.

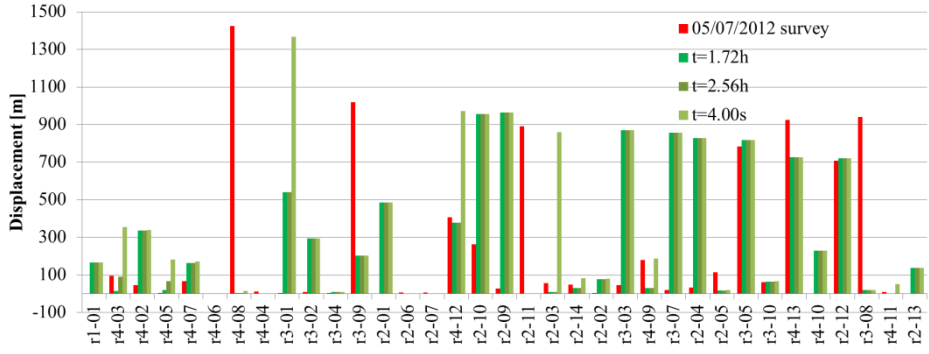

Figure 6.16 Comparison of the displacement between the field survey and the simulation at different time step: after the first peak (t = 1.72h), before the second peak (t = 2.56h) and at the end of the simulation (t = 4.00h).

It appears that simulated displacements are different from the measured ones. Most of the logs move during the first peak, then they stop due to the lowering of the discharge. Some of them are remobilized by the second peak. The comparison of logs displacement among the two peaks (t =

1.72h and t = 2.56h) shows that no transport occurs in that time interval, except for logs r4-03 and r4-05, which present different values of the displacement at the considered times. This implies that, in general, mobilized logs reach a stable positioning and do not move for lower values of the discharge. As regards the displacement after the second peak, only 12 logs move again.

For 70% of logs, the simulated displacement is higher than expected, with an average error (i.e. the difference among the expected and simulated displacement) of 383 m, showing an easier mobilization of the trunks. For the remaining percentage the mobility is underestimated, with an average error of -485 m. In this case, the logs stop earlier than expected or do not move at all. For the 18% of the samples the average absolute error is smaller than 10 m, so we can assume that their final position is well replicated.

The average displacement measured during the surveys is 249 m, while the average displacement simulated by ORSA2D_WT is 384 m. A smaller difference is observed for the maximum displacement, with the simulated maximum distance equal to the 96% of the measured maximum, 1426 m. The average values and percentage are computed excluding logs r4-10 and r2-13, since their surveyed final positions were not available.

6.4. Analysis of the results

The comparison of the simulated and expected displacement may help in understanding the reasons for the large differences observed. In the field survey, the motion of 31 logs over the 33 considered was observed while in the simulation, 29 logs over 33 move. In Tab. 6.3 the measured and simulated displacement of the logs which present opposite behaviour (i.e. move in the survey, not in the simulation, or vice versa) is shown.

Log ID	Measured displacement [m]	Simulated displacement [m]
r1-01	0.0	167.3
r4-04	12.4	0.0
r2-06	6.4	0.0
r2-07	5.9	0.0

Table 6.3 Comparison of the displacement of logs which present opposite behaviour in the simulation with respect to the field survey.

Except for log r1-01, for which the error in computing the displacement is very high, for the other three logs the measured displacement is small (less or near 10 m). This datum can be thus considered in agreement with the zero-displacement obtained by ORSA2D_WT, denoting a low mobility of the logs due to their initial positioning (on the river banks).

As previously highlighted, ORSA2D_WT tends in general to overestimate the log transport. In particular, considering the 5 classes of displacement presented in Tab. 6.4, we can observe that real logs tend to move for shorter distances (11 logs move less than 10 m and other 11 move between 10 m and 100 m), while increasing the considered distance, a smaller number of logs appears. In the simulation, on the contrary, fewer elements are found in the first two classes (5 and 8 respectively), while 9 and 10 logs move between 100 m and 500 m and between 500 m and 1000 m. This analysis confirms the fact that ORSA2D_WT tends to provide higher values of displacement. The factors that contributes to this mistake are those previously discussed for the case of the stationary simulation, in particular the simplified geometry and boulders representation which may introduce a lack of anchorage for the cylinders.

	<10m	**10m-100m**	**100m-500m**	**500m-1000m**	**>1000m**
Field survey	11	11	4	5	2
ORSA2D_WT	5	8	9	10	1

Table 6.4 Number of logs for displacement classes. Comparison of the measured and simulated displacement.

In Figs. 6.17 to 6.19 the simulated and measured displacement are presented as a function of the diameter, length and slenderness of the samples, respectively. Once again, the figures do not include the trunks r4-10 and r2-13.

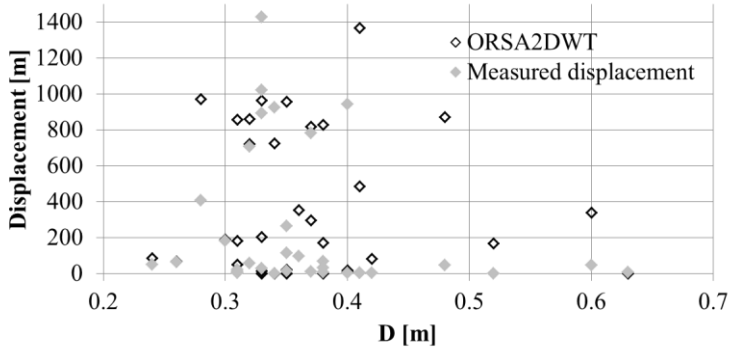

Figure 6.17 Comparison of the displacement between the field survey and the simulation as a function of the log average diameter D.

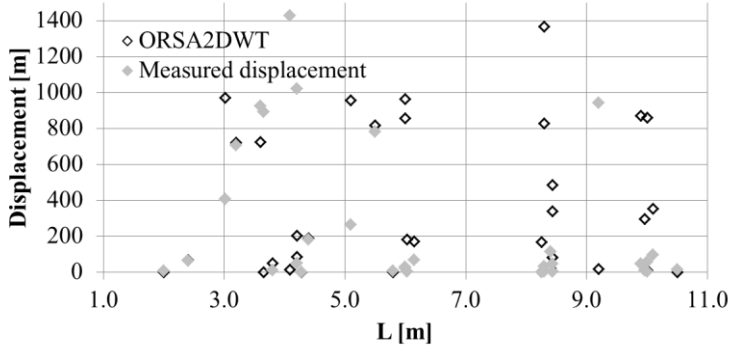

Figure 6.18 Comparison of the displacement between the field survey and the simulation as a function of the log length L.

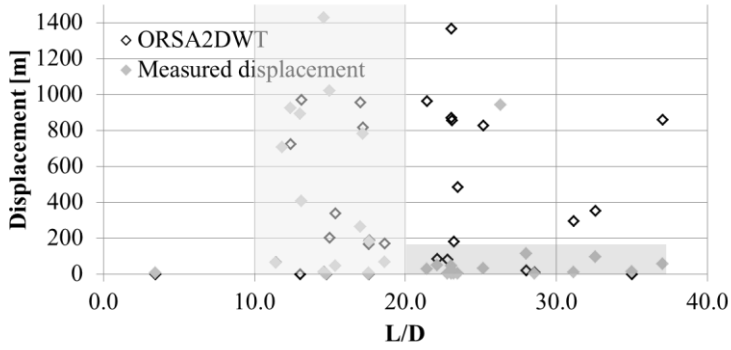

Figure 6.19 Comparison of the displacement between the field survey and the simulation as a function of the log slenderness. Light grey rectangles show the observed displacement range for two classes of slenderness: 10 < L/D < 20 and 20 < L/D < 36.

As regards the correlation with the samples length, the data provided by the University of Bolzano show that a higher mobility is expected for shorter trunks, while the longer elements (L > 8.0 m, 42% of the set) do not go farther than 200 m from their initial position, with the exception of one sample. ORSA2D_WT presents a different trend, with longer and shorter elements reaching similar distances.

A similar behaviour is observed in Fig. 6.19, where the displacement is related to the log slenderness. For a higher slenderness, the modelled displacement is up to 7 times higher than the real one, while for mean values of L/D (from 10 to 20), simulated logs move less than real ones. For the smallest slenderness value (log r2-06) the sample do not move in the simulation and moves a little in the field survey (6 m).

In general, field observations show that the motion of the logs depends on their length and slenderness. The real logs are transported more easily if they are short and present a small slenderness ratio. Since, on overall, the logs with the higher slenderness present the higher length (see Fig. 6.20), the reason for the reduced mobility of long, slender samples can be basically sought in the fact that these logs are more easily stopped by river banks irregularities or by large boulders.

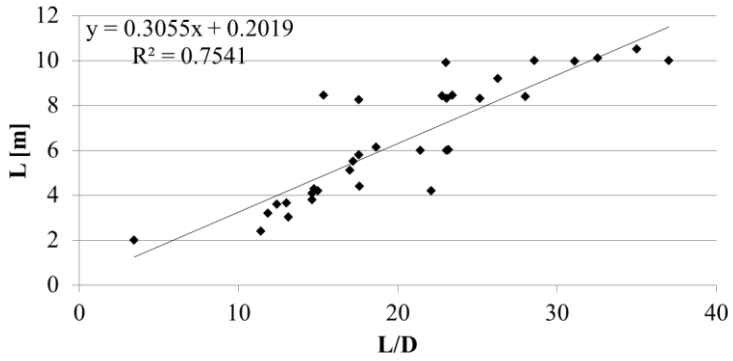

Figure 6.20 Comparison of the log slenderness ratio (L/D) and length.

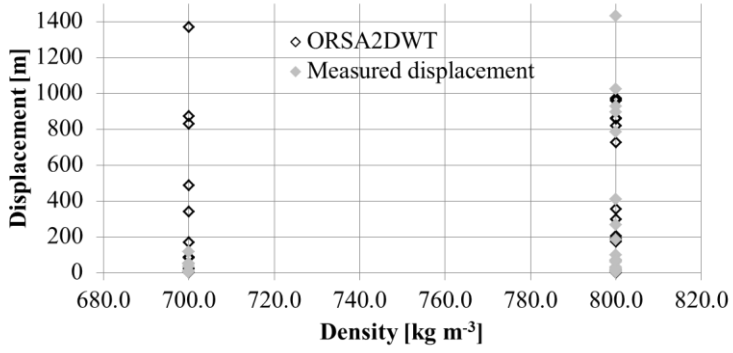

Figure 6.21 Comparison of the displacement between the field survey and the simulation as a function of the tree type, considered in terms of wood density: conifers (700 kg m^{-3}) and broadleaves (800 kg m^{-3}).

Another factor that may influence the logs motion is their density. As said, the real density of the samples was unknown, so two values are implemented according to the two types of trees, conifer or broadleaves. Fig. 6.21 shows that ORSA2D_WT computes a higher displacement for the wood with lower density (conifers), while in the field observation the opposite behaviour was instead deduced from field observations, with the maximum displacement being 114 m for conifer logs and 1426 m for broadleaves logs. It is thus possible that the densities assigned to the logs in the model are different from the ones of the real woods, leading to an error in the log entrainment and deposition.

This uncertainty, added to the ones related to the geometry discretization, to the boulders simplified representation and to the initial position of the logs, contributes to the overall low accuracy of the model when focusing on the simulation of the displacement of each single log. For this reason, as it was done for the semi-congested experiment in the previous chapter, the overall behaviour of the entire group of samples is analysed, too. Fig. 6.22 compares the positions of the logs observed during the field survey of July 5th and the final positions computed with ORSA2D_WT.

Observed data show that the logs tend to accumulate in four areas: in upstream and downstream parts of the reach, and in the two areas where the boulders are located. Only two logs were eventually found in an intermediate position upstream of the area with boulders ($x \approx 730150$ m) and two went beyond the end of the reach analysed in the simulation($x < 729300$ m).

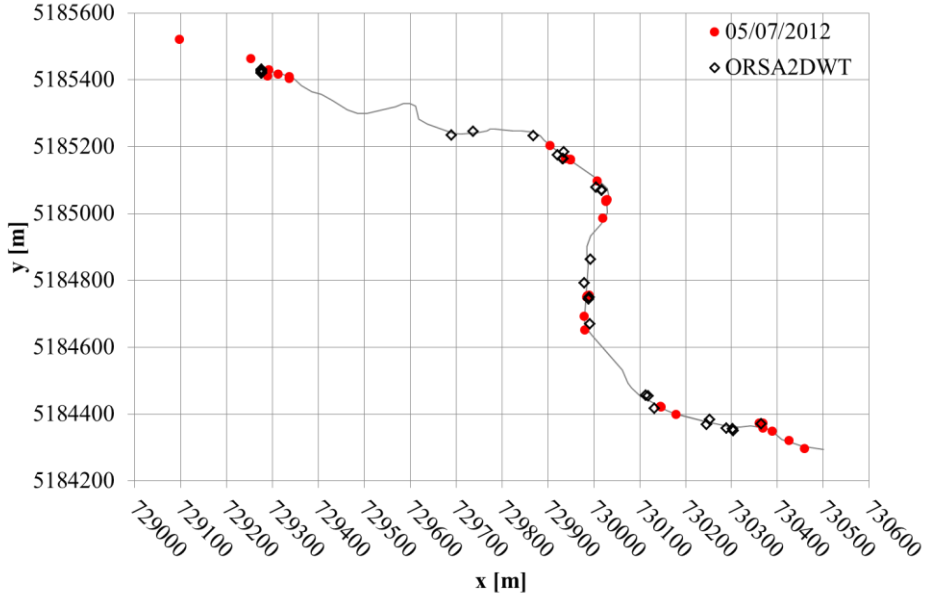

Figure 6.22 Final position observed on July 5th 2012 (red circles) and simulated with ORSA2D_WT (empty diamonds) along the reach of the Rienz river.

Simulated logs are distributed more evenly along the river reach. In the first part, fewer elements are found, while the majority stops in the two

central areas. Some logs travel to the end of the reach and result located in the final section only conventionally, since their position outside the mesh cannot be further computed.

The comparison of the number of logs resulting in each part of the river reach (Fig. 6.23) confirms that the larger error is made in the first part (from 0 to 200 m from the initial section), where only 1 log is found respect to the 6 observed in the field survey. It must be also stressed that the notes describing the field surveys outline that the presence of trees on the riverbanks – which are not included in the model – played a major role in arresting the log motion in this part of the reach.

On the contrary, some more logs are found in the second interval considered while in two central intervals (600-800 and 1000-1200 m) the same number of surveyed and simulated logs is encountered. In the interval 800-1000 m fewer logs are found in the simulation, which are probably those observed in the final section. Furthermore, two logs can be found in the interval 400-600m, in which no field observations were recorded. Note that the boulders included in the domain are located in the intervals 400-600 m (6), 600-800 m (25) and 800-1000 m (33), where a large island is also found near the left bank.

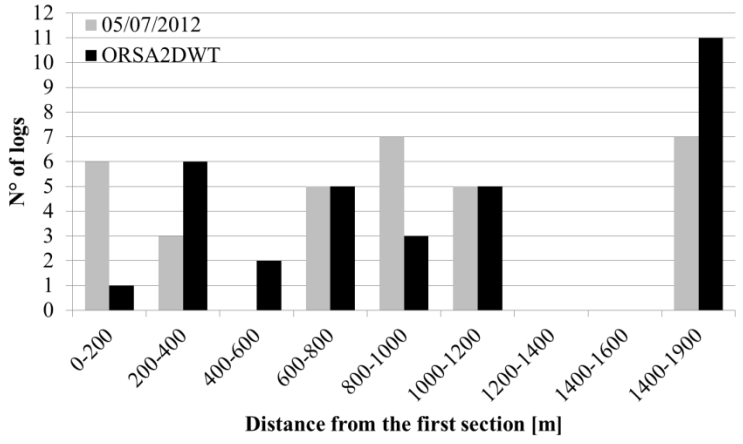

Figure 6.23 Number of logs for distance intervals. Data observed on July 5th 2012 (grey rectangles) and simulated with ORSA2D_WT (black rectangles). The distance is computed from the first section of the domain.

To better understand if the the river characteristics, and consequently their modelling, may affect the deposition of the logs, the reach is divided according to its peculiarity, considering variable intervals:

- 0-450 m, upstream reach;
- 450-650 m, first group of boulders;
- 650-800 m, intermediate reach with no boulders;
- 800-950 m, second group of boulders;
- 950-1900 m, downstream reach.

The number of logs in each interval, observed in the field survey, simulated after the first peak and after the second peak is shown in Fig. 6.24.

The implementation of a variable interval shows that in the upstream reach and in the first group of boulders, the same number of logs can be found. Then some variation is observed: comparing the simulated results after the first and after the second peak, it is shown that logs tend to move downstream. Fewer logs stop in the second group of boulders, and a higher number of elements is found in the final part, with respect to that observed during the field survey.

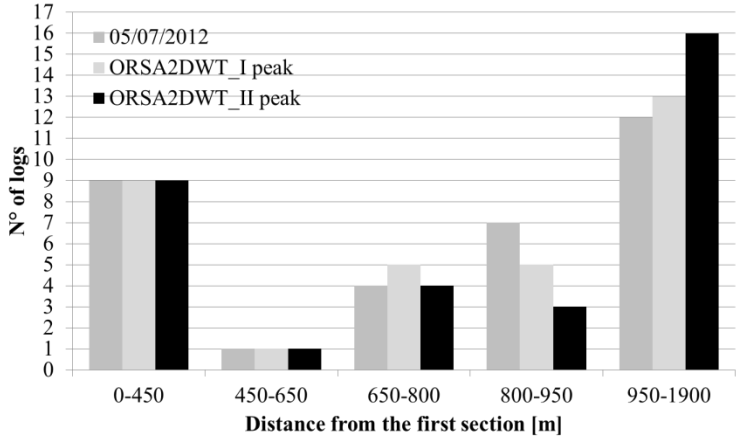

Figure 6.24 Number of logs for variable distance intervals. Data observed on July 5th 2012 (grey rectangles) and simulated with ORSA2D_WT after the first peak (light grey rectangles) and after the second peak (black rectangles). The distance is computed from the first section of the domain.

To summarize, the application of the proposed model to the field case highlights both its limits and strengths. The 2D model cannot include all the singularities of the real domain, such as small boulders, section irregularities on a scale smaller than the cell dimension (1.20-2.50 m) or the presence of trees along the river banks. The uncertainties on log orientation, vertical positioning and density do not allow to compute the exact displacement of each log.

However, if the overall trend of log displacement is considered, the pattern of the deposited logs is quite well reproduced, in particular in the first part of the reach (between 0 and 800 m), while some mistakes in log arrest are highlighted for the second group of boulders. See Appendix C for the maps of log positioning.

Conclusions

The thesis proposes a method for the simulation of the planar motion of rigid bodies on the water surface. It represents a preliminary step towards the computation of the flood risk associated to the presence of floating debris during an inundation.

The choice to consider each body as a discrete element leads to the one-way coupling of a Lagrangian approach for the description of the bodies planar motion with the two-dimensional Eulerian solution of the Shallow Water Equations, provided by the code ORSA2D. This Eulerian-Lagrangian approach has been selected since the main interest is on large bodies transported by the flow, so the nature of the two phases is different (continuum for water, discrete for floating bodies). The one-way coupled code is named ORSA2D_WT

The equation of transport is obtained by adapting the Maxey-Riley equation to the case of floating spheres or cylinders, and follows a dynamic approach. The adaptation to the case of floating large objects is obtained by taking into account the distribution of the flow velocity on the major body dimension, thus including the effect of non-negligible velocity gradients along the body main axis. The body is therefore divided into subsegments and the forces are estimated from flow velocities and accelerations on each section. The validity of this subdivision is verified with dedicated numerical simulations, which show that the approximate procedure is rather independent from the number of points along the body where flow quantities are evaluated.

The rotation formulation takes advantage of the detailed description of the forces on the body and presents an original form, at least for applications in this field. It accounts for the torque generated by the force distribution around the centre of mass and includes an added inertia term, which models the resistance of the body to rotation due to differences between the angular velocities of the body and of the surrounding fluid. This form has been selected because it provides better results with respect to the formulation found in the literature.

Working with simple objects, like spheres and cylinders, allows one to set up the basic features of the coupled model, avoiding the complex interactions among flow and irregular bodies. It helps in calibrating the model and verifying its effectiveness, referring to conditions which are easier to repeat and to model. This simplification is acceptable for this stage of the research, in which the validity of the model has to be assessed. Although the considered objects have simple shapes, a fundamental distinction can be done, which is the elongated shape of cylinders and the consequential possibility of changing their orientation toward the flow. This behaviour is included in ORSA2D_WT, not only by computing the body rotation around its vertical axis (planar rotation), but including the effect of the orientation in the computation of the hydrodynamic force, through the measure of the drag and side coefficients for floating bodies.

The experimental campaign, carried out with an *ad hoc* built hydrodynamic balance in an open channel, provided values of the drag and side coefficients as a function of the yaw angle of the cylinder. The effect of body submergence was also investigated and the results highlighted that the influence of the free surface plays a significant role: for cylinders very near to the water surface, higher values of the coefficients were obtained with respect to more deeply submerged cylinders. In the latter case, the disturbance of the free surface was reduced, thus leading to smaller drag and side forces on the body. A different situation was observed for floating bodies, whose configuration was replicated in the experiments by placing the centre of mass of the cylinder at the same height as the undis-

turbed water level. In this case, the interference with the free surface was significant, but the area available to the flow was smaller and a reduction in the coefficient was observed, although not proportional to the area reduction. The results are validated by comparison with the available literature data for totally submerged bodies and the curves obtained for floating cylinders are implemented in the model.

To validate the model, several aspects need to be considered. First of all, different mechanisms arise for spheres and cylinders, so peculiar conditions have to be tested. Rotation of spheres may appear less significant with reference to the body orientation, but has a large influence on the body trajectory, through the lift induced and Magnus effects. These forces are included in the model and their effectiveness is verified.

When dealing with cylinders, translation and rotation have to be simultaneously taken into account. For this reason, specific experiments have been realized in a laboratory flume at the University of Zaragoza, with and without side obstacles, for spherical and cylindrical samples. Despite the uniform characteristics of the cylindrical samples, the analysis of the outcome of the experiments highlighted the variability both in trajectories and orientation. It is probable that the turbulence and the small surface waves randomly affect the body behaviour.

The detailed comparison of the measured and simulated body position and orientation shows that, on overall, the model is able to predict the behaviour of single logs. Rotation presents, in general, a smaller accuracy, especially in the final part of the channel where the turbulence is higher. The analysis of the effects of variation of the coefficients (added mass, added inertia) and of the initial conditions shows that, once again, orientation is more sensitive to the model parameters than the linear displacement.

Also the way of representing obstacles in the 2D numerical flow model has an effect on the body motion. The best solution, among the three tested strategies (obstacles as boundaries in the mesh, as mesh cells charac-

terized by higher roughness or as cells with higher bottom elevation) is the assignment of a very high Manning coefficient to the cells representing the obstacles. This strategy was applied to a test experiment in the laboratory flume, performed in stationary conditions, with obstacles never surmounted by the water and the value of roughness was calibrated thanks to the measured velocity upstream and downstream the obstacle, leading to a coefficient 1000 higher than the base one (10 s $m^{-1/3}$ instead of 0.01 s $m^{-1/3}$). Its application in a real channel is not trivial, because of the higher difficulties in estimating the proper roughness value which mimic the presence of the obstacle. Furthermore, the effect of the obstacle may change depending on the water level, e.g. boulders can be surmounted by the flow. For real channels, the proper representation of the obstacle elevation is then considered the best strategy, and is employed for the application of ORSA2D_WT to a real-scale experiment.

Once assessed the applicability of the model to the case of a single floating cylinder, the attention is moved to the simulation of multiple log transport. This lead to estimate the value of the restitution coefficient included in the collision model and to verify how the model behaves in case of semi-congested transport. As regards collisions, the detection of the impact among floating bodies is well performed and the deduced value for the restitution coefficient, valid for floating bodies collision, is 0.1, which means that the water has a strong effect in reducing the elasticity of the collision. Despite that, the collision model seems to overestimate the effect on the body rotation, so that further investigation is needed to check if some variation should be introduced, due to the particular conditions of bodies floating on the water surface.

The simulation of an experiment with semi-congested transport has highlighted that the experimental data may present uncertainties not predictable by ORSA2D_WT. If one element follows a different trajectory, it influences all the other logs, making it extremely hard to assess the performances of the model. Overall, this application has shown that the simulated displacement of cylinders in time is similar to the experimental one

and that the logs tend to occupy the same areas as the real samples. In this condition, however, a two-way coupling among the Eulerian and Lagrangian approach may be required to improve the accuracy of the simulation.

The application of ORSA2D_WT to the real-scale experiment performed in the Rienz river was important to assess the model behaviour in real conditions. This simulation, in fact, is half-way between a laboratory experiment and a real field application. The domain is quite regular, the flow conditions can be verified to a certain extent and the motion of the bodies, which are cylindrical and with known characteristics, has been periodically monitored by researchers of the University of Bolzano. The stationary simulation has highlighted some limits of ORSA2D_WT with regard to the model of incipient motion. In particular, some logs move even under a low-flow, steady state condition (during which they should not be transported, as reported by the field surveys), leading to an overestimation of the displacement. This problem should be attributed both to the lack of precise knowledge on logs properties (real density, planar and vertical position) and to some inaccuracies in representing log anchoring, when it does not involve boulders or inline obstacles. Another possibility is the variation of the friction coefficient and of the apparent drag coefficient, which was estimated only from laboratory experiments.

When the simulation of the selected event is performed, the displacements of single logs are well reproduced only for the 18% of the samples. The average simulated displacement is slightly higher than the measured one, while the maximum travelled length is near the expected value (96%). On overall, ORSA2D_WT tends to overestimate the log entrainment, with the exception of those cases in which the logs result within a cell whose centre is higher than the water level.

The peculiarities of each log (real orientation, exact vertical positioning, moisture and anchorage) affect the outcome of the simulation, introducing large uncertainties which could be clarified only with specific investigations. It has to be highlighted that in real-case applications similar doubt would remain, since detailed information as those obtained for the Rienz

river are rarely found. This limit can be overcome if the model is intended not for a deterministic use, i.e. to predict the particular situation of a specific piece of wood, but as a statistical instrument, which can mimic the behaviour of large groups of logs, providing a general description of their motion and arrest, describing the effect of their presence with different scenarios determined by varying the initial and boundary conditions. According to this point of view, the ability of the model to simulate the distribution of the logs along the reach and accordingly to the reach singularities is a positive aspect, so that it can be considered a valuable instrument for the prediction of the areas more prone to log deposition.

Overall, ORSA2D_WT provides an acceptable estimation of the trajectories and orientation of spherical and cylindrical bodies floating on the water surface. Since several aspects have to be taken into account, it is important to check all of them to assess its reliability and use it for the estimation of the hydraulic risk.

The entrainment and arrest are not investigated in detail in the present dissertation, since they are modelled with approaches taken from literature. However, the effects of the dynamic friction and of the variable apparent drag coefficient require further analysis, as highlighted by the application to the case of the Rienz river. Similarly, additional investigation is requested for the added mass coefficient, set constant in this formulation but which may vary with orientation.

Particular attention should be paid to the collision model, which is a fundamental step for the formation of log-jams upstream of obstacles and for the simulation of the joint motion of cylindrical bodies. The analysis should investigate more in depth if the model is appropriate for the problem of floating bodies, providing a solution which is able to simulate the diverse condition of collisions and the possibilities for wooden elements to get stuck even in sections with no recognized obstacles.

One more fundamental step is the implementation of a two-way coupling strategy among the Lagrangian and Eulerian methods. The simulations

with more than one log in the laboratory channel highlighted this need, which becomes even more significant when dealing with congested transport and obstruction formation. A force exerted by the rigid bodies should be then applied to compute updated quantities of the flow; the question on how to apply the force on the flow, and in particular in which cells, has to be examined in detail for a good reproduction of the phenomenon.

ORSA2D_WT represents an important step for the inclusion of the effect of large debris on the flood risk estimation. Its application to laboratory and field experiment has proved its validity, providing also important clues about the aspects that need to be further analysed and which implementation have to be improved, most importantly the full coupling among the Eulerian and Lagrangian models and the modelling of the solid-solid interactions.

Appendix A

Hydraulic simulation

The comparison of the measured and simulated velocities is here reported for configurations with two rectangular obstacle and with one rectangular obstacle.

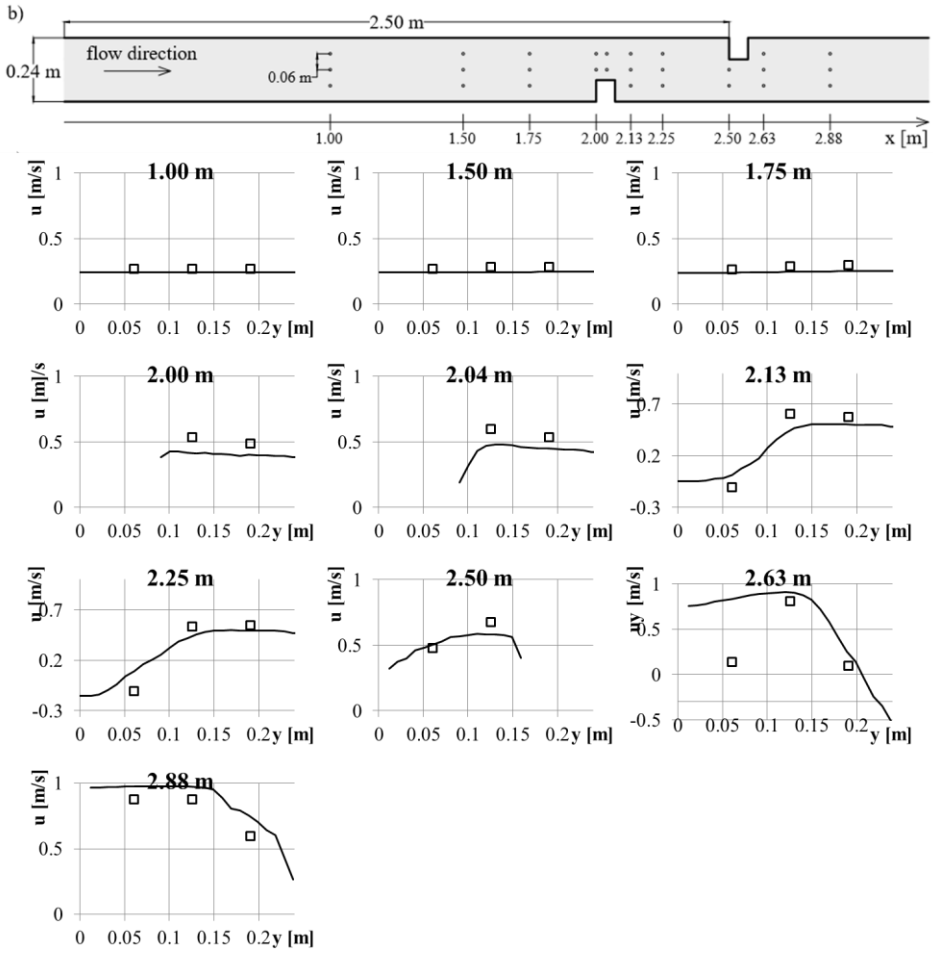

Figure A.1 Comparison of the measured and simulated longitudinal flow velocity, for the case with two side obstacles. Beware different axes limits.

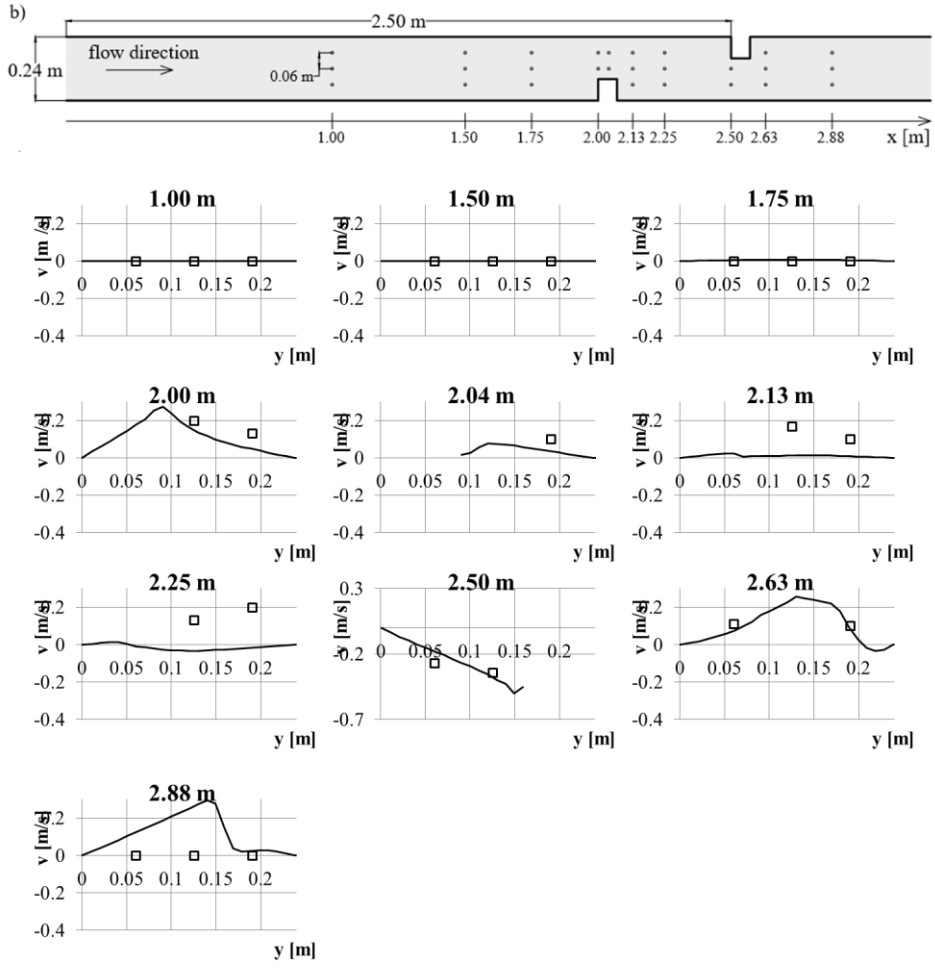

Figure A.2 Comparison of the measured and simulated transverse flow velocity, for the case with two side obstacles. Beware different axes limits.

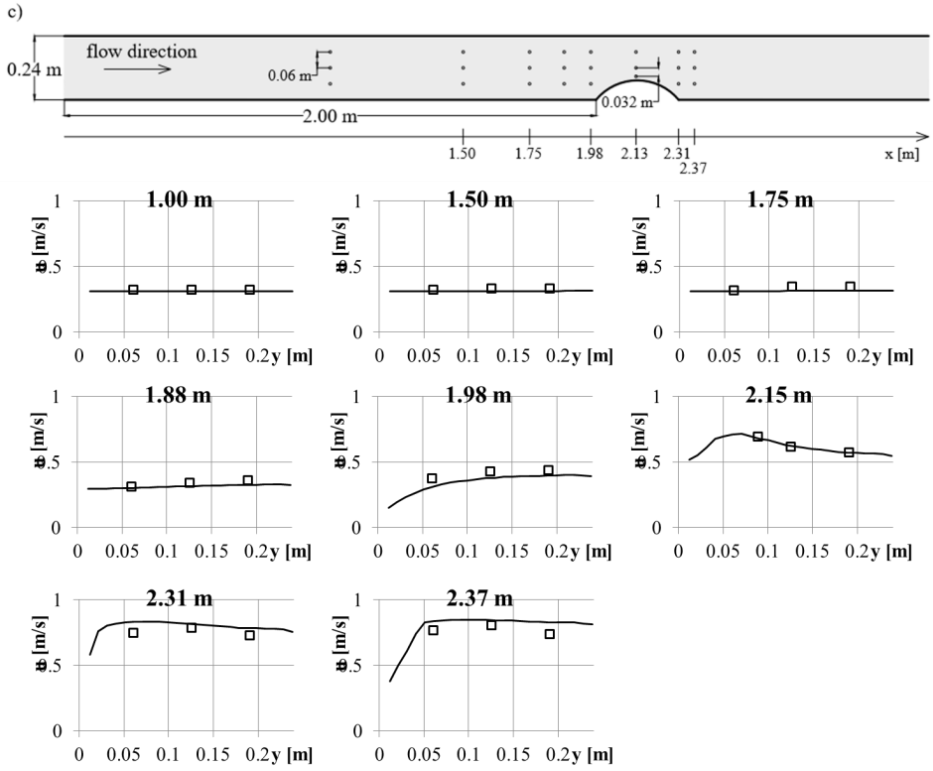

Figure A.3 Comparison of the measured and simulated longitudinal flow velocity, for the case with one smooth obstacle. Beware different axes limits.

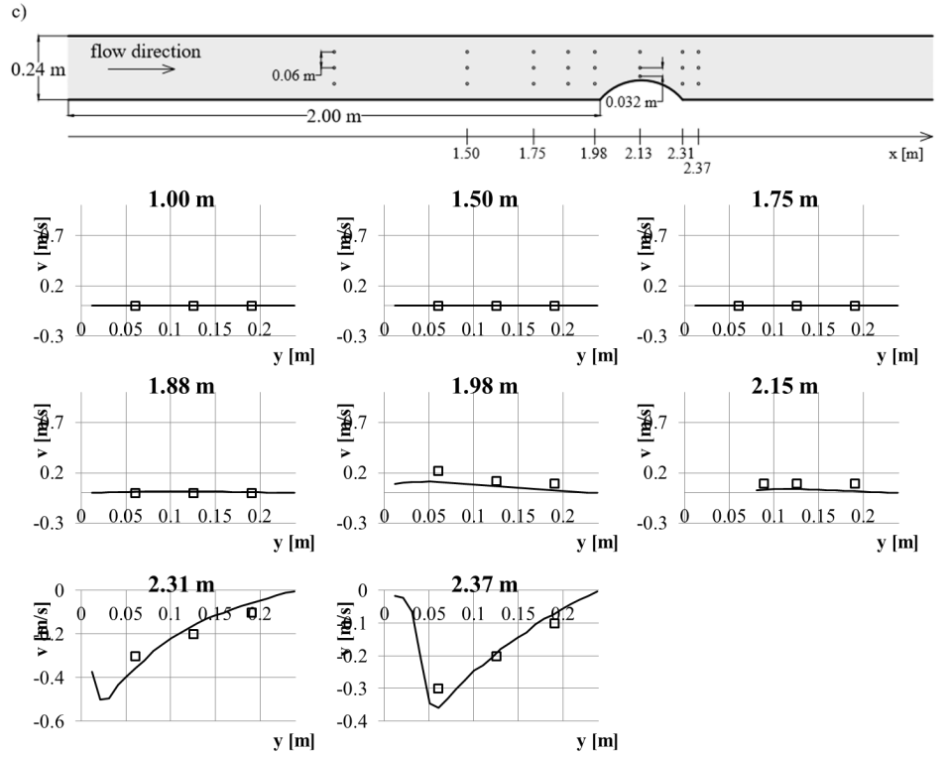

Figure A.4 Comparison of the measured and simulated transverse flow velocity, for the case with one smooth obstacle. Beware different axes limits.

For the configuration with one smooth obstacle, a detailed measurement was performed in the vicinity of the curve. In the following figures, the comparison of the velocity measured with the ADV and the simulated velocity is provided. Note that for the right side, only 2 measures were performed, due to the presence of the obstacle.

The simulated axial velocity are very similar to the measured ones, and the determination coefficient is 0.977 and 0.985 for the central and the left longitudinal sections. The values of the transverse velocity present some discrepancy especially in the two final sections. The determination coefficients are 0.897 for the axial section and 0.032 for the left section.

The determination coefficients are slightly less than the values reported in Tabs. 5.3 and 5.4, computed for the entire length of the channel. It is probably connected to the fact that near the obstacles there are more inac-

curacies the in the initial part of the channel. However, these measures basically confirm the results obtained with the digital flowmeter and may be considered as a validation of the analysis on flow simulation.

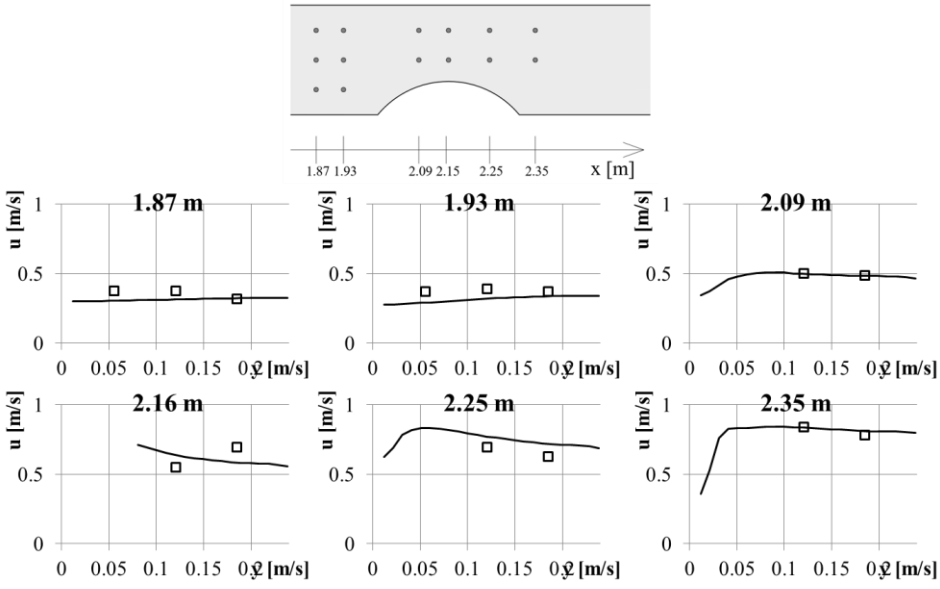

Figure A.5 Comparison of the measured and simulated longitudinal flow velocity, for the case with one smooth obstacle. Measurements are performed with the ADV. Beware different axes limits.

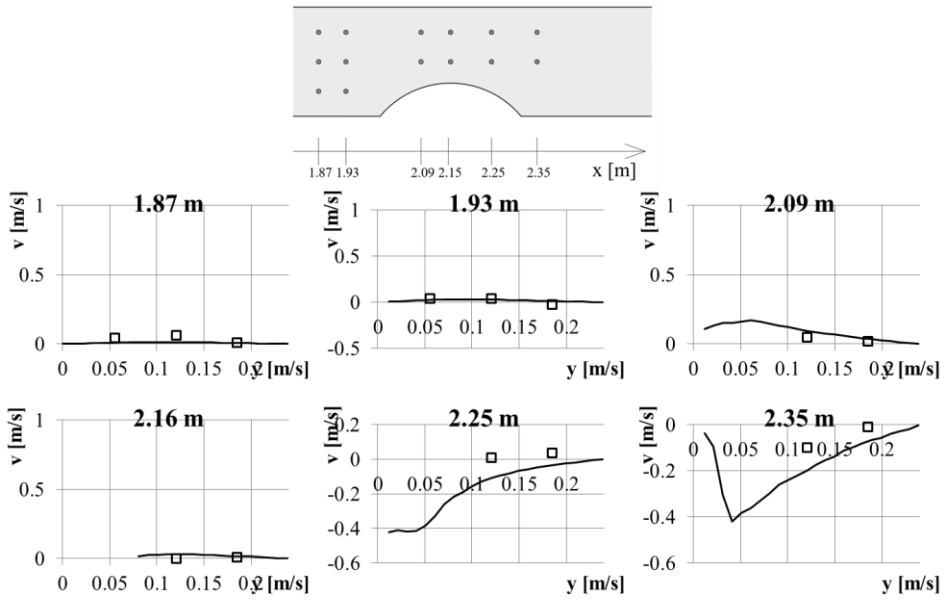

Figure A.6 Comparison of the measured and simulated transverse flow velocity, for the case with one smooth obstacle. Measurements are performed with the ADV. Beware different axes limits.

The longitudinal and transverse velocity are reported also for the longitudinal cross sections, in order to highlight the how the velocity vary along the channel. Figures A.7 to A.12 refer to the configuration with two side obstacles, from A.13 to A.18 for the configuration with one smooth obstacle and from A.19 to A.24. Images confirm that the larger inaccuracies are provided by the configuration with two rectangular side obstacles, especially between the obstacles themselves. This condition may affect the outcome of the transport of floating objects.

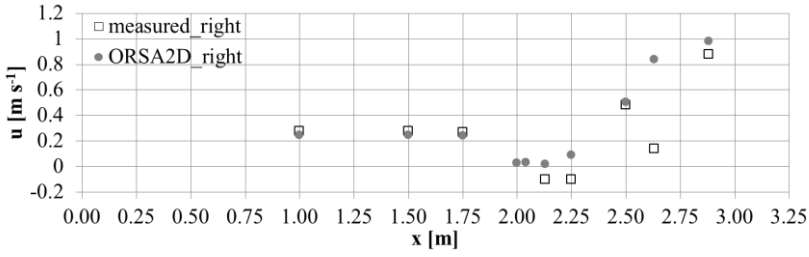

Figure A.7 Comparison of the measured and simulated longitudinal flow velocity, for the configuration with two side obstacles. Right side of the channel.

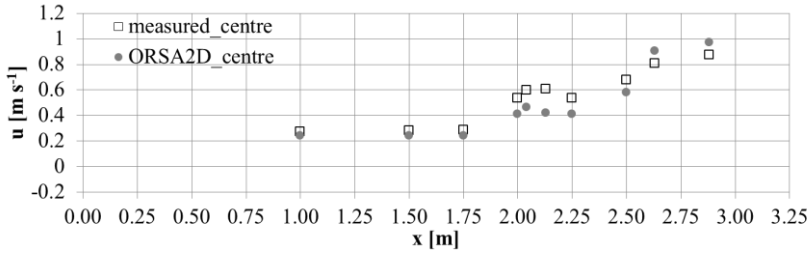

Figure A.8 Comparison of the measured and simulated longitudinal flow velocity, for the configuration with two side obstacles. Channel axis.

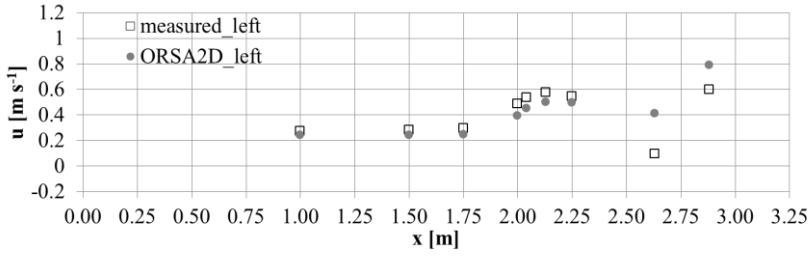

Figure A.9 Comparison of the measured and simulated longitudinal flow velocity, for the configuration with two side obstacles. Left side of the channel.

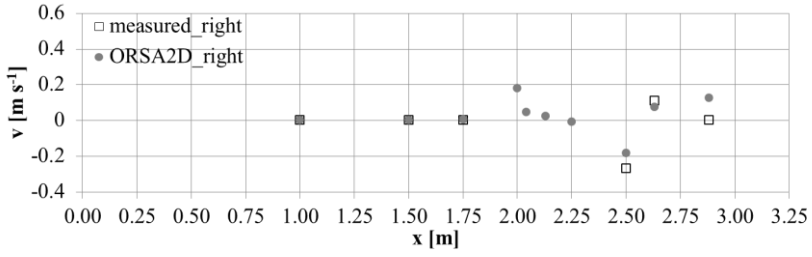

Figure A.10 Comparison of the measured and simulated transverse flow velocity, for the configuration with two side obstacles. Right side of the channel.

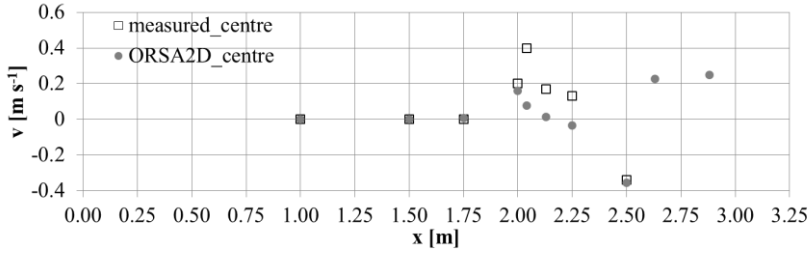

Figure A.11 Comparison of the measured and simulated transverse flow velocity, for the configuration with two side obstacles. Channel axis.

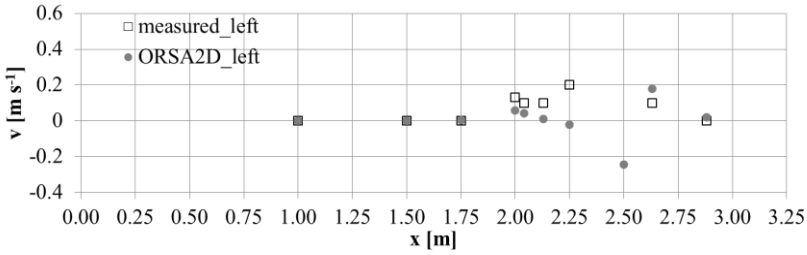

Figure A.12 Comparison of the measured and simulated transverse flow velocity, for the configuration with two side obstacles. Left side of the channel.

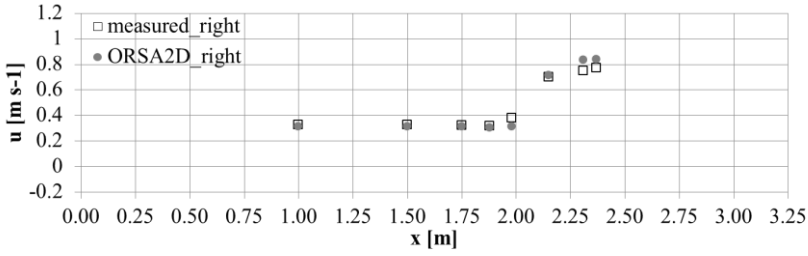

Figure A.13 Comparison of the measured and simulated longitudinal flow velocity, for the configuration with one smooth obstacle. Right side of the channel.

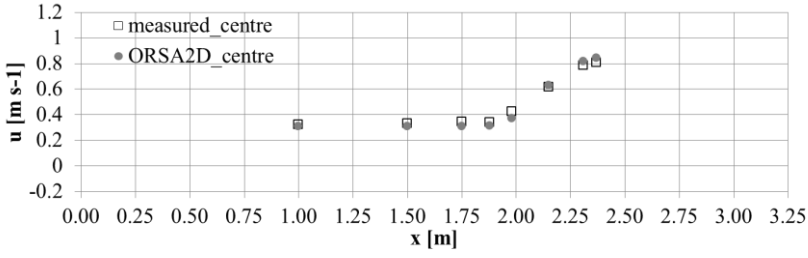

Figure A.14 Comparison of the measured and simulated longitudinal flow velocity, for the configuration with one smooth obstacle. Channel axis.

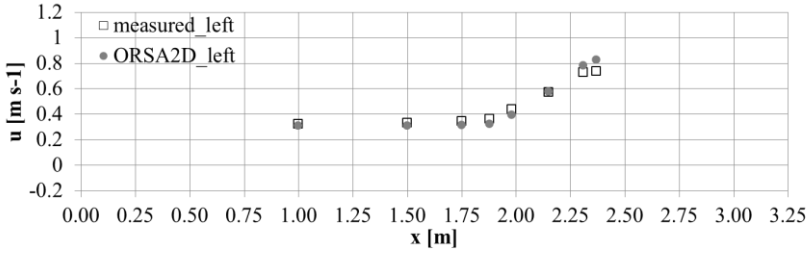

Figure A.15 Comparison of the measured and simulated longitudinal flow velocity, for the configuration with one smooth obstacle. Left side of the channel.

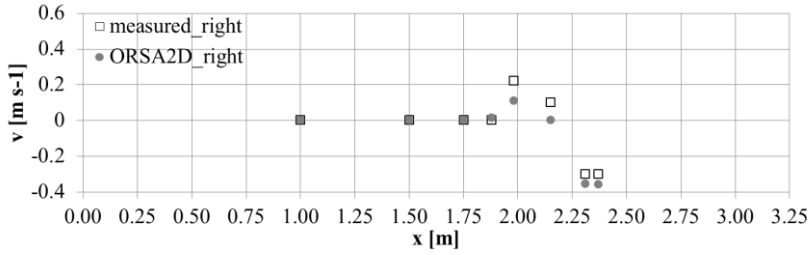

Figure A.16 Comparison of the measured and simulated transverse flow velocity, for the configuration with one smooth obstacle. Right side of the channel.

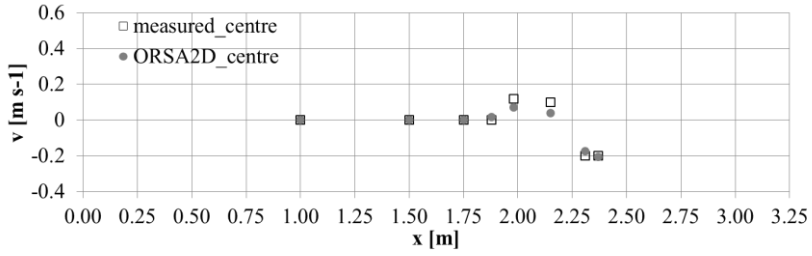

Figure A.17 Comparison of the measured and simulated transverse flow velocity, for the configuration with one smooth obstacle. Channel axis.

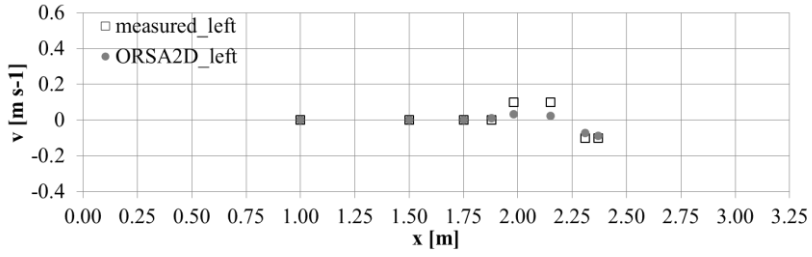

Figure A.18 Comparison of the measured and simulated transverse flow velocity, for the configuration with one smooth obstacle. Left side of the channel.

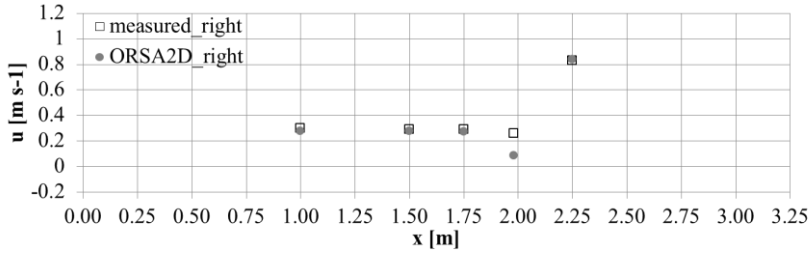

Figure A.19 Comparison of the measured and simulated longitudinal flow velocity, for the configuration with one smooth obstacle. Right side of the channel.

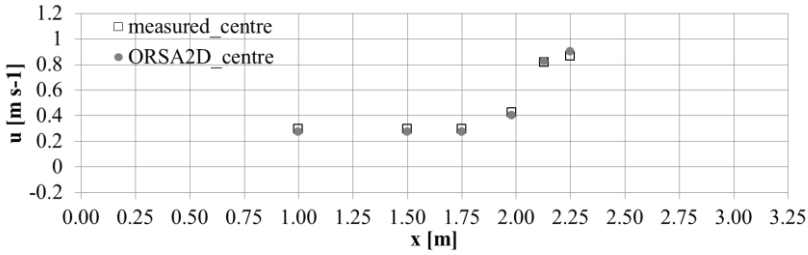

Figure A.20 Comparison of the measured and simulated longitudinal flow velocity, for the configuration with one smooth obstacle. Channel axis.

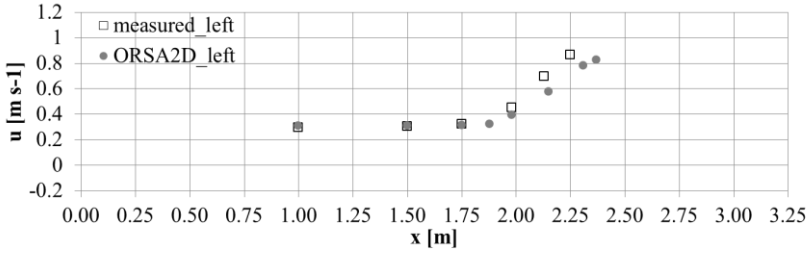

Figure A.21 Comparison of the measured and simulated longitudinal flow velocity, for the configuration with one smooth obstacle. Left side of the channel.

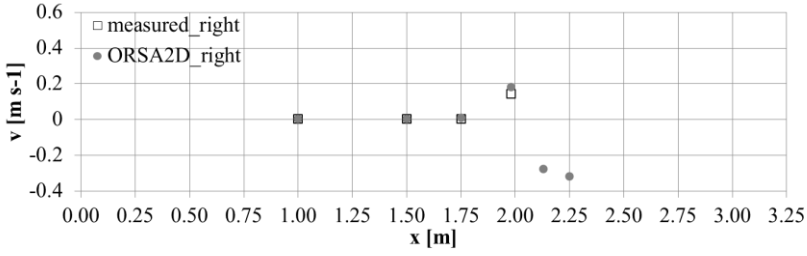

Figure A.22 Comparison of the measured and simulated transverse flow velocity, for the configuration with one smooth obstacle. Right side of the channel.

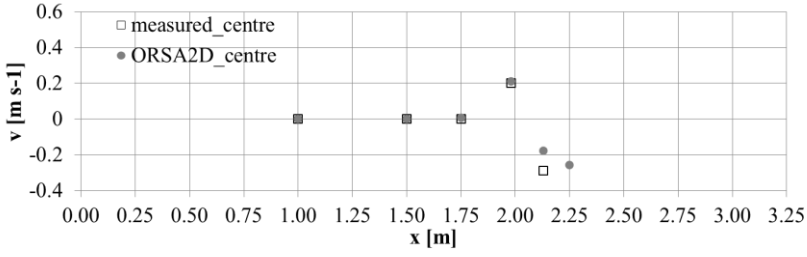

Figure A.23 Comparison of the measured and simulated transverse flow velocity, for the configuration with one smooth obstacle. Channel axis.

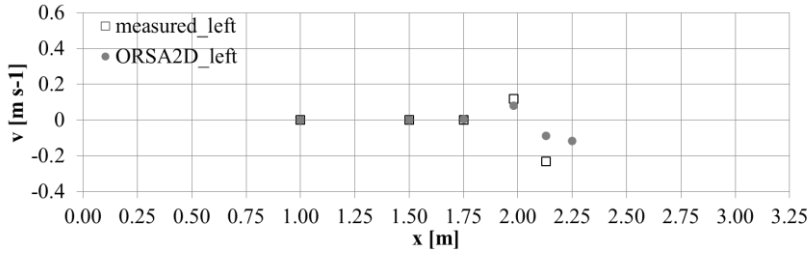

Figure A.24 Comparison of the measured and simulated transverse flow velocity, for the configuration with one smooth obstacle. Left side of the channel.

Appendix B

Comparison of angular velocity for the choice of the rotation formulation

The angular velocity of the log computed with the two proposed formulations (formulation 1, with offset torque and resistance, and formulation 2, with angular momentum and added inertia)is compared in the following figures, for cylinders in the channel with two side rectangular obstacles.

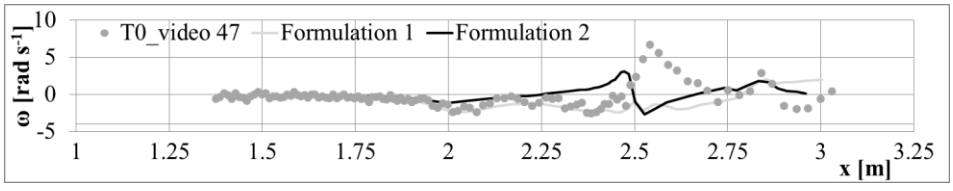

Figure B.1 Comparison of the experimental and simulated angular velocity, for the two formulation of rotation. Grey line for formulation 1 and black line for formulation 2.

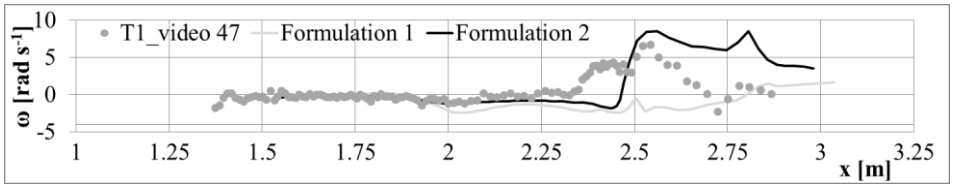

Figure B.2 Comparison of the experimental and simulated angular velocity, for the two formulation of rotation. Grey line for formulation 1 and black line for formulation 2.

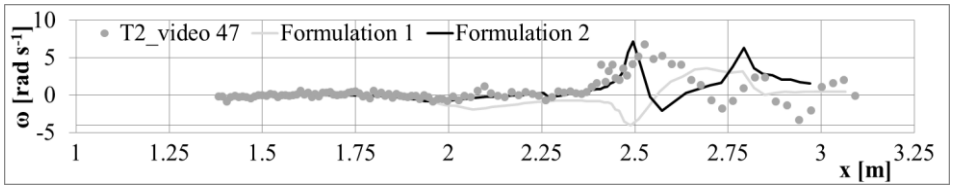

Figure B.3 Comparison of the experimental and simulated angular velocity, for the two formulation of rotation. Grey line for formulation 1 and black line for formulation 2.

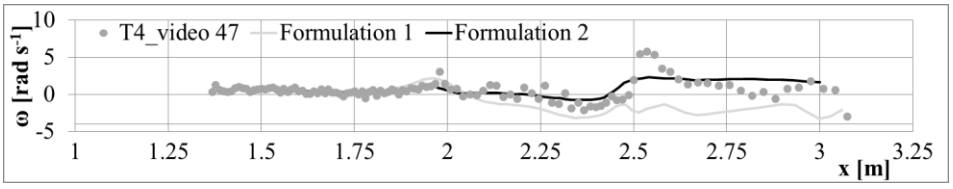

Figure B.4 Comparison of the experimental and simulated angular velocity, for the two formulation of rotation. Grey line for formulation 1 and black line for formulation 2.

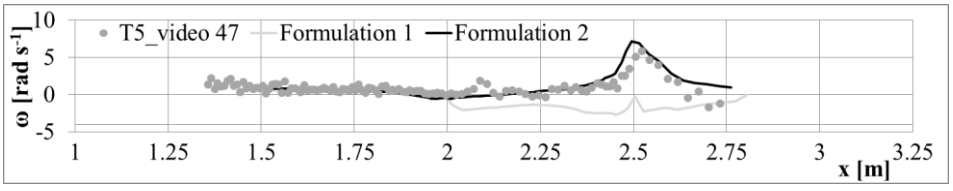

Figure B.5 Comparison of the experimental and simulated angular velocity, for the two formulation of rotation. Grey line for formulation 1 and black line for formulation 2.

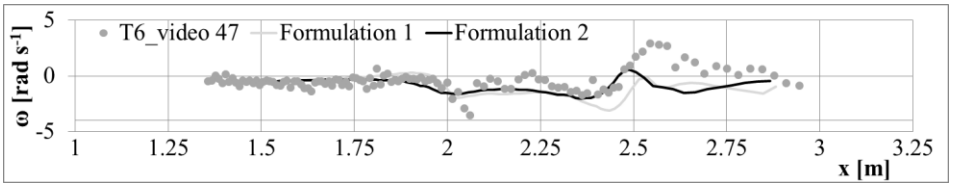

Figure B.6 Comparison of the experimental and simulated angular velocity, for the two formulation of rotation. Grey line for formulation 1 and black line for formulation 2.

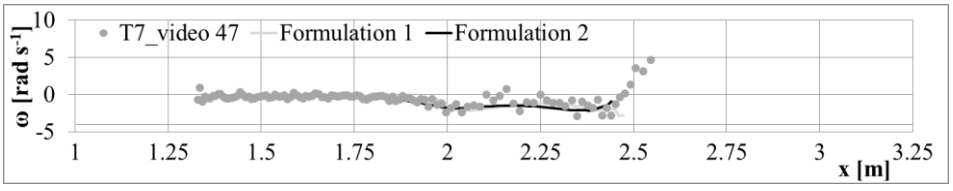

Figure B.7 Comparison of the experimental and simulated angular velocity, for the two formulation of rotation. Grey line for formulation 1 and black line for formulation 2.

As was in Fig. 5.30, the formulation 2 is nearer to the experimental results than the angular velocity computed with formulation 1. The moment of increasing of body angular velocity is well replicated, while the amplitude is generally different from the observed one.

Formulation 1 always miss both the timing and the extension of body angular velocity increasing, thus resulting in less accuracy in the modelling of cylinder orientation.

Appendix C

Rienz river wood transport data

In these Appendix, the information provided by A. Lucía about wood samples are reported. Tab. C.1 refers to the first field survey, June 26th, 2012, and summarize also the logs characteristics (length, diameter, estimated orientation and theoretical density). Tab. C.2 reports the position, displacement and orientation (parallel, perpendicular or oblique) observed during the final field survey, of July 5th, 2012.

Note that the orientation in Tab. C.1 has been determined by taking into account both the generic information (log parallel, perpendicular or oblique to the section) and the orientation observed in the pictures taken during the field survey. This value is, however, estimated, and some inaccuracies may remain in the implementation of the initial conditions.

Finally, in Figs. C.1, C.2 and C.3 the positions of the logs at the final survey and after the first and second simulated peak are respectively reported. By comparing these images, it appear evident the higher dispersion of logs in the simulation. Note that in Fig. C.1 the log orientation is estimated on the basis of the picture taken during the survey, and has just a qualitative meaning.

ID	x [m]	y [m]	z [m]	L [m]	D [m]	ϑ [°]	ρ [kg m^{-3}]
r1-01	730460.72	5184297.37	973.78	8.25	0.47	220.0	700.0
r4-03	730443.98	5184313.18	973.59	10.10	0.31	280.0	800.0
r4-02	730425.81	5184320.31	973.68	8.44	0.55	300.0	700.0
r4-05	730423.57	5184320.96	973.53	6.03	0.26	330.0	800.0
r4-07	730412.84	5184328.85	973.77	6.15	0.33	280.0	800.0
r4-06	730304.95	5184350.52	974.01	4.28	0.29	70.0	800.0
r4-08	730302.98	5184354.88	973.00	4.09	0.28	70.0	800.0
r4-04	730365.49	5184370.41	974.97	10.50	0.30	350.0	800.0
r3-01	730180.10	5184394.75	970.92	8.30	0.36	35.0	700.0
r3-02	730141.10	5184416.64	970.64	9.96	0.32	330.0	800.0
r3-04	730143.08	5184420.26	970.23	10.00	0.35	330.0	800.0
r3-09	729981.53	5184662.35	967.58	4.20	0.28	320.0	800.0
r2-01	729979.83	5184693.56	967.59	8.44	0.36	10.0	700.0
r2-06	729989.04	5184745.51	968.66	2.00	0.58	120.0	700.0
r2-07	729991.04	5184750.04	968.66	5.80	0.33	270.0	800.0
r4-12	729984.91	5184755.74	966.76	3.02	0.23	70.0	800.0
r2-10	729985.67	5184779.67	966.70	5.10	0.30	355.0	800.0
r2-09	729989.88	5184783.51	966.87	6.00	0.28	355.0	800.0
r2-11	729980.24	5184792.59	967.13	3.65	0.28	270.0	800.0
r2-03	730017.48	5184984.98	965.53	10.00	0.27	340.0	800.0
r2-14	730029.72	5184989.41	965.26	4.20	0.19	50.0	700.0
r2-02	730023.56	5184989.47	965.54	8.43	0.37	100.0	700.0
r3-03	730028.40	5184991.04	965.36	9.90	0.43	260.0	700.0
r4-09	730023.79	5184998.52	965.10	4.40	0.25	340.0	800.0
r3-07	730033.59	5185021.96	965.53	6.00	0.26	10.0	800.0
r2-04	730021.14	5185068.29	965.48	8.30	0.33	310.0	700.0
r2-05	730023.98	5185072.66	964.86	8.40	0.30	310.0	700.0
r3-05	730019.67	5185078.39	964.75	5.50	0.32	45.0	800.0
r3-10	729979.06	5185117.59	964.18	2.40	0.21	45.0	800.0
r4-13	729948.72	5185154.52	963.51	3.60	0.29	250.0	800.0
r4-10	729947.78	5185155.47	963.51	2.80	0.26	250.0	800.0
r2-12	729948.45	5185163.77	963.61	3.20	0.27	220.0	800.0
r3-08	729947.53	5185170.30	964.17	9.20	0.35	320.0	800.0
r4-11	729902.30	5185195.34	963.98	3.80	0.26	310.0	800.0
r2-13	729826.78	5185250.46	962.55	3.05	0.25	80.0	800.0

Table C.1 Logs ID, position (x and y), initial elevation, length, diameter, orientation and density.

ID	x [m]	y [m]	Displacement [m]	Orientation
r1-01	728841.25	5185742.22	0.0	O
r4-03	730369.62	5184373.76	95.9	O
r4-02	730389.71	5184348.49	45.8	O
r4-05	730426.64	5184320.53	3.1	PE
r4-07	730362.09	5184372.84	67.2	O
r4-06	730304.95	5184350.52	0.0	O
r4-08	729338.11	5185404.57	1425.8	O
r4-04	730370.23	5184358.91	12.4	O
r3-01	730180.79	5184399.11	4.4	O
r3-02	730147.11	5184423.15	8.9	PE
r3-04	730147.39	5184422.08	4.7	PE
r3-09	729291.14	5185411.72	1018.9	PA
r2-01	729980.20	5184692.12	1.5	O
r2-06	729986.01	5184751.20	6.4	O
r2-07	729986.42	5184753.68	5.9	PE
r4-12	729950.85	5185160.02	405.7	O
r2-10	730027.24	5185039.54	263.2	PA
r2-09	729990.55	5184756.66	26.9	PA
r2-11	729337.96	5185409.31	890.4	PE
r2-03	730029.43	5185040.42	56.7	PA
r2-14	730020.73	5184986.39	4.2	O
r2-02	730029.49	5185037.45	48.0	O
r3-03	730027.75	5185035.80	44.8	PE
r4-09	729951.16	5185163.54	180.3	PE
r3-07	730030.73	5185042.40	20.6	PE
r2-04	730008.78	5185097.83	32.0	PE
r2-05	729951.15	5185161.02	114.5	O
r3-05	729314.27	5185417.97	782.9	PA
r3-10	729939.87	5185165.55	61.9	PA
r4-13	*729099.17*	*5185522.15*	*925.7*	*PE*
r4-10	LOST			
r2-12	729293.62	5185430.18	706.95	PA
r3-08	*729254.25*	*5184534.68*	*940.56*	*PE*
r4-11	729905.56	5185204.39	9.62	PE
r2-13	LOST			

Table C.2 Logs ID, final position (x and y), displacement and orientation. O, oblique, PA, parallel to the channel, PE, perpendicular to the channel.

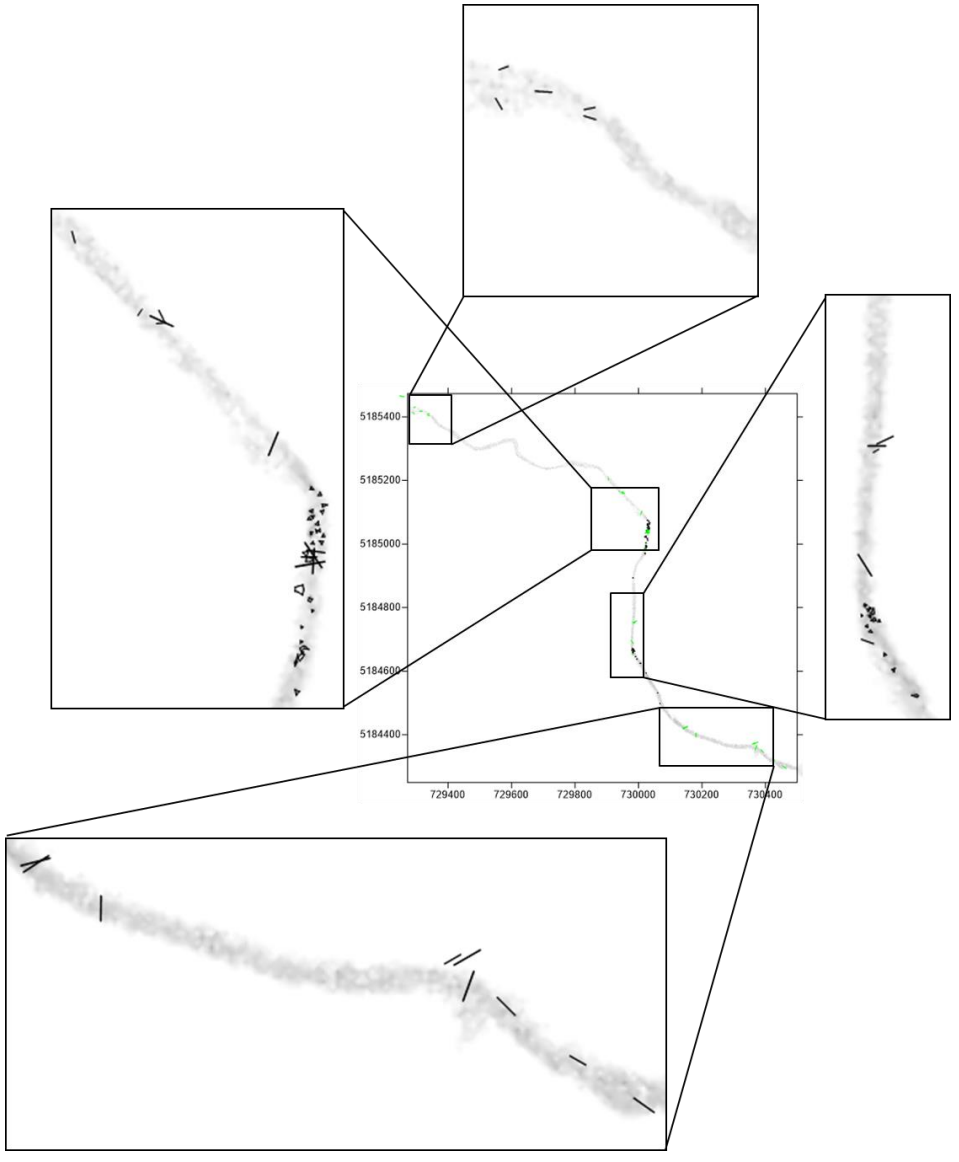

Figure C.1 Final location of the logs (black lines), derived from the data collected by the field survey on the 05/07/2012.

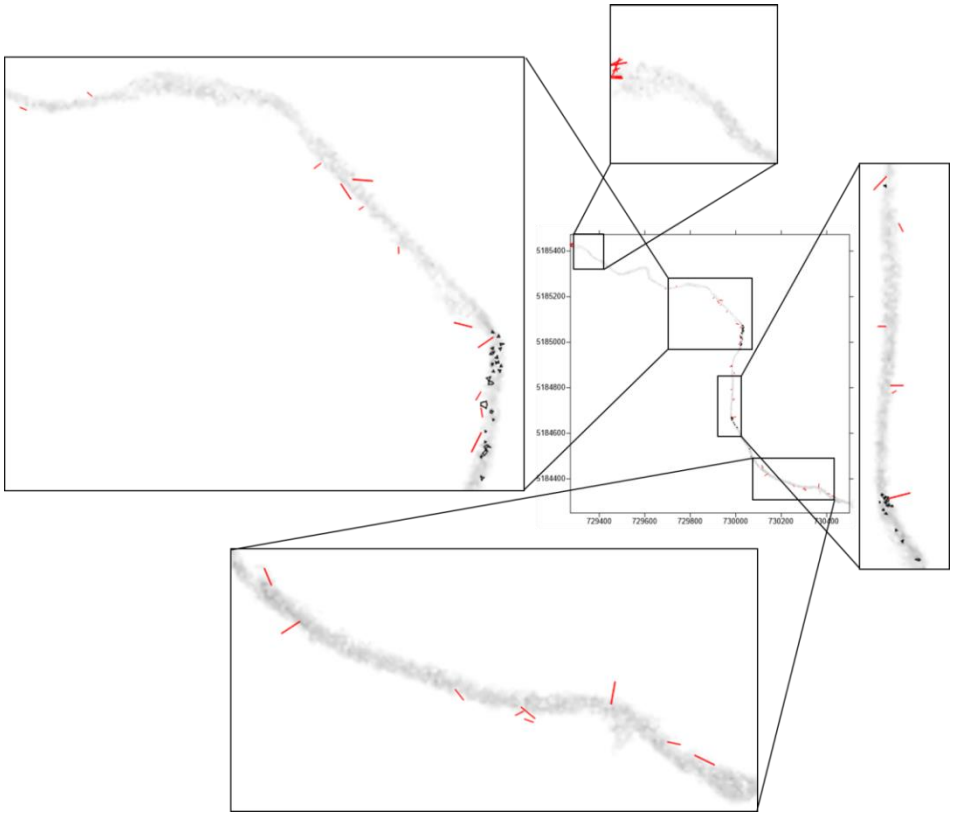

Figure C.2 Location of the logs (black lines) as computed by ORSA2D_WT after the first peak.

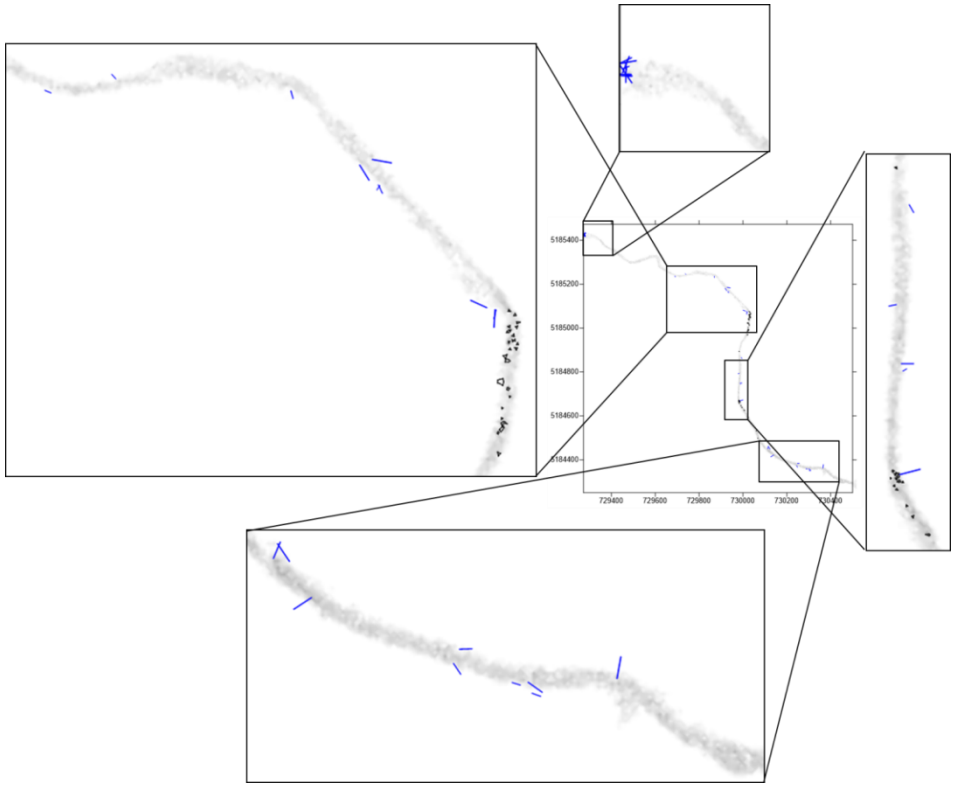

Figure C.3 Location of the logs (black lines) as computed by ORSA2D_WT after the second peak.

References

Abbe TB, Montgomery DR (1996) Large woody debris jams, channel hydraulics and habitat formation in large rivers. *Regulated Rivers*, 12, 2-3, 201–221. doi:10.1002/(SICI)1099-1646(199603)12:2/3<201::AID-RRR390>3.0.CO;2-A

Allen D, Arthur S, Haynes H, Wallis SG, Wallerstein N (2014). Influences and drivers of woody debris movement in urban watercourses. *Science China Technological Sciences*, 57, 1512–1521. doi:10.1007/s11431-014-5607-0

Ahmed F, Rajaratnam N (1998) Flow around bridge piers. *Journal of Hydraulic Engineering*, 124(3), 288–300.

Alcrudo F, García-Navarro P (1993) A high resolution Goudonov type scheme in finite volumes for two dimensional shallow water equations. *International Journal of Numerical Methods in Fluids*, 16, 489–585. doi:10.1002/fld.1650160604

Alonso CV (2004) Transport Mechanics of Stream-Borne Logs. *Riparian vegetation and fluvial geomorphology*, 59–69. doi:10.1029/008WSA05

Amicarelli A, Albano R, Mirauda D, Agate G, Sole A, Guandalini R (2015) A Smoothed Particle Hydrodynamics model for 3D solid body transport in free surface flows. *Computers & Fluids*, 116, 205–228. doi:10.1016/j.compfluid.2015 .04.018.

Andrus CW, Long BA, Froehlich HA (1989) Woody debris and its contribution to pool formation in a coastal stream 50 years after logging. *Canadian Journal of Fisheries and Aquatic Sciences*, 45, 12, 2080–2086.

Aronica G, Bates P D, Horritt MS (2002) Assessing the uncertainty in distributed model predictions using observed binary pattern information within GLUE. *Hydrological Processes*, 16, 2001–2016. doi:10.1002/hyp.398

Arrighi C, Alcèrreca-Huerta JC, Oumeraci H, Castelli F (2015) Drag and lift contribution to the incipient motion of partly submerged flooded vehicles. *Journal of Fluids and Structures*, 57, 170–184. doi:10.1016/j.jfluidstructs.2015.06.010

Auton TR (1987). The lift force on a spherical body in a rotational flow. *Journal of Fluid Mechanics*, 183, 199–218. doi:10.1017/S002211208700260X

Auton TR, Hunt JCR, Prud'Homme M (1988) The force exerted on a body in inviscid unsteady non-uniform rotational flow. *Journal of Fluid Mechanics*, 197, 241–257. doi:10.1017/S0022112088003246

Baber R (2006) Rigid body simulation, Ph.D. Dissertation, University of Warwick, United Kingdom.

Badoux A, Graf C, Rhyner J, Kuntner R, McArdell BW (2009) A debris-flow alarm system for the Alpine Illgraben catchment: design and performance. *Natural Hazards*, 49(3), 517–539. doi:10.1007/s11069-008-9303-x

Bagchi P, Balachandar S (2002) Effect of free rotation on the motion of a solid sphere in linear shear flow at moderate Re. *Physics of Fluids*, 14(8), 2719-2737. doi:10.1063/1.1487378

Barkla M, Auchterlonie LJ (1971) The Magnus or Robins effect on rotating spheres. *Journal of Fluid Mechanics*, 47, 437. doi:10.1017/S0022112071001150

Batchelor GK (1967) An introduction to fluid dynamics. Cambridge University press.

Benacchio V, Piégay H, Buffin-Bélanger T, Vaudor L (2017) A new methodology for monitoring wood fluxes in rivers using a ground camera: Potential and limits. *Geomorphology*, 279, 44–58. doi:10.1016/j.geomorph.2016.07.019

Bermúdez A, Dervieux A, Desideri J A, Vázquez ME (1998) Upwind schemes for the two dimensional shallow water equations with variable depth using unstructured meshes. *Computer Methods in Applied Mechanics and Engineering*, 155, 1-2, 49–72. doi:10.1016/S0045-7825(97)85625-3

Bertoldi W, Welber M, Mao L, Zanella S, Comiti F (2014) A flume experiment on wood storage and remobilization in braided river systems. *Earth Surface Processes and Landforms*, 39, 6, 804–813. doi:10.1002/esp.3537

Bezzola GR, Sigg H, Lange D (2004) Driftwood retention works in Switzerland. Proceedings of *INTERPRAEVENT Conf*erence, Riva del Garda, Italy, 29–40.

Bilotta G, Voroboyev A, Erault AH, Mayrhofer A, Violeau D (2014) Modelling real-life flows in hydraulic waterworks with GPUSPH. Proceedings of the 9th SPHERIC, International Workshop 3–5 June 2014, Paris.

Blau PJ (2001) The significance and use of the friction coefficient. *Tribology International*, 34(9), 585–591.

Bluemink JJ, Lohse D, Prosperetti A, Van Wijngaarden L (2008) A sphere in a uniformly rotating or shearing flow. *Journal of Fluid Mechanics*, 600, 201–233. doi:10.1017/ S0022112008000438

Bocchiola D, Rulli MC, Rosso R (2005) Transport of large woody debris in the presence of obstacles. *Geomorphology*, 76, 1-2, 166–178. doi:10.1016/j.geomorph.2005.08.016

Bocchiola D, Rulli MC, Rosso R (2006) Flume experiments on wood entrainment in rivers *Advances in Water Resources* 29, 8, 1182–1195. doi.10.1016/j.advwatres.2005.09.006

Bocchiola D, Rulli MC, Rosso R (2008) A flume experiment on the formation of wood jams in rivers. *Water Resources Research*, 44, 2. doi:10.1029/2006WR005846

Bocchiola D (2011) Hydraulic characteristics and habitat suitability in presence of woody debris: A flume experiment. *Advances in Water Resources*, 34, 10, 1304–1319. doi:10.1016/j.advwatres.2011.06.011

Bombardelli, F. A., González, A. E., & Niño, Y. I. (2008). Computation of the particle Basset force with a fractional-derivative approach. *Journal of Hydraulic Engineering*, 134(10), 1513–1520. doi:10.1061/(ASCE)0733-9429(2008)134:10(1513)

Brach R (1989) Rigid body collisions. *ASME, Transactions, Journal of Applied Mechanics*, 56, 133–138.

Bradley JB, Richards DL, Bahner CC (2005) *Debris control structures: Evaluation and countermeasures.* US Department of Transportation, Federal Highway Administration.

Braudrick CA, Grant GE (2000) When do logs move in rivers? *Water Resources Research*, 36, 2, 571–583. doi:10.1029/1999WR900290

Braudrick CA, Grant GE (2001) Transport and deposition of large woody debris in streams: A flume experiment. *Geomorphology*, 41, 4, 263–283. doi:10.1016/S0169-555X(01)00058-7

Brennen CE (1982) *A Review of Added Mass and Fluid Inertial Forces*. Department of the Navy , Port Hueneme, CA, USA.

Brown D, Christian W (2011) Simulating what you see: combining computer modeling with video analysis. *Proceedings of MPTL16*, 15-17 September, Ljubljana.

Cadol D, Wohl E (2010) Wood retention and transport in tropical, headwater streams, La Selva biological station, Costa Rica. *Geomorphology* 123, 61–73. doi:10.1016/j.geomorph.2010.06.015

Chaplin JR, Subbiah K (1998) Hydrodynamic damping of a cylinder in still water and in a transverse current. *Applied Ocean Research*, 20(4), 251-259.

Chhabra RP, Agarwal L., Sinha NK (1999) Drag on non-spherical particles: an evaluation of available methods. *Powder Technology*, 101(3), 288-295. doi:10.1016/S0032-5910(98)00178-8

Chow CY (1979) An introduction to computational fluid mechanics. Seminole Publishing Company, Boulder, Colorado.

Chow VT (1959) Open channel hydraulics. McGraw-Hill Book Company, Inc; New York.

Comiti F, Mao L, Preciso E, Picco L, Marchi L, Borg M (2008) Large wood and flash floods: Evidence from the 2007 event in the Davča basin (Slovenia). *WIT Transactions on Engineering Sciences*, 60, 173–182. doi:10.2495/DEB080181

Comiti F, Agostino VD, Moser M, Lenzi MA, Bettella F, Agnese A D, Rigon E, Gius S, Mazzorana B (2012) Preventing wood-related hazards in mountain basins: from wood load estimation to designing retention structures. Proceedings of the 12th Congress INTERPRAEVENT, Grenoble, France 23–26.

Comiti F, Marchi L, Macconi P, Arattano M, Bertoldi G, Borga M, Brardinoni F, Cavalli M, D'Agostino V, Penna D, Theule J (2014) A new monitoring station for debris flows in the European Alps: first observations in the Gadria basin. *Natural Hazards*, 73(3), 1175–1198. doi:10.1007/s11069-014-1088-5

Comiti F, Lucía A, Rickenmann D (2016) Large wood recruitment and transport during large floods: A review. *Geomorphology*, 269, 23–39. doi:10.1016/j.geomorph.2016.06.016

Corrsin S, Lumley J (1956) On the equation of motion for a particle in turbulent fluid. *Applied Science Research*, Sect A, 6, 114–116. doi:10.1007/BF03185030

Corsini A, Ciccarese G, Diena M, Truffelli G, Alberoni PP, Amorati R (2017) Debris flows in Val Parma and Val Baganza (Northern Apennines) during the 12-13th October 2014 alluvial event in Parma province (Italy). *Italian Journal of Engineering Geology and Environment*, 29–38. doi:10.4408/IJEGE.2017-01.S-03

Costabile P, Macchione F, Natale L, Petaccia G (2015) Flood mapping using LIDAR DEM. Limitations of the 1-D modeling highlighted by the 2-D approach. *Natural Hazards*, 77, 2, 181–204. doi:10.1007/s11069-015-1606-0

Costabile P, Costanzo C, Macchione F (2016) Performances and limitations of the diffusive approximation of the 2-d shallow water equations for flood simulation in urban and rural areas. *Applied Numerical Mathematics*, 116, 141–156. doi:10.1016/j.apnum. 2016.07.003

Cowan WL (1956) Estimating hydraulic roughness coefficients. *Agricultural Engineering*, 473 – 475.

Cox RG (1970) The motion of long slender bodies in a viscous fluid part 1. General theory. *Journal of Fluid Mechanics*, 44(4), 791–810. doi:10.1017/S002211207000215X

Cox RG (1971) The motion of long slender bodies in a viscous fluid. Part 2. Shear flow. *Journal of Fluid Mechanics*, 45(4), 625–657. doi:10.1017/S0022112071000259

Crosato A, Rajbhandari N, Comiti F, Cherradi X, Uijttewaal W (2013) Flume experiments on entrainment of large wood in low-land rivers. *Journal of Hydraulic Research*, 51, 5, 581–588. doi:10.1080/00221686.2013.796573

Cunge JA, Holly FM, Verwey A (1980) Practical aspects of computational river hydraulics. Pitman, London.

Dean RG and Dalrymple RA (1991) Water wave mechanics for engineers and scientists, Advanced Series on Ocean Engineering.

De Cicco PN, Paris E, Solari L (2015) Flume experiments on bridge clogging by woody debris: the effect of shape of piers. Proceedings of the 36th IAHR World Congress, The Hague, The Netherlands.

Denk M, Rimböck A (2008) Driftwood retention, bedload retention, and debris flow retention with flexible ring net barriers [Schwemmholz-, geschiebe-und murgangrückhalt mit flexiblen ringentzsperren].VAW-Mitteilung ETH Zurich, 207, 431–400 (in German).

Devillers O, Pion S, Teillaud M (2001) Walking in a triangulation. *International Journal of Foundations of Computer Science*, 13, 2, 181-199.

Diehl TH (1997) *Potential drift accumulation at bridges.* US Department of Transportation, Federal Highway Administration, Research and Development, Turner-Fairbank Highway Research Center.

Dorgan AJ, Loth E (2007) Efficient calculation of the history force at finite Reynolds numbers. *International Journal of Multiphase Flow*, 33(8), 833–848. doi:10.1016/j.ijmultiphaseflow.2007.02.005

Fekken G, Veldman AEP, Buchner B (1999) Simulation of green-water loading using the Navier-Stokes equations. *Proceedings 7th Intern. Conf. on Numerical Ship Hydrodynamics, Nantes*, 1, 745-752.

Fenocchi A, Petaccia G, Sibilla S (2016) Modelling flows in shallow (fluvial) lakes with prevailing circulations in the horizontal plane: limits of 2D compared to 3D models, *Journal of Hydroinformatics*, 18, 928–945. doi:10.2166/hydro.2016.033

Fewtrell TJ, Duncan A, Sampson CC, Neal JC, Bates PD (2011) Benchmarking urban flood models of varying complexity and scale using high resolution terrestrial LiDAR data. *Physics and Chemestry of the Earth*, 36, 7-8, 281–291. doi:10.1016/j.pce.2010.12.011

Geng YAN, Dalhaimer P, Cai S, Tsai R, Tewar, M, Minko T, Discher DE (2007) Shape effects of filaments versus spherical particles in flow and drug delivery. *Nature nanotechnology*, *2*(4), 249–255. doi:10.1038/nnano.2007.70

Gippel CJ, O'Neill IC, Finlayson BL, Schnatz INGO (1996) Hydraulic guidelines for the re-introduction and management of large woody debris in lowland rivers. *Regulated Rivers Research & Management*, 12(23), 223–236.

Gurnell A (2012) Fluvial geomorphology: Wood and river landscapes. *Nature Geoscinence*, 5, 2, 93–94. doi:10.1038/ngeo1382

Hartlieb A (2012) Physical scale model tests on the clogging of a spillway by large wood [Modellversuche zur Verklausung von Hochwasserentlastungsanlagen mit Schwemmholz]. *Wasserwirtschaft*, 6, 98–9104 (in German).

Hecker C (1997) Physics, Part 3: Collision response. Game Developer Magazine, 11–18.

Van Hinsberg MAT, ten Thije Boonkkamp JHM, Clercx HJH (2011) An efficient, second order method for the approximation of the Basset history force. *Journal of Computational Physics*, 230(4), 1465–1478. doi:10.1016/j.jcp.2010.11.014

Hirsch C (2007) Numerical computation of internal and external flows. Butterworth-Heinmann, Oxford.

Haehnel RB, Daly SF (2004) Maximum impact force of woody debris on floodplain structures. *Journal of Hydraulic Engineering*, *130*(2), 112-120. doi:10.1061/(ASCE)0733-9429(2004)130:2(120)

Hoang MC, Laneville A, Légeron F (2015) Experimental study on aerodynamic coefficients of yawed cylinders. *Journal of Fluids and Structures*, 54, 597-611. doi:10.1016/j.jfluidstructs.2015.01.002

Hoerner, S. F. (1965). Fluid-dynamic drag: practical information on aerodynamic drag and hydrodynamic resistance. Hoerner Fluid Dynamics.

Holloway JV, Rillig MC, Gurnell AM (2017). Underground riparian wood: Reconstructing the processes influencing buried stem and coarse root structures of Black Poplar (Populus nigra L.). *Geomorphology*, *279*, 199–208. doi:10.1016/j.geomorph.2016.07.027

Hunter NM, Bates PD, Neelz S, Pender G, Villanueva I, Wright NG, Liang D, Falconer RA, Lin B, Waller S, Crossley AJ, Mason DC (2008) Benchmarking 2D hydraulic models for urban flooding. *Proceedings of the institution of civil engineers: water management*, 161(1), 13–30. doi:10.1680/wama.2008.161.1.13

Hürlimann M, Rickenmann D, Graf C (2003) Field and monitoring data of debris-flow events in the Swiss Alps. *Canadian Geotechnical Journal*, 40(1), 161–175. doi:10.1139/t02-087

Hygelund B, Manga M (2003) Field measurements of drag coefficients for model large woody debris. *Geomorphology*, 51(1), 175-185.

IshikawaY (1989) Studies on disasters caused by debris flows carrying logs down mountain streams. Ph.D. Dissertation, Kyoto University, Japan.

Jeffery GB (1922) The motion of ellipsoidal particles immersed in a viscous fluid. *Proceedings of the Royal Society of London A: Mathematical, physical and engineering sciences* 102(715), 161–179.

Kasai S, Ohgi Y, Mizoguchi I, Matsuda A, Aramaki H, Tanami M (1996) Structural characteristics of wood-debris entrapment facilities. Proceedings of *INTERPRAEVENT Conf*erence, Garmisch-Partenkirchen, Germany, 5, 271– 277.

Keller, E. A., & Swanson, F. J. (1979). Effects of large organic material on channel form and fluvial processes. *Earth Surface Processes and Landforms*, 4(4), 361-380.

Lange D, Bezzola GR (2006) Driftwood: problems and solutions [Schwemmholz: Probleme und Lösungsansätze]. VAW-Mitteilung ETH Zurich, 188, 1–125 (in German)

Lenzi MA, Picco L, Bettella F (2013) Sediment management (including LW). Presentation of Work Package 7 within the project SedAlp, Sediment Management in alpine basins: integrating sediment continuum, risk mitigation and hydropower.

Lucía A., Antonello A, Campana D, Cavalli M, Crema S, Franceschi S, Marchese E, Niedrist M, Schneiderbauer S, Comiti F (2015) Monitoring and modeling marge wood recruitment and transport in a mountain basin of North-Eastern Italy. In: Lollino G, Arattano M, Rinaldi M, Giustolisi O, Marechal JC, Grant G (eds) Engineering Geology for Society and Territory - Volume 3. Springer, Cham. doi:10.1007/978-3-319-09054-2_31

MacVicar B, Piégay H (2012) Implementation and validation of video monitoring for wood budgeting in a wandering piedmont river, the Ain River (France). *Earth Surface Processes and Landforms*, 37, 1272–1289. doi:10.1002/esp.3240.

Magnaudet J and Eames I (2000) The motion of high-reynolds-number bubbles in inhomogeneous flows. *Annual Review of Fluid Mechanics*, 32, 659–708. doi:10.1146/annurev.fluid.32.1.659

Mandø M, Rosendahl L (2010) On the motion of non-spherical particles at high Reynolds number. *Powder Technology*, 202, 1-3, 1–13. doi:10.1016/j.powtec.2010.05.001

Marchildon EK, Clamen A, Gauvin WH (1964) Drag and oscillatory motion of freely falling cylindrical particles. *The Canadian Journal of Chemical Engineering*, 42(4), 178-182. doi: 10.1002/cjce.5450420401

Martínez-Gomariz E, Gómez M, Russo B (2016). Experimental study of the stability of pedestrians exposed to urban pluvial flooding. *Natural Hazards*, 82(2), 1259-1278. doi: 10.1007/s11069-016-2242-z

Maxey MR, Riley JJ (1983) Equation of motion for a small rigid sphere in a nonuniform flow. *Physics of Fluids*, 26, 4, 883–889. doi:10.1063/1.864230

Mazzorana B, Hübl J, Zischg A, Largiader A (2011) Modelling woody material transport and deposition in alpine rivers. *Natural Hazards*, 56, 2, 425–449. doi:10.1007/s11069-009-9492-y

Melville BW (1975) Local scour at bridge sites. Ph.D. Dissertation, University of Auckland, New Zeland.

Merten E, Finlay J, Johnson L, Newman R, Stefan H, Vondracek B (2010) Factors influencing wood mobilization in streams. *Water Resources Research*, 46, 10, W10514. doi:10.1029/2009WR008772

Merten EC, Vaz PG, Decker-Fritz JA, Finlay JC, Stefan HG (2013) Relative importance of breakage and decay as processes depleting large wood from streams. *Geomorphology* 190, 40–47. doi:10.1016/j.geomorph.2013.02.006.

Meyer M, Barr A, Lee H, Desbrun M (2002) Generalized barycentric coordinates on irregular polygons. *Journal of Graphics Tools*, 7(1), 13-22. doi:10.1080/10867651.2002.10487551

Michaelides EE (1992) A novel way of computing the Basset term in unsteady multiphase flow computations. *Physics of Fluids A: Fluid Dynamics*, 4(7), 1579–1582. doi:10.1063/1.858430

Mordant N, Pinton JF (2000) Velocity measurement of a settling sphere. *European Physical Journal B*, 18, 343–352. doi:10.1007/PL00011074

Murase Y (1984) Friction of wood sliding on various materials. *Journal of the Faculty of Agriculture, Kyushu University*, 28, 147–160.

Nepf HM (1999) Drag, turbulence, and diffusion in flow through emergent vegetation. *Water Resources Research*, *35*(2), 479-489. doi:10.1029/1998WR900069

Newman DJ, Karniadakis GE (1997) A direct numerical simulation study of flow past a freely vibrating cable. *Journal of Fluid Mechanics*, 344, 95–136. doi:10.1017/S002211209700582X

Van Nierop EA, Luther S, Bluemink JJ, Magnaudet J, Prosperetti A, Lohse D (2007) Drag and lift forces on bubbles in a rotating flow. *Journal of Fluid Mechanics*, 571, 439–454. doi:10.1017/S0022112006003387

Niño I, García M (1998) Using Lagrangian particle saltation observations for bedload sediment transport modelling. *Hydrological Processes*, 12, 1197–1218. doi:10.1002/(SICI)1099-1085(19980630)12:8<1197::AID-HYP612>3.0.CO;2-U

Olivieri S (2013) *Analysis of the forces acting on particles in homogeneous isotropic turbulence*. Master Degree Thesis, Università degli Studi di Genova.

Petaccia G (2003) *Propagazione di onde a fronte ripido per rottura di sbarramenti in alvei naturali*. Ph.D Dissertation, University of Pavia, Italy (in Italian).

Petaccia G, Soares-Frazão S, Savi F, Natale L, Zech Y (2010) Simplified versus detailed two-dimensional approaches to transient flow modeling in urban areas. *Journal of Hydraulic Engineering-ASCE*, 136, 4, 262–266. doi:10.1061/(ASCE)HY.1943-7900.0000154

Petaccia G, Leporati F, Torti E (2016) OpenMP and CUDA simulations of Sella Zerbino Dam break on unstructured grids, *Computer & Geosciences*, 20, 5, 1123–1132. doi:10.1007/s10596-016-9580-5

Picco L, Tonon A, Rainato R, Lenzi M (2016) Bank erosion and large wood recruitment along a gravel bed river. *Journal Of Agricultural Engineering*, 47(2), 72-81. doi:10.4081/jae.2016.488

Picco L., Bertoldi W, Comiti F (2017). Dynamics and ecology of wood in world rivers. *Geomorphology*, 279: 10–11. doi:10.1016/j.geomorph.2016.11.020

Prakash M, Rothauge K, Cleary PW (2014) Modelling the impact of dam failure scenarios on flood inundation using SPH. *Applied Mathematical Modelling*, 38(23), 5515-5534. doi:10.1080/19479832.2012.716084

Pritchard, R. W. (2013). 2011 to 2012 Queensland floods and cyclone events: Lessons learnt for bridge transport infrastructure. *Australian Journal of Structural Engineering*, 14(2), 167–176.

Rabinowicz E (1951) The nature of the static and kinetic coefficients of friction. *Journal of applied physics*, 22(11), 1373–1379. doi:10.1063/1.1699869

Ravazzolo D, Mao L, Picco L, Lenzi M A (2014). Tracking log displacement during floods in the Tagliamento River using RFID and GPS tracker devices. *Geomorphology*, 228, 226–233. doi:10.1016/j.geomorph.2014.09.012

Ravazzolo D, Mao L, Picco L, Sitzia T, Lenzi MA (2015) Geomorphic effects of wood quantity and characteristics in three Italian gravel-bed rivers. *Geomorphology*, 246, 79–89. doi:10.1016/j.geomorph.2015.06.012

Remaître A, Van Asch TW, Malet JP, Maquaire O (2008) Influence of check dams on debris-flow run-out intensity. *Natural Hazards and Earth System Sciences*, 8(6), 1403–1416.

Rodríguez H, Quarantelli EL, Dynes RD (2006). *Handbook of disaster research.* Handbooks of sociology and social research, Springer, New York.

Roe PL (1981) Approximate Riemann solvers, parameter vectors, and difference schemes. *Journal of Computational Physics*, 43, 2, 357–372. doi:10.1016/0021-9991(81)90128-5

Rosendahl L (2000) Using a multi-parameter particle shape description to predict the motion of non-spherical particle shapes in swirling flow. *Applied Mathematical Modelling*, 24(1), 11–25. doi:10.1016/S0307-904X(99)00023-2

Ruiz-Villanueva V, Bodoque JM, Díez-Herrero A, Bladé E (2014a) Large wood transport as significant influence on flood risk in a mountain village. *Natural Hazards*, 74, 2, 967–987. doi:10.1007/s11069-014-1222-4

Ruiz-Villanueva V, Bladé Castellet E, Díez-Herrero A, Bodoque JM, Sánchez-Juny M (2014b) Two-dimensional modelling of large wood transport during flash floods. *Earth Surface Processes and Landforms*, 39, 4, 438–449. doi:10.1002/esp.3456

Ruiz-Villanueva V, Piégay V, Gaertner V, Perret F, Stoffel M (2016) Wood density and moisture sorption and its influence on large wood mobility in rivers. *Catena*, 140, 182–194. doi:10.1016/j.catena.2016.02.001

Rubinow SI, Keller JB (1961) The transverse force on a spinning sphere moving in a viscous fluid. *Journal of Fluid Mechanics*, 11(3), 447-459. doi:10.1017/S0022112061000640

Russo B, Gómez M, Macchione F (2013) Pedestrian hazard criteria for flooded urban areas. *Natural Hazards*, 69(1), 251–265. doi:10.1007/s11069-013-0702-2

Saffman PGT (1965) The lift on a small sphere in a slow shear flow. *Journal of Fluid Mechanics*, 22(2), 385–400. doi:10.1017/S0022112065000824

Salvesen N, Tuck EO, Faltinsen O (1970) Ship motions and sea loads. *Trans. SNAME*, 78(8), 250–287.

Sarpkaya T (1986) Force on a circular cylinder in viscous oscillatory flow at low Keulegan–Carpenter numbers. *Journal of Fluid Mechanics*, 165, 61-71. doi:10.1017/S0022112086002999

Schenk ER, Moulin B, Hupp CR, Richter JM (2014) Large wood budget and transport dynamics on a large river using radio telemetry. *Earth Surface Processes and Landforms*, 39 (4), 487–498. doi:10.1002/esp.3463.

Schmocker L, Hager WH (2011) Probability of Drift Blockage at Bridge Decks. *Journal of Hydraulic Engineering-ASCE*, 137, 4, 470–479. doi:10.1061/(ASCE)HY.1943-7900.0000319

Schmocker L, Weitbrecht V (2013) Driftwood: Risk analysis and engineering measures. *Journal of Hydraulic Engineering-ASCE*, 139, 7, 683–695. doi:10.1061/(ASCE)HY.1943-7900.0000728

Silvestro F, Rebora N, Rossi L, Dolia D, Gabellani S, Pignone F, Trasforini E, Rudari R, De Angeli S, Masciulli C (2016a) What if the 25 October 2011 event that struck Cinque Terre (Liguria) had happened in Genoa, Italy? Flooding scenarios, hazard mapping and damage estimation. *Natural Hazards and Earth System Sciences*, *16*(8), 1737–1753. doi:10.5194/nhess-16-1737-2016

Silvestro F, Rebora N, Giannoni F, Cavallo A, Ferraris L (2016b) The flash flood of the Bisagno Creek on 9th October 2014: An "unfortunate" combination of spatial and temporal scales. *Journal of Hydrology*, 541, 50–62. doi:10.1016/j.jhydrol.2015.08.004

Solenthaler B, Bucher P, Chentanez N, Müller M, Gross M (2011) SPH Based Shallow Water Simulation. *Workshop on Virtual Reality Interaction and Physical Simulation VRIPHYS*, Bender, Erleben, Galin (Editors)

Soukal R, Málková M, Vomácka T, Kolingerová I (2011) Hybrid Walking Point Location Algorithm. *Proceedings of the 5th International Conference on Advanced Engineering Computing and Applications in Sciences*, November 20-25, Lisbon, Portugal.

Sridhar G, Katz J (1995) Drag and lift forces on microscopic bubbles entrained by a vortex. *Physics of Fluids*, 7(2), 389–399. doi:10.1063/1.868637

Steeb N, Rickenmann D, Badoux A, Rickli C, Waldner P (2017). Large wood recruitment processes and transported volumes in Swiss mountain streams during the extreme flood of August 2005. *Geomorphology*, 279, 112–127.

Stockstill RL, Daly SF, Hopkins MA (2009) Modeling floating objects at river structures. *Journal of Hydraulic Engineering-ASCE*, 135, 5, 403–414. doi:10.1061/(ASCE)0733-9429(2009)135:5(403)

Sukumar N, Tabarraei A (2004) Conforming polygonal finite elements. *International Journal for Numerical Methods in Engineering*, 61(12), 2045-2066. doi:10.1002/nme.1141

Tagawa Y, van der Molen J, van Wijngaarden L, Sun C (2013) Wall forces on a sphere in a rotating liquid-filled cylinder. *Physics of Fluids*, 25, 6, 063302. doi:10.1063/1.4811406

Takahashi, T. (2014). *Debris flow: mechanics, prediction and countermeasures.* CRC press.

Teng, J, Jakeman AJ, Vaze J, Croke BF, Dutta D, Kim S (2017) Flood inundation modelling: A review of methods, recent advances and uncertainty analysis. *Environmental Modelling & Software*, 90, 201-216. doi:10.1016/j.envsoft.2017.01.006

Teo FY, Xia J, Falconer RA, Lin B (2012). Experimental studies on the interaction between vehicles and floodplain flows. *International Journal of River Basin Management*, 10(2), 149–160.

Teo FY, Liew YS, Falconer RA, Lin B (2013) Estimation of flood hazard risk relating to vehicles. *Proceedings of the 35th IAHR World Congress*, 8-16 September, Chengdu, China.

Thome CR, Zevenbergen LW (1985) Estimating mean velocity in mountain rivers. *Journal of Hydraulic Engineering*, 111(4), 612–624. doi:10.1061/(ASCE)0733-9429(1985)111:4(612)

Tinker DB, Knight DH (2000) Coarse woody debris following fire and logging in Wyoming lodgepole pine forests. *Ecosystems*, 3(5), 472–483. doi:10.1007/s100210000041

Tonon A, Iroumé A, Picco L, Oss-Cazzador D, Lenzi MA (2017) Temporal variations of large wood abundance and mobility in the Blanco River affected by the Chaitén volcanic eruption, southern Chile. *Catena*, 156, 149–160. doi:10.1016/j.catena.2017.03.025

Toro E (2009) Riemann solvers and numerical methods for fluid dynamics: a practical introduction. Springer Berlin Heidelberg

Troesch AW, Kim SK (1991) Hydrodynamic forces acting on cylinders oscillating at small amplitudes. *Journal of Fluids and Structures*, 5(1), 113-126. doi:10.1016/0889-9746(91)80014-5

Truscott TT, Techet AH (2009) Water entry of spinning spheres. *Journal of Fluid Mechanics*, 625, 135–165. doi:10.1017/S0022112008005533

Tsuji Y, Morikawa Y, Mizuno O (1985) Experimental measurement of the Magnus force on a rotating sphere at low Reynolds numbers. *Journal of Fluids Engineering*, 107, 484. doi:10.1115/1.3242517

Uchiogi T, Shima J, Tajima H, Ishikawa Y (1996) Design methods for wood-debris entrapment. Proceedings of *INTERPRAEVENT Conf*erence, Garmisch-Partenkirchen, Germany, 5, 279–288.

Velasco M, Cabello À, Russo B (2016) Flood damage assessment in urban areas. Application to the Raval district of Barcelona using synthetic depth damage curves. *Urban Water Journal*, 13(4), 426–440. doi:10.1080/1573062X.2014.994005

Watts RG, Ferrer R (1987) The lateral force on a spinning sphere: Aerodynamics of a curveball. *American Journal of Physics*, 55(1), 40–44. doi:10.1119/1.14969

Welber M, Bertoldi W, Tubino M (2013) Wood dispersal in braided streams: Results from physical modelling. *Water Resources Research*, 49, 11, 7388–7400. doi:10.1002/2013WR014046

West GS, Apelt CJ (1982) The effects of tunnel blockage and aspect ratio on the mean flow past a circular cylinder with Reynolds numbers between 10^4 and 10^5. *Journal of Fluid Mechanics, 114,* 361-377. Doi:10.1017/S0022112082000202

White FM (1991) *Viscous fluid flow. Second edition*. McGraw-Hill.

Xia J, Teo FY, Lin B, Falconer RA (2011) Formula of incipient velocity for flooded vehicles. *Natural Hazards*, 58(1), 1–14. doi:10.1007/s11069-010-9639-x

Yin C, Rosendahl L, Knudsen KS, Sørensen H (2003) Modelling the motion of cylindrical particles in a nonuniform flow. *Chemical Engineering Science*, 58, 15, 3489–3498. doi:10.1016/S0009-2509(03)00214-8

Zdravkovich MM (1997) *Flow around Circular Cylinders: Volume 2: Applications* (Vol. 2). Oxford University Press.

Zhao M, Cheng L, Zhou T (2009) Direct numerical simulation of three-dimensional flow past a yawed circular cylinder of infinite length. *Journal of Fluids and Structures*, *25*(5), 831–847. doi:10.1016/j.jfluidstructs.2009.02.004